Model-based study of the five main influencing factors on the wind speed error of lidars in complex and forested terrain

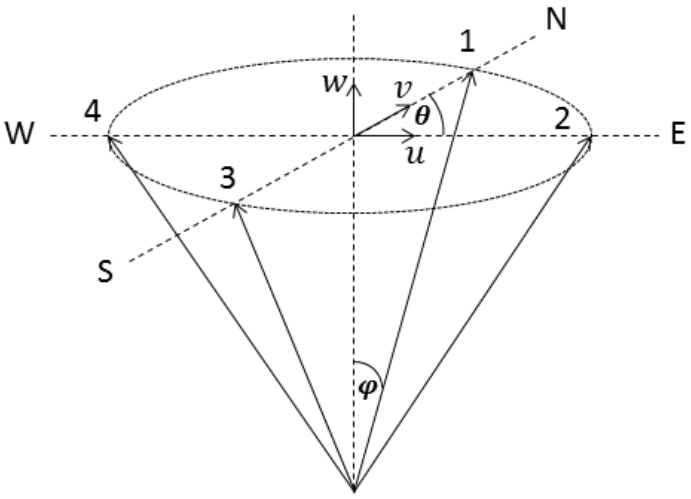

Inaugural-Dissertation

zur

Erlangung des Doktorgrades

der Mathematisch-Naturwissenschaftlichen Fakultät

der Universität zu Köln

vorgelegt von

Tobias Klaas

aus Hofgeismar

Universität zu Köln

Fraunhofer IEE

Berichterstatter (Gutachter):	Prof. Dr. Stefan Emeis Prof. Dr. Yaping Shao
Tag der letzten mündlichen Prüfung:	Dienstag, 5. Mai 2020

Contents

Abstract

Wind energy will significantly contribute to renewable power generation in the future. Much of the onshore wind energy potential is located at complex and forested sites. Remote sensing, in particular, light detection and ranging (lidar), has become a valuable technology to assess the wind resource at hub height of modern wind turbines. However, common wind profile Doppler lidars suffer from errors at complex terrain sites because of their measurement principle that assumes homogeneous flow between the measurement points.

This dissertation answers the question about how well lidars measure at complex terrain sites. The five main influencing factors on the lidar error are orographic complexity, measurement height, surface roughness and forest, atmospheric stability and half-cone opening angle. Structured by five hypotheses, the impact of the different factors is analyzed in a model-based parameter study.

In a novel approach, the lidar error due to orographic complexity ε is split up into the part ε_c, caused by flow curvature at the measurement points of the lidar and the part ε_s, caused by the local speed-up effects between the measurement points. This approach, e.g., allows for a systematic and complete interpretation of the influence of the half-cone opening angle φ of the lidar. It also provides information about the uncertainty of simple lidar error estimations that are based on inflow and outflow angles at the measurement points.

A non-dimensional approach is chosen to ensure the transferability of the acquired results to actual applications at real-world sites. The model-based parameter study is limited to two-dimensional Gaussian hills with hill height H and hill half-width L, facilitating the possibility to cover a wide range of terrain complexities and variations of the model parameters. H/L and z/L are identified as the main scaling factors for the lidar error. With a potential flow model, the linearized flow model WEng and the RANS CFD model Meteodyn WT, three models of different complexity are used. The outcome of the study provides manifold findings that enable an assessment of the applicability of these flow models.

Separating the lidar error ε into ε_c and ε_s shows that, depending on the z/L ratio, speed-up effects cause 10-30 % of the total lidar error. Therefore, a significant uncertainty must be assigned on simple lidar error estimation approaches, which are based on flow inclination angles at the measurement points and neglect this effect.

Orographic complexity is found to be the major influencing factor on the lidar error. Depending on the flow model used, the lidar error is about 4-5 times larger when increasing the H/L ratio from 0.1 to 0.4. It is furthermore dependent on measurement height and reaches a maximum at a z equal to 50-60 % of the hill half-width L. Below and above the maximum point, the lidar error decreases and becomes negligible at low and high levels above ground. The height-dependence is sensitive to H/L and z/L and should be assessed before a planned measurement campaign.

Opposed effects of reduced φ are found on ε_c and ε_s. This explains the small differences in the total lidar error for symmetric flows in the literature. Contrary to that, in asymmetric flow situations (e.g. forested hills), φ can significantly influence the lidar error. An adaption to the actual flow situation might reduce the lidar error, but would require a more flexible technology, such as a scanning lidar.

Non-linear or detached flow effects in the lee of the steep hills, induced by high surface roughness or forest, significantly reduce the lidar error. Therefore, potential flow and linearized models should not be applied at such sites, as they generally overestimate the lidar error. In an evaluation campaign, these findings are confirmed and the best results of lidar error estimation are achieved when considering the forest in the flow model.

The influence of atmospheric stability in the lidar error estimations from Meteodyn WT is significant, particularly for stable stratification. At sites where significant changes in atmospheric stability occur, the lidar error is potentially overestimated by assuming neutral stratification.

The dissertation clearly shows that orographic complexity, roughness and forest characteristics, as well as atmospheric stability, have a significant influence on lidar error estimation. The choice and parameterization of flow models and the design of methods for lidar error estimation are essential to achieve accurate results. The use of a RANS CFD model in conjunction with an appropriate forest model is highly recommended for lidar error estimations in complex terrain. If atmospheric stability variation at a measurement site plays a vital role, it should also be considered in the modeling. Under certain flow conditions, the half-cone opening angle can additionally affect the magnitude of the lidar error. When planning a wind farm, an accurate estimation of the prospective lidar error should be carried out before the measurement campaign. The additional uncertainty of the lidar error correction should be assessed in this context to make a profound decision on whether a lidar measurement is feasible at the given site.

Kurzzusammenfassung

Die Windenergie wird in Zukunft einen wesentlichen Beitrag zur erneuerbaren Stromerzeugung leisten. Ein Großteil des Onshore-Windenergiepotenzials befindet sich an komplexen und bewaldeten Standorten. Die Fernerkundung, insbesondere light detection and ranging (Lidar), hat sich zu einer wertvollen Technologie zur Beurteilung der Windressourcen in Nabenhöhe moderner Windkraftanlagen entwickelt. Die gängigen Windprofil-Doppler-Lidars leiden jedoch im komplexen Gelände unter Fehlern, da ihr Messprinzip eine homogene Strömung zwischen den Messpunkten voraussetzt.

Diese Dissertation beantwortet die Frage, wie gut Lidars an komplexen Standorten messen. Die fünf wichtigsten Einflussfaktoren auf den Lidarfehler sind orographische Komplexität, Messhöhe, Oberflächenrauigkeit und Wald, atmosphärische Stabilität und Öffnungswinkel des Lidars. Strukturiert durch fünf Hypothesen, wird die Auswirkung der verschiedenen Faktoren in einer modellbasierten Parameterstudie analysiert.

In einem neuartigen Ansatz wird der Lidarfehler durch orographische Komplexität ε in einen Teil ε_c, verursacht durch die Strömungskrümmung an den Messpunkten des Lidars, und einen Teil ε_s, verursacht durch die lokalen Beschleunigungseffekte zwischen den Messpunkten, aufgeteilt. Dieser Ansatz ermöglicht z.B. eine systematische und vollständige Interpretation des Einflusses des Öffnungswinkels. Er liefert auch Informationen über die Unsicherheit einfacher Lidar-Fehlerschätzungen, die ausschließlich auf den Strömungswinkeln an den Messpunkten basieren.

Es wird ein nichtdimensionaler Ansatz gewählt, um die Übertragbarkeit der gewonnenen Ergebnisse auf tatsächliche Anwendungen an realen Standorten zu gewährleisten. Die modellbasierte Parameterstudie beschränkt sich auf zweidimensionale Gaußsche Hügel mit Hügelhöhe H und Hügelhalbbreite L, was die Möglichkeit bietet, ein breites Spektrum an Geländekomplexitäten und Variationen der Modellparameter abzudecken. H/L und z/L werden als die wichtigsten Skalierungsfaktoren für den Lidarfehler identifiziert. Mit einem Potentialflussmodell, dem linearisierten Strömungsmodell WEng und dem RANS CFD-Modell Meteodyn WT werden drei Modelle unterschiedlicher Komplexität verwendet. Das Ergebnis der Studie liefert vielfältige Ergebnisse, die eine Beurteilung der Anwendbarkeit dieser Strömungsmodelle ermöglichen.

Die Aufteilung des Lidarfehlers ε in ε_c und ε_s zeigt, dass je nach z/L-Verhältnis Beschleunigungseffekte 10-30 % des gesamten Lidarfehlers verursachen. Daher muss bei einfachen Ansätzen zur Lidar-Fehlerschätzung, die auf Strömungsneigungswinkeln an den Messpunkten basieren und diesen Effekt vernachlässigen, eine signifikante Unsicherheit angenommen werden.

Die orographische Komplexität ist der wichtigste Einflussfaktor auf den Lidarfehler. Abhängig vom verwendeten Strömungsmodell ist der Lidarfehler etwa 4-5 mal größer, wenn das H/L-Verhältnis von 0,1 auf 0,4 erhöht wird. Er ist außerdem von der Messhöhe abhängig und erreicht ein Maximum bei 50-60 % der Hügelhalbbreite L. Unter- und oberhalb des Maximalpunktes nimmt der Lidarfehler ab und wird bei niedrigen und großen Höhen über Grund vernachlässigbar. Die Höhenabhängigkeit ist abhängig von H/L und z/L und sollte vor einer geplanten Messkampagne bewertet werden.

Es zeigen sich gegenläufige Effekte von reduzierten φ auf ε_c und ε_s. Dies erklärt die kleinen Unterschiede im gesamten Lidarfehler für symmetrische Strömungen in der Literatur. Im Gegensatz dazu kann φ in asymmetrischen Strömungssituationen (z.B. bewaldete Hügel) den Lidarfehler erheblich beeinflussen. Eine Anpassung an die aktuelle Strömungssituation könnte den Lidarfehler reduzieren, erfordert aber eine flexiblere Technologie, wie z.B. ein scannendes Lidar.

Nichtlineare oder abgelöste Strömung im Lee von steilen Hügeln, hervorgerufen durch hohe Oberflächenrauheit oder Wald, reduzieren den Lidarfehler deutlich. Potentialströmungs- und linearisierte Modelle sollten daher an solchen Standorten nicht angewendet werden, da sie den Lidarfehler im Allgemeinen überschätzen. In einer Messkampagne werden diese Ergebnisse bestätigt und die besten Ergebnisse der Lidar-Fehlerschätzung bei der Berücksichtigung des Waldes im Strömungsmodell erzielt.

Der Einfluss der atmosphärischen Stabilität auf die Lidar-Fehlerschätzung von Meteodyn WT ist signifikant, insbesondere für stabile Schichtung. An Standorten, an denen signifikante Veränderungen der atmosphärischen Stabilität auftreten, wird der Lidarfehler möglicherweise durch die Annahme einer neutralen Schichtung überschätzt.

Die Dissertation zeigt deutlich, dass orographische Komplexität, Rauigkeit und Waldeigenschaften sowie atmosphärische Stabilität einen signifikanten Einfluss auf die Lidar-Fehlerschätzung haben. Die Auswahl und Parametrisierung von Strömungsmodellen sowie die Entwicklung von Methoden zur Lidar-Fehlerschätzung ist wichtig, um genaue Ergebnisse zu erzielen. Die Verwendung eines RANS-CFD-Modells in Verbindung mit einem geeigneten Waldmodell wird für Lidar-Fehlerschätzung in komplexem Gelände dringend empfohlen. Wenn die Variation der atmosphärischen Stabilität an einem Messstandort von Bedeutung ist, sollte sie auch bei der Modellierung berücksichtigt werden. Unter bestimmten Strömungsbedingungen kann der Öffnungswinkel die Größe des Lidarfehlers zusätzlich beeinflussen. Bei der Planung eines Windparks sollte vor der Messkampagne eine genaue Abschätzung der voraussichtlichen Lidarfehler durchgeführt werden. Die zusätzliche Unsicherheit der Lidar-Fehlerkorrektur sollte in diesem Zusammenhang bewertet werden, um eine fundierte Entscheidung darüber zu treffen, ob eine Lidarmessung am jeweiligen Standort möglich ist.

Danksagung

Ich möchte an dieser Stelle allen, die mich auf meinem Weg zur Vollendung meiner Promotion unterstützt und begleitet haben herzlich danken.

Bei Herrn Prof. Dr. Stefan Emeis bedanke ich mich für die hervorragende Betreuung und die vielen Stunden, die er mit dem Lesen meiner Arbeit verbracht hat. Die Vielzahl konstruktiver und offener Gespräche und Diskussion waren für mich stets wertvolle Leitplanken und Denkanstöße, die mir geholfen haben mein Ziel zu erreichen.

Insbesondere meinem Kollegen Doron Callies danke ich für die viele Zeit für Gespräche, Diskussionen und das Korrekturlesen meiner Arbeit sowie den hilfreichen Erfahrungsaustausch. Bei meinen Kollegen Lukas Pauscher, Paul Kühn, Zouhair Khadiri-Yazami, Richard Döpfer, Klaus Otto und Florian Jäger, bedanke ich mich für die vielen anregenden Gespräche, den Austausch von Ideen und Erfahrungen sowie die Unterstützung.

Ein besonderer Dank gilt meinen Eltern, die mir die Möglichkeit zum Studium und damit zur Promotion eröffnet und mich auch in den zurückliegenden Jahren stets unterstützt haben. Meinem Bruder Oliver, der stets ein offenes Ohr und einen guten Rat für mich hatte, danke ich ebenfalls.

Nicht zuletzt danke ich herzlich meiner Partnerin Claudia, die mich, gerade in der intensiven, abschließenden Phase meiner Promotion, Tag für Tag unterstützt, mir stets Mut gemacht und den Rücken freigehalten hat. Erst dadurch konnte ich mich voll und ganz auf meine Arbeit konzentrieren. Für die vielen schönen Stunden, in denen ich neue Kraft und Energie schöpfen konnte, danke ich außerdem Carlotta, Kalle und meiner Tochter Ida.

1 Introduction

The introductory chapter starts with a general background and motivation for the topic (chapter 1.1). Then, the structure of the thesis is explained, providing an overview to guide the reader through the text (chapter 1.2). Following this, a profound literature review is presented (chapter 1.3), that serves as a basis for positioning the research questions and the scientific work of this thesis into the scholarly debate (chapter 1.4).

1.1 Background and motivation

The following subchapters provide basic information about climate change (chapter 1.1.1)., the necessity of the energy transition to renewable energy sources and the political framework to enable this transition (chapter 1.1.2).Then, the need to develop forested, complex terrain sites for wind energy projects is explained, in order to make use of the available wind energy potential (chapter 1.1.3). A brief introduction to the research on wind conditions in complex terrain is also given, which provides a starting point to this topic for the reader (chapter 1.1.4). Here, also, the overall aim of this doctoral thesis is described.

1.1.1 Climate change and global warming

In its recent Synthesis Report, the Intergovernmental Panel on Climate Change (IPCC) states that "Warming of the climate system is unequivocal […]" (IPCC 2015, p. 2). Moreover, it is clearly linked to the anthropogenic emissions of greenhouse gases, which have led to atmospheric concentrations of carbon dioxide, methane and nitrous oxide, higher than in the previous 800,000 years. The negative impacts of climate change have already been observed all over the world (IPCC 2015). The latest estimates of IPCC attribute approximately 1.0°C of global warming by 2017 to human activities, which underlines the need to strongly decrease greenhouse gas emissions in the future (IPCC 2018).

In terms of an integrated strategy for sustainable future development, the defossilization of electrical power generation is one of the critical aspects in order to avoid or at least mitigate predicted impacts and lower the risks of climate change (IPCC 2015). So far, 185 nations have ratified the Paris Agreement 2016, which aims at limiting global warming to approximately 2 °C by the end of the century (UNFCCC 2019, 2016). To reach this goal, the share of low-carbon electricity supply has to be increased to more than 80 % by 2050, which includes the use of renewable energy (IPCC 2015, p. 26).

1.1.2 European and German renewable energy politics

In 2009 the European Union (EU) had set its long term goal to reduce greenhouse gases by 80-95 % until 2050 (European Commission 2018). Resulting from the EU politics, in 2016, the share of renewable electricity in the EU reached 29.6 % and has more than doubled within ten years. With a share of 27 % of this renewable electricity, onshore wind energy delivers the second largest part of electricity from renewable energy sources in the EU, only topped by hydropower (EEA 2018). This increase is according to the EU targets set up by the directive on the use of energy from renewable sources from 2009, aiming at a share of approx. 34 % by 2020 (European Commission 2019; The European Parliament and the Council of the European Union 2009).

Following the targets of the recently released succeeding directive, the share of renewable electricity will increase up to 57 % until 2030. Wind power will then be the most essential element of the power system, delivering 26 % of EU's electrical power (The European Parliament and the Council of the European Union 2018; Buck et al. 2019).

In 2010 the German government passed its energy concept that sets Germany's long term goals to "[…] secure a reliable, economic and sustainable energy supply […]" (Bundesregierung 2010, p. 3). It adapts the targets of the international and European agreements to reduce greenhouse gas emissions by 80 to 95 % until 2050. Regarding the share of renewable electricity, Germany aims at 50 % until 2030 and 80 % until 2050 (Bundesregierung 2010). In 2016 it had reached 31,6 % (BMWI 2018b). In 2017 the share of renewable electricity in Germany passed one third, with 2017 being a record year regarding the installation of 5,514 MW of new onshore wind power capacity. About 50 % of renewable electrical power was produced by onshore wind energy in 2017. Estimations of the Fraunhofer Institute for Energy Economics and Energy System Technology IEE[1] expect an increase in onshore wind power capacity by about 20 GW up to almost 70 GW until 2030 (Rohrig 2018).

1.1.3 Wind energy potential

Considering these ambitious goals, the question arises, if the overall wind energy potential in Europe and Germany is available to reach the aspired wind power capacity. One of the key findings of the European Environment Agency's study on Europe's wind energy potential was that wind energy could cover 20 times the energy demand of the whole European Union expected in 2020. Additionally, it is found that a significant share of the area available for wind power is situated in forested areas, which often comes together with complex mountainous or hilly terrain (EEA 2009).

In Germany, several more detailed studies followed to find a better estimate for the wind energy potential regarding the quantity and type of available area, the technical potential and its sensitivity to restrictions due to environmental or other constraints (Lütkehaus et al. 2013; Callies 2014; Masurowski 2016). In his study based on high-resolution geographic data, Callies 2014 states that more than 50 % of the available area for wind energy in Germany can be found in forests. Historically forested areas are further away from settlements, which are usually placed in valleys, surrounded by agricultural land (Callies 2014).

More and more wind farms have been installed in forested terrain. In order to make use of the wind resources at such sites, a diversification of wind turbine characteristics has taken place. While there is a general increase of hub height, turbine power and rotor diameter, the relation of the latter two is strongly dependent on the actual site. Mostly large rotor diameters come together with relatively low rated power at inland sites with lower mean wind speeds. Additionally, to overcome the impact of the rough,

[1] Fraunhofer IEE has become an independent Fraunhofer institute in January 2018. Previously, it has been founded as Fraunhofer Institute for Wind Energy and Energy System Technology IWES. The first project phase of "Utilization of Wind Power" started in 2009 and was managed by Dr. Doron Calllies. This first phase involved the erection of the 200 m high measurement mast as well as the acquisition of several Leosphere Windcube v1 Doppler wind lidars. The second project phase, starting as of January 2012, was managed by the author of this thesis. It contained several measurement campaigns to compare lidar data to data from cup anemometry on the measurement mast.

forested surface, hub heights at these sites are reaching up to 160 m, increasing the upper tip height of the turbines to about 230 m (Rohrig 2018; Emeis 2014).

1.1.4 Research on wind in complex and forested terrain

These findings and developments emphasize the need to assess the usability of those sites for wind turbine installations and to gain a better understanding of the wind resources over forested and orographically complex terrain in recent years. Research on complex terrain has been on the agenda of European and national research programs for many years (TPWind 2014; ETIP Wind 2016, 2018; BMWI 2014, 2018a). Still, there is a need for better understanding, measuring and modeling of the wind conditions at complex terrain sites. To accurately assess the resources of potential wind energy sites, the latest German research program emphasizes the need for appropriate and economical methods that might replace met masts (BMWI 2018a, p. 40). The general aim of research on wind resource assessment is a significant reduction of the overall uncertainty in the predicted annual energy production from currently 10-15 % to well below 10 % (TPWind 2014). Having in mind the dimensions of current wind turbines, the only economically feasible way for this will be the extension or replacement of conventional, mast-based measurement techniques by novel technologies that can measure the wind conditions at great heights, best over the full rotor area (TPWind 2014; BMWI 2018a).

Optical remote sensing, namely light detection and ranging (lidar), has proven to be one of the most promising measurement technologies to achieve these goals (Emeis et al. 2007; Emeis 2014; Bradley et al. 2015; Courtney et al. 2008). However, commonly used lidar devices are prone to wind speed errors in complex terrain (Bradley et al. (2015)).

Building upon the current state of research on this topic (chapter 1.3), the aim of this thesis is to perform a systematic model-based study, that answers the question: How well do lidars measure at complex terrain sites and which factors are influencing the magnitude of the so-called "lidar error[2]"?

1.2 Structure of the thesis

The thesis starts with a general introduction to the background and motivation for the topic and the main research question of the thesis (chapter 1.1). The aim of the introduction is to point out the overall importance of the topic of wind measurements in complex and forested terrain. Moreover, it leads to the fundamental aim of the thesis. Then, chapter 1.2 explains the structure to guide the reader through the text. The sub-chapter lays out the "red thread" of the thesis and clarifies its design. A profound literature study has been part of the work within the doctoral thesis. The results of this are given in chapter 1.3. Based on the analysis of the available literature, open questions and gaps in the state of research regarding the topic of the thesis are identified. Chapter 1.4 then develops the research questions of the doctoral thesis based on a structured summary of the literature review.

[2] In consistence with other related studies (e.g. Bingöl et al. 2009; Bradley et al. 2015; Klaas et al. 2015) the measurement error in wind speed due to complex terrain, that occurs for common Doppler wind profiling lidars, is termed as "lidar error" in the context of this thesis. This definition is detailed out in chapter 3.2.

Chapter 2 lays out the scientific structure and context of the dissertation. The aims of the thesis and five hypotheses are deduced in chapter 2.1. These hypotheses are used to structure the results and form the basis for the scientific work of this thesis. They are later referred to in the summary and conclusions in chapter 7. The novelty value of the work carried out in the context of this doctoral thesis is pointed out in chapter 2.2.

As the theoretical background about lidar measurement principles and error sources in complex terrain is of fundamental importance for the work within this thesis, it is detailed out in chapter 3. Basic equations and definitions of variables and parameters of the measurement geometry are given in subchapter 3.1. The aim of subchapter 3.2 is to explain error sources in complex terrain and provide definitions of the lidar error.

Chapter 4 gives an overview of the methods used in this thesis. Chapters 4.1 and 4.2 aim on presenting basic knowledge about wind flow in complex and forested terrain as well as the influence of atmospheric stability on wind characteristics. To estimate the wind flow over two-dimensional hills and to answer the research questions that are defined beforehand, three different models are. In order to provide the theoretical fundaments for the application of these models and the analyses of their results, their basic working principles and equations are given in chapter 4.3. The method that is used to carry out the systematic model-based parameter study is then elaborated in chapter 4.4. This chapter provides the reasons for doing a non-dimensional analysis and defines the non-dimensional parameters that are used. Having explained the methods and approach, the data basis and setup for the modeling are given in chapter 4.5.

The results of the parameter study are presented in chapter 5. To understand the impact of different model parameterization on the wind flow, the model results are illustrated in chapter 5.1. In the subchapters 5.1.2 and 5.1.3, the flow angles and speed-up effects are presented in detail as they are of major importance for the resulting lidar errors. Chapter 5.1 is, therefore, helping to interpret the influence of model parameterization on lidar errors in complex terrain. Chapter 0 then contains the results of the lidar error estimation for the different models. It is structured with reference to the research questions and hypothesis and consecutively presents the results for orographic complexity (chapter 5.2.1), terrain roughness (chapter 5.2.2), forest (chapter 5.2.3) and atmospheric stability (chapter 5.2.4) as well as for the influence of measurement height (chapter 5.2.5) and changing the half-cone opening angle (chapter 5.2.6).

Having carried out the model-based study, the question remains of how well the results agree with real-world measurements. In chapter 6, a measurement campaign in complex and forested terrain is used to evaluate the model results. After a short description of the measurement site (chapter 6.1.1) and the data basis (chapter 6.1.2), an evaluation approach is described that allows to compare the non-dimensional results to the measured lidar error by fitting the terrain from the site to Gaussian hill shapes (chapter 6.2). The evaluation results are then presented in two different ways. First, based on mean statistics and lidar-mast deviations in dependence on wind direction (chapter 6.3.1). Second, following the non-dimensional approach, where the measured lidar errors are assigned to results from the parameter-study. Chapter 6.4 concludes the evaluation by presenting flow model results for lidar error estimation based on the actual three-dimensional terrain data at the measurement site for different parametrizations.

The key findings of the thesis are summed up in chapter 7. The hypotheses formulated in chapter 1.4 are evaluated and contrasted to the achieved results. The aim of the

chapter is to provide a reasonable overview of what was found out during the course of the doctoral thesis. It assesses the importance of the different considered parameters and provides a guideline for the reader on the application of wind flow models for lidar error estimation in complex terrain.

An outlook regarding open research questions and further remarks is formulated in chapter 8.

1.3 Lidar wind measurements

This subchapter gives a broad overview of the topic of lidar wind measurements. A short synopsis of the historical development of wind lidars describes the way to today's most often used Doppler lidars (chapter 1.3.1). Then the reader is informed about the measurement accuracy of these lidars against conventional, mast-based anemometry in flat terrain (chapter 1.3.2). A short subchapter explains the differences between continuous-wave and pulsed Doppler lidars (chapter 1.3.3). As the issue of measuring the wind in complex terrain site with wind lidars is in the focus of this work, a detailed literature overview on that is given in chapter 1.3.4. Brief introductions to the relevant standards and guidelines for wind measurements (chapter 1.3.5) and alternative methods and approaches to overcome the challenges of complex terrain for lidars (chapter 1.3.6) complete the literature overview.

1.3.1 A short history of lidar measurements

Several publications give an overview of the history of optical remote sensing. The following are given exemplarily and can be used as a starting point for a more comprehensive literature study: An extensive description of the historical development of wind lidars from its very beginning in the 1930s until the first years of the 21st century is given in Fujii and Fukuchi 2005. Wandinger 2005 provides a concise introduction that also briefly summarizes the most common lidar techniques. A review of optical remote sensing in the context of wind energy is given by Emeis et al. 2007. Therein, aspects of and requirements for lidar wind measurements for wind energy applications are described, followed by an overview of at that time available studies.

Lidars have been applied for atmospheric boundary layer research for a long time. Although there were first attempts using searchlight beams or flashlights to determine atmospheric conditions in the 1930s, the development of what is understood today by the term "lidar" started with the invention of laser technology in the 1960s (Fujii and Fukuchi 2005; Wandinger 2005).

For many years CO_2-lasers have been used for lidars, since they have some significant advantages over prior ruby or helium-neon lasers, such as eye-safety or the ability to operate in continuous-wave as well as in pulsed mode (Fujii and Fukuchi 2005). With shorter wavelengths around 1 to 1.6 µm, solid-state lasers (e.g., Nd:YAG) became an alternative to CO_2-lasers, operating at 10.6 µm. Besides other advantages, shorter wavelength results in an improvement of range resolution while keeping the velocity resolution constant (Fujii and Fukuchi 2005).

Today, most lidars applied for wind measurements, use wavelengths around 1.5 µm. Driven by the necessity to reduce costs, increase (energy) efficiency and build compact and mobile systems, the developments of the telecommunications industry were picked up (Emeis et al. 2007; Mikkelsen 2014). Those systems use so-called EDFA

(Erbium-doped fiber amplifiers) based lasers that are widely used, for example, for data transmission for telecommunication (Fujii and Fukuchi 2005).

With the introduction of these relatively cheap, lightweight, robust and portable systems, lidars became an appealing tool for wind-energy-related applications (Courtney et al. 2008). As all of the lidar systems used within the context of this thesis are using the latter technology, further literature research is limited to studies about these systems for wind energy applications. Details on the measurement principle can be found in chapter 3.

1.3.2 Lidar-mast comparisons in flat terrain

In order to poof the accuracy of lidar wind measurements, it is mandatory to test the systems in flat terrain first next to a met mast. Here, the influence of the terrain on the wind flow can be neglected, and it is possible to assess the unbiased measurement accuracy of the lidar against cup anemometers.

One of the first comparisons between a fiber-based Doppler wind lidar and a measurement mast on a wind energy test site was carried out by Smith et al. (2006) next to a mast at Høvsøre Test Station in 2004 in Denmark. The lidar used was a prototype of the newly developed continuous wave (CW) "ZephIR" lidar, which performs conical scans at a fixed elevation angle of 30°, while focusing the laser beam on each measurement height consecutively. The study shows high correlation coefficients and an error in wind speed measurements of less than 1 % for heights between 40 and 100 m, but the amount of data is meager (24 h) (Smith et al. 2006). The first production version of the QinetiQ ZephIR lidar was tested by Kindler et al. (2007) within an onshore and an offshore campaign in 2005, each of several months duration. The onshore results show an excellent agreement between lidar and mast, although the slope decreases from 0.99 on 60 m to 0.96 on 120 m, which is thought to be due to the increase of measurement volume with height. The offshore results are even better, leading to the overall conclusion that the ZephIR lidar is a valuable tool for acquiring wind data helping to understand the wind flow at flat onshore and offshore sites (Kindler et al. 2007). Comparably good results were also achieved in a test at a 124 m mast at a test site of Deutsche Windguard in 2006 (Albers 2006).

At the end of 2006, the French company Leosphere introduced a pulsed fiber-based Doppler lidar called "Windcube" (Courtney et al. 2008; Cariou 2007). A prototype of the "Windcube" lidar was tested against a 98.7 m high measurement mast in Siemenswolde, close to the North Sea at a test site of Deutsche Windguard. The results show a very high correlation between the lidar and mast measurements at 98.7 m of 0.996 and a slope very close to unity with the mean deviation between both measurement systems being -0.3 % (Albers and Janssen 2008). In another test, three Windcube systems were tested in parallel against the mast at Høvsøre Test Station. Although the amount of data is small, the results for all three units are excellent, with correlation coefficients above 0.999 and small deviations between lidar and mast (Gottschall and Courtney 2010).

A third lidar, which is used in wind energy applications, is the SgurrEnergy "Galion" of which a prototype was tested in 2009 at Høvsøre Test Station. The Galion has been developed by the company HALO Photonics and is distributed by SgurrEnergy (HALO Photonics 2019). In contrast to the ZephIR and the Windcube, this device has the flexibility to modify the elevation angle as well. However, for a configuration comparable to the other two lidars, similar results are achieved within the test. The

lidar data correlates very well with the mast data, and for 116 m measurement height, the mean difference between mast and lidar is only -0.10 m/s (Gottschall et al. 2009).

From these studies, it can be concluded that lidars can potentially be used in addition to or even as a replacement for masts in flat terrain. Consequently, the different approaches are analyzed in order to gain experience in using lidars for wind energy applications.

1.3.3 Continuous-wave versus pulsed lidars

In several studies, the specific characteristics, advantages and disadvantages of the two different measurement principles (CW and pulsed) are discussed. In comparison to the pulsed systems, the CW ZephIR lidar has two critical challenges: First, there is an ambiguity in the determination of wind direction since the ZephIR cannot distinguish between winds moving towards or away from the lidar. This ambiguity results in the possibility of a 180° offset in wind direction measurements. To overcome this issue the ZephIR is equipped with a conventional wind direction sensor in order to roughly measure the correct wind direction (Emeis et al. 2007; Lindelöw 2007; Courtney et al. 2008).

In contrast to that, the Windcube (and other pulsed lidars) apply a fixed frequency offset to the local oscillator, which then enables the system to determine the wind direction correctly (Courtney et al. 2008). Second, the measurement range is determined by actually focusing the laser at the desired range. Based on the assumption of a constant aerosol concentration with height, the bulk of the backscattered signal will then stem from the measurement height. A weighting function is applied to retrieve the radial wind speed. However, this assumption is only valid unless there is no cloud layer present, which would contain significantly more aerosols. Without the application of a correction algorithm the retrieved radial wind speed will be biased due to the significant backscatter from the elevated cloud layer (Courtney et al. 2008)

Additionally, resulting from basic optical laws, the focal length, and therefore, the measurement volume increases proportional to the square of the measurement range, resulting in vast measurement volumes for the upper heights (Lindelöw 2007). The measurement volume of the Windcube and the ZephIR is comparable for heights between 100 and 120 m. Below, the ZephIR has a smaller probed volume, above it becomes significantly larger (Courtney et al. 2008). As all pulsed systems, the Windcube uses a time-of-flight method to assign the backscattered signal to the desired measurement heights (Emeis et al. 2007). Because of that, the measurement volume stays consistent at approximately 30 m independent of measurement height, and there is no bias due to backscatter from clouds (Courtney et al. 2008). From these considerations Courtney et al. (2008) conclude that the Windcube (i.e. a pulsed lidar) is better suited for measurements above 130 m than the ZephIR (i.e., a CW lidar).

1.3.4 Lidar-mast comparisons in complex terrain

As already stated above, many wind farms are planned in complex terrain. It is, therefore, necessary to test lidars at these sites to assess their applicability, identify challenges, and find solutions in order to be able to keep measurement uncertainty on acceptable levels. As this is one of the essential aspects of the doctoral thesis, details on the challenges posed by complex terrain are given in chapter 3.2.

All of the mentioned lidars have in common that they rely on the so-called "homogeneous flow assumption." In order to be able to reconstruct the horizontal wind speed, the lidars measure the radial velocity at different locations in the atmosphere. Under the assumption of equivalent wind speed at these locations, simple trigonometric functions can be used to calculate the horizontal wind speed. This assumption is not valid for measurement sites with significant spatial changes in wind speed, e.g. complex terrain sites (Courtney et al. 2008; Clive, Peter J. M. 2008). As the measurement principles of wind sodars (sound detection and ranging) and lidars are generally comparable, they also face the same limitations and drawbacks in complex flow situations (Emeis et al. 2007). Thus, in the following paragraphs, existing studies from the sodar community are presented in case they describe the same problems or provide analyses and solutions that are relevant for lidars as well.

One of the first relevant comparisons between a lidar and a 100 m mast was carried out by Antoniou et al. (2007). A ZephIR was placed at the Center For Renewable Energy Sources (CRES) test station in Greece, which is located in complex terrain. On the one hand, the results show a high correlation of 0.996 (R^2) for 99 m and 78 m between lidar and mast, which is comparable to flat terrain sites (e.g., Smith et al. 2006). On the other hand, a significant underestimation of the wind speed by the lidar is observed, with a slope of 0.943 at 99 m and 0.918 for the 78 m measurement height (Antoniou et al. 2007). Courtney et al. (2008) state that errors in the determination of mean wind speed in the order of 5-10 % is not uncommon for complex terrain sites. As a solution, they propose to reduce the lidar cone angle from 30° to 15° in order to reduce flow complexity between the measurement points.

A first attempt to explain and model the error of monostatic remote sensing instruments in complex terrain (lidar and sodar) is presented by Bradley (2008). He applies a simple two-dimensional potential flow model to estimate the wind flow and uses the model results to correct the error due to the homogeneous flow assumption. Depending on the shape of the hill and the measurement height, he finds sodar errors between 5 and 20 % for a cone angle of 20°. Contrary to his hypothesis (and the one from Courtney et al. (2008)), there is no significant increase in the errors when increasing the cone angle to 30° (which is typical for most lidars) (Bradley 2008).

Bingöl et al. (2009) study the lidar error at two complex terrain sites in Greece. Here the lidar errors of a ZephIR reach up to a magnitude of 10 % depending on wind direction and for heights between 30 and 80 m. An algorithm is implemented into WAsP Engineering (WEng) that uses the model results to calculate an estimation for the lidar error at the two sites. Although the model is simple and limited to low slopes only, the estimated errors fit well to the observed results for the main wind directions. For the wind directions with increased slope (south-west), the results do not fit very well, which is attributed to limitations in WEng. In a simple, two-dimensional analytical consideration, Bingöl et al. (2009) also show that the lidar error is not dependent on the cone angle, but only on the horizontal homogeneity of the flow. These analytical findings are verified by Foussekis (2009), who compares the results for the ZephIR and two Windcube lidars, one with a 30° and one with a 15° cone angle against a 100 m mast at the complex terrain CRES test station in Greece. Here, an underestimation of about 6 % is found for all three lidars, independent of measurement principle (CW and pulsed) and cone angle (15° or 30°). Additionally, the study states that the lidar error is independent of height at this site (Foussekis 2009).

Reacting on these results, Natural Power, the marketing company of the ZephIR lidar, developed a method to estimate the lidar error for complex terrain with the Reynolds-averaged Navier-Stokes (RANS) computational fluid dynamics (CFD) code "Ventos" (Harris et al. 2010). They apply the method proposed by Bingöl et al. (2009) on the results from the CFD code for a complex terrain site in the United Kingdom. The estimated lidar errors are then also compared to those from a WEng simulation. Their results emphasize that, for the given site, WEng overestimates the lidar error, especially for those wind direction sectors that have the steepest slopes. The CFD code provides a better estimate for the inhomogeneous flow above the terrain. The authors conclude that these findings show the limitations of the WEng model in terms of terrain complexity (Harris et al. 2010).

The approach of using RANS CFD modeling was also followed by Leosphere as they worked together with WindSim (Meissner and Boquet 2011) and Meteodyn WT (Bezault et al. 2012) to implement methods for lidar error estimation into this commercial software. Tests and validations of the WindSim correction module are reported in Meissner and Boquet (2011), Jokela et al. (2013) and Kim and Meissner (2017). All three studies have in common that they generally show a better agreement between lidar and reference data after application of the CFD correction. Bezault et al. (2012) present results from an estimation of the lidar error based on Meteodyn WT, both for a ZephIR and a Windcube data set at two different complex terrain sites. For these two sites, the quality of the correction is very good, correcting the slope to almost 1.0.

Other studies rely on different CFD software to correct for the lidar error. For example, Boquet et al. (2010) use a CFD model called "ARIA" to correct the lidar error at a complex site for three different heights (56, 78 and 100 m). For all three heights, the correction significantly reduces the bias between lidar and mast.

Based on his previous study, Bradley (2012) extends his potential flow model to sodar and lidar data on a simple two-dimensional hill and an escarpment. Additionally, the results from the simple model are compared to more advanced CFD models (WindSim and OpenFOAM) from Behrens et al. (2012) at two different complex terrain sites in Scotland and New Zealand. Results show that the simple potential flow model is mostly sufficient to estimate the lidar error at these sites (Bradley 2012), although there are some cases where CFD provides better results (Behrens et al. 2012).

In 2011 Leosphere introduced the second version of the Windcube lidar ("Windcube v2"), which was tested at the CRES Test Station in Greece (Foussekis 2011). For the Windcube v2, Leosphere introduced a proprietary method called "flow complexity recognition" (FCR) to correct for the lidar error in complex terrain already during the measurement, so that the system generates two data files: One with corrected data and one in default mode, with uncorrected data. At that time, the principle of this method was not revealed due to confidentiality (Foussekis 2011, p. 10). In default mode (without FCR), results are almost the same as for the previous comparison with the first version of the Windcube (Foussekis 2009), showing a very high correlation and a significant underestimation of the wind speed by the lidar due to the influence of the complex terrain. With FCR the bias between lidar and mast is significantly reduced (Foussekis 2011). FCR was also tested by Wagner and Bejdic (2014) at a complex terrain site in Hrgud, Bosnia and Herzegovina. Here, wind speeds are underestimated by 4 % in default mode. With FCR turned on, there is a slight overestimation of 1.5 %, which means at this site FCR over-corrects for the lidar error. According to the authors,

this has also been observed in previous studies (Wagner and Bejdic 2014). In an inter-comparison of FCR results for sites of various complexities, this effect is also evident for several sites, although the magnitude of the bias is mostly reduced by FCR. It is interesting to note that in this study, FCR heavily over-corrects the measurement data at the highly-complex site by 20 %, which implicates that FCR might not be suitable for this site (Krishnamurthy and Boquet 2014). In 2017, Leosphere revealed the method behind FCR in a detailed technical report (Leosphere 2017). FCR requires Shuttle Radar Topography Mission (SRTM) orography data (that is stored on the device), the geographical coordinates of the measurement site and the north orientation of the lidar at the actual site. Then it uses the 3D wind field model "SWIFT" to calculate the wind flow in the closer proximity of the lidar to estimate the lidar error. It is, therefore, comparable to the other model-based correction approaches, apart from the fact that the model is run for each 10-minute-value instantly on the lidar. In this report, Leosphere also states that FCR is limited to moderately complex terrain and low surface roughness (Leosphere 2017). In its complexity, the model is comparable to WEng, which might explain its incapability to be applied at very complex and forested sites.

A systematic review over the at that time available studies and open research questions regarding remote sensing in complex terrain is given in Bradley et al. (2015). The study concludes that simple models, e.g., potential flow models, can often correct for the lidar error acceptably well. However, as soon as recirculation or detached flow situations occur, more sophisticated models are needed that are capable of modeling those flow features. Also, more detailed characteristics of the atmospheric boundary layer flow (e.g., low-level jets or atmospheric stability) are so far not treated in the context of remote sensing in complex terrain (Bradley et al. 2015).

1.3.5 Lidars in standards and guidelines

Based on the above-described research and testing results and driven by the industry's need for accurate wind measurements at large heights, the most relevant standards and guidelines have recently included instructions for the use of lidar measurements. Usually, the International Electrotechnical Commission (IEC) standard 61400-12-1 for power performance assessment of wind turbines is used for most wind energy applications since it precisely describes the procedures for accurate wind measurements (IEC 61400-12-1). Conventionally, classified and calibrated cup anemometers mounted on tall masts are used for the assessment of, e.g., power curves of wind turbines and also for wind resource assessment. In its recent version 2.0, the standard also allows for the use of classified and calibrated lidars, but under consideration of specific requirements: It limits lidar measurements to flat terrain sites, and it asks for an obligatory monitoring mast for the continuous tracing of the lidar data (IEC 61400-12-1)

In comparison to other guidelines, these regulations can be seen as relatively conservative. A procedure published by the International Network for Harmonised and Recognised Measurements in Wind Energy (MEASNET) on the evaluation of site-specific wind conditions allows the use of lidars also at complex terrain sites, given that at least one measurement mast is present at the site (Measnet 2016). The most progressive approach can be found in the German technical guideline on wind resource assessment (TR6) developed by the Fördergesellschaft Windenergie und andere Dezentrale Energien e.V. (FGW), that even allows the stand-alone use of lidars in complex terrain, without a mast being present, but under the consideration of

appropriate correction methods (FGW e.V. 2017). Concluding from this, it is evident that there are a lot of open questions and disagreements regarding the application of lidars and that the industry has a vital need to improve understanding and extent the experience on the application of lidars, especially in complex terrain.

1.3.6 Multi-lidar measurements and alternative measurement principles

There are other pathways to overcome the lidar error in complex terrain. One is the application of so-called "multi-lidar" measurements, where multiple laser beams are focused at the measurement point. The development of alternative measurement principles, that inherently avoid the homogeneous flow assumption represents another possibility.

As described above, standard profiling lidars measure the radial wind speeds at different points in the atmosphere along the line of sight of the laser beam. Then, the horizontal wind speed is reconstructed under the assumption of homogeneous flow. A straightforward approach to overcome this assumption is to measure at one point, by intersecting the beams of two or more lidars from different locations. One of the first realizations of such a multi-lidar measurement is the "Musketeer Experiment" in the WindScanner.dk project, showing promising results (Vasiljevic 2014). Another experiment is the Kassel 2014 experiment carried out at the complex terrain test site of Fraunhofer IEE at Roedeser Berg. Several combinations of two or three scanning lidars are used to estimate the horizontal wind speed close to a sonic anemometer at the mast. The results are also compared to a Windcube lidar installed next to the mast. The study demonstrates an excellent agreement of the horizontal wind speed to the reference sonic anemometer at the mast (Pauscher et al. 2016).

Additionally, the multi-lidar results correlate better to the sonic than those from the standard Windcube measurement, and also, the deviation in wind speed is lower (Pauscher et al. 2016). In the New European Wind Atlas (NEWA) project, several, more advanced and sophisticated multi-lidar measurement campaigns were carried out at different sites in Europe (Mann et al. 2017). Besides the overall aim of the project to generate a publically available and highly resolved wind atlas for whole of Europe, the database from the experiments will be made available for the validation of atmospheric flow models (Mann et al. 2017). Exemplarily, one of these validations is presented in Wagner et al. (2019), demonstrating the high flexibility and usefulness of lidar measurements to understand the flow over complex terrains.

Doppler lidars like the Windcube or ZephIR are using the "coherent detection" approach. An alternative to this is "direct detection," which directly uses the backscattered signal from aerosols or air (Emeis et al. 2007). Different methods to measure the wind speed based on direct detection are, e.g., described in Howard and Naini (2012). The cross-correlation method described there is implemented in the "SpiDAR" lidar, which was introduced by the Israeli company Pentalum in 2012, which was recently acquired by NRG Systems (NRG Systems 2018). A short verification campaign was carried at the Janneby test site in northern Germany by DNV GL. A report from this verification was provided by NRG systems, showing promising results at both 57 m and 100 m measurement height with a slope close to one and also R^2 values of 0.98 and 0.99 for the horizontal wind speed measurement (Stein 2014).

The Merlis lidar, developed at Fraunhofer IEE within a research project, aims at a fully-integrated multi-lidar measurement. The first results from the development of the

novel approach were presented at the recent Resource Assessment Workshop of the Wind Europe, providing details on the project state (Khadiri-Yazami et al. 2019).

The Physikalisch-Technische Bundesanstalt (PTB) in Germany has developed a bistatic lidar system that uses one laser source that is transmitted to the atmosphere and three receivers that are separated in space but only in a radius of 1 m around the transmitter (Oertel et al. 2019). Based on highly accurate components, it measures the wind speed vector of single particles in a minimal measurement volume (Eggert et al. 2015). In a recent study, the bistatic lidar shows excellent agreement to a measurement mast in flat terrain and a Leosphere Windcube lidar. In that study, it is also compared to a laser Doppler anemometer in a wind tunnel showing excellent agreement. The authors conclude that the bistatic lidar will potentially be able to measure with high accuracy in flat as well as in complex terrain (Oertel et al. 2019).

1.4 Summary of the literature review and research questions

Vertical profiling monostatic Doppler lidars are by far the most often used lidar systems in wind energy applications because they are readily available, flexible and easy to use even at remote locations (Clifton et al. 2018; Gottschall et al. 2011; Klaas et al. 2015). The most promising approach to account for their lack of accuracy at complex terrain sites is the application of wind flow models (Bradley et al. 2015).

The above-given literature study (e.g., Bingöl et al. 2009; Bradley 2012; Bradley et al. 2015; Klaas et al. 2015) and the state of international standards and guidelines (FGW e.V. 2017; Measnet 2016; IEC 61400-12-1) reveal that there is a need for a better understanding of the applicability of lidars at complex terrain sites.

Based on the findings in the literature review, five governing influencing factors on the lidar error in complex terrain are found: Orographic complexity, terrain roughness and vegetation, atmospheric stability, measurement height and half-cone opening angle. Summing up the results from the literature review in the introductory chapter in a systematic way, five main research questions can be derived with regard to these influencing factors. These research questions are developed in the following text.

1.4.1 Orographic complexity

In all available studies on lidar-mast comparisons at complex terrain sites, it is found that the lidar error is dependent on orographic complexity. Lidar errors measured at sites of different complexity and for distinct wind directions vary in magnitude and can either be negative or positive (e.g., Bingöl et al. 2009; Antoniou et al. 2007). The respective literature lacks a systematic comparison of lidar measurement accuracy concerning different orographic complexities. Existing experimental studies mostly focus on the results from a single site. Comparing different studies with sites of different orographic complexity is difficult, as the used anemometry and equipment, as well as the methods and definitions for data preparation and analysis, are usually not the same. In addition to that, it is not always the same type or even technology of wind lidar that is used for the evaluation, and the results (e.g., from pulsed and continuous-wave lidars) are not directly comparable.

Resulting from this, the first research question arises: How well do lidar measurements perform for sites of varying orographic complexity? Alternatively, how does different orography (from flat to hilly terrain) influence the measurement accuracy of lidar measurements and what is the dependence of the lidar error on terrain inclination?

1.4.2 Measurement height

As already stated in the previous chapter, there are many studies focusing on lidar measurements in flat and complex terrain (Antoniou et al. 2004; Bingöl 2009; Foussekis 2011). As those have been the standard for wind energy applications in the last decades, lidars are usually referenced to measurements from the mast-based cup or sonic anemometers within these studies to evaluate their accuracy in the wind speed and wind direction measurements. Nearly all studies have in common that the reference masts are lower than or equal to 100 m, as these are common and economically feasible mast heights. Contrary to that, wind turbines have been increasing in both hub height and rotor diameter, leading to upper tip heights of modern wind turbines in the range of 200 m (Rohrig 2018).

This leads to the second research question: How do lidar measurements perform for greater heights? Or to be more precise: How accurate are lidar measurements at heights well above 100 m, i.e., at hub heights of current wind turbines (140 m) and for the whole rotor swept area (up to 200 m)? In the context of the complex terrain lidar error, the question could also be: How does measurement height affect the magnitude of the lidar error? Is there a decrease or an increase in the error with increasing measurement height? Furthermore: Is there a measurement height at which the lidar error becomes negligible?

1.4.3 Terrain roughness and vegetation

Measurement sites do not only differ in terms of orographic complexity but also in land cover and, therefore, terrain roughness and vegetation. Many complex terrain sites that are used for current wind energy projects are located in forested terrain (Callies 2014). It is well known that terrain roughness and especially forest heavily influence the wind flow above the terrain (Belcher et al. 2008; Finnigan and Belcher 2004). Roughness elements and forest induce turbulence and shear in the wind profile or even enhance the formation of flow separation zones (Belcher et al. 2012; Shannak et al. 2012). With this in mind, the assessment of the individual influence of single parameters of different sites on the actual lidar error is challenging. Comparing the accuracy of lidar measurements between sites of different orographic complexity, for example, is hindered by the influence of terrain roughness and vegetation. For example, results from Klaas et al. (2015) at a forested site show much smaller lidar errors than those found in Bingöl et al. (2009) or Foussekis (2011), which are both not forested.

Resulting from that, the third research question is: How does different terrain roughness (from bare soil to bushes) influence the accuracy of lidar measurements? Moreover: What is the impact of forest on the magnitude of the lidar error in complex terrain?

1.4.4 Atmospheric stability

Another aspect that has not yet been treated in literature is the influence of atmospheric stability on lidar measurement accuracy. Although it is stated in a few studies that there might be an effect from this (e.g., Bradley et al. 2015), the author is not aware of any piece of work that examines the dependence of lidar measurement accuracy in terms of varying atmospheric stability in any kind.

Because there is a significant influence of atmospheric stability on the wind profile and the wind flow over or around hilly terrain (Ross et al. 2004; Leo et al. 2016), the fourth research question reads as follows: Is there an influence of atmospheric stability on lidar measurement accuracy? Or more precisely: How does stable, neutral or unstable stratification affect the magnitude of the lidar error?

1.4.5 Half-cone opening angle

Within the context of measurement height, the half-cone opening angle of the lidar is another factor that must be considered. With increasing measurement height, the distance between the measurement points of the lidar also increases significantly. Courtney et al. (2008) are proposing to reduce the half-cone opening angle from 30° to 15° in order to reduce the lidar error in complex terrain. This suggestion is interrogated and tested experimentally by Bingöl (2009) and Foussekis (2009), who come to the conclusion that the half-cone angle does not influence the lidar error. Also, Bradley et al. (2015) derive lidar error estimations that are solely dependent on flow curvature and independent of the half-cone opening angle. However, these findings are based on the assumption of symmetric flow and constant flow curvature. For flow simulations that consider surface roughness and forest as well as atmospheric stability, these assumptions are not necessarily valid (compare e.g. Belcher et al. (2008) and Ross et al. (2004)).

The absolute distance depends on the half-cone opening angle and decreases when smaller angles than the standard 30° are used. The resulting research fifths question reads as follows: Does a smaller angle have positive effects on the lidar error, because the measurement points are closer together? Or, more generally: Is there an effect of changing the half-cone opening angle in the presence of asymmetric flow above forested terrain or under distinct atmospheric stability situations?

2 Aim of the doctoral thesis and novelty value

Based on the research questions developed in chapter 1.4, the overall aims of the doctoral thesis and five hypotheses are formulated in chapter 2.1. These hypotheses are used as a leading thread throughout the whole thesis. The novelty value of the thesis and its contribution to the scholarly debate are then elaborated in chapter 2.2.

2.1 Aims of the doctoral thesis and hypotheses

The doctoral thesis aims at providing a guideline for lidar users in the wind energy sector to assess the applicability of lidars at complex terrain sites. Although there are some studies that compare lidar correction with different flow models in complex terrain, a holistic examination of the limits of these models concerning their ability to estimate the lidar error does not exist.

The overall aim is a systematic expansion of knowledge and understanding of the applicability and limits of current Doppler lidars for wind measurements in complex terrain under consideration of the above-explained influencing factors (see chapter 1.4). To understand their particular influence, it is vital to examine them separately. The following hypotheses, which are derived from the research questions, are going to be tested within the doctoral thesis, providing a clear and structured approach for the reader:

A) The lidar error is dependent on orographic complexity. It increases with increasing terrain curvature that causes the wind flow to bend and accelerate.
B) The lidar error is dependent on measurement height. It decreases with increasing height, while terrain effects on the wind flow diminish.
C) The lidar error in complex terrain is dependent on terrain roughness. It is, in particular, sensitive to the presence or absence of forest. Roughness and forest increase shear and turbulence and facilitate flow separation effects. All these effects influence the flow curvature and speed-up.
D) The lidar error in complex terrain is dependent on atmospheric stratification. It decreases for stable cases, which is because, in this case, the wind flow is less bent when passing a hill.
E) The lidar error is dependent on the half-cone opening angle of the lidar measurement geometry. It decreases when the angle is decreased because the measurement points are closer together and the wind vectors are more similar.

These hypotheses are again referred to in chapter 7 when they are contrasted to the results achieved within this doctoral thesis. However, having in mind the strong interdependency of the different influencing factors, they can be considered as function parameters spanning a four-dimensional parameter space that relates the lidar error to the actual measurement site. Consequently, the doctoral thesis aims at an integrated analysis of this interdependency, which is presented in the concluding chapter.

2.2 Novelty value and contribution to scholarly debate

The doctoral thesis firstly analyses the influence of the most governing factors on lidar errors in complex terrain in a systematic way revealing the actual influence and importance of each. Secondly, it combines these findings to an overall perspective that can be used as a practical guideline for the application of lidars in the terrain of various complexities. Considering the available literature, there is no comprehensive

assessment like this so far. The findings of Klaas et al. 2015 were a trigger to intensify research on model parameterization in the context of lidar error estimation, which is done in the parameter study within this thesis.

Moreover, due to the model-based approach of the thesis, it can also answer questions of the applicability and limitations as well as the strengths and weaknesses of the different flow models that are used to estimate the lidar error. It, therefore, provides helpful guidance on the necessary complexity of the flow model to be used for lidar error estimation in a particular situation or at a specific site.

Especially the work on atmospheric stability and its impact on the lidar error in complex terrain has not been treated in literature so far. The thesis closes a gap between the knowledge about the influence of atmospheric stability from a meteorological perspective on the one hand and its implications on the lidar error on the other hand.

Furthermore, the lidar error estimation follows a novel approach where the lidar error is separated into its two main parts: Lidar error due to flow curvature effects and lidar error due to speed-up effects. A comparable approach was not found in the relevant literature. This approach gives a more detailed and structured insight into the flow effects that cause lidar errors in complex terrain. Especially the question, if the lidar half-cone opening angle is an important parameter that has to be considered, can be answered by this approach.

Additionally, in the evaluation part of the thesis, the findings are compared to measurements from a 200 m high met mast at a complex and forested site. Considering the measurement height, the data quality, availability and the possibility to measure the directional dependence of the lidar error at a complex terrain site, there is no comparable study available in the literature. The met mast has been erected and operated within the context of the project “Windenergienutzung im Binnenland” (“Utilization of inland wind power”), funded by the Federal Ministry for Economic Affairs and Energy (BMWi), at the Fraunhofer IEE test site in complex terrain “Roedeser Berg.” A Doppler wind lidar was compared to the 200 m mast within the research project, providing a unique data basis for the examination of lidars errors up to great heights at a complex and forested site. This data set is used to compare the model-based results to real-world data in chapter 6. Results based on this dataset are also published in Klaas et al. (2015) and author contributions are given in Appendix 10.4. However, the dataset is evaluated following a novel approach that puts the measurement results into the context of this dissertation.

Within the frame of the European NEWA project, additional, more advanced lidar measurements have been carried out at the site of the 200 m mast using, e.g., long-range scanning lidars. With these measurements, it is possible to visualize the overall flow pattern in main wind direction, revealing features like flow-separation that – as already stated above – might also influence the magnitude of lidar errors in complex terrain. In the outlook in chapter 8, a possible application of scanning lidars is described to continue the research on lidar error estimation and evaluate the findings of this dissertation.

3 Lidar measurement principle and possible error sources

The following chapter briefly describes the fundamental physical principles that are used to measure the wind speed with monostatic pulsed Doppler lidars. It then explains the measurement principles and scanning modes (geometries) that are used in commercially available lidar profilers while focusing on the Leosphere Windcube that has been used in the experiments for this thesis. By defining the geometrical parameters of the measurement setup, the chapter provides the basis for analyzing the lidar error due to complex terrain.

3.1 The measurement principle of monostatic pulsed Doppler wind lidars

The Doppler Effect describes the frequency shift between emitted and received radiation that is observed when radiation source and receiver are moving relative to each other. For acoustic waves, this phenomenon was first described by Christian Doppler, but it occurs for electromagnetic waves (such as light) as well. By measuring this change in frequency, it is possible to determine the relative speed between source and receiver (Weitkamp 2005).

The effect is used by monostatic pulsed Doppler wind lidars (or simply "Doppler lidars") to measure the wind speed remotely: Pulsed laser light is emitted by a lidar placed on the ground. As the light is transmitted through the atmosphere, it is reflected by aerosols that move with wind speed (see Figure 3.1). A part of the light is scattered back to the receiver that is located inside the lidar (i.e., monostatic) (Weitkamp 2005). Because the speed of light and the frequency of the emitted light are precisely known, it is possible to determine the wind speed relative to the lidar. This speed is the projection of the three-dimensional wind vector to the line-of-sight of the laser beam. It is therefore called line-of-sight velocity v_{los} or radial velocity v_r, defined positive for a movement toward the lidar and negative for a movement away from the lidar (Weitkamp 2005; Emeis et al. 2007).

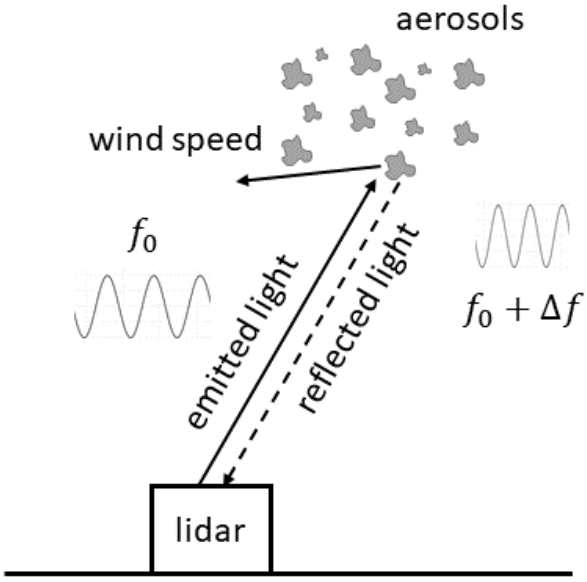

Figure 3.1: Schematic illustration of the Doppler Effect. A lidar is placed on the ground emitting light at a fixed frequency $\boldsymbol{f_0}$. The light is backscattered at aerosols moving with wind speed. Due to the relative movement of the (fixed) lidar against the aerosols carried with the wind, the frequency of the light is shifted to the frequency $\boldsymbol{f_0 + \Delta f}$.

The frequency of the light received by the measurement device is defined by

$$f = f_0 + \Delta f = f_0(1 + \frac{2v_r}{c}) \quad (1)$$

with f_0 being the frequency of the emitted light and v_r/c the ratio of radial wind speed to the speed of light. From this equation, it becomes obvious that the frequency shift that has to be detected is very small. Wind speeds are usually in the range of 0 to 50 m/s, while the speed of light is approximately $3x10^8$ m/s. Furthermore, only a small portion of the emitted light is received back, increasing the challenges in signal processing (Weitkamp 2005).

Pulsed Doppler lidars used for wind speed measurements are usually following the heterodyne detection principle. The lidar emits a pulsed beam that is then backscattered by aerosols in the atmosphere. The reflected light that reaches the lidar is mixed with a continuous wave laser that is locally oscillating in the lidar. By this, the system can measure the frequency difference between the emitted and received light (Weitkamp 2005). By adding a defined frequency offset to the local oscillator signal, a heterodyne lidar is also able to measure the sign of the frequency shift and, therefore, of the radial velocity (Courtney et al. 2008). The Leosphere Windcube lidar, which was used in the experiments presented within this thesis, is based on the heterodyne technique and operating a solid-state laser with a wavelength of 1.54 µm. For this system, a Doppler shift of 1.3 MHz corresponds to a radial wind speed of 1 m/s (Pauliac 2009). Because the returned signal from a single pulse (or shot) of the laser contains random noise, pulsed lidars need to emit many shots and then calculate a time average to filter out the noise (Weitkamp 2005). The Windcube in its first version uses, for example, pre-defined values of 5,000 to 10,000 shots (Courtney et al. 2008). The received signal is separated into range gates by the time-of-flight method. This enables the system to measure simultaneously at multiple heights with each laser beam (Emeis et al. 2007; Courtney et al. 2008). In a signal-processing unit, the signal is Fourier-transformed, and the peak of the frequency spectra is detected by the application of a mathematical model (Courtney et al. 2008).

As already explained above, the radial wind speed is a projection of the three-dimensional wind vector to the line-of-sight of the laser beam. This can mathematically be described by the following equation:

$$v_r = u \sin\varphi \sin\theta + v \sin\varphi \cos\theta + w \cos\varphi \quad (2)$$

with u, v and w being the three wind vector components in x, y and z direction, φ the half-cone opening angle (or prism angle) of the lidar against the vertical and θ the azimuth angle counted clockwise positive from the north. Here, u is oriented along the positive x-axis from west to east and v along the positive y-axis from south to north. The vertical wind speed w is defined positive along the positive y-axis pointing upwards (compare Figure 3.2). Following this definition, radial wind speeds are positive for winds moving towards the lidar and negative for winds moving away from the lidar.

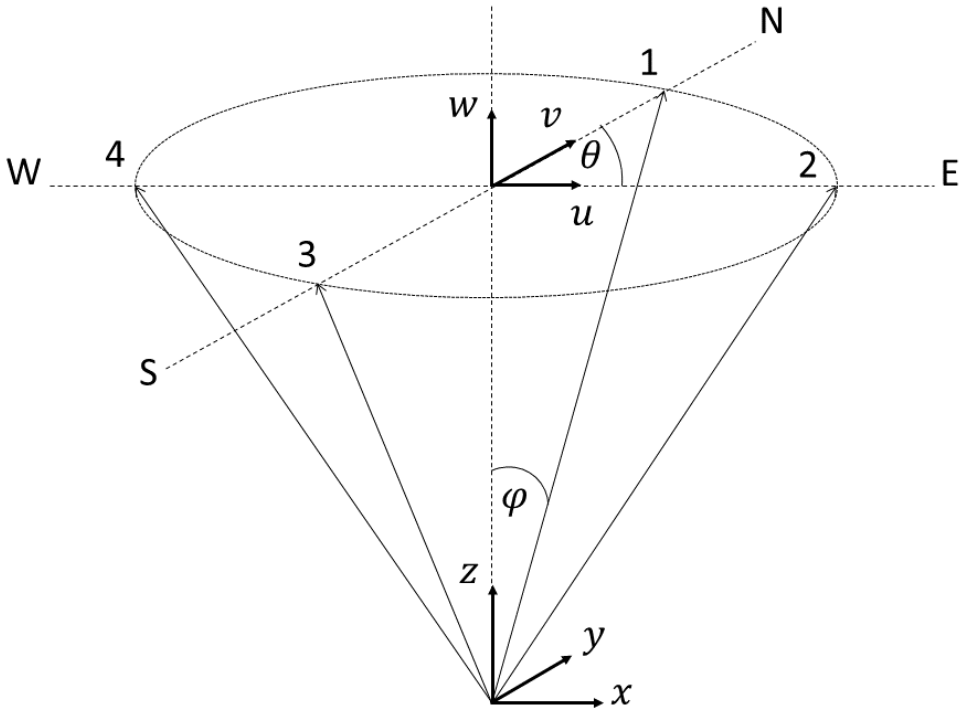

Figure 3.2: Lidar measurement geometry and definitions of the local coordinate system $(\boldsymbol{x}, \boldsymbol{y}, \boldsymbol{z})$ and the wind vector components $(\boldsymbol{u}, \boldsymbol{v}, \boldsymbol{w})$ as well as the half-cone opening angle $\boldsymbol{\varphi}$ and the azimuth angle $\boldsymbol{\theta}$ (here for the second measurement location, 90° from the north). The measurement locations are numbered starting from North (N) clock-wise to West (W). The measurement locations are shown for an example measurement height at a plane defined by the circle. This measurement geometry equals the one that is used in the Leosphere Windcube v1. In the successive version Windcube v2, a fifths measurement location has been added with $\boldsymbol{\varphi} = \mathbf{0}$ directly above the origin at measurement height.

The vertical wind speed can directly be measured by a vertical laser beam at $\varphi = 0°$. In order to measure the horizontal wind speed components (and the wind direction), different scan techniques can be applied where the lidar consecutively measures radial wind speed at multiple measurement points in the atmosphere. From these measurements, the horizontal wind speed at a reconstruction point can be derived. The position of the reconstruction point is usually a point at the desired measurement height directly above the lidar location. However, particular assumptions have to be made to carry out this wind vector reconstruction (Weitkamp 2005). The central assumption is that the flow between the measurement points is homogeneous, i.e., wind speed does not change among the different measurement points and the reconstruction point (Weitkamp 2005; Courtney et al. 2008; Bingöl 2009). The implications of this assumption are explained in detail in chapter 3.2.

The Windcube uses the Doppler beam swinging (DBS) scan technique, which is a simplification of the velocity-azimuth-display (VAD) technique (Pauliac 2009). For a VAD scan, the laser beam is tilted out of the vertical by a fixed angle φ. Then a circular scan is performed, and radial wind speeds are measured at different azimuth angles θ (Figure 3.3). Visualizing the radial wind speed against the azimuth angle then ideally shows a sine wave from which horizontal wind speed and wind direction can be approximated (Weitkamp 2005).

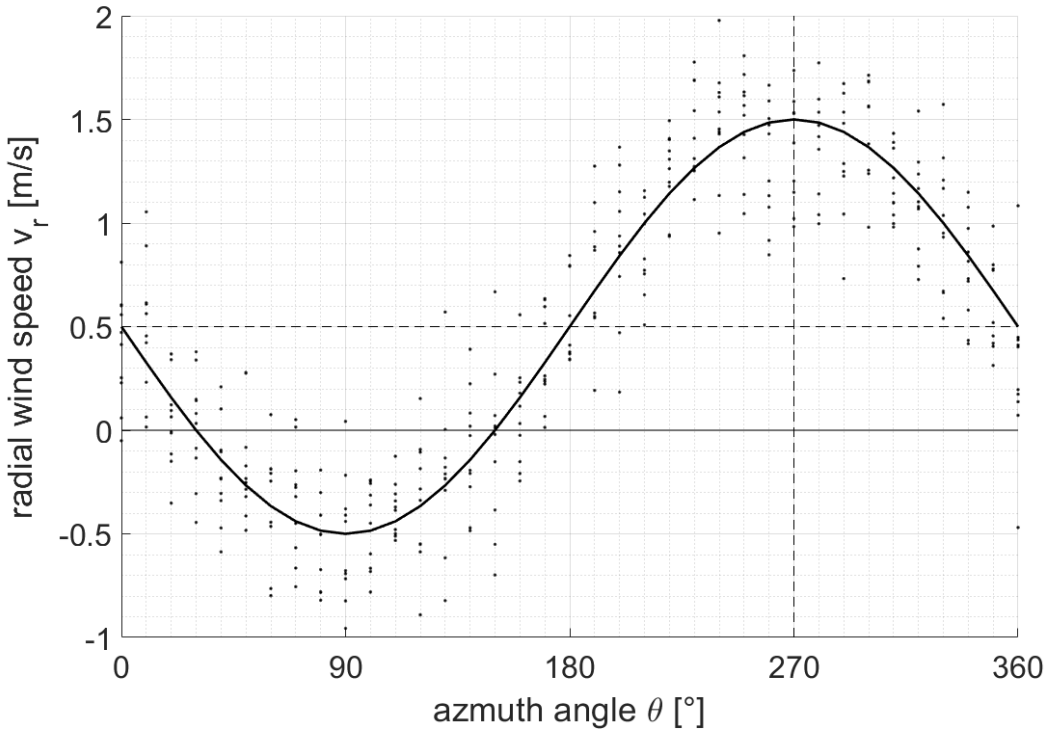

Figure 3.3: Illustration of a typical VAD scan result of the radial wind speed against the azimuth angle oft he measurements. Here ten measurement rounds are simulated for given wind speed and wind direction. Radial wind speeds are assumed to be normally distributed around a mean value. In this example, the wind direction is located at the maximum (or minimum) of the sine wave curve (270 or 90°). The horizontal wind speed can be calculated from the radial wind speeds at the maxima based on $\boldsymbol{\theta}$ and half-cone opening angle $\boldsymbol{\varphi}$. An y-offset of the curve is caused by the contribution of a vertical wind speed component. The illustration is based upon the one given in (Werner 2005, p. 340).

However, in order to calculate the three wind vector components, three independent radial measurements are sufficient. In its simplest form, the DBS technique relies on two measurements tilted from the vertical to estimate the horizontal wind speed and one vertical measurement to directly measure the vertical wind speed (Weitkamp 2005). The analysis within this thesis is based on the DBS scheme that is used in the Windcube lidars as it is the most common scheme and can easily be simplified from a three-dimensional to a two-dimensional case. Definitions and nomenclature are also presented in Klaas et al. (2015) and used throughout the whole thesis.

Based on the above-stated definitions, the Windcube lidar uses the following equations to derive the three wind vector components:

$$\begin{aligned} u_L &= \frac{v_{r4} - v_{r2}}{2 \sin\varphi \sin\theta} \\ v_L &= \frac{v_{r3} - v_{r1}}{2 \sin\varphi \cos\theta} \\ w_L &= \frac{-v_{r1} + v_{r2} - v_{r3} + v_{r4}}{4 \cos\varphi} = -v_{r5} \end{aligned} \tag{3}$$

with $v_{r,i}$ being the four (or five) radial wind speed measurements at measurement points i that are carried out by the Windcube lidar (Pauliac 2009). The measurement

geometry is illustrated in Figure 3.2. Assuming the lidar being oriented following the coordinate system, the four tilted measurements are consecutively performed in the north, east, south and west direction. Each pair of opposed radial wind speeds can then be used to calculate the related wind vector component directly. The vertical wind speed can be reconstructed either from all four radial wind speeds or directly from a fifths vertical measurement. In case of an offset against the horizontal coordinates, which often occurs due to practical limitations in measurement campaigns, the result must be corrected for this as a part of the reconstruction.

The (horizontal) wind speed increases with height, which is usually modeled as the logarithmic wind profile within the surface layer, as described in Stull (1988) (see also chapter 4.1). A Doppler lidar emits laser pulses of a defined length, which implies that the returned signal corresponds to a measurement volume or probe volume along the line of sight of the laser beam (Weitkamp 2005). In the case of the Windcube lidar, the probed volume extends roughly 26 m along the beam and is constant with height (Courtney et al. 2008). The effects of probe volume size have been analyzed in detail, for example, by Pauscher et al. (2016). However, under consideration of common vertical wind shear values (Emeis 2018, p. 34), the effects of the vertical extent of the probe volume can be neglected in comparison to other, more dominating error sources for lidars in complex terrain which are described in the following chapter.

3.2 Lidar error sources in complex terrain

The homogeneous flow assumption described above is applicable for flat terrain sites that, in particular, do not introduce any speed-up or flow curvature effects on the mean wind flow (Courtney et al. 2008). The mean horizontal wind speed measured by a lidar agrees well with measurements from cup anemometers in that case (compare, e.g. Antoniou et al. 2007 and chapter 1.3.2).

In the case of a lidar placed at a complex terrain site, the homogeneous flow assumption is violated. Generally speaking, the wind speed vectors at the different measurement points of the lidar are no longer equivalent, which introduces errors in the wind vector reconstruction method described above. Additionally, the wind speed vector at the reconstruction point itself, i.e., at measurement height above the lidar location, is also different from the wind speeds at the different measurement points. Due to the change in terrain elevation, the measurement points are at a different height above ground than the reconstruction point. This adds more complexity to the problem of wind vector reconstruction due to the vertical wind shear.

The above-given equation for the radial wind speed can be changed in order to consider the inhomogeneous wind field:

$$v_{ri} = u_i \sin\varphi \sin\theta + v_i \sin\varphi \cos\theta + w_i \cos\varphi \qquad (4)$$

with i being the number of the measurement point with the specific wind vector $(u_i \quad v_i \quad w_i)^T$.

For the case of homogeneous wind flow among the measurement points of the lidar, the reconstructed wind vector is equivalent to the actual wind vector above the lidar. At a distinct measurement height, horizontally homogeneous wind flow can be described mathematically by the wind speed gradient being zero in all horizontal dimensions:

$$\boldsymbol{\nabla} \cdot \mathbf{V} = \begin{pmatrix} \frac{\partial u}{\partial x} & \frac{\partial v}{\partial x} & \frac{\partial w}{\partial x} \\ \frac{\partial u}{\partial y} & \frac{\partial v}{\partial y} & \frac{\partial w}{\partial y} \\ \frac{\partial u}{\partial z} & \frac{\partial v}{\partial z} & \frac{\partial w}{\partial z} \end{pmatrix} = \begin{pmatrix} 0 & 0 & 0 \\ 0 & 0 & 0 \\ \frac{\partial u}{\partial z} & \frac{\partial v}{\partial z} & \frac{\partial w}{\partial z} \end{pmatrix} \tag{5}$$

with $\boldsymbol{V}$ being the wind vector $(u, v, w)^T$. It can be seen that the wind vector components do not change horizontally in that case. As already described in the preceding chapter, in case of no change in terrain elevation among the measurement points and the reconstruction point, the vertical change in wind speed is negligible concerning the wind vector reconstruction.

In the case of complex terrain and, therefore, inhomogeneous flow, all components of the wind speed gradient remain and contribute to the (biased) reconstructed wind speed.

The effects of inhomogeneous wind flow on the accuracy of wind vector reconstruction can best be explained by simplifying the problem to the two-dimensional space. Figure 3.4 a) shows the two-dimensional representation of a lidar placed at a flat terrain site. The local coordinate system has its origin at the lidar location, with x being the positive direction for the u component and z being the positive direction for the w component of the wind speed. In this simple case, $w = 0$ and u is horizontally homogeneous which means it does not change along the x-coordinate. Independent of the actual measurement height, the wind vector reconstruction following equation (3) will always result in the actual wind speed at the reconstruction point without any bias.

Figure 3.4 b) shows a slightly more complex flow situation. Here the lidar is placed on a tilted plane with increasing terrain elevation in x direction. Due to the change in terrain elevation, it becomes evident that the lidar measures at the same z coordinate in its local coordinate system, but at a different height above ground at the two measurement points. Considering the flow being horizontally homogeneous in this case as well, the u and w components of the wind speed do not change in flow direction parallel to the plane. With the plane only being slightly tilted, it can also be assumed that the vertical wind shear between the left and the right measurement point can be approximated to be constant, resulting in a linearly increasing u component. The application of equation (3) for wind vector reconstruction, in this case, will also lead to an unbiased result for the reconstructed wind speed compared to the actual wind speed at the reconstruction point. The vertical change in horizontal wind speed between the measurement points levels out in that case. However, in case the assumption of a linearly increasing horizontal wind speed is false, this case will also introduce bias.

A representative case for complex terrain is shown in Figure 3.5 c). Here the lidar is placed on top of a simple two-dimensional hill. Several things change in this situation, leading to a biased result of the wind vector reconstruction in the end.

First, there is a nonlinear change of the u-component of the wind speed vector in x-direction due to the influence of the terrain. Above the hill, the wind speed increases compared to the freestream wind speed. This effect is usually referred to as "speed-up" and is strongly dependent on the shape of the hill and the height above ground. However, the lidar does not see the whole speed-up effect, as the measurement points are usually never located in the freestream area of the flow. The only part of the speed-up that is relevant for wind vector reconstruction is between the measurement points and the reconstruction point. The influence of wind speed increase in the inflow region and wind speed decrease in the downflow reason can either be equivalent (symmetric) or not, depending on terrain complexity. The effect of speed-up must be considered a relevant factor for the lidar error in complex terrain. Therefore, based on the later definition of the lidar error in this thesis, the speed-up effects are considered separately.

Second, there is a change of the w-component of the wind speed vector in x-direction due to the influence of the terrain. As the wind passes the hill, it first streams upwards, implying a positive vertical wind speed. Then there is a turning point at the top of the hill, after which the wind streams downwards, resulting in negative vertical wind speed. However, both – the positive and the negative vertical wind speed – decrease the radial wind speed measured by the lidar at the respective measurement points. This leads to an overall decrease of the reconstructed wind speed following equation (3) and, therefore, an underestimation of the actual wind speed at the reconstruction point by a lidar placed on top of a hill.

a) lidar placed in flat terrain

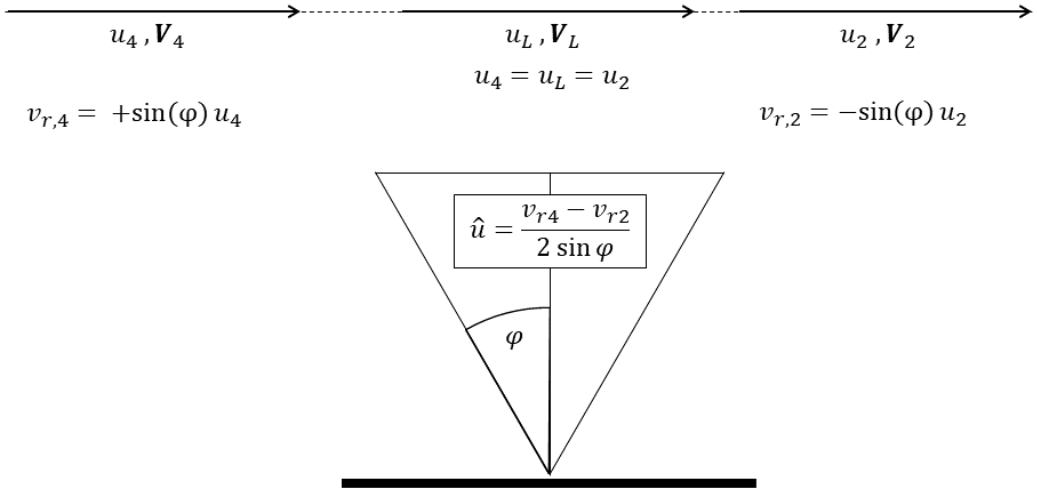

b) lidar placed on a tilted plane

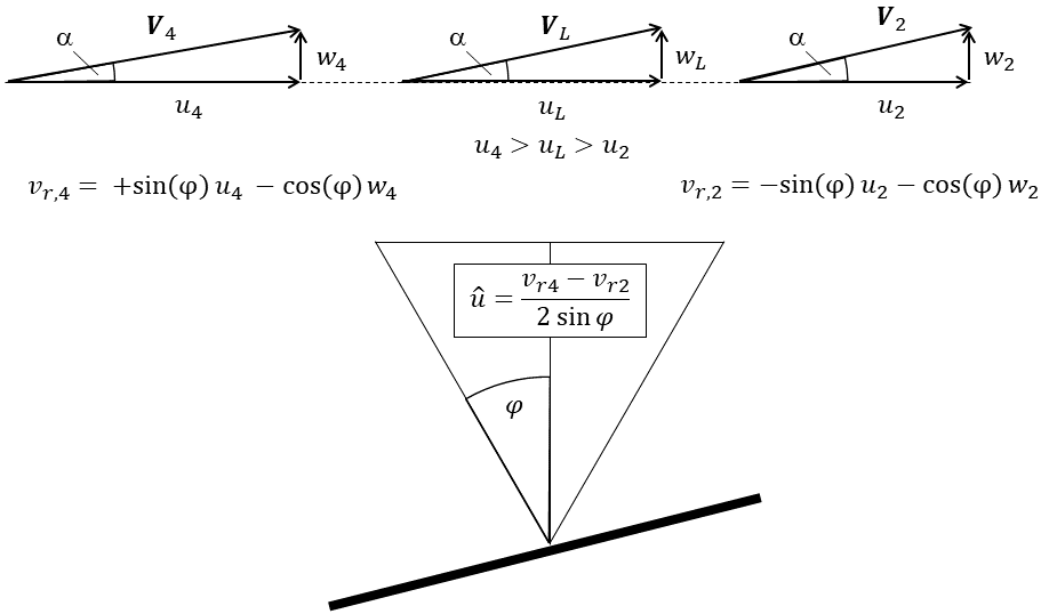

Figure 3.4: Two different generic flow cases with a lidar placed in flat terrain (a) and on a tilted plane (b). In case a), the reconstructed wind speed $\hat{\boldsymbol{u}}$ is equivalent to the actual wind speed above the lidar $\boldsymbol{u_L}$ and there is no lidar error. Case b) introduces more complexity, adding a constant vertical wind speed component to the flow. However, its influence on the radial wind speed equals out. A small lidar error may be present because the two measurement points are located at different levels above the ground.

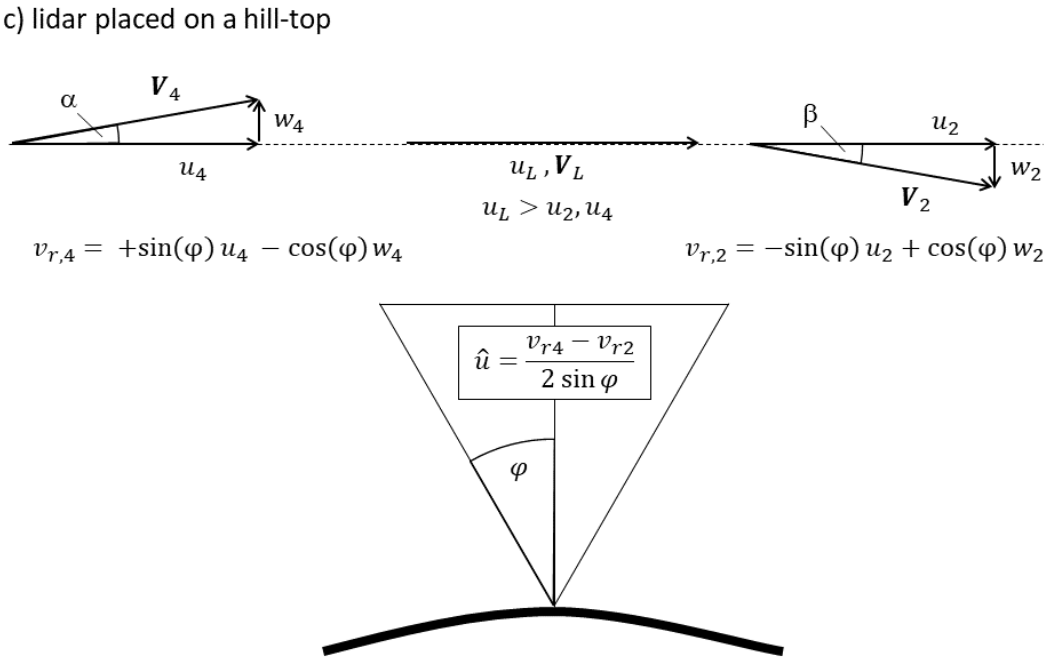

Figure 3.5: Generic flow cases (continued) with a lidar placed on a hill-top (c). As a typical complex terrain example, case c) shows a lidar placed on top of a hill within symmetric flow conditions. The changing vertical wind speed component introduces a lidar error. Additionally, there is a speed-up effect on the horizontal component that causes a part of the total lidar error.

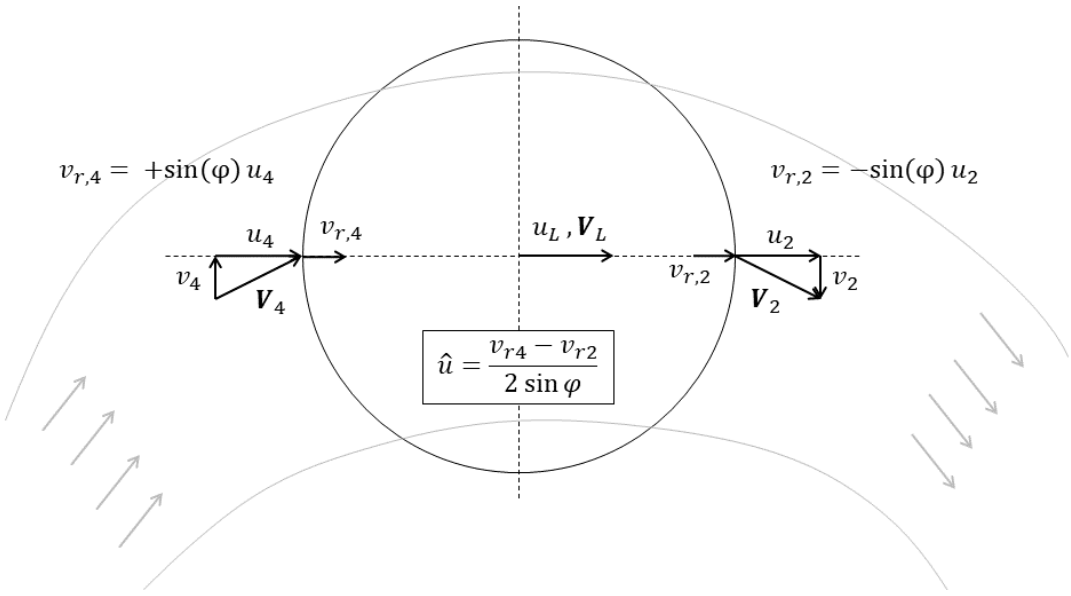

Figure 3.6: Illustration of a lidar placed in a curved valley. The flow is following the valley curvature (grey lines and arrows). In a simplified two-dimensional case the reconstructed wind speed $\hat{\boldsymbol{u}}$ underestimates the actual wind speed at the lidar location $\boldsymbol{u_L}$, because of the impacts of the changing $\boldsymbol{v}$-component of the horizontal wind speed along the valley. The behavior is similar to the hill-top flow case shown before.

Based on the above-given explanations, the lidar error ε for the two-dimensional case can be defined as follows:

$$\varepsilon = \frac{\hat{u} - u_L}{u_L} = \varepsilon_c + \varepsilon_s \tag{6}$$

with $\hat{u}$ being the reconstructed wind speed and u_L the actual horizontal wind speed at the reconstruction point. Following this definition, an underestimation of the actual wind speed at the reconstruction point will lead to a negative lidar error and an overestimation will lead to a positive lidar error. In order to separate the two effects, the lidar error can be divided into a part being caused by flow curvature (ε_c) and another part due to speed-up effects (ε_s). As presented in the results chapter 5.2.6, this distinction will give insight into the influence of the half-cone angle (beam tilting angle) on the lidar error.

Equation (3) for wind vector reconstruction can be rewritten for the two-dimensional case:

$$\hat{u} = \frac{v_{r,in} - v_{r,out}}{2\sin\varphi} = \frac{V_{in}\sin(\varphi - \alpha) + V_{out}\sin(\varphi + \beta)}{2\sin\varphi} \tag{7}$$

Here the radial wind speeds left and right from the lidar (inflow and outflow) are referenced to as $v_{r,in}$ and $v_{r,out}$ and the magnitude of the wind vector at the same points as V_{in} and V_{out}. The inflow and outflow inclination angles of the flow are defined as α and β and combine with the half-cone opening angle (or prism angle) of the lidar φ.

For simplification of the above-given equation (7), the following relationship can be derived:

$$u_L = \frac{u_{in} + u_{out}}{2} = \frac{V_{in}\cos\alpha + V_{out}\cos\beta}{2} \tag{8}$$

By making use of this equation and by defining the factor $k = \frac{V_{out}}{V_{in}}$ equation (7) can be written as:

$$\hat{u} = u_L\left(1 - \frac{1}{\tan\varphi}\frac{\sin\alpha - k\sin\beta}{\cos\alpha + k\cos\beta}\right) \tag{9}$$

Neglecting changes in the magnitude of wind speed between the two measurement points here (they will be considered in the second part of the error equation later) by assuming $k = 1$, results in an equation that is independent of the actual wind speed, but only dependent on geometric properties of the wind flow and the lidar:

$$\varepsilon_c = -\frac{\tan\frac{\alpha - \beta}{2}}{\tan\varphi} \tag{10}$$

And, with $\alpha = \beta$, as it is the case in symmetrical flow situations the equation reduces to

$$\varepsilon_c = -\frac{\tan \alpha}{\tan \varphi} \tag{11}$$

The speed-up of the horizontal wind speed component between a measurement location i and the reconstruction point can be written as

$$\Delta u = u_L - u_i \tag{12}$$

Keeping in mind that the speed-up between both, the inflow and the outflow measurement point and the reconstruction point have to be considered, the lidar error due to speed-up can be defined by

$$\varepsilon_s = \frac{u_{in} + u_{out}}{2u_L} - 1 \tag{13}$$

Here the difference between inflow and outflow horizontal component of the wind flow is considered as u_{in} and u_{out}.

Combining equations (11) and (13) leads to the equation used for the assessment of the total lidar error due to complex terrain in this study:

$$\varepsilon = \left[-\frac{\tan\frac{\alpha - \beta}{2}}{\tan \varphi}\right] + \left[\frac{u_{in} + u_{out}}{2u_L} - 1\right] \tag{14}$$

In chapter 5, the effects of complex terrain are modeled for simplified two-dimensional geometries. However, considering the measurement geometry of e.g. a Leosphere Windcube with four measurement points (compare Figure 3.2), the two-dimensional approach is applicable with only minor uncertainties, in case the measurement points are aligned along with the wind direction. The radial wind speeds at the measurement points perpendicular to the wind direction are then close to zero (see equation (3)).

For real-world applications with arbitrary terrain, the three-dimensional flow field is relevant and must be considered in order to achieve an accurate assessment of the lidar error. The following text will, therefore, describe the more general, three-dimensional case.

In a three-dimensional wind field, with the lidar being placed on an arbitrary three-dimensional surface, the wind vector components do change in all three coordinates. The speed-up and the curvature of the flow are dependent on wind direction. Different terrain shapes in different flow directions will lead to different lidar errors.

Additionally, the wind flow direction might change between the measurement points, while the magnitude of u and v are changing. A simple example for this case might be the flow through a curved valley: A positive y-component at the inflow that linearly decreases towards zero at the reconstruction point and then decreases further to negative values at the outflow results in an underestimation of the horizontal wind

speed at the reconstruction point (Figure 3.6). This behavior is equivalent to the before described flow over a two-dimensional hill.

Generally speaking, the flow curvature or bending in any dimension introduces errors in the wind vector reconstruction. The speed-up part of the lidar error in a three-dimensional case must be extended to the speed-up or horizontal change in wind speed between both pairs of opposing measurement points. Depending on the wind direction and terrain surface, the speed-up part will also change.

3.3 Lidar error in the context of wind resource assessment

As detailed out in the above chapter 3.2, lidar errors in complex terrain are systematic and need to be corrected before the measured wind data can be used for wind resource assessments (WRA) or other wind energy applications. The application of flow models for lidar error estimation is a common approach (see chapter 1.4). However, modeling the wind field with CFD comes with uncertainties that mainly depend on model complexity and the characteristics of the actual measurement site (e.g., Bechmann et al. 2011). Following from this, also the estimation of the lidar error introduces additional uncertainties into the WRA. The German guideline on WRA assigns 50 % of the estimated error as an additional uncertainty in the wind measurement (FGW e.V. 2017) and this approach is usually followed, at least in the German wind industry.

Increasing lidar errors, therefore, also increases the magnitude of the additional uncertainty. The question arises up to which magnitude of lidar error the application of lidars is still feasible at a certain measurement site.

The total uncertainty in predicted annual energy production (AEP) of a planned wind farm is in the order of 10-15 % for flat terrain and can, in dependence of the data basis, exceed 15 % in complex terrain (Basse et al. 2017). In a round-robin test of the German Wind Energy Association about WRA at a slightly complex and partly forested site, the mean estimated total uncertainty was 14.8 % (Fiedler et al. 2015). Based on economic considerations and financial risk, the total uncertainty should be as low as possible because it directly affects the yield deductions and, consequently, the interest rates and equity capital of the project (Schorer et al. 2015; Mehnert 2017).

Following the technical guideline TR6 (FGW e.V. 2017), the total uncertainty in a WRA consists of the different and independent uncertainty components of the wind data basis, modeling of the wind field, modeling of park efficiency, power curve and energy loss factors.

The total uncertainty is calculated by the root-sum-square technique (RSS) (compare, e.g., Lackner et al. 2007). This method is also used here to assess the maximum acceptable contribution of the lidar error correction to the total uncertainty. The RSS of all uncertainties in a WRA, except the additional uncertainty due to lidar error correction, is assumed to be 12 % in AEP. The additional uncertainty is given as 50 % of the lidar error estimation in wind speed. It is converted to uncertainty in AEP by application of a common AEP factor of 2.0 (Basse et al. 2017). Table 1 then provides the resulting total uncertainty for different lidar errors.

In order to keep the total uncertainty below 15%, the lidar correction must not exceed 9 % for these assumptions. However, changing the assumptions changes this value a lot. E.g., changing the AEP factor in the interval from 1.5 to 2.5 (Basse et al. 2017) results in tolerable lidar errors is between 7% and 12%. An increased basic uncertainty

decreases the possible margin for lidar error correction. It is, therefore important to put the estimated lidar error into the context of the actual site and the preconditions of the WRA to decide on whether a lidar or a mast measurement campaign is reasonable in a given case.

Table 1: Additional uncertainty because of lidar error correction at a complex terrain site and resulting total uncertainty of the wind resource assessment (WRA). The basic total uncertainty for zero lidar error is assumed to be 12 %. The additional uncertainty from lidar error correction is 50 % of the lidar error and the AEP factor used in the calculation is 2.0. Uncertainties are assumed to be independent.

absolute lidar error [%]	additional uncertainty from correction [%]	additional uncertainty in WRA	total uncertainty of WRA	uncertainty difference [%]
0	0	0	12,0	0,0
1	0,5	1	12,0	0,0
2	1	2	12,2	0,2
3	1,5	3	12,4	0,4
4	2	4	12,6	0,6
5	2,5	5	13,0	1,0
6	3	6	13,4	1,4
7	3,5	7	13,9	1,9
8	4	8	14,4	2,4
9	4,5	9	15,0	3,0
10	5	10	15,6	3,6
11	5,5	11	16,3	4,3
12	6	12	17,0	5,0

4 Modeling methods and strategies

As already described in chapter 3.2 the method of choice within this thesis to estimate the lidar error due to complex terrain is to model the wind flow. For this, different analytical and numerical flow models are available. They can be distinguished by their modeling approach and level of detail.

The following chapter 4.1 will give a short introduction to the atmospheric boundary layer (ABL) and wind flow in complex terrain. Due to its importance for this study, the effects of atmospheric stability are discussed separately in chapter 4.2. As different models have been used within the thesis, chapter 4.3 and sub-chapters will introduce their methodology and characteristics.

To achieve the aims of the doctoral thesis, a systematic model-based parameter study has been carried out, using the different flow models described. The approach and method of this study are described in chapter 4.4.

Chapter 4.5 will then describe how the different models were set up and applied and also give an overview of the geographical data that has been used for flow modeling.

4.1 Wind in complex and forested terrain

The wind profile in the lower part of the ABL in flat terrain with homogeneous land cover can be described by the logarithmic wind profile. The following equation is valid for the surface layer or Prandtl layer that reaches up to about 100 m above ground. It is dominated by surface roughness effects (Stull 1988):

$$u(z) = \frac{u_*}{\kappa} \ln\left(\frac{z-d}{z_0}\right) \tag{15}$$

Here $\kappa = 0.4$ is the van Kármán constant and u_* the friction velocity. The change of wind speed with height can be approximated by a logarithmic function that is dependent on the height above ground z, surface roughness or roughness length z_0 and – in case of the presence of forest or other obstacles – a displacement height d. Typical values for the roughness length are 0.01 m for grassland of 0.1 m for shrubs (compare Emeis 2018, p. 34; Troen 1989). The displacement height is used to shift the wind profile vertically. It is dependent on the density and height of the obstacles or the trees. Trees standing close together result in a larger displacement height (Emeis 2018; Stull 1988). An overview of displacement height modeling in wind energy can be found in Dellwik et al. (2006).

For complex terrain, this simple equation is no longer valid, as additional effects have to be considered to accurately model the wind profile and other wind characteristics. Within the context of this thesis, complex terrain is defined by the presence of at least one of the following two elements:

1. Inhomogeneity in land cover (forest, grassland, bushes, clearings, …) and therefore surface properties z_0 and d
2. Significant variation of terrain elevation (hills, mountains, valleys, escarpments, …)

This definition is, e.g., comparable to other definitions in Emeis (2018) or Clifton (2015).

To estimate the wind profiles or the overall wind field at a complex terrain site, flow models are needed that are able to model the influence of orography and land cover on the wind flow (Emeis 2018).

Flow models used for wind energy applications differ in terms of complexity and their capability to model, e.g. non-linear effects as flow-separation. The linear models (e.g., WAsP) have been used for many years to estimate the wind resource in flat terrain or in gently sloping terrain. However, as more and more wind turbines are erected at complex and forested sites, with significant terrain elevations, RANS CFD models have shown to provide more accurate results (Bowen and Mortensen 1996; Palma et al. 2008).

4.2 Atmospheric stability

The state of the ABL can roughly be classified into three different atmospheric stability classes: A convective (or unstable) boundary layer, a stable boundary layer and a neutral (or dynamical) boundary layer (Stull 1988; Emeis 2018). The three different types and the preconditions for their occurrence are described in the following text.

The structure of the ABL develops with the diurnal cycle. Starting with sunrise and increased heating of the surface, a convective boundary layer is evolving. It is growing with time and, due to the heating of the surface, characterized by vertical mixing (mixing layer), which results in low wind shear. With the beginning of sunset, the thermal convection ends and less turbulence is produced. The remaining layer is called the residual layer, which is neutrally stratified. At the same time, a stable boundary layer is forming at the surface, which has low turbulence intensity and large wind shear. Its vertical extent is growing during nighttime. After sunrise, the stable boundary layer is dissolved and a new convective boundary layer develops. However, in case of the presence of clouds and precipitation or strong winds that cancel out the influence of radiative heating by the sun, the diurnal variation of the ABL is less pronounced. In this case, a neutral boundary layer remains (Stull 1988; Emeis 2018; Foken 2016).

A common approach to adapt the logarithmic wind profile to different atmospheric stabilities is the introduction of a stability correction function. This is, i.e., described for stable and unstable stratification in Emeis (2018). A comparable approach is also used to determine the boundary wind profiles in the RANS CFD model Meteodyn WT, which is used within this dissertation to model the influence of atmospheric stability on the flow above a hill (Meteodyn 2014).

4.3 Modeling of the wind flow

The following chapter describes the three types of wind flow models that are used within the context of this thesis to model the flow over two-dimensional hills:

- An inviscid, potential flow model introduced by Bradley (2008) (chapter 4.3.1)
- A model based on a linearized version of the Navies-Stokes equations, namely WAsP Engineering 2.0 (chapter 4.3.1)
- A model based on RANS equations, namely Meteodyn WT (chapter 4.3.3)

These three models differ in complexity, computational efforts for calculations as well as available model parameters. The characteristics and capabilities of the three models are briefly described in the following sub-chapters.

4.3.1 Potential flow model

Potential flow models provide a very much-simplified solution for the wind flow over a surface. They do not cover any kind of friction, i.e., friction induced by the ground due to roughness or vegetation or friction within the flow. However, for simple flow situations where friction on the ground is not of interest or negligible, potential flow solutions can provide useful approximations to more complex numeric solutions such as the RANS equations. One of their big advantages is that it is often possible to give an analytical solution for a distinct flow situation. This makes the computation of the flow field under different parameterizations very fast and easy (Emeis 2018; Bradley 2008).

A simple inviscid and two-dimensional potential flow model has been introduced by Bradley (2008) in the context of sodar measurements in complex terrain. It is capable of modeling the wind flow on a bell-shaped hill. The model is also applied and discussed in Bradley (2012), where it is used to study the errors of a sodar and a lidar.

The model is used within this thesis as a reference or baseline case for the more complex CFD models in the parameter study presented in chapter 5. It is implemented in MATLAB and the equations are adapted to the measurement geometry of a two-dimensional simplification of the Windcube lidar as described in chapter 3.2. All equations given in the following text are taken from this implementation but are based on those given in Bradley (2008) and Bradley (2012).

The flow model is based on the well-known potential flow solution around a cylinder, which is placed in the center of the coordinate system used. It provides a stream function and a streamline function that can be used to approximate the flow over a bell-shaped hill very much similar to a Gaussian hill shape (Bradley 2008):

$$\psi = U\eta\left(1 - \frac{R^2}{\zeta^2 + \eta^2}\right)$$
$$\eta_0 = \eta\left(1 - \frac{R^2}{\zeta^2 + \eta^2}\right) \tag{16}$$

Stream function ψ and streamlines η_0 are only dependent on the horizontal inflow speed U and the radius of the cylinder R. The coordinates ζ and η represent the ordinate and abscissa of the two-dimensional coordinate system centered at the cylinder (compare Figure 4.1).

The fundamental assumption of the model is that any of the streamlines resulting from the flow around a cylinder can be considered as the hill surface and that all streamlines following upwards can be seen as the flow field over this hill. Bradley (2008) then introduces a parameterization of the potential flow solution that links its parameters to those of a two-dimensional hill.

The streamline that represents the hill surface η_0 and the radius of the central cylinder R are calculated from the hill height H and the hill half-width L:

$$\eta_0 = \sqrt{L^2 + \frac{H^2}{4}} - H \tag{17}$$

$$R^2 = HL\sqrt{1 + \left(\frac{H}{2L}\right)^2} \tag{18}$$

The horizontal and vertical wind vector component u and w can then be calculated by the following equations in which the coordinate system is centered at the location of the lidar, which is typically at the peak of the hill:

$$u(x,z) = U\left(1 - R^2\frac{(x^2 - z^2)}{(x^2 + z^2)^2}\right) \tag{19}$$

$$w(x,z) = U\left(-2R^2\frac{xz}{(x^2 + z^2)^2}\right) \tag{20}$$

with $x = \zeta - \zeta_L$ and $z = \eta - \eta_L$ being the coordinates centered on the lidar location. The flow solution is scaled by the wind flow at the inflow of the model domain U.

The hill surface is given by the streamline starting at η_0, which represents the ground height of the flat terrain at the border of the model domain. Following the streamline at η_0 gives the shape of the hill. The wind vector components can then be calculated for arbitrary points above that streamline.

The set of H/L ratios that are used in the parameter study is detailed out in chapter 4.5.

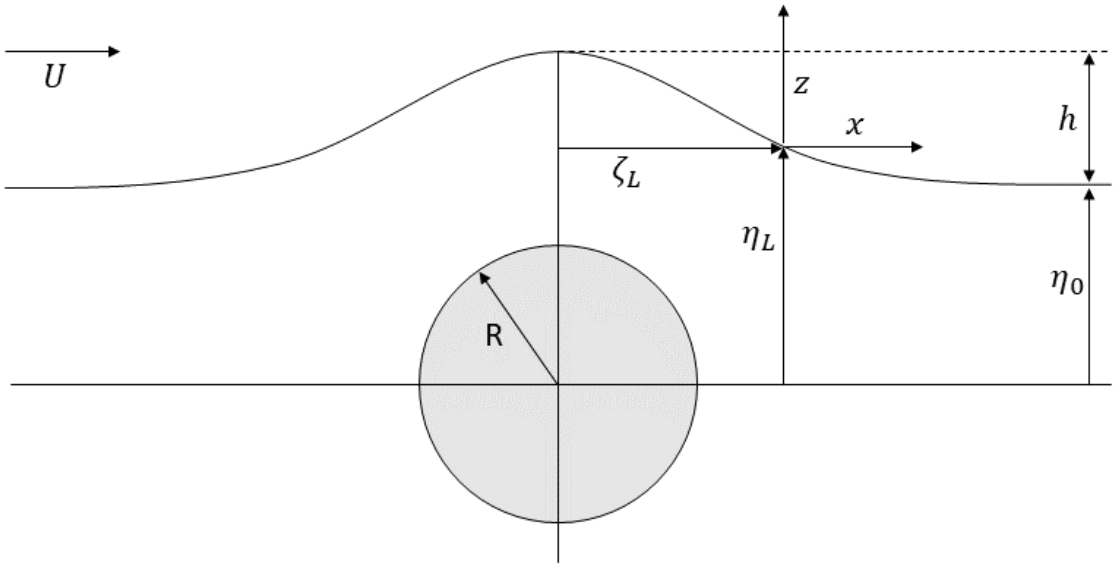

Figure 4.1: Geometry and definitions in the potential flow model following Bradley (2008). The figure has been copied from Bradley (2008) with minor adaption. In this example, the lidar is placed at an arbitrary point at the surface of the hill in order to illustrate the shift of the coordinates.

4.3.2 Linearized model

WAsP Engineering (WEng) is a well-known flow model that is often used for wind energy applications (Mann et al. 2002). The model is a so-called "linearized" model, which is based on a linearized version of the Navier-Stokes equations. Since its publication in 1975, it was under further development (Jackson and Hunt, J. C. R. 1975; Troen and Baas 1990; Mann et al. 2002). Its basic concept is to model the influence of orography (i.e., hills or valleys) as perturbations to the boundary-layer flow over flat terrain. Due to the simplifications that are made in the linearization, it is only applicable for flat and moderately complex sites. According to the recommendations of the developer, it should not be used in complex terrain with steep inclinations where flow separation might occur (Mann et al. 2002). There is no forest model in WEng, but a common way to represent forest is the use of a displacement height and increased roughness lengths (Dellwik et al. 2004). Further details on how the model is used within this dissertation can be found in chapter 4.5. It has also been used by Klaas et al. (2015) to estimate the lidar error and the work presented in this thesis builds upon the work for that study.

4.3.3 RANS model

With the increasing computational power of modern desktop PCs, the application of three-dimensional RANS CFD models has become more popular. RANS CFD models in combination with a turbulence closure, are capable of modeling the atmospheric boundary layer flow at complex terrain sites (Palma et al. 2008; Mann et al. 2017).

Today there are multiple commercial and non-commercial software available that are used in the wind industry (Palma et al. 2008). The software Meteodyn WT, developed by the French company Meteodyn is used in version 5.3 within this dissertation to perform modeling of complex, forested terrain, also under different atmospheric stability conditions. Most information about the model is provided within the software documentation (Meteodyn 2014), a presentation from a Webinar (Meteodyn 2017) and a white paper provided by the software developer (Jiang et al.). Wherever possible, literature references to original publications of the fundamental model equations are given.

In Meteodyn WT, steady-state RANS equations for incompressible flow are used in combination with a K-closure scheme for turbulence parameterization (Meteodyn 2014; Hurley 1997).

Meteodyn WT models the forest as a porous medium that introduces an additional sink term to the RANS equations within the forest cells. The forest height can be adapted and the forest density can be changed, providing the possibility to model low, medium and high forest density. The sink term is defined by the following equation (Meteodyn 2014; Wilson et al. 1998):

$$F_V = -\rho C_d \boldsymbol{U}|\boldsymbol{U}| \tag{21}$$

When the forest model is activated, the local roughness length is directly related to the tree-height to roughness-length ratio (Meteodyn 2014):

$$A = \frac{h_t}{z_0} \tag{22}$$

A value of $A = 20$ is suggested by the developer, although it can be changed by the user in order to adjust the tree height. However, within the simulations carried out in the parameter study, the value is set to 20 (Meteodyn 2014).

Within the forest cells, the forest model affects several parameters of the turbulence model. In particular, the dissipation term[3] ε is defined as follows Wilson et al. (1998):

$$\varepsilon = \max\left(\varepsilon_{cc}, \varepsilon_{fd}\right) \; with \begin{cases} \varepsilon_{cc} = C_\mu \dfrac{\nu_T}{{L_T}^2} k \\ \varepsilon_{fd} = C_d |\boldsymbol{U}| k \end{cases} \tag{23}$$

with $\boldsymbol{U}$ being the wind vector, ν_T the turbulent viscosity, L_T the turbulent length scale and k the turbulent kinetic energy. C_μ is dependent on the Richardson number and C_d is the drag force coefficient, that is adapted for different atmospheric stabilities based on an empirical study by the software developer (Meteodyn 2014). Detailed information on ε_{cc} and ε_{fd} can be found in Wilson et al. (1998).

There are two different forest models Meteodyn WT: the "robust" and the "dissipative" model. The dissipative forest model is used here, as the software developer recommends it. It provides better results on turbulence intensity due to the presence of forest (Meteodyn 2014). The forest model introduces a dissipative zone above the forest, and the mixing length becomes (Meteodyn 2014):

$$\frac{1}{l} = \begin{cases} \dfrac{1}{2} & for\ z < h_t \\ (1-\mathrm{a})\dfrac{1}{2} + \mathrm{a}\left(\dfrac{1}{l_0} + \dfrac{1}{\kappa z}\right) & for\ h_t < z \le h_t + 15\ m \\ & with\ \mathrm{a} = \dfrac{z - h_t}{15\ m} \\ \dfrac{1}{l_0} + \dfrac{1}{\kappa z} & for\ z > h_t + 15\ m \end{cases} \tag{24}$$

The drag force coefficient C_d can be changed by the user as the forest density from the default setting "normal" to either "low" or "high," which means decreasing or increasing the drag force coefficient for the model (Meteodyn 2014; Ross and Vosper 2005). The C_d values used in Meteodyn WT are 0.001, 0.005 and 0.01 for low, normal and high forest density.

The atmospheric stability model in Meteodyn WT is considering ten different atmospheric stability classes (compare Table 2). Neutral stratification is given for stability class 2. Lower stability classes refer to unstable stratification and higher stability classes to stable stratification (Meteodyn 2014).

[3] To ensure consistency of the model equations with the literature, the symbol ε is kept for the dissipation rate within this sub-chapter in the dissertation. However, in all other chapters, the symbol ε is referring to the lidar error and not to the dissipation rate.

Stability classification is based on the Monin-Obukhov length L^* in the form of

$$L^* = -\frac{{u_*}^3}{\kappa(\frac{g}{\overline{T}})(\frac{Q_H}{c_p\rho})} \tag{25}$$

with c_p being the specific heat, T the air temperature, g the gravitational constant and Q_H the kinematic heat flux (Meteodyn 2014). This definition is derived based on Monin-Obukhov similarity theory (MOST) which provides the following relation for the heat flux $\overline{w'T'}$ (Foken 2016):

$$\overline{w'T'} = \frac{Q_H}{\rho c_p} \tag{26}$$

Details on the similarity theory can e.g. be found in Stull (1988). The Monin-Obhukov length can be interpreted as the height above ground "at which buoyant factors first dominate over mechanical (shear) production of turbulence" (Stull, p. 188).

There are two different stability models in Meteodyn WT that set up the boundary conditions for the inlet wind profiles and the turbulent kinetic energy profiles in dependency of the chosen stability class in accordance with the MOST (Meteodyn 2014).

In the case of stability classes 0 to 6, the boundary layer is subdivided into a surface layer and a transitional layer with equations for determination of wind and turbulence profiles for each of the two layers. At the top of the transitional layer, the wind speed reaches the geostrophic wind speed that is also dependent on the stability class (Meteodyn 2014).

In the case of the highest stability classes 7 to 9, a three-layer model is used that adds an outer layer to the two other layers (Figure 4.2). However, also the equations for the other two layers differ from the two-layer model in this case (Meteodyn 2014). An evaluation of the three-layer model is given in the webinar by Meteodyn (2017).

Detailed equations for the boundary conditions in the stability model are given in Appendix 10.1.

Apart from the boundary conditions, the turbulence model of Meteodyn WT is also influenced by the choice of the atmospheric stability class. In particular, the turbulent length scale L_t is affected by the flux Richardson number Ri_f. The flux Richardson number is calculated from the Richardson number based on the chosen Monin-Obukhov length, as given in Table 2. Again, detailed equations on the turbulence model are given in Appendix 10.1.

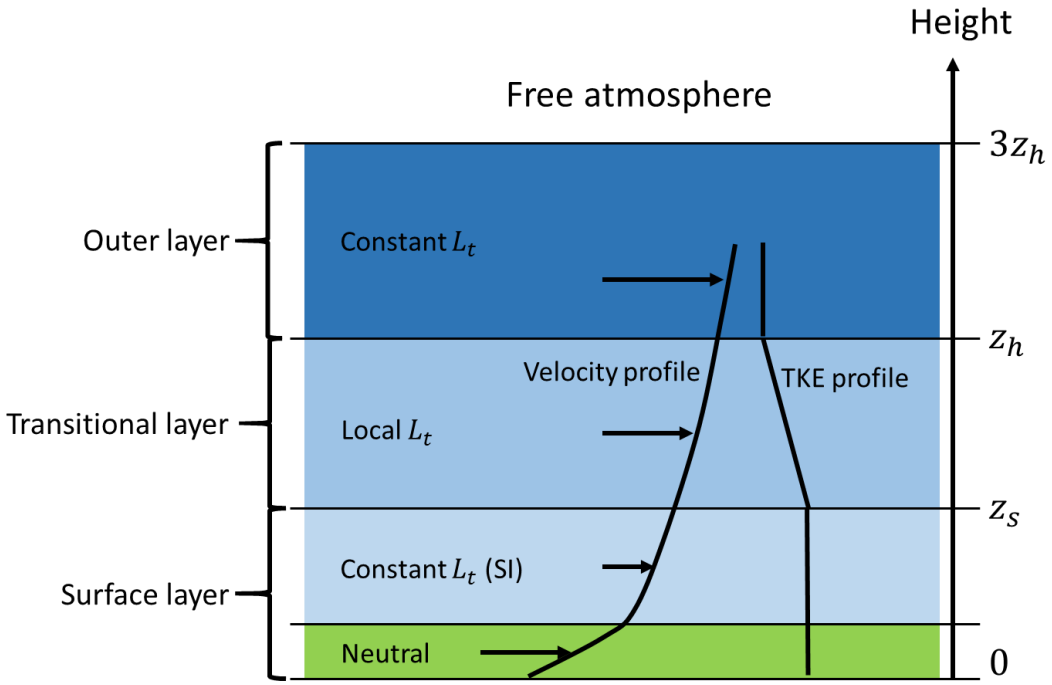

Figure 4.2: Schematic illustration of the three-layer model for high stability classes (7, 8 and 9) in Meteodyn WT. The ABL is modeled with three layers: The surface layer up to a height z_s with constant turbulent kinetic energy (TKE), the local Monin-Obukhov-Similarity-Theory (MOST) layer between z_s and z_h with a linear decrease of TKE and the outer layer between z_h and three z_h with a constant TKE again. The layer heights are dependent on the atmospheric stability classes. The figure is redrawn after Meteodyn (2014).

Table 2: Atmospheric stability classes from Meteodyn WT (Meteodyn 2014).

Stability class	**Stability**	**L_*[m]**
0	Very unstable	-80
1	Unstable	-500
2	Neutral	10.000
3	Slightly Stable	1.500
4	Stable	800
5	Stable	500
6	Stable	300
7	Very Stable	200
8	Very Stable	130
9	Strongly Stable	60

4.4 Method of the systematic parameter study

When applying a model for wind resource assessment, it is obligatory to find the right parameterization to fit the model to the considered site and measured wind profiles. The model is then used to perform vertical and horizontal extrapolation of a wind measurement (Ayotte 2008). Usually, this is achieved by making use of available knowledge about land-use, roughness lengths, forest heights and density from maps and other geodata. Additionally, the experience of the model user and expert guesses are used to find the most appropriate parameterization for the flow model. If possible,

a comparison of measured and modeled wind profiles for different parameter settings are carried out at one or multiple measurement locations within the area of interest (e.g. (Palma et al. 2008).

However, if only lidar measurements are available at a complex terrain site, the measured wind profiles are likely to be affected by the complex terrain lidar error (compare chapter 1.3.4). It is, therefore, not possible to entirely rely on the measured data for model evaluation. It is necessary to estimate the uncertainty in the lidar data due to complex terrain before comparing it to the model. Alternatively, a correction of the lidar data can be carried out, but then the uncertainty of this correction must be estimated as well (FGW e.V. 2017; Clifton et al. 2018).

For lidar correction, currently available literature usually states the "best" results that have been achieved using a specific parameter set for the given model at the prospected site. In these cases, the model parameterization has either been validated against a measured wind profile from a close-by mast. Or the lidar error estimation itself is validated if measurement data from a mast and a lidar at the same location is available (e.g., Klaas et al. 2015; Bingöl et al. 2009).

There is no systematic evaluation available on using different parameterizations for modeling the lidar error with a particular model in the literature so far (compare chapter 1.4). Also, there is no profound uncertainty assessment regarding the accuracy of the lidar error estimation. One aim of this parameter study is, therefore, to raise awareness about the importance of the different model parameters on lidar error estimation. The analysis also includes the sensitivity of the lidar error correction on the different parameters at different terrain settings, which can be translated into uncertainty.

To isolate the influence of the different parameters on the wind flow, different models are used in this study:

First, a simple potential flow model (see chapter 4.3.1) is used to analyze the terrain effects on the wind flow over two-dimensional Gaussian hills. The model results are used to fix the parameter space for the hill geometries (H and L, see chapter 4.5.1) in order to cover all relevant effects on the lidar error. Due to its simplicity, the model can be run fast and for many different cases. It is used as a baseline or reference case to depict the influence of the diverse parameters on the results of the other, more complex models.

The second model that is used, WEng, is based on linearized Navier Stokes Equations (chapter 4.3.1) and a very common model for wind energy applications. It is able to model the influence of roughness on the wind flow. There is no forest model implemented. The only possibility for adapting the model to a forested site is the use of displacement heights, which is not done in this dissertation.

The third model, Meteodyn WT, is a RANS CFD model, that is able to model roughness and forests (chapter 4.3.3). It has also a simplified method to account for atmospheric stability. This model is more and more used for wind resource assessments as it more appropriate for complex and forested sites wind turbines are often placed in today.

The results from the more complex models are compared to those from the potential flow model in chapters 5.1 and 0. By this approach, it is possible to isolate the influence

of the additional effects (roughness, forest, atmospheric stability) that are taken into account by the more complex models.

In order to make the results applicable to, e.g. arbitrary hill geometries and measurement heights, the results are presented in a non-dimensional way wherever possible. This is especially true for the results of the lidar error estimations in chapter 0. The lidar error ε and also its parts due ε_c (flow curvature) and ε_s (speed-up) are usually plotted against the ratio of measurement height over the hill half-width z/L. By this it is possible to extract results for different measurement height as well as different hill dimensions from a single non-dimensional figure. The amount of terrain inclination is in most figures shown for groups of a constant ratio of hill height over the hill half-width H/L. In reference to Table 3, mainly four of these groups are analyzed for slight slopes up to high slopes in the order of 0.3 (compare chapter 4.5.1).

The study is limited to simplified, two-dimensional Gaussian hills. However, the evaluation of the results in chapter 6 shows their applicability to the situation in real complex terrain.

4.5 Flow model setup

The following chapter briefly describes the actual setup and parameterization of the models used in this thesis. First, the preparation of geodata for the model-based parameter study is described (chapter 4.5.1). This includes the generation of model terrain of different orographic complexity as well as the generation of roughness data. Second, the setup of the three models, the potential flow model, WEng and Meteodyn WT is given.

4.5.1 Terrain data for the parameter study

The parameter study is based on a set of two-dimensional, respectively, quasi-two-dimensional Gaussian hills. The set covers four different H/L ratios (see Table 3) that range from low maximum terrain elevations of 0.07 to significant slopes of 0.29. The range of fixed L values reaches from 50 to 750 m and the minimum and maximum H values are 5 and 300 m, depending on the actual H/L ratio.

This choice of absolute values is a trade-off between model resolution and calculation time. In the case of very small hills, a high model resolution is needed to resolve the influence of the hill geometry on the flow is needed. In the case of very large hills, the domain size has to be increased significantly in order to ensure undisturbed flow at the model domain borders. For WEng and Meteodyn WT, the hill geometry is symmetrically extended into the third dimensional, resulting in a very long ridge. Results are then taken from the mid-point of the geometry that can be assumed to be undisturbed by effects from the model domain borders.

For the two-dimensional potential flow model (compare chapter 4.3.1), the hill shapes are generated from the resulting streamlines. They do not exactly match the Gaussian hill shapes but are – especially in the area of interest in the vicinity of the lidar measurement points – very similar to those. A comparison of a Gaussian hill shape and a hill shape for the potential flow model is shown in Figure 4.4. Because the model runs in the potential flow model are very fast, much more hill geometries were simulated with this model than with the three-dimensional RANS model or the linearized model. For the H/L ratios from 0.1 to 0.4 the L values were modified

between 10 and 1000 m in 10 m steps. Additionally, L of 2000 m and 4000 m were chosen.

The results from the potential flow (see chapter 5.2.1) model were used to find the necessary H for fixed L values for the other models. In order to minimize the calculation efforts, the number of different hill geometries was limited so that the most relevant parts of the resulting lidar error plot could be mapped. That means the analysis process was iterative in this part.

All geometry data was generated in MATLAB. For Weng and Meteodyn WT xyz-files were exported, which contain the coordinates and heights of the terrain in 5 m horizontal resolution and 1 cm vertical resolution (i.e., the resolution of the elevation values). For WEng, these files were converted to ".map"-files of height contour lines, a proprietary format of WAsP.

Due to its conception, the potential flow model does not require any roughness information. For the other models, roughness maps have been created that contain constant roughness values. The roughness length z_0 ranges from a very low value of 0.005 m to a large value of 1.5 m.

All roughness data was generated in MATLAB and exported to xyz-files that contain the coordinates and roughness of the terrain in 5 m horizontal resolution and 1 cm roughness resolution (i.e., the resolution of the roughness length z_0). For WEng, these files were converted to ".map"-files.

Table 4 shows the different roughness length and the surface characteristics that are attributed to those. The table also indicates for which purposes the roughness maps are used in the parameter study. While only roughness lengths up to 0.5 m are used in WEng, also maps with 1.0 and 1.5 m roughness length were used in Meteodyn WT. However, these were used in conjunction with the forest model, which translates roughness length into tree heights, as described in chapter 4.3.3.

Table 3: Set of Gaussian hill geometries used in the parameter study. The table provides information about the hill height H, the hill half-width L and the corresponding ratio H/L. Addtionally the maximum slope (maximum terrain inclination) at the flanks of the hill is calculated for the four different used ratios.

H/L	**L [m]**	**50**	**100**	**150**	**200**	**250**	**500**	**750**	**Max. slope**
0.1	**H [m]**	5	10	15	20	25	50	75	0.07
0.2		10	20	30	40	50	100	150	0.14
0.3		15	30	45	60	75	150	225	0.21
0.4		20	40	60	80	100	200	300	0.29

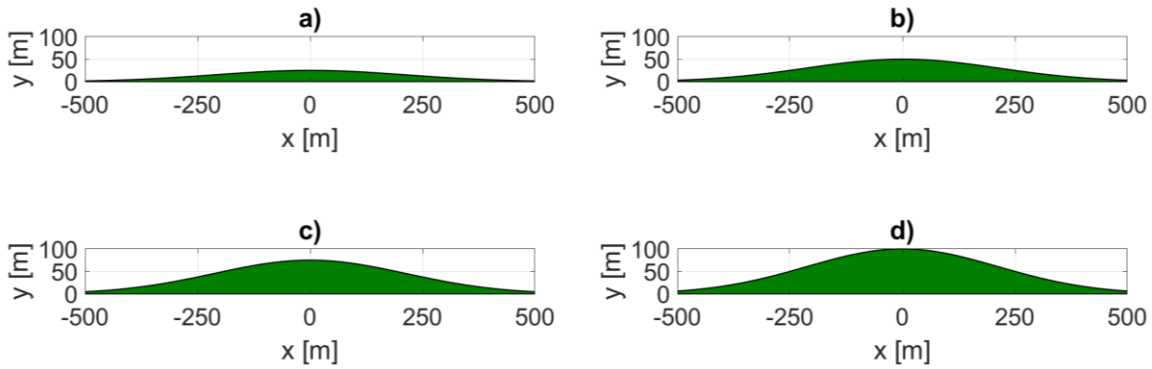

Figure 4.3: Four examples of Gaussian hills for the $\boldsymbol{H/L}$ ratios a) 0.1, b) 0.2, c) 0.3 and d) 0.4. The same scaling for the four plots is chosen in order to emphasize the difference in terrain inclination for increasing $\boldsymbol{H/L}$ ratios.

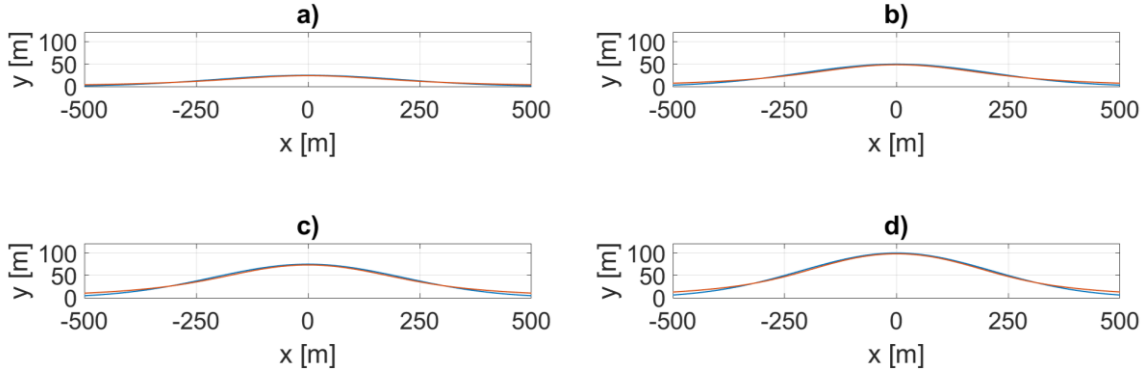

Figure 4.4: Approximation of the four examples of Gaussian hills (blue line) by a streamline of the potential flow model (red line).

Table 4: Roughness lengths $\boldsymbol{z_0}$ of the different roughness maps that were used in the flow models. The purpose of the maps is also given, which includes the corresponding tree heights in Meteodyn WT. Surface characteristics were taken from Troen (1989).

Roughness length [m]	Surface characteristics	Tree height [m]	Used in WEng	Used in Meteodyn WT
0.005	bare soil	-	yes	yes
0.100	farmland	-	yes	yes
0.500	bushes, suburbs	10	yes	yes (forest and roughness)
1.000	city, forest	20	no	yes (forest)
1.500	city, forest	30	no	yes (forest)

4.5.2 Model setup and simulation runs

The potential flow model was run in MATLAB with the hill geometries described in chapter 4.5.1. Results were stored in a two-dimensional data array with a resolution of 5 m in the vertical direction and 10 m in the horizontal direction. Streamlines were calculated with the built-in MATLAB function.

For WEng, simulation projects were set up for each pair of orography and roughness with the heights 50, 100, 150 and 200 m. The background roughness is set to the value of the roughness map file that is used. Depending on the domain size, a horizontal resolution of either 5 or 10 m is used, in order to limit the number of cells below a reasonable threshold. A script originally developed by Bingöl (2009) was adapted to the methodology used within this thesis. The script calculates all simulation results for western wind direction (wind positive along the x-axis) that are needed for lidar error estimation and exports the results to an Excel-File. Using internal functions, the script calculates the wind vector components and the horizontal wind speed and the flow angles at the lidar measurement location at each measurement height and at the lidar measurement points upwind and downwind the hill for a given half-cone opening angle. It then calculates the lidar errors ε, ε_c and ε_s. There is no function available to calculate streamlines. As the export of wind vector components at a regularly gridded plane is not possible, streamlines were not calculated for this model.

For Meteodyn, a project was set up for each orography and roughness. Additionally, projects were set up for three different tree heights and for three different forest densities. To consider atmospheric stability, for the H/L ratio of 0.3, one project for each orography and stability class was set up for the lowest roughness, the highest roughness and a medium dense forest with 20 m tree height. In total 216 simulation projects were set up in Meteodyn WT for the parameter study. All projects were run with a horizontal resolution of 8 m in the proximity of the lidar location and for western wind direction (positive along the x-axis). The model results were exported to tecplot-files (a proprietary data format) and imported to MATLAB for further analyses. Lidar error estimation, as well as calculation of streamlines and other flow parameters, was carried out in MATLAB. As the lidar measurement geometry and error estimation were modeled in MATLAB, the half-cone opening angle and measurement heights were set up in MATLAB scripts and not within the Meteodyn WT projects. This approach allows for the possibility of quickly changing the lidar setup and measurement heights without running further simulations.

5 Estimation of lidar errors in complex terrain

In this thesis, the method of choice to understand and analyze the impact of complex terrain on lidar measurement accuracy is a systematic model-based parameter study. The methodology for this study is given in chapter 4.4. The most relevant influencing factors regarding the actual measurement site, as already described in chapter 1.4, are orographic complexity, terrain roughness and forest cover. Atmospheric stability influences the lidar measurement accuracy as well because it has an impact on the characteristic of the wind flow.

From the measurement device and setup point of view, the considered measurement height and the (usually fixed) half-cone opening angle of the lidar device are of relevance for the lidar measurement accuracy.

Consequently, the following chapter contains results from the parameter study for each of those factors. The results are structured and presented in a way that allows the reader to see the individual contributions of the different parameters on the wind flow as well as on the lidar measurement accuracy.

First, the results from the different flow model runs (i.e., the wind flow field) are described in chapter 5.1. The sub-chapter aims at analyzing the general flow features and their dependence on parameterization. Following the description of the lidar error sources in complex terrain in chapter 3.2, a particular focus is put on the inflow and outflow inclination angles of the wind flow at the lidar measurement points (chapter 5.1.2) and the speed-up effects between these points and the central measurement location above the lidar (chapter 5.1.3).

The results from the flow models are then used as an input for the estimation of the lidar measurement error due to complex terrain in chapter 0, which represents the central part of the results section. Here, results for the total lidar error ε and its parts ε_c and ε_s are presented. The chapter is subdivided into one section per influencing factor. Starting with orographic complexity (chapter 5.2.1), first, the results from the simple potential flow model are presented. Then the influence of different terrain roughness parameterizations is illustrated in chapter 5.2.2 for both the linearized model WEng and the RANS CFD model Meteodyn WT. As forest and atmospheric stability can only be modeled within Meteodyn WT, results for different setups of these parameters are presented in chapters 5.2.3 and 5.2.4.

Wherever possible, the results from the more complex model are compared to those from the potential flow model, which forms a basis or reference for the calculations.

In order to analyze the applicability to the non-dimensional number z/L, calculations for different z, i.e., different measurement heights, are presented in chapter 5.2.5. Finally, the impact of smaller half-cone opening angles in the lidar setup is shown in chapter 5.2.6. for the potential flow model and Meteodyn WT.

5.1 Model results for the wind flow

The following chapter analyses the results from the different flow models that have been used for the parameter study. Starting with the streamlines from the potential flow model and the RANS CFD model Meteodyn WT in chapter 5.1.1, it illustrates the hill flow for different parameterizations. Due to technical reasons, there are no streamlines available from the linearized model. However, the most crucial flow features for the lidar error are the inflow and outflow angles at the lidar measurement points and the speed-up effects in-between. These are analyzed in the subsequent chapters 5.1.2 and 5.1.3 for all three, the potential flow model, the linearized model WEng and Meteodyn WT. Wherever possible, the streamlines, speed-up effects and flow angles from the WEng and Meteodyn WT are compared to those from the potential flow model. By this approach, it is possible to isolate the effects of roughness and vegetation (forest) from the orographically induced flow field. The results will later be used to explain and analyze the impacts of the different influencing factors on the lidar error in complex terrain in chapter 0.

5.1.1 Streamlines

To illustrate the flow that was modeled with the potential flow model, four different results are shown in Figure 5.1. These results represent the column with constant L of 250 m in Table 3, each with a different H/L ratio. The corresponding hill heights are 25, 50, 75 and 100 m. The four shown streamlines originate at 50, 100, 150 and 200 m above ground in the freestream at the upwind side of the hills. In order to relate the flow field to the dimensions of the lidar measurement geometry, two laser beams of a lidar placed on top of the hill are shown as well. A half-cone opening angle of 30 ° is used and the two measurement points mark a measurement height of 150 m above the lidar. For this measurement height, the ratio z/L is 0.6 for these four hill geometries. With reference to Figure 5.25, this is approximately the z/L ratio for which maximum lidar errors are found, which is described in the subsequent chapter 5.2.1. Note that due to the different scaling of the x- and the y-axis the opening angle appears distorted.

First, it can be noted that the flow fields resulting from the potential flow model are symmetric. This is because the flow is assumed entirely frictionless. For the z/L ratio of 0.6, the lidar measurement points are well within the area of curved flow above the hilltop. With a distance of 86.6 m from the centerline, the measurement points are at about $0.69L$ apart from each other.

With increasing hill height H and constant hill half-width L, the flow curvature is significantly increasing as well. While the streamlines appear to be only slightly curved in Figure 5.1 a), the curvature becomes more and more severe for hills b), c) and d).

Additionally, the measurement points are leaving the 150 m streamline and moving toward the 200 m streamline with increasing hill height. This emphasizes the increasing speed-up effect for the larger hills.

In addition to the four already described hill geometries, two extreme cases have been chosen in Figure 5.2 and Figure 5.3. Figure 5.2 shows a small hill in comparison to the lidar measurement geometry ($H = 15\,m, L = 50\,m$). In this case, the measurement points are located above the flanks of the hill. Also, it can be seen that the effects of the hill and the modeled flow are significant for the lower heights but rapidly decrease with increasing height above the ground. For the measurement height of 150 m, the

flow curvature has almost decreased to zero. On the other side of the hill geometry range, the case shown in Figure 5.3 can be found ($H = 225\,m$, $L = 750\,m$). Here the measurement geometry is small when compared to the size of the hill. The measurement points are located close to the hilltop. Flow effects at the flanks of the hill have no direct impact at these points. Within the proximity of the lidar, the flow can be assumed to be following the hill curvature. Moreover, due to the vast extent of the hill, the curvature is relatively small around the hilltop. The two latter examples have been chosen in order to illustrate the importance of the dimension of the hill in relation to the distance and height of the measurement points above the lidar.

a)

b)

c)

d)

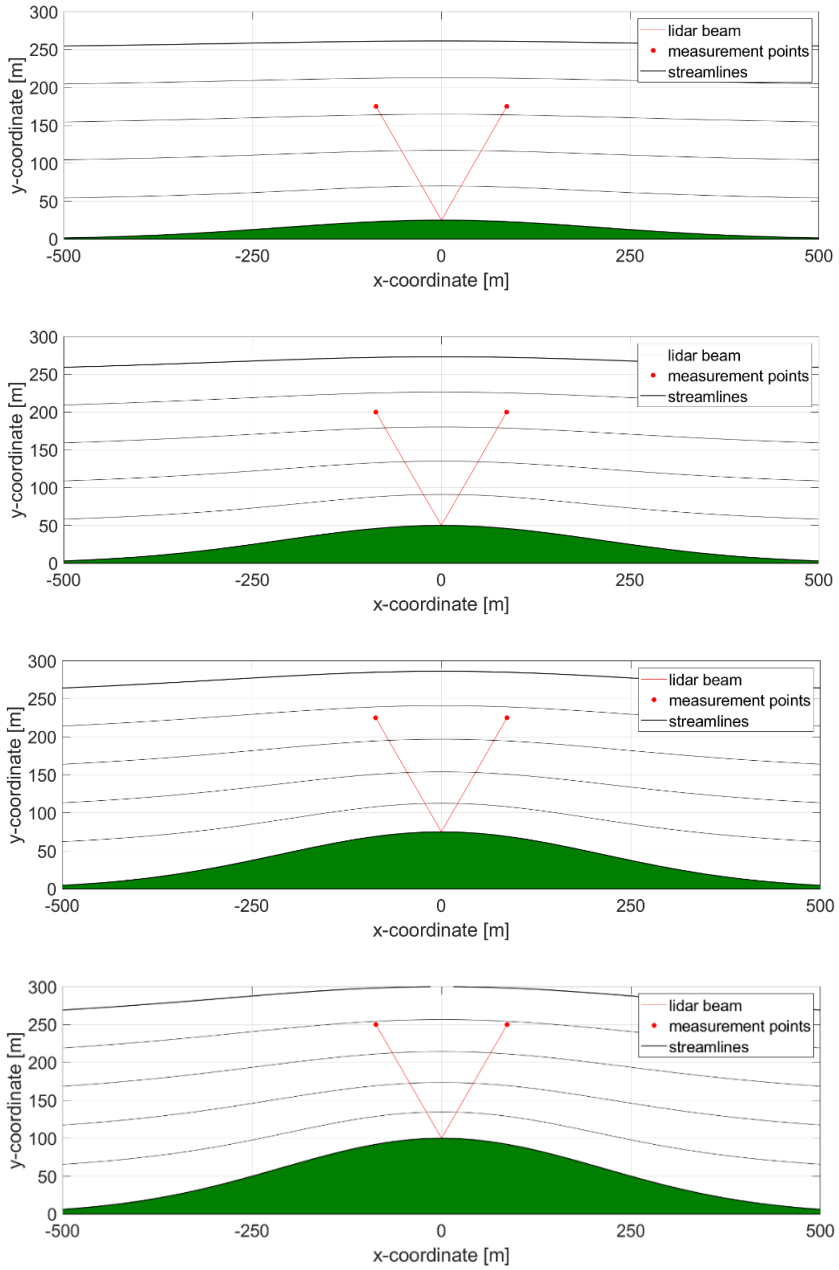

Figure 5.1: Results from the potential flow model for $\boldsymbol{L = 250\,m}$ and the four different $\boldsymbol{H/L}$ ratios with $\boldsymbol{H = 25, 50, 75\ and\ 100\,m}$ from a) to d). The lidar position is marked at the top of the hills and the beams are tilted by a half-cone opening angle $\boldsymbol{\varphi = 30°}$. The measurement points are located at $\boldsymbol{z = 150\,m}$ above the lidar. The points, therefore, are equal to a $\boldsymbol{z/L}$ ratio of 0.6.

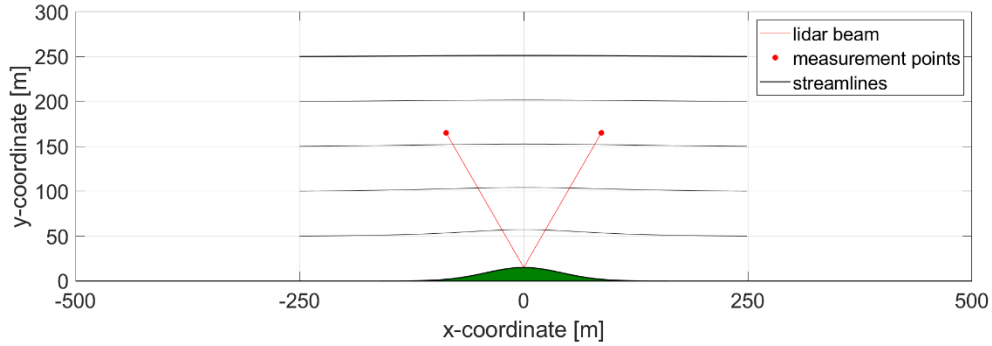

Figure 5.2: Results from the potential flow model for $\boldsymbol{L = 50\ m}$ and an $\boldsymbol{H/L}$ ratio of 0.3. The lidar position is marked at the top of the hills and the beams are tilted by a half-cone opening angle $\boldsymbol{\varphi = 30°}$. The measurement points are located at $\boldsymbol{z = 150\ m}$ above the lidar. The points, therefore, are equal to a $\boldsymbol{z/L}$ ratio of 3.

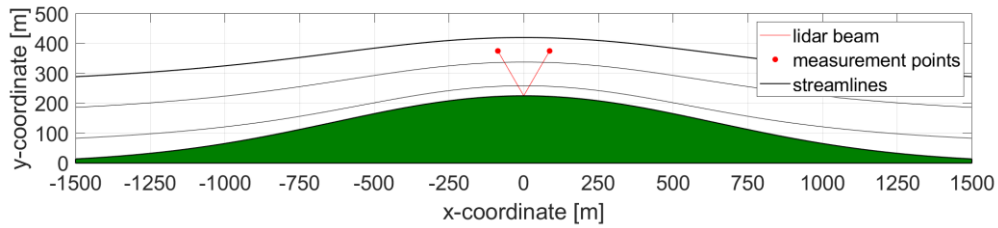

Figure 5.3: Results from the potential flow model for $\boldsymbol{L = 750\ m}$ and an $\boldsymbol{H/L}$ ratio of 0.3. The lidar position is marked at the top of the hills and the beams are tilted by a half-cone opening angle $\boldsymbol{\varphi = 30°}$. The measurement points are located at $\boldsymbol{z = 150\ m}$ above the lidar. The points, therefore, are equal to a $\boldsymbol{z/L}$ ratio of 0.2.

For Meteodyn WT, the streamlines are illustrated for different roughness lengths z_0 of 0.005, 0.1 and 0.5 m for the four different H/L ratios (Figure 5.4 to Figure 5.7). The streamlines in these four figures are shown in the same axis scaling, to emphasize the influence of the H/L ratio on the flow curvature and the symmetry of the model results.

For H/L ratios of 0.1 and 0.2, there is only a small difference between the three roughness parameterizations. Additionally, the results are comparable to those from the potential flow model. Especially for the minimal H/L of 0.1, the results from Meteodyn WT are almost symmetric. When the H/L ratio is increased to 0.3 and 0.4, the differences between the potential flow solution and Meteodyn WT are increasing. First, it can be noted that the results are no longer symmetric, but the flow curvature is different for the upwind and downwind part of the streamlines. Additionally, the influence of terrain roughness becomes significant. Particularly in the downwind section of the flow, streamlines for increased roughness lengths deviate from those for the lowest roughness. While for a z_0 of 0.005 m, the results for the highest H/L ratio are still very close to the potential flow solution, the streamlines for increased roughness lengths are lifted upwards, which leads to an overall reduced flow curvature.

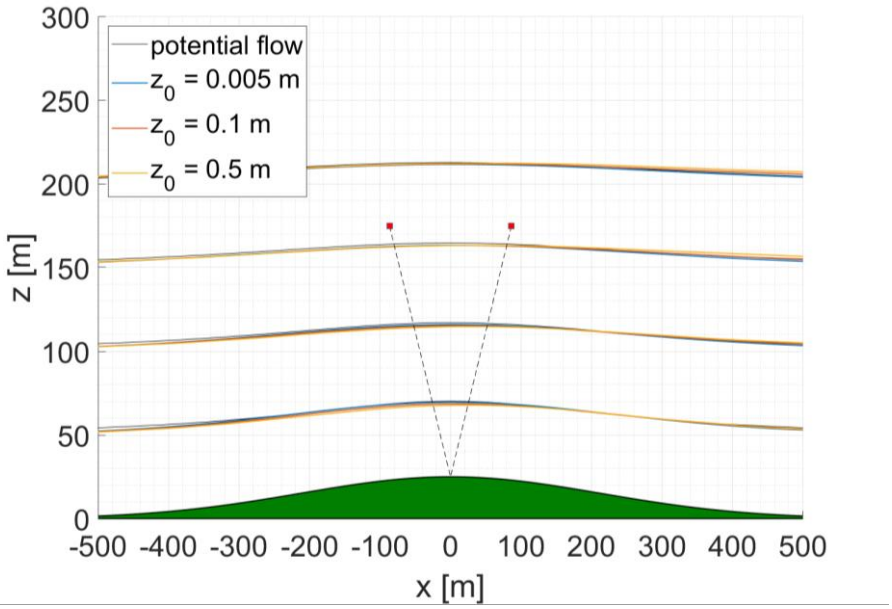

Figure 5.4: Streamlines in dependence of roughness length $\boldsymbol{z_0}$ ($\boldsymbol{H/L}$ ratio 0.1). Streamlines from Meteodyn WT (colored) and from the potential flow model (black) are starting at z of 50, 100, 150 and 200 m in front of the hill. Lidar measurement points at 150 m measurement height with a $\boldsymbol{\varphi}$ of 30 ° are marked in red.

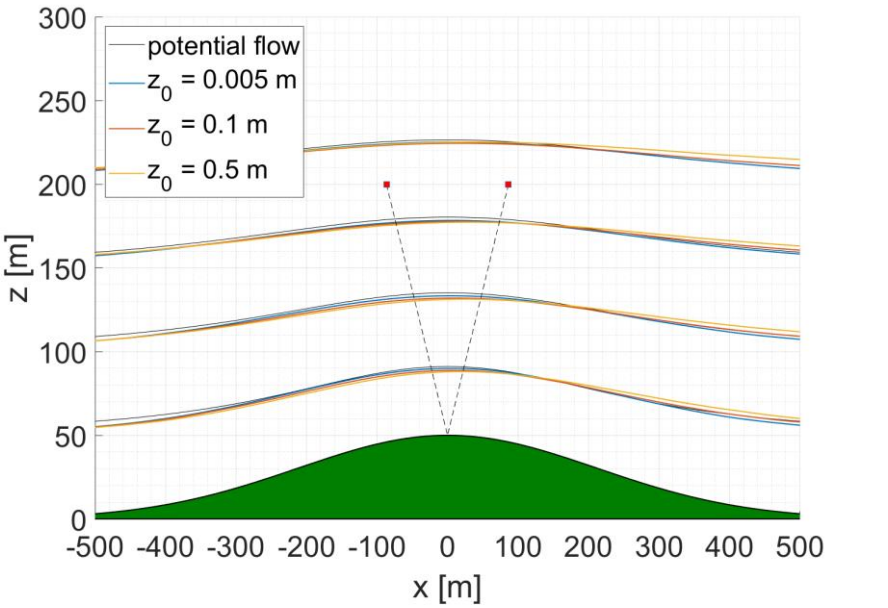

Figure 5.5: Streamlines in dependence of roughness length $\boldsymbol{z_0}$ ($\boldsymbol{H/L}$ ratio 0.2). Streamlines from Meteodyn WT (colored) and from the potential flow model (black) are starting at z of 50, 100, 150 and 200 m in front of the hill. Lidar measurement points at 150 m measurement height with a $\boldsymbol{\varphi}$ of 30 ° are marked in red.

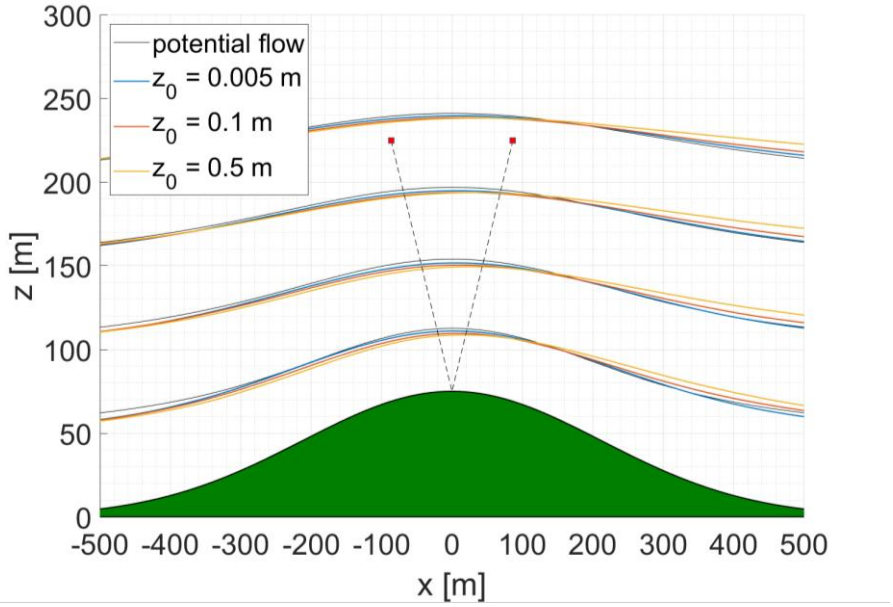

Figure 5.6: Streamlines in dependence of roughness length $\boldsymbol{z_0}$ ($\boldsymbol{H/L}$ ratio 0.3). Streamlines from Meteodyn WT (colored) and from the potential flow model (black) are starting at z of 50, 100, 150 and 200 m in front of the hill. Lidar measurement points at 150 m measurement height with a $\boldsymbol{\varphi}$ of 30 ° are marked in red.

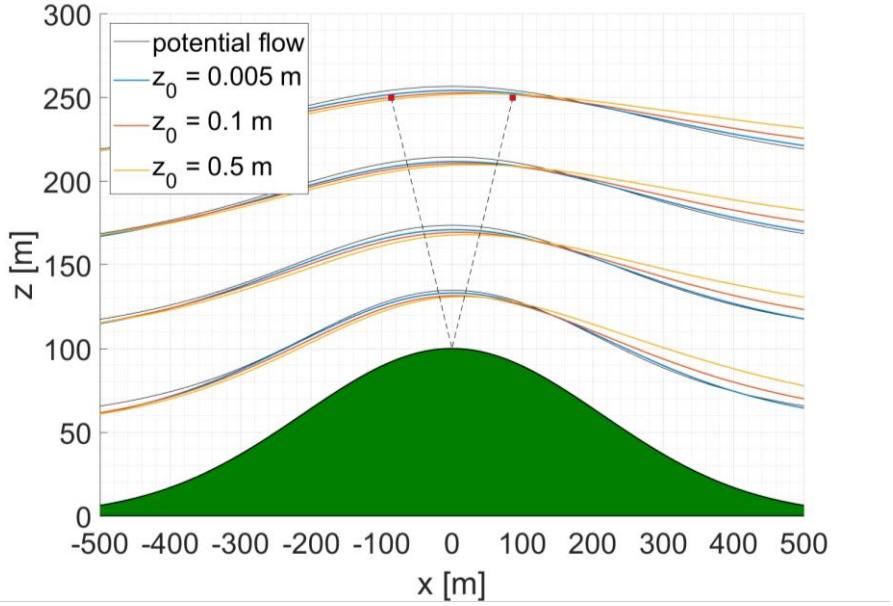

Figure 5.7: Streamlines in dependence of roughness length $\boldsymbol{z_0}$ ($\boldsymbol{H/L}$ ratio 0.4). Streamlines from Meteodyn WT (colored) and from the potential flow model (black) are starting at z of 50, 100, 150 and 200 m in front of the hill. Lidar measurement points at 150 m measurement height with a $\boldsymbol{\varphi}$ of 30 ° are marked in red

Adding forest to the terrain has a significant influence on the flow field, which is exemplarily illustrated in Figure 5.8 and Figure 5.9 for H/L ratios of 0.2 and 0.3. The results shown in these two figures are based on medium forest density and each cover tree heights of 10, 20 and 30 m, which might all be found at a forested site in reality. Although the effect of small trees with 10 m height is comparable to results with a large roughness length of 0.5 m, the lift-up of the downwind streamlines is more significant. Increasing the tree heights results in even more detached streamlines from the actual terrain shape. Additionally, depending on tree height, the turning point of the streamlines is moving from the center above hilltop to the right-hand side of the plot, i.e., into the downwind region. In the case of trees with heights of 20 and 30 m and an H/L ratio of 0.3, this leads to the effect that the flow inclination is positive in the area of the lidar measurement points. This is contrary to the cases without forest, where the lidar measurement points are seeing positive inflow angles and negative outflow angles.

As an example for the influence of forest density on the flow field in Meteodyn WT, results for a tree height of 30 m and an H/L ratio of 0.3 are shown in Figure 5.10 for the three different density parameterizations "low," "medium" and "high," which all correspond to different C_d values in the forest model (compare chapter 4.5.2).

It can be seen that the influence of the forest model with this tree height, even with low forest density, is severe when compared to the potential flow model results. The streamlines are lifted upwards in the downwind section and the turning point is slightly shifted to the right as well. The effects of forest modeling become very strong for medium and high forest densities. However, the results for both are very similar. The shape of the streamlines is significantly changed and the turning point is shifted to about 150 to 200 m behind the hilltop. The downwind streamlines are strongly detached from the hill shape. These two effects have a strong influence on flow curvature in the area of the lidar measurement points.

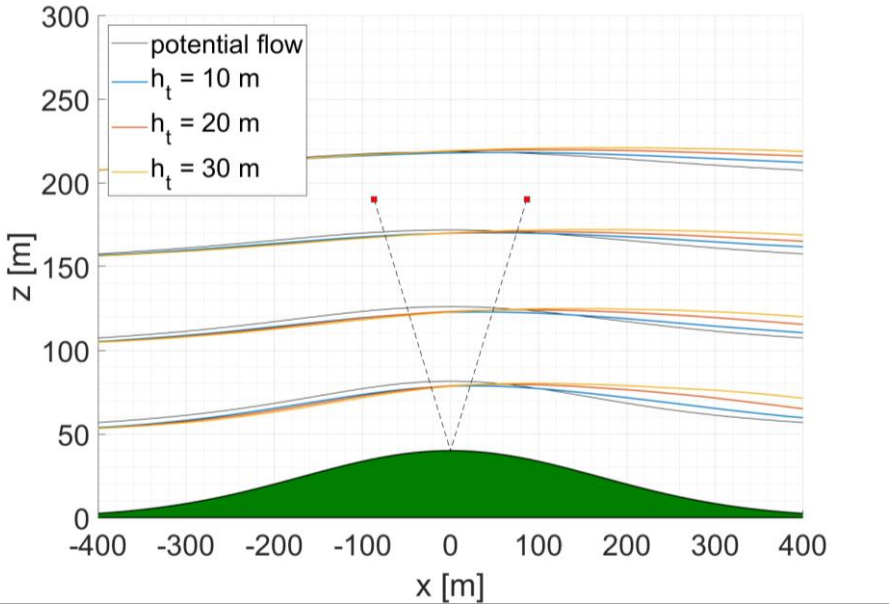

Figure 5.8: Streamlines in dependence of tree height h_t (H/L ratio 0.2). Streamlines from Meteodyn WT (colored) and from the potential flow model (black) are starting at z of 50, 100, 150 and 200 m in front of the hill. Lidar measurement points at 150 m measurement height with a φ of 30 ° are marked in red.

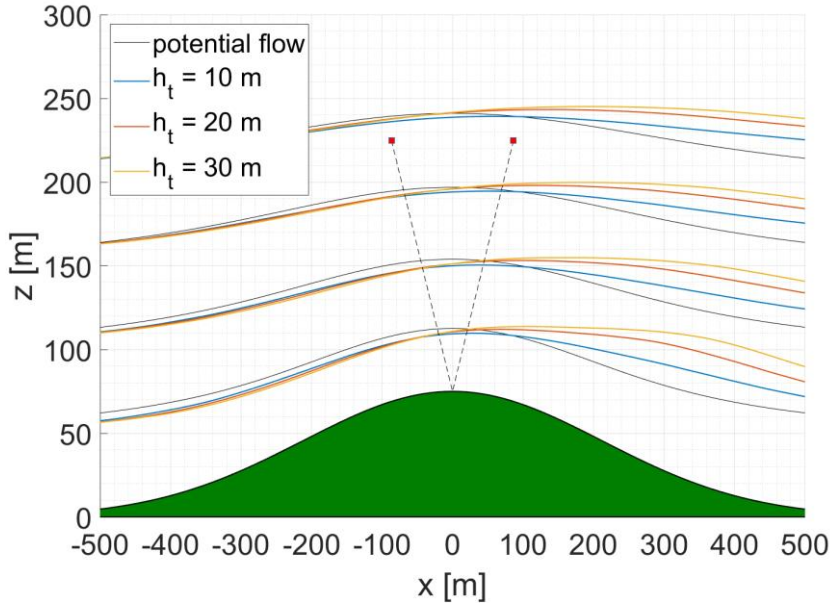

Figure 5.9: Streamlines in dependence of tree height $\boldsymbol{h_t}$ ($\boldsymbol{H/L}$ ratio 0.3). Streamlines from Meteodyn WT (colored) and from the potential flow model (black) are starting at z of 50, 100, 150 and 200 m in front of the hill. Lidar measurement points at 150 m measurement height with a $\boldsymbol{\varphi}$ of 30 ° are marked in red.

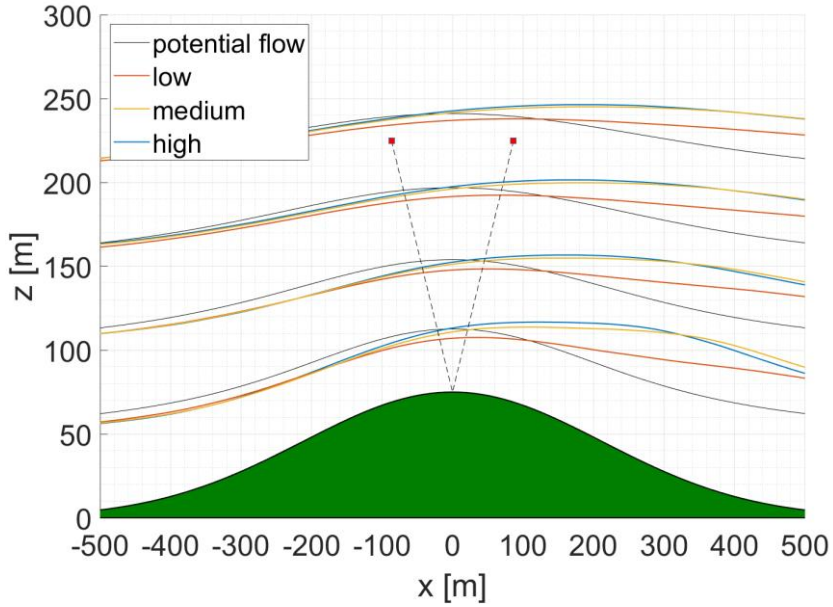

Figure 5.10: Streamlines in dependence of forest density ($\boldsymbol{H/L}$ ratio 0.3). Streamlines from Meteodyn WT (colored) and from the potential flow model (black) are starting at z of 50, 100, 150 and 200 m in front of the hill. Lidar measurement points at 150 m measurement height with a $\boldsymbol{\varphi}$ of 30 ° are marked in red.

Meteodyn WT can model different atmospheric stability classes. There are ten classes available. The two lowest classes 0 and 1 refer to unstable cases, class 2 to neutral cases and classes 3 to 9 to stable up to strongly stable cases (see chapter 4.3.3). The results presented in the following figures show the influence of "moderate" atmospheric stability classes (1 and 6 compared to 2) and "extreme" classes (0 and 9 compared to 2). Following an analysis by Pauscher et al. (2018) about the occurrence of different stability classes at "Rödeser Berg" (see evaluation in chapter 6), the full range of these stability classes can be observed.

For both, the moderate and the extreme classes, results are shown for a H/L ratio of 0.3 for the low roughness case with a z_0 of 0.005 m, the high roughness case with a roughness length of 0.5 m and a case of medium dense forest with a tree height of 20 m.

Starting with Figure 5.11, it can be seen that the influence of atmospheric stability classes 1 and 6 is minimal for the low roughness case. When looking at the high roughness case (Figure 5.12) and the forested case (Figure 5.13), a strong influence of atmospheric stability on the shape of the streamline is observed. The effects are most substantial for stable cases and low heights at the downwind side of the hill. Here, the streamlines are lifted even more upwards than in the neutral case and the flow needs a longer distance to recover from the influence due to the hill. For the unstable case, the influence on the streamlines is significantly smaller than in the stable case. However, for a high roughness and the forested case, the impact is still noticeable in the shape of the streamlines. While for the high roughness case, the streamlines are slightly lifted upwards compared to the neutral case, this behavior is reversed for the forested case. Here the streamlines for unstable conditions are below the neutral case streamlines in the downwind section. However, this is only the case for distances beyond 250 to 300 m behind the hill.

Results for the extreme stability classes "very unstable" and "strongly stable" are shown in Figure 5.14, Figure 5.15 and Figure 5.16 for the same hill geometries and parameterizations. Again, the influence in the low roughness case is minimal. However, for strongly stable atmospheric stability conditions, a change in the shape of the streamlines can be noticed. In the proximity of the hilltop, the streamlines are slightly shifted downwards in this case.

For the high roughness and the forested case, the effects of extreme stability conditions are severe. This is particularly true for strongly stable cases, where the downwind streamlines are lifted upwards in the lee of the hill and no turning point or recovery can be seen up to 500 m distance behind the hilltop. This strong influence on the hill overflow changes the shape of the streamlines in this case already in the upwind section of the hill and will, therefore, also clearly affect inflow and outflow angles at the lidar measurement points.

The results for very unstable atmospheric conditions are very similar to those with neutral conditions in case of both low and high roughness. A small difference can be noted in the upwind section of the flow for the high roughness case. For the forested case, the streamline in very unstable conditions are influenced and different from those for neutral conditions. Here, unstable conditions seem to have a contrary effect on the downwind side than strongly stable conditions. Streamlines are shifted downwards and are below those for neutral conditions at all shown heights. Resulting from that, flow curvature in the proximity of the lidar measurement points is increased.

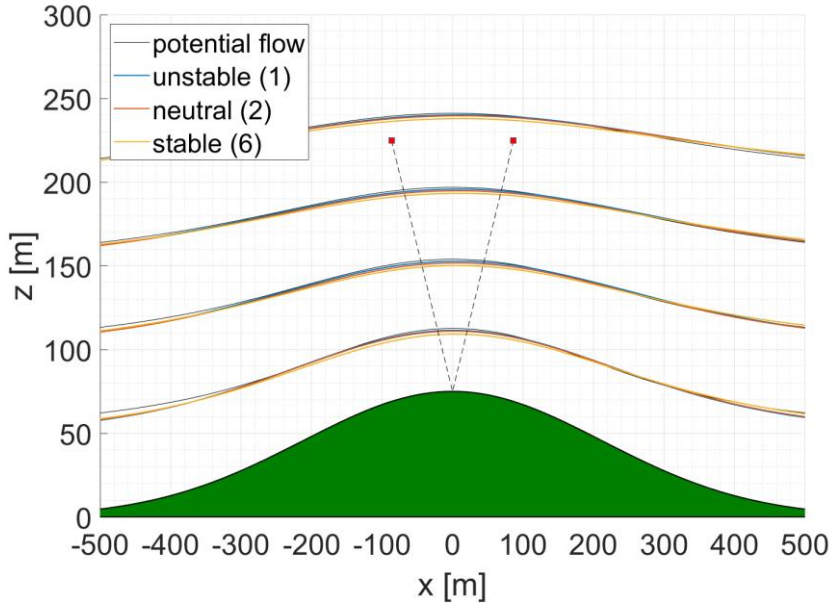

Figure 5.11: Streamlines in dependence of atmospheric stability ($\boldsymbol{H/L}$ ratio 0.3, $\boldsymbol{z_0}$ of 0.005 m). Streamlines from Meteodyn WT (colored) and from the potential flow model (black) are starting at z of 50, 100, 150 and 200 m in front of the hill. Lidar measurement points at 150 m measurement height with a $\boldsymbol{\varphi}$ of 30 ° are marked in red.

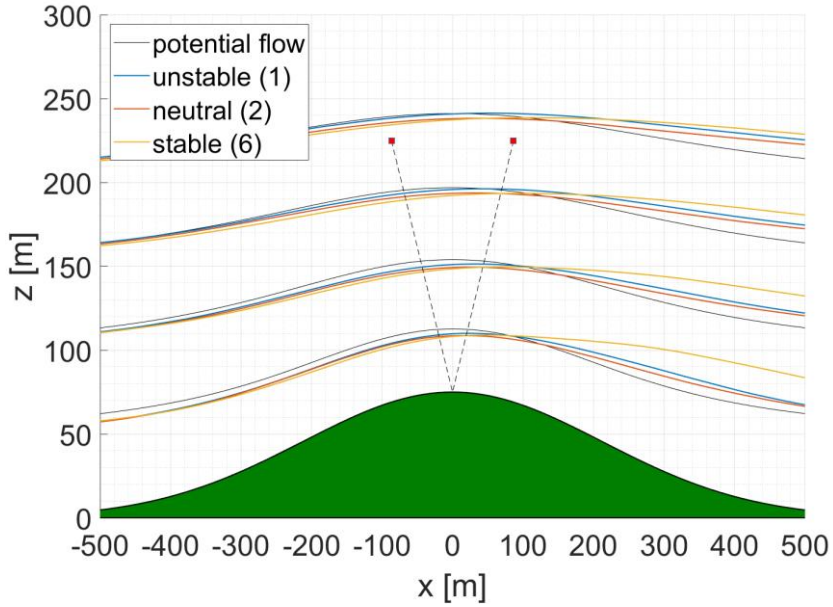

Figure 5.12: Streamlines in dependence of atmospheric stability ($\boldsymbol{H/L}$ ratio 0.3, $\boldsymbol{z_0}$ of 0.5 m). Streamlines from Meteodyn WT (colored) and from the potential flow model (black) are starting at z of 50, 100, 150 and 200 m in front of the hill. Lidar measurement points at 150 m measurement height with a $\boldsymbol{\varphi}$ of 30 ° are marked in red.

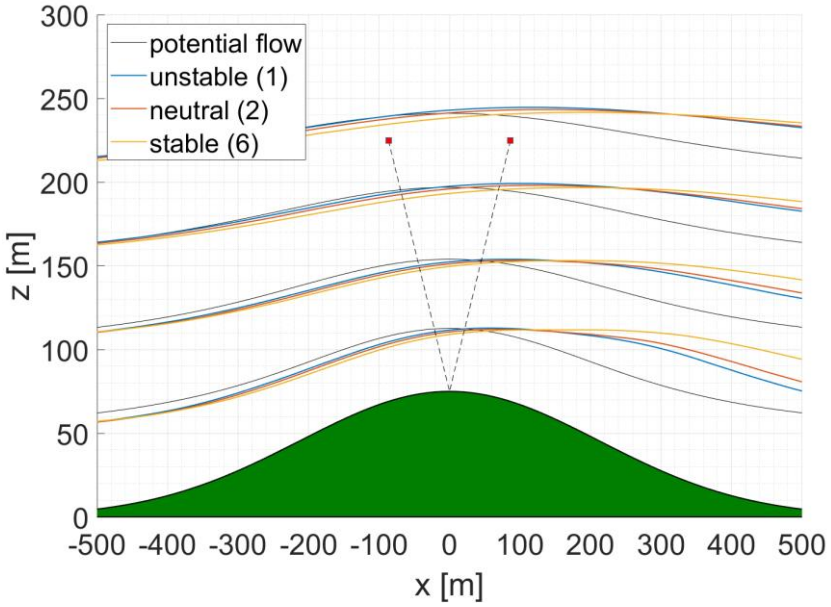

Figure 5.13: Streamlines in dependence of atmospheric stability ($\boldsymbol{H/L}$ ratio 0.3, $\boldsymbol{h_t}$ of 20 m, medium forest density). Streamlines from Meteodyn WT (colored) and from the potential flow model (black) are starting at z of 50, 100, 150 and 200 m in front of the hill. Lidar measurement points at 150 m measurement height with a $\boldsymbol{\varphi}$ of 30 ° are marked in red.

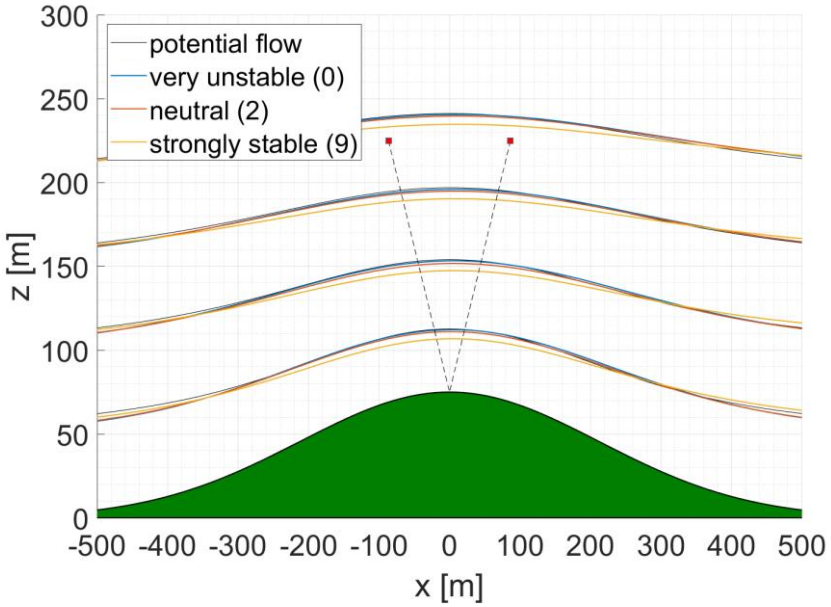

Figure 5.14: Streamlines in dependence of atmospheric stability ($\boldsymbol{H/L}$ ratio 0.3, $\boldsymbol{z_0}$ of 0.005 m). Streamlines from Meteodyn WT (colored) and from the potential flow model (black) are starting at z of 50, 100, 150 and 200 m in front of the hill. Lidar measurement points at 150 m measurement height with a $\boldsymbol{\varphi}$ of 30 ° are marked in red.

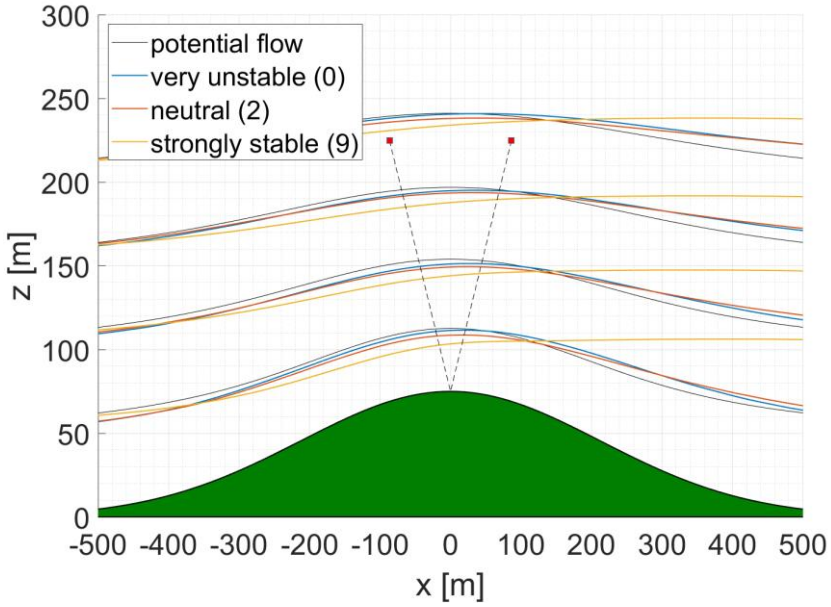

Figure 5.15: Streamlines in dependence of atmospheric stability (***H/L*** ratio 0.3, z_0 of 0.5 m). Streamlines from Meteodyn WT (colored) and from the potential flow model (black) are starting at z of 50, 100, 150 and 200 m in front of the hill. Lidar measurement points at 150 m measurement height with a φ of 30 ° are marked in red.

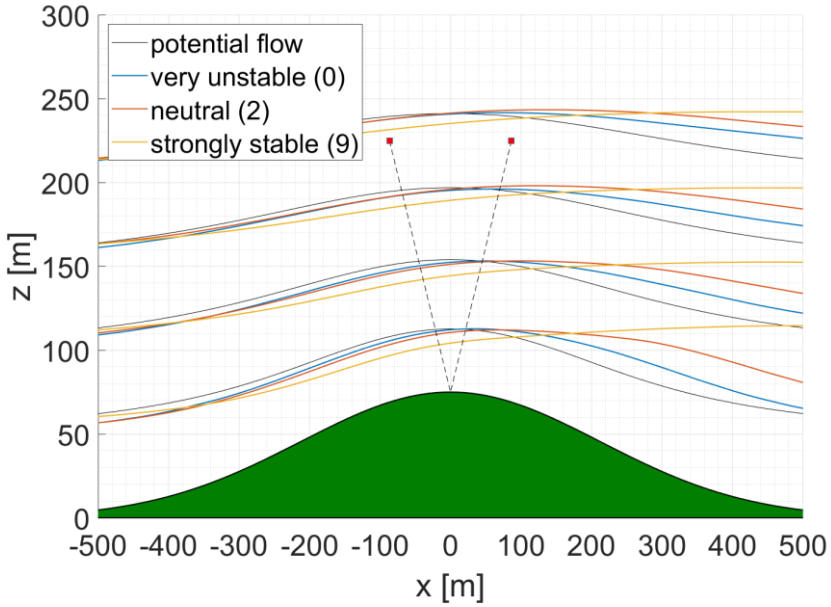

Figure 5.16: Streamlines in dependence of atmospheric stability (***H/L*** ratio 0.3, h_t of 20 m, medium forest density). Streamlines from Meteodyn WT (colored) and from the potential flow model (black) are starting at z of 50, 100, 150 and 200 m in front of the hill. Lidar measurement points at 150 m measurement height with a φ of 30 ° are marked in red.

5.1.2 Inflow and outflow angles

The lidar error part ε_c describes the lidar error in complex terrain due to flow curvature. Following its definition in chapter 3.2, it is only dependent on the inflow angle α and the outflow angle β. To understand the results from the different models and different parametrizations used and link them to the estimated lidar error ε_c, the flow inclination angles are illustrated in the following chapter.

The results are presented for different H/L ratios and different z/L ratios on the y-axis of the figures. This presentation is analogous to the later presentation of the lidar errors in chapter 0. It will, therefore, help the reader to understand the impact of the parameterizations on the different flow features. In any case, the results are compared to those from the potential flow model. As these are symmetric, the magnitude of the outflow angle equals the inflow angle.

From the results from WEng in Figure 5.17, it is obvious that also the results from the linearized model are symmetric. The results for the inflow and outflow angles are first shown for the four different H/L ratios for a low roughness length z_0 of 0.005 m (Figure 5.17, left). Inflow and outflow angles for the lowest H/L ratio of 0.1 are very similar to those from the potential flow model for z/L up to 1.0, but only slightly higher in magnitude. For z/L 1.5, the angles are close to zero, which is not the case for the reference model.

For larger H/L ratios, the difference to the potential flow model is increasing. In particular, for z/L between 0.2 and 1.0, α and β a significantly larger than in the potential flow model. For the larger z/L ratios, the WEng results are converging towards the potential flow solution. However, the maximum angles of about 5° for an H/L of 0.3 and 6° for an H/L of 0.4 is twice as high as in the potential flow model, although the general shape of the curves is comparable.

The results for different roughness lengths z_0 of 0.005, 0.1 and 0.5 m for WEng are exemplarily shown for a H/L ratio of 0.3 in Figure 5.17 (right). For z/L ratios up to 1.5, there is a clear tendency of reduced inflow and outflow angles for increasing roughness lengths. This effect is largest at a z/L of 1.5. At the maximum point, the difference between the lowest and highest roughness length is about 0.8°. For a z/L ratio of 0.2 there is no significant difference. It is interesting to note that for high z/L ratios of 1.5 and 3.0 and the medium and high roughness lengths, negative inflow and positive outflow angles can be observed in this model, which is marked by the crossing points of the full and the dashed line in these cases.

The large inflow and outflow angles for large H/L ratios can be explained by the fundamental assumption of attached flow in the linearized model (Bowen and Mortensen 1996). As no flow separation is modeled in WEng, especially the results in the lee of the hill show unrealistically high flow inclinations. Because the model is symmetric, the same results are found at the luv side of the hill.

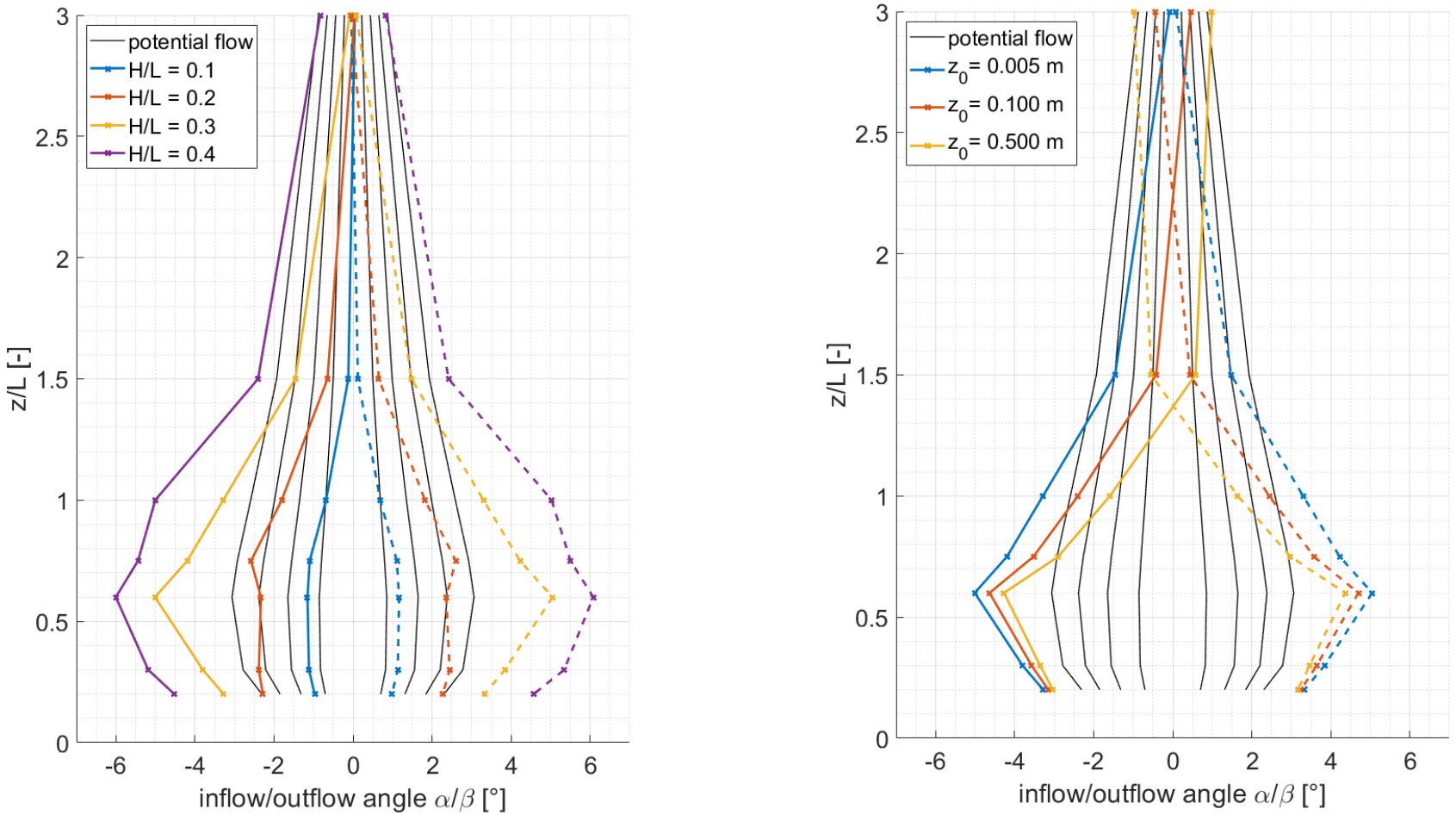

Figure 5.17: Inflow angle $\boldsymbol{\alpha}$ (dashed) and outflow angle $\boldsymbol{\beta}$ (solid) in dependence of $\boldsymbol{H/L}$ ratio (left) and roughness length $\boldsymbol{z_0}$ (right)**.** Results from WEng (colored) and from the potential flow model (black) at 150 m measurement height and for a $\boldsymbol{\varphi}$ of 30°. For the left plot, the roughness length $\boldsymbol{z_0}$ is 0.005 m.

The inflow and outflow angles based on Meteodyn WT for the low roughness cases are shown in Figure 5.18 (left). It can be seen that the inflow angles highly agree with the potential solution, in particular for H/L ratios of 0.1 and 0.2. For H/L ratios of 0.3 and 0.4, the inflow angles are slightly smaller for z/L between 0.6 and 1.5. For the lowest z/L of 0.2 and 0.3 and this highest value of 3.0, the results are very similar to those from the potential flow solution. In contrast to that, the outflow angles are smaller than in the reference for most cases. The difference to the potential flow solution increases for increasing H/L ratios and is largest for the maximum angles around z/L ratios of 0.6.

The comparison of inflow and outflow angles from Meteodyn WT for different roughness length is exemplarily shown for a H/L ratio of 0.3 in Figure 5.18 (right). Again, it can be noted that the inflow angles are very similar for all three roughness lengths. However, the influence of z_0 on the outflow angles is significant. At z/L ratios of 0.6, the influence is most significant and outflow angles change from about 2° for the low roughness case to about 1° for the highest roughness. The asymmetry of the RANS CFD model increases with increasing roughness length.

As already seen in the above-given streamline plots in chapter 5.1.1, the introduction of the forest has a significant impact on the flow features. This is also strongly reflected in the inflow and outflow angles, which are shown for the H/L ratios 0.3 for three different tree heights in Figure 5.19 (left). Because the turning point of the streamlines is shifted to the right (compare, e.g., Figure 5.9), the outflow angles for the forested case are significantly decreased. For the maximum tree height of 30 m in case of an H/L ratio of 0.2 the outflow angles are even positive for most z/L ratios (see Figure 10.1 in Appendix 10.3). For an H/L ratio of 0.3 this can be observed for almost all z/L ratios for tree heights of 20 m and 30 m.

Looking at the inflow angles for the forested cases, a significant increase can be seen for z/L ratios between 0.2 and 1.0 for both shown H/L ratios. For z/L ratios of 1.5 and 3.0, there is no influence of tree height on the inflow angles.

Maximum inflow and outflow angles can be seen at z/L ratios of 0.3, which is different from the position of the maximum values in cases without forest, where the maximum was found at z/L ratios of 0.6.

The influence of forest density is shown for the H/L ratio of 0.3 and a tree height of 30 m in Figure 5.19 (right). While there is no significant difference between medium and high forest densities, the inflow and outflow angles for a low forest density are different. The inflow angles, in this case, are generally smaller and the outflow angles do only cross the zero line for z/L ratios of 0.2 and 0.3.

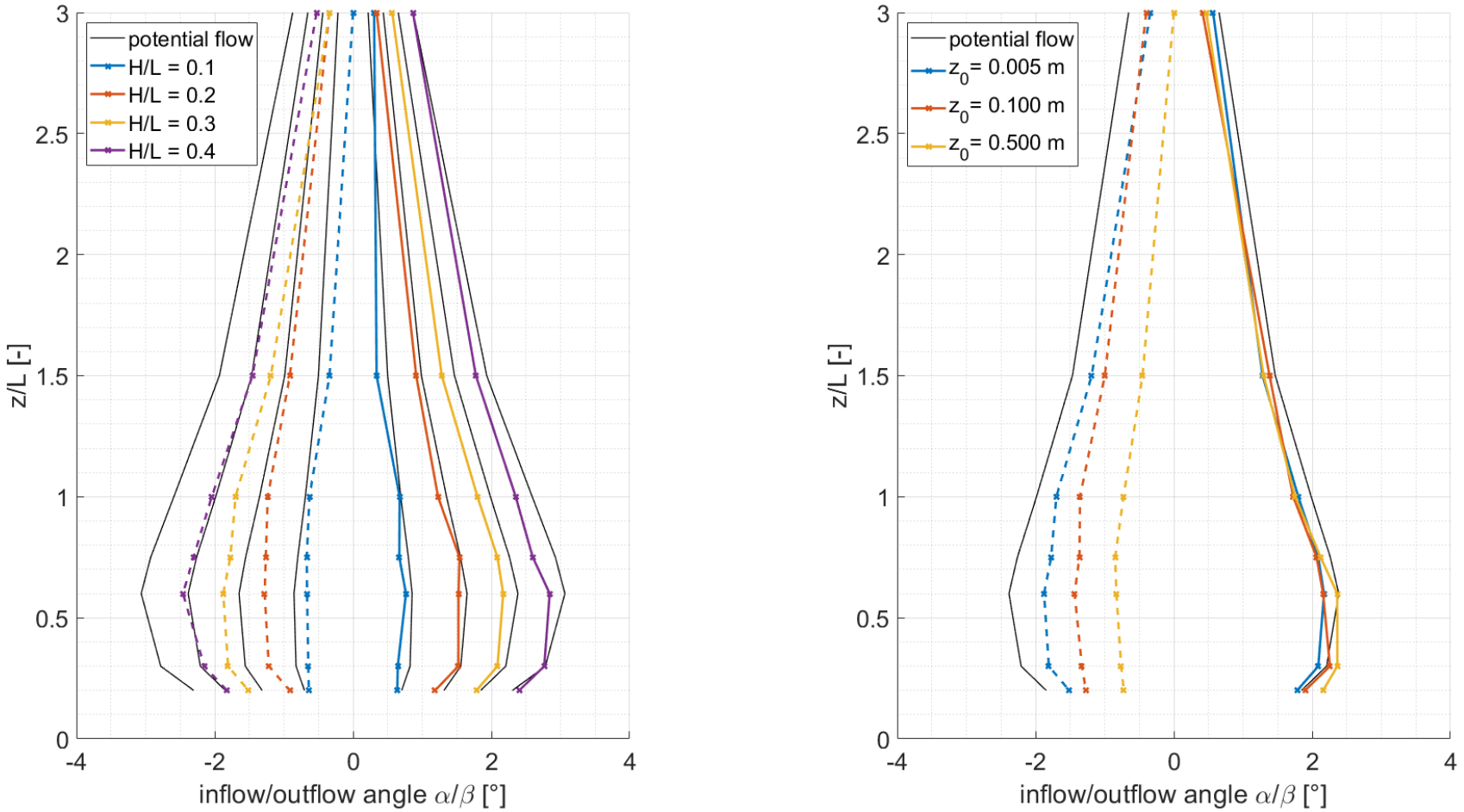

Figure 5.18: Inflow angle $\boldsymbol{\alpha}$ (dashed) and outflow angle $\boldsymbol{\beta}$ (solid) in dependence of $\boldsymbol{H/L}$ ratio (left) and roughness length $\boldsymbol{z_0}$ (right)**.** Results from Meteodyn WT (colored) and from the potential flow model (black) at 150 m measurement height and for a $\boldsymbol{\varphi}$ of 30°. For the left plot, the roughness length $\boldsymbol{z_0}$ is 0.005 m.

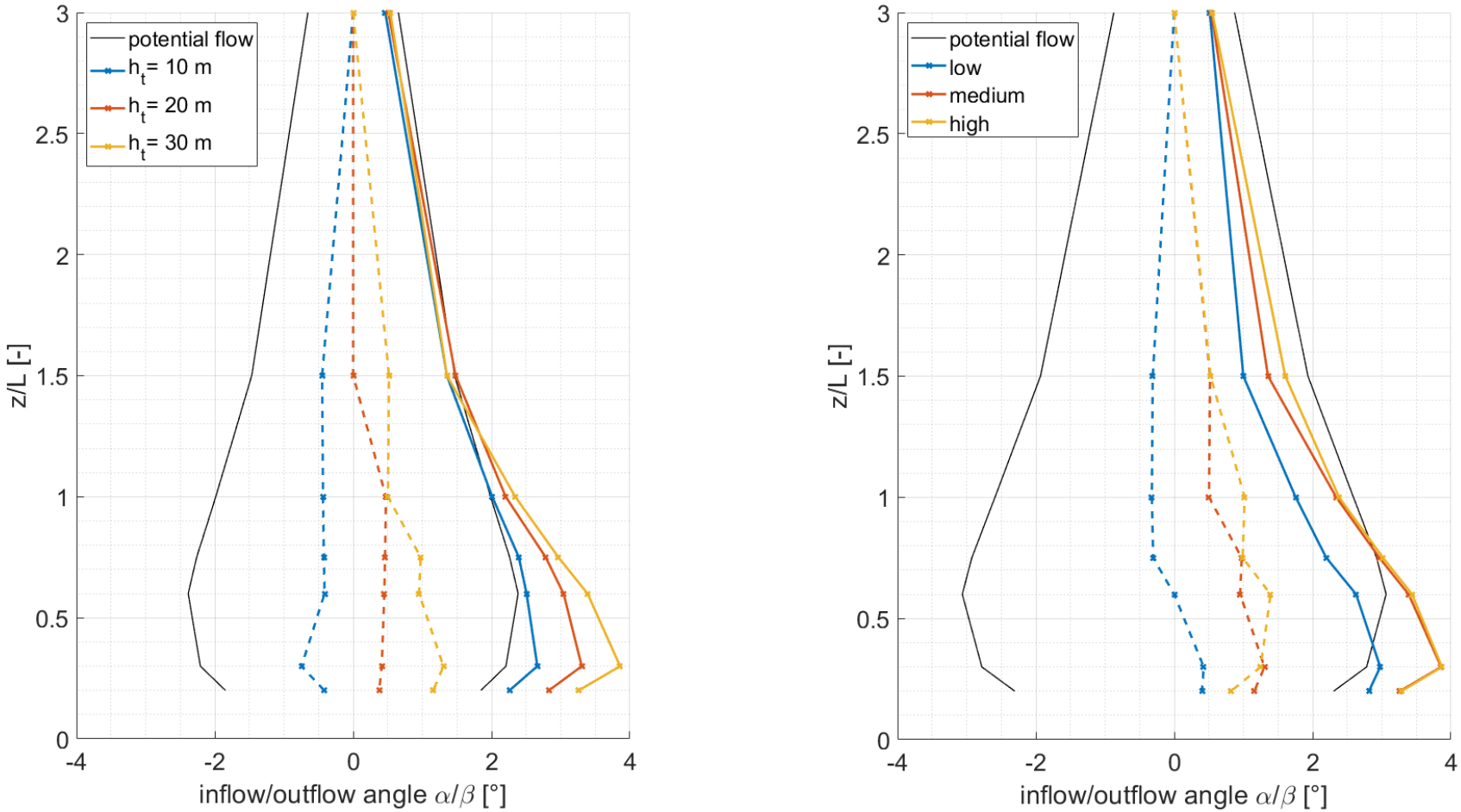

Figure 5.19: Inflow angle $\boldsymbol{\alpha}$ (dashed) and outflow angle $\boldsymbol{\beta}$ (solid) in dependence of tree height $\boldsymbol{h_t}$ (left) and forest densities (right)**.** Results from Meteodyn WT (colored) and from the potential flow model (black) at 150 m measurement height and for a $\boldsymbol{\varphi}$ of 30° for an $\boldsymbol{H/L}$ ratio of 0.3. For the left plot, the forest density is medium. For the right plot, the tree height $\boldsymbol{h_t}$ is 20 m.

Figure 5.20 shows the flow inclination results for four different atmospheric stability classes (very unstable, neutral, stable, strongly stable) for a H/L ratio of 0.3 and cases with medium dense forest and a forest height of 30 m. Figure 10.2 and Figure 10.3 for the low and high roughness cases can be found in Appendix 10.3.

For the low roughness cases, the influence of atmospheric stability on the inflow and outflow angles is relatively small for most z/L ratios. However, a general tendency for decreasing angles from unstable over neutral to stable cases can be observed for all z/L ratios.

In the case of high roughness and forested cases, the influence of atmospheric stability is more complex. For a roughness length z_0 of 0.5 m and z/L ratios of 1.5 and 3.0, the tendency of decreasing flow angles with increasing stability can also be seen. In these cases, the influence is also relatively small when compared to the smaller z/L ratios.

For strongly stable cases, the inflow angles are significantly increased for z/L ratios of 0.2 and 0.3, which is in contrast to the overall trend of decreasing flow angles for stable cases. For stable and strongly stable cases, different behavior of the outflow angles can also be observed for z/L ratios below 1.5. For stable cases, the outflow angles are around 0°, while they are about -2° for neutral cases. For unstable cases, the outflow angles increase from 0° for a z/L of 1.5 to about 2° for the smallest z/L ratio.

Regarding the unstable cases, the results for z/L ratios of 0.2 and 0.3 also show different behavior than for the other z/L ratios. While for larger z/L ratios the unstable cases or very close to the neutral cases, for the lowest two ratios, positive outflow angles can be observed.

The inflow angles for the forested cases are comparable to those from the high roughness cases. While there is a small tendency of decreasing angles when coming from unstable to stable cases, there is a significantly different behavior for the strongly stable cases at low z/L ratios. The outflow angles, on the other hand, show different results for the forested cases. The atmospheric stability has a significant impact on outflow angles for z/L ratios from 0.2 to 1.0. For these cases, neutral, stable and strongly stable cases show positive outflow angles. Most considerable positive outflow angles can be observed for the strongly stable cases. For very unstable cases, the outflow angles remain negative for z/L ratios of 0.2 to 1.0 and are around 0° for the two largest z/L ratios.

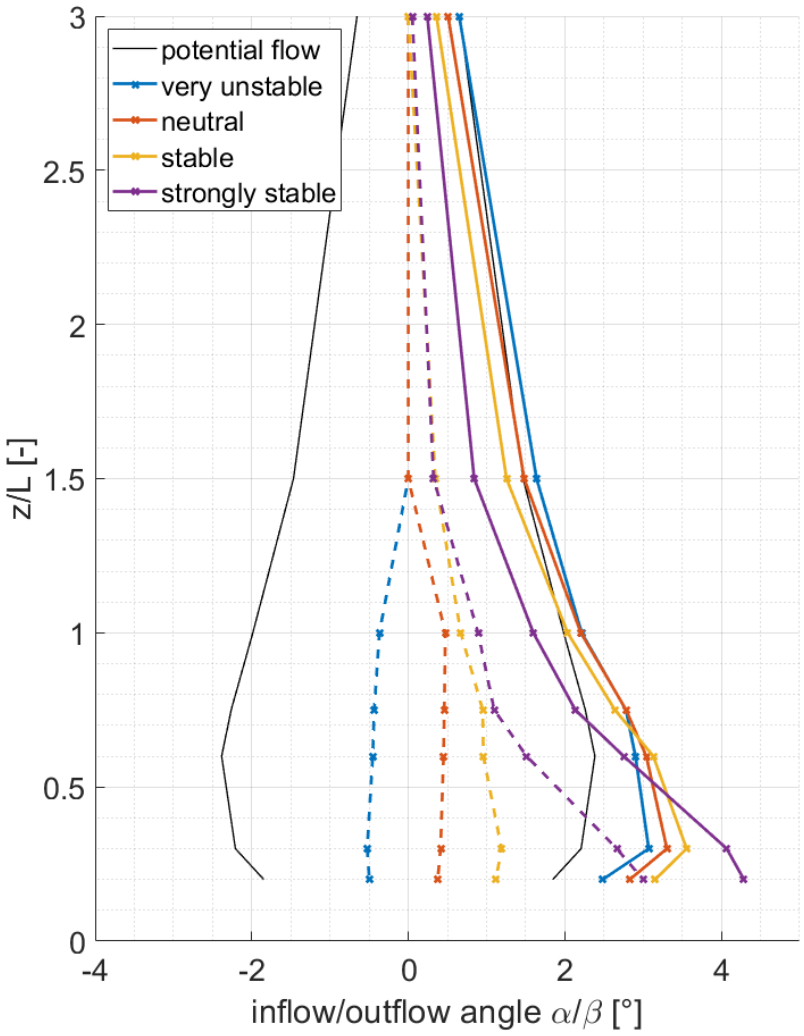

Figure 5.20: Inflow angle $\boldsymbol{\alpha}$ (dashed) and outflow angle $\boldsymbol{\beta}$ (solid) in dependence of atmospheric stability**.** Results from Meteodyn WT (colored) and from the potential flow model (black) at 150 m measurement height and for a $\boldsymbol{\varphi}$ of 30° for an $\boldsymbol{H/L}$ ratio of 0.3. Meteodyn WT results for a tree height $\boldsymbol{h_t}$ of 20 m and medium forest density.

5.1.3 Speed-up effects

The lidar error part ε_s describes the lidar error in complex terrain due to the speed-up between the measurement points of the lidar and the reconstruction point in the center above the lidar. Following its definition in chapter 3.2, it is the mean relative speed-up between the mentioned locations. To understand the results from the different models and different parametrizations used and link them to the estimated lidar error ε_s, the speed-ups between the inflow measurement point and the center point, as well as between the outflow measurement point and the center point, are illustrated in the following chapter.

The results are presented for different H/L ratios and different z/L ratios on the y-axis of the figures. This presentation is analogous to the later presentation of the lidar errors in chapter 0. It will, therefore, help the reader to understand the impact of the parameterizations on the different flow features.

Starting with the linearized flow model WEng, the results for the speed-ups are shown for the four different H/L ratios for the low roughness cases in Figure 5.21 (left). Again, it can be seen that the flow model results from WEng are symmetric. For small z/L ratios of 0.2, 0.3 and 0.6, the results are similar to those from the potential flow model. However, with an increasing z/L ratio, the deviation between the two models increases significantly. For H/L ratios of 0.3 and 0.4, this deviation is most abundant and the calculated speed-up effects are more than 50 % higher than in the potential flow solution for z/L ratios of 1.5 and 3.0.

As discussed, e.g. in Bowen and Mortensen (1996) and Rathmann et al. (1996), linearized wind models usually show an overestimation of speed-up effects at complex terrain sites with large terrain inclination. The errors in speed-up are largest at the lee side of the hill because the linearized model assumes attached flow fields, following the shape of the terrain. These over-predictions are analyzed and compared to the results of RANS CFD models in a blind-test presented in Bechmann et al. (2011). Here, the speed-up errors in the linearized model were twice as high as the errors in the RANS models.

When looking at the results for three different roughness lengths z_0 Figure 5.21 (right), this effect is increasing for increased roughness. There is a general tendency for a significant increase in speed-up for all z/L ratios. The difference is largest for z/L ratios above 1.0. Maximum speed-up effects from WEng can be observed at a z/L ratio of 1.5, which is higher than in the potential flow model.

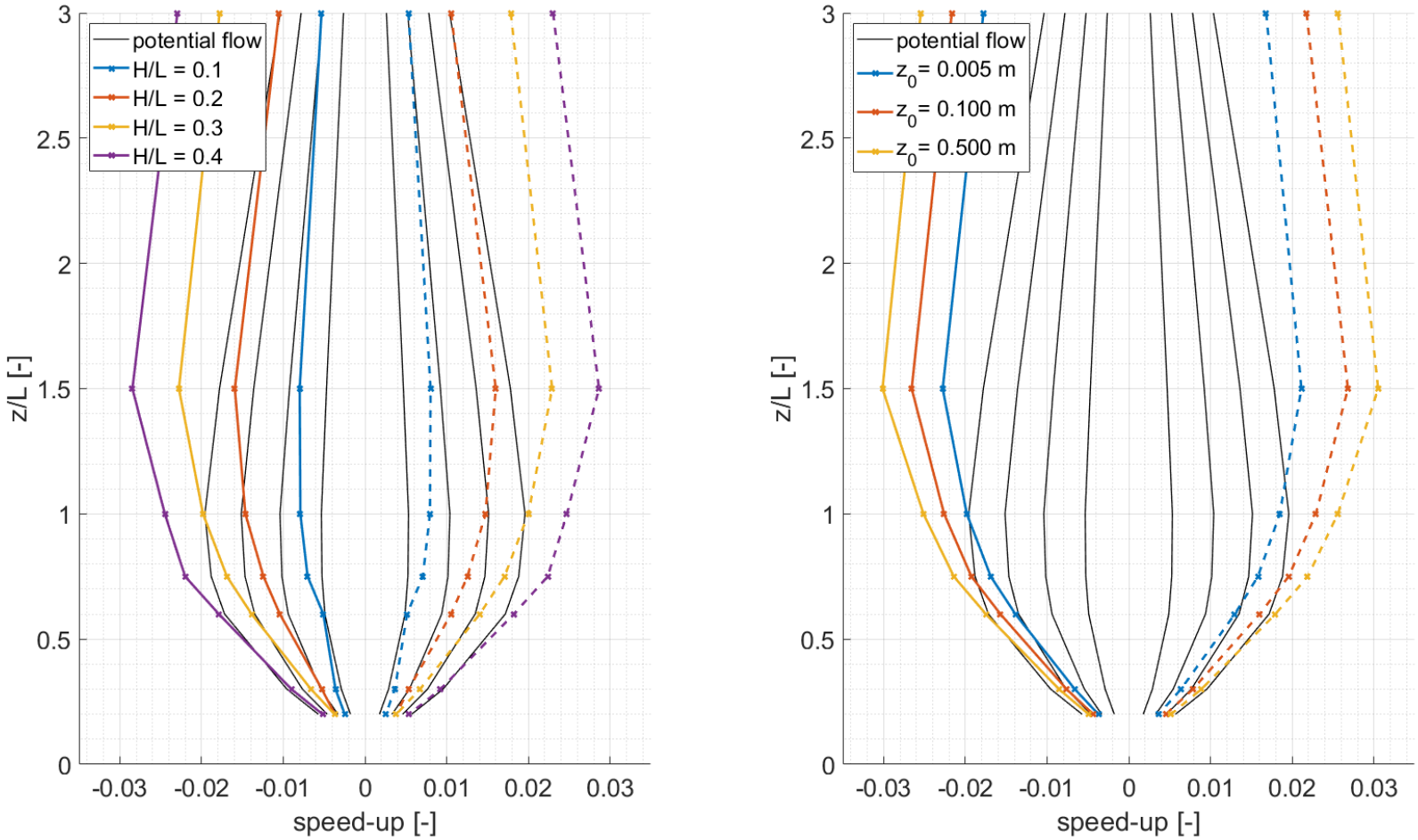

Figure 5.21: Inflow speed-up (dashed) and outflow speed-up (solid) in dependence of $\boldsymbol{H/L}$ ratio (left) and roughness length $\boldsymbol{z_0}$ (right)**.** Results from WEng (colored) and from the potential flow model (black) at 150 m measurement height and for a $\boldsymbol{\varphi}$ of 30°. For the left plot, the roughness length $\boldsymbol{z_0}$ is 0.005 m.

In the following, the results for the speed-up effects from Meteodyn WT are illustrated for H/L ratios of 0.3. Due to technical limitations in the flow model, it can generally be noted, that it is difficult to compare the speed-up effects for small H/L ratios to the potential flow model and WEng. It was not possible to export the model results with a precision of more than one position after the decimal points. This resolution is too small to resolve the small differences between the wind speeds at the lidar measurement points in case of small hill inclinations and, therefore, small speed-ups.

Figure 5.23 (left) shows the speed-ups for the four different H/L ratios for the low roughness cases. As the low roughness case shows the overall highest speed-up effects, it can be compared to the potential flow model despite the low data precision. Speed-ups at the outflow measurement point are very similar to what was found in the potential flow model. At the inflow, the speed-ups are comparable for the low H/L ratios 0.1 and 0.2. At higher H/L ratios the speed-ups in Meteodyn are significantly smaller than in the potential flow solution. However, fluctuations in the results are hindering the comparison of the inflow results.

The speed-up effects from Meteodyn WT for the three different roughness lengths at a H/L ratio of 0.3 given in Figure 5.22 (right) show that they are in the same order than those from the potential flow model and that the shape of the curve is similar as well. The results are approximately symmetric. For the lowest roughness lengths, the most considerable speed-up effects can be observed, which is contrary to the results from WEng. However, the differences between the results for the three roughness lengths are minimal. Additionally, there is interference due to rounding errors because of the low data accuracy in the export function, which causes the leaps in the curves.

The results for the forested cases with different three heights, which are shown in Figure 5.23 (left), indicate that also here the speed-up effects are very close to those from the potential flow model. Only for large tree heights of 30 m, there is a significant deviation at z/L ratios of 0.6 and 0.75 for both the inflow and outflow parts of the flow.

When looking at the results for three different forest densities in Figure 5.23 (right), not much difference can be seen between low, medium and high forest densities. However, it is interesting to note that the previously described differences for large tree heights are only present for medium forest densities.

In Figure 5.24, the results for different atmospheric stability classes on the speed-up effects for the forested cases with a tree height of 20 m and medium forest density are illustrated. Figure 10.5 and Figure 10.6 in Appendix 10.3 provide results for the low and high roughness cases in dependence of atmospheric stability.

Atmospheric stability seems to have the strongest influence on speed-up, at least when the extreme stability cases are considered. Smallest speed-up can be observed for strongly stable cases and the largest speed-ups for very unstable cases. Additionally, the results are no longer symmetric when atmospheric stability is considered in high roughness and forested cases. Especially speed-ups on the downwind side are generally decreased for stable and strongly stable cases. Note that, in accordance to the literature (Emeis 2011), the speed-up effects between freestream and hilltop are increased for stable cases in the simulations. However, this is not the case for the speed-ups between the measurement points and the reconstruction point when compared to neutral cases (compare e.g. Figure 5.14).

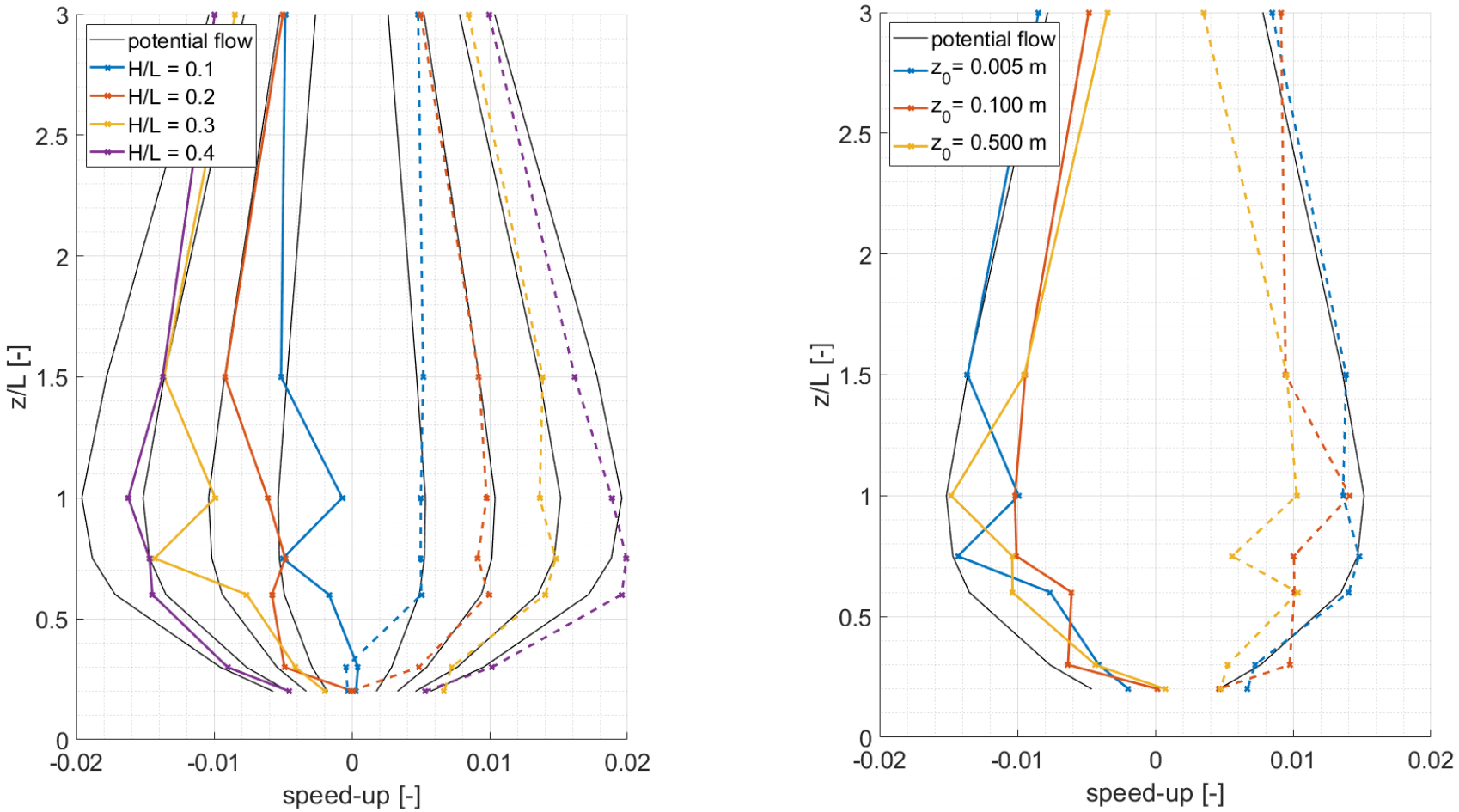

Figure 5.22: Inflow speed-up (dashed) and outflow speed-up (solid) in dependence of $\boldsymbol{H/L}$ ratio (left) and roughness length $\boldsymbol{z_0}$ (right)**.** Results from Meteodyn WT (colored) and from the potential flow model (black) at 150 m measurement height and for a $\boldsymbol{\varphi}$ of 30°. For the left plot, the roughness length $\boldsymbol{z_0}$ is 0.005 m.

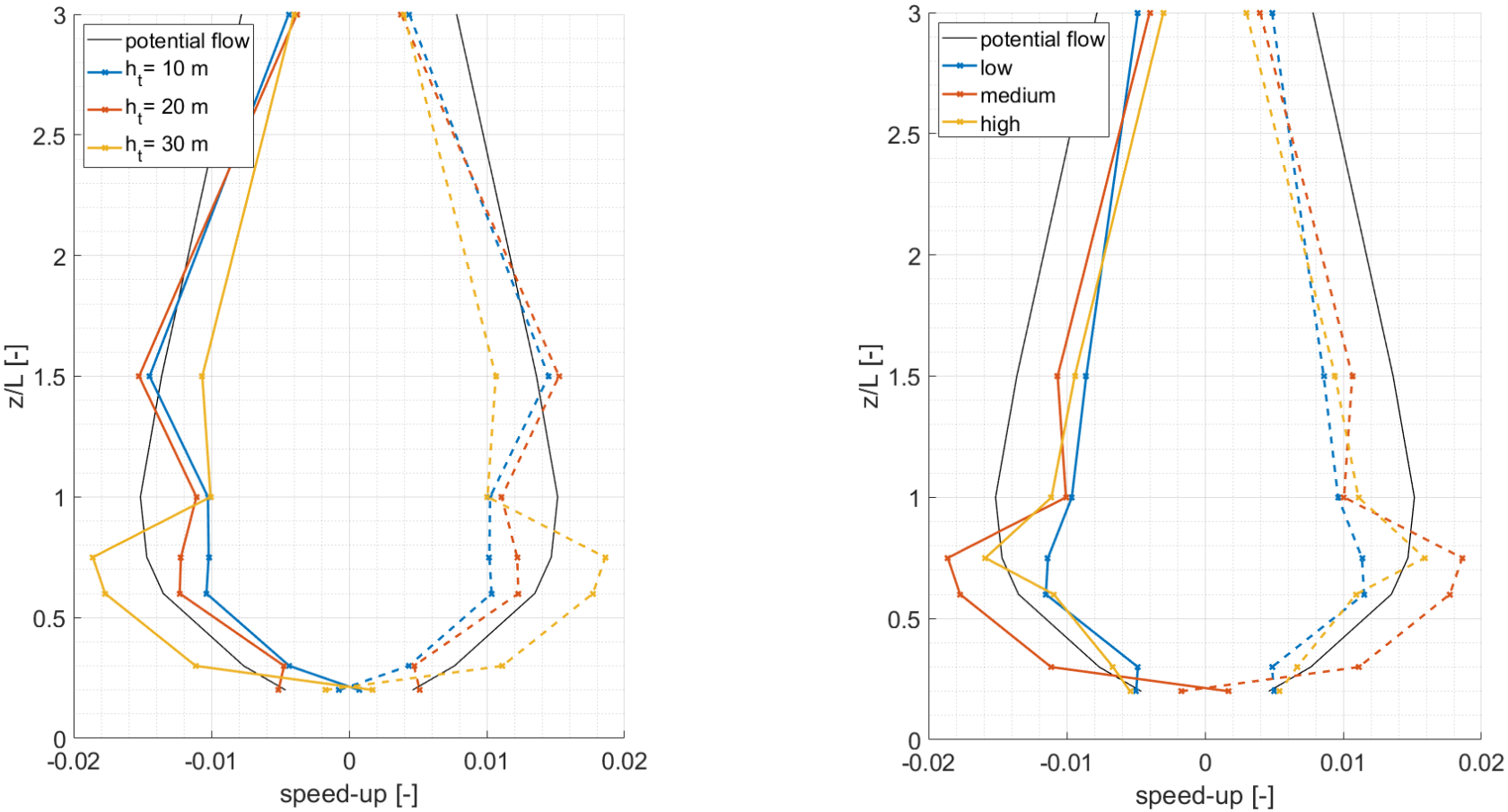

Figure 5.23: Inflow speed-up (dashed) and outflow speed-up (solid) in dependence of tree height $\boldsymbol{h_t}$ (left) and forest densities (right)**.** Results from Meteodyn WT (colored) and from the potential flow model (black) at 150 m measurement height and for a $\boldsymbol{\varphi}$ of 30° for an $\boldsymbol{H/L}$ ratio of 0.3. For the left plot, the forest density is medium. For the right plot, the tree height is 20 m.

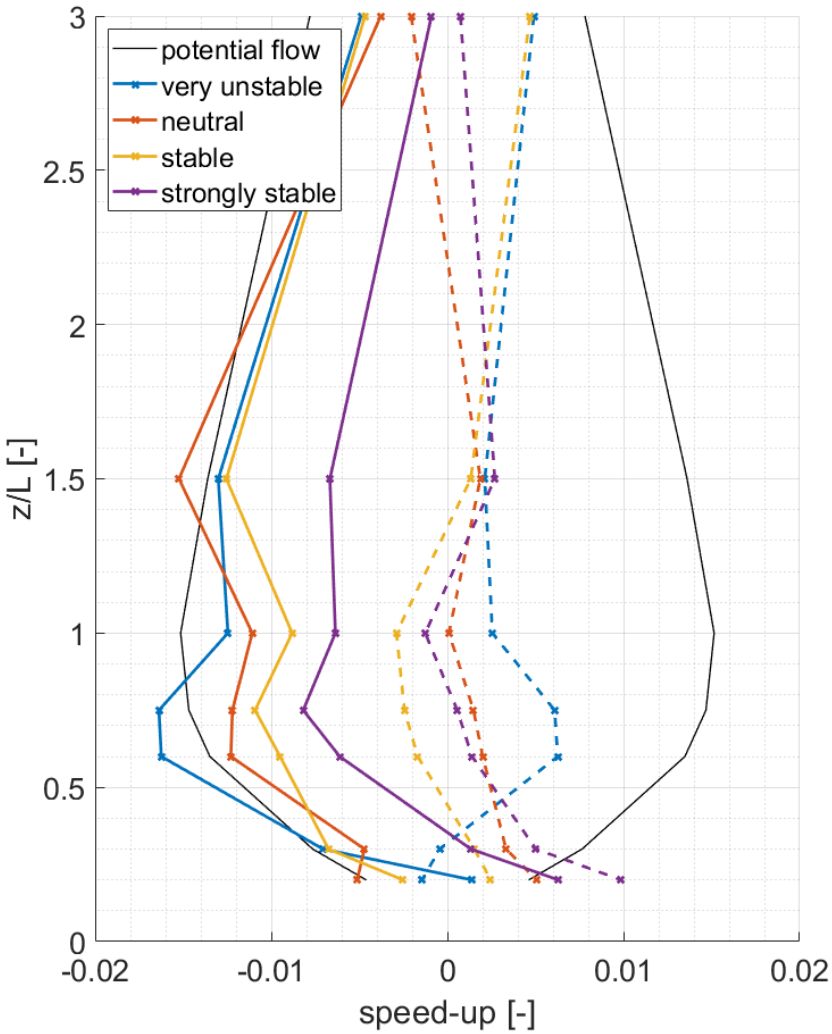

Figure 5.24: Inflow speed-up (dashed) and speed-up (solid) in dependence of atmospheric stability**.** Results from Meteodyn WT (colored) and from the potential flow model (black) at 150 m measurement height and for a $\boldsymbol{\varphi}$ of 30° for an $\boldsymbol{H/L}$ ratio of 0.3. Meteodyn WT results for a tree height $\boldsymbol{h_t}$ of 20 m and medium forest density.

5.2 Model results for the lidar error

The results for the lidar error are presented in a non-dimensional way. For this, the results for the different H/L ratios are grouped and the lidar error is usually plotted against the ratio of height above ground z against hill half-width L (ratio z/L). If reasonable, the results are shown for all four H/L ratios (0.1, 0.2, 0.3 and 0.4). In many cases, it makes more sense to focus on the results of one or two H/L ratios. In the latter case, the detailed results can be found in the appendix. The methodology for the parameter-study is described in more detail in chapter 4.4.

The following chapter is divided into the parts "orographic complexity" (chapter 5.2.1), "terrain roughness" (chapter 5.2.2), "forest height and density" (chapter 5.2.3) and "atmospheric stability" (chapter 5.2.4).

The dependence of the lidar error on measurement height h (respectively, the height above ground z) is treated separately in chapter 5.2.5, which also serves as an evaluation of the assumption of the applicability of the non-dimensional number z/L. The influence of half-cone opening angle φ is discussed in chapter 5.2.6 for the potential flow model different model parameterizations of Meteodyn WT.

This structure reflects the order and structure of the four main hypotheses discussed in chapter 1.4.

All results presented in the following are based on $\varphi = 30°$ unless otherwise noted.

5.2.1 Orographic complexity

As already described above, one of the big advantages of the potential flow model is the possibility to run it fast and easy for many different terrain parameters. Within this thesis, it is therefore used as a baseline or reference for the more complex models.

In a first step, the results from the potential flow model are presented to illustrate the general behavior of the lidar error concerning the relevant terrain parameters hill height H and hill half-width L. In a subsequent step, these results are used to define the parameter space for the more complex models WEng and Meteodyn WT in order to cover the most relevant effects. Due to economic reasons, the number of simulations had to be limited for these models.

Figure 5.25 shows the results for the lidar error ε versus the ratio z/L for four different H/L ranging from 0.1 to 0.4. There is a maximum lidar error that can be found in the range of z/L between 0.5 and 0.6. The exact position is slightly dependent on the H/L ratio and increases with increasing H/L. The maximum lidar error significantly increases with increasing terrain inclination. For a H/L ratio of 0.1, it is slightly larger than -3 %. For a H/L ratio of 0.4, it reaches up to about -11 %.

For lower and higher values of z/L, the lidar error rapidly decreases. For better readability, a cutout of the relevant area is shown in Figure 5.26. Especially a decrease of z/L results in a strong decrease of the lidar error ε. In comparison to that, the decrease of ε for increasing z/L is less pronounced.

Figure 5.25 and Figure 5.26 contain two dashed lines. The -2 % line marks a typical uncertainty of wind measurements based on cup-anemometers as a reference (Basse et al. 2017). Lidar measurement errors below -2 % are in the same order as uncertainties of mast-based measurement. Such small errors will not add much uncertainty to the

wind measurement. However, because lidar errors are systematic (compare chapter 3.3), a correction is mandatory also in case of small errors.

The -10 % line marks an approximate upper limit for a reasonable correction of lidar errors in complex terrain. Details on this approximation can be found in chapter 3.3.

For a discussion of the model results at a later point, it is recommended to keep in mind the range of lidar errors between -10 % and -2 %. By comparing changes in estimated lidar errors caused by parameter variations in the subsequent chapters to this range, it also becomes obvious which parameters are essential for lidar error correction and which are not.

From Figure 5.25 and Figure 5.26, it can be noticed that the 2 % line is crossed for the steepest hills (H/L of 0.4) at a z/L of about 4.5 and for the lowest slopes (H/L of 0.1) at z/L of 1.5. For low z/L ratios (broadest hills), the three lines for H/L of 0.2, 0.3 and 0.4 are crossing the 2 % line close together between 0.04 and 0.07. For the least complex hill, the lidar error already decreases below 2 % at a $z/L$of 0.16.

Following this, it can be concluded that for a small H/L of 0.1, only a very limited parameter range between z/L of 0.16 and 1.5 is relevant for correction. Additionally, the necessary corrections are relatively small, with maximum errors in the range of -3 %.

For more complex terrain and therefore larger H/L, a much larger parameter space must be considered. Significant lidar errors can be found for large hills down to a z/L of 0.04 and also very narrow but steep hills in the range of z/L from 2 to 4.5 for H/L between 0.2 and 0.4. The magnitude of the lidar errors for those terrains is also much higher.

The -10 % line is only crossed by the maximum error for the steepest terrain of H/L of 0.4 cases between z/L between 0.35 and 0.9.

Based on the above-given considerations, the relevant terrain parameter settings for more complex CFD calculations have been chosen (compare chapter 4.5).

As defined in chapter 3.2, the lidar error ε can be subdivided into a part ε_c caused by flow curvature and a part ε_s caused by speed-up between the measurement points. Figure 5.27 illustrates ε_c and ε_s next to each other in the same way that ε is presented above.

The general shape of the four curves is similar to that presented in Figure 5.25. The maximum errors ε_c (Figure 5.27, left) are slightly smaller compared to ε. For an H/L ratio of 0.4, the error is no longer exceeding the -10 % line. For a H/L of 0.1, the maximum error is about 2.5 %. The maximum error is now located between z/L of 0.45 and 0.51. Also, the point of intersection with the 2 % line on the right-hand side is significantly shifted downwards.

Looking at Figure 5.27, right, which shows the speed-up part ε_s, it becomes obvious that this part is much smaller in magnitude than the curvature part. However, it reaches up to -1.95 % for a H/L ratio of 0.4 and also the magnitudes for H/L ratios 0.2 and 0.3 are not negligible. The position z/L of the maximum error due to speed-up is between 0.9 and 1.0. The lidar error caused by speed-up, therefore, shifts the resulting curves for the total lidar error ε upwards.

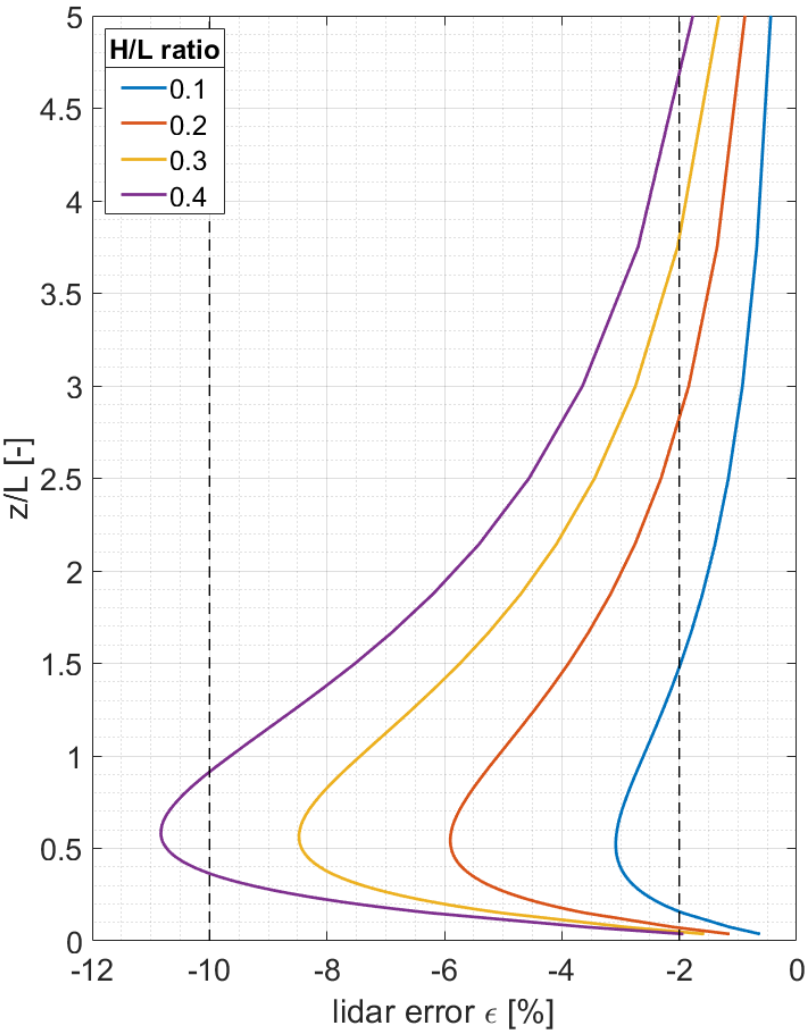

Figure 5.25: Lidar error $\boldsymbol{\varepsilon}$ in dependence of the ratio $\boldsymbol{H/L}$ between $\boldsymbol{z/L}$ ratios from 0 to 5. Results are based on the potential flow model. The two dashed lines mark a typical uncertainty of wind measurements (-2 %) and a reasonable limit for acceptable lidar errors in wind resource assessments (-10 %).

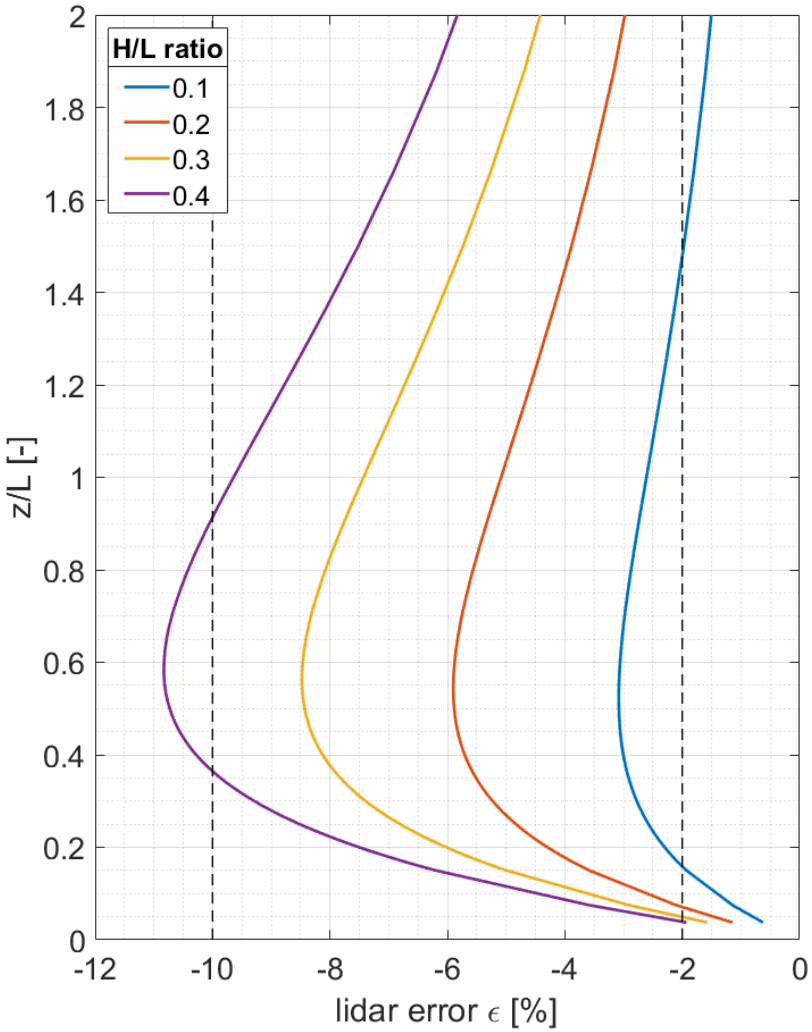

Figure 5.26: Lidar error $\boldsymbol{\varepsilon}$ in dependence of the ratio $\boldsymbol{H/L}$ between $\boldsymbol{z/L}$ ratios from 0 to 2. Results are based on the potential flow model. The two dashed lines mark a typical uncertainty of wind measurements (-2 %) and a reasonable limit for acceptable lidar errors in wind resource estimations (-10 %).

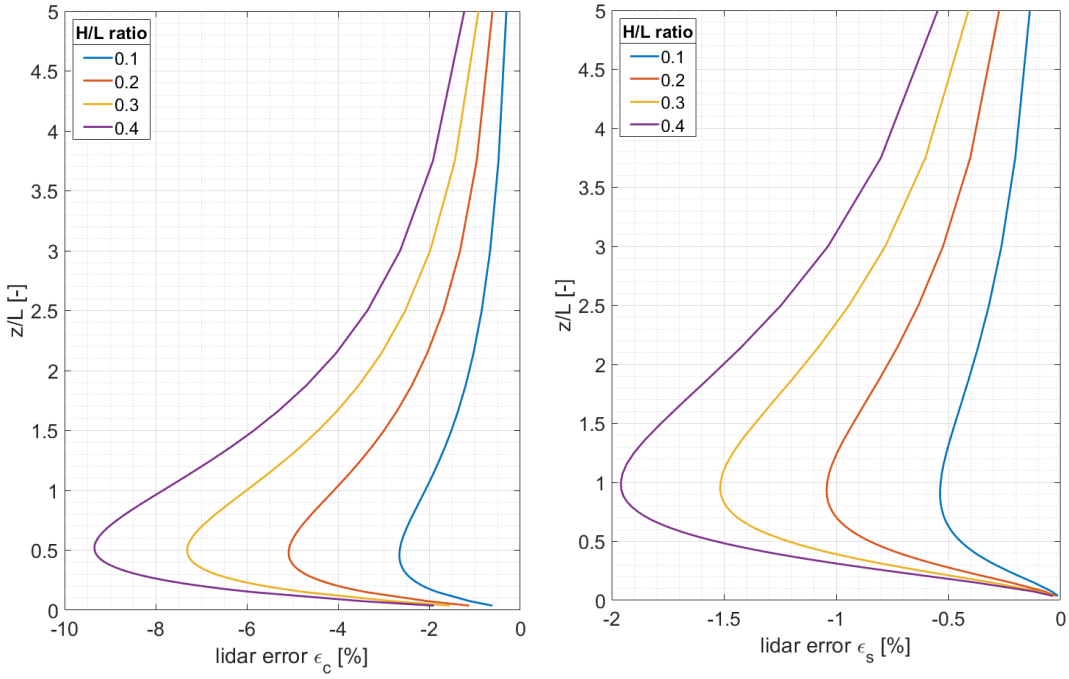

Figure 5.27: Lidar error $\boldsymbol{\varepsilon_c}$ (left) and $\boldsymbol{\varepsilon_s}$ (right) in dependence of the ratio $\boldsymbol{H/L}$ between $\boldsymbol{z/L}$ ratios from 0 to 5. Results are based on the potential flow model. Note the different scaling of the x-axes.

5.2.2 Terrain roughness

Having defined the relevant parameter space for the more advanced models WEng and Meteodyn WT, the influence of terrain roughness is analyzed in the following chapter. Wherever possible, the results are compared to those from the potential flow model shown in chapter 5.2.1. For WEng and Meteodyn WT, the results are composed of seven data points per H/L ratio that cover a z/L range from 0.2 to 3.0 with a sufficient resolution around the area of maximum expected lidar errors (compare simulation setup in chapter 4.5).

5.2.2.1 WAsP Engineering

Figure 5.30 shows the results from WEng for the four different H/L ratios for the low roughness value of 0.005 m. The results are generally relatively close to those from the potential flow model as a reference. Especially for z/L values between 0.2 and 0.3 as well as for cases with $z/L \geq 1.5$, the results of the low roughness case are very close to the reference. Also, the shape of the curves is comparable to that from the potential flow model.

For H/L ratios of 0.1 and 0.2, all lidar errors from WEng are smaller than or equal to those from the potential flow model. The maximum errors for these cases can be found at z/L of 0.75 with -2.6 % and -5.7 %. For a H/L ratio of 0.3 and 0.4, the lidar error exceeds the maximum found with the potential flow model. Here the maximum values are found at z/L of 0.6 with -10 % and -12 %, which is significantly larger than in the reference. Also, at z/L up to 1.0, the lidar errors estimated from WEng exceed those from the potential flow model, showing a maximum lidar error in the same z/L range as found in the potential flow model. Also, the estimated lidar error decreases strongly for smaller and larger z/L.

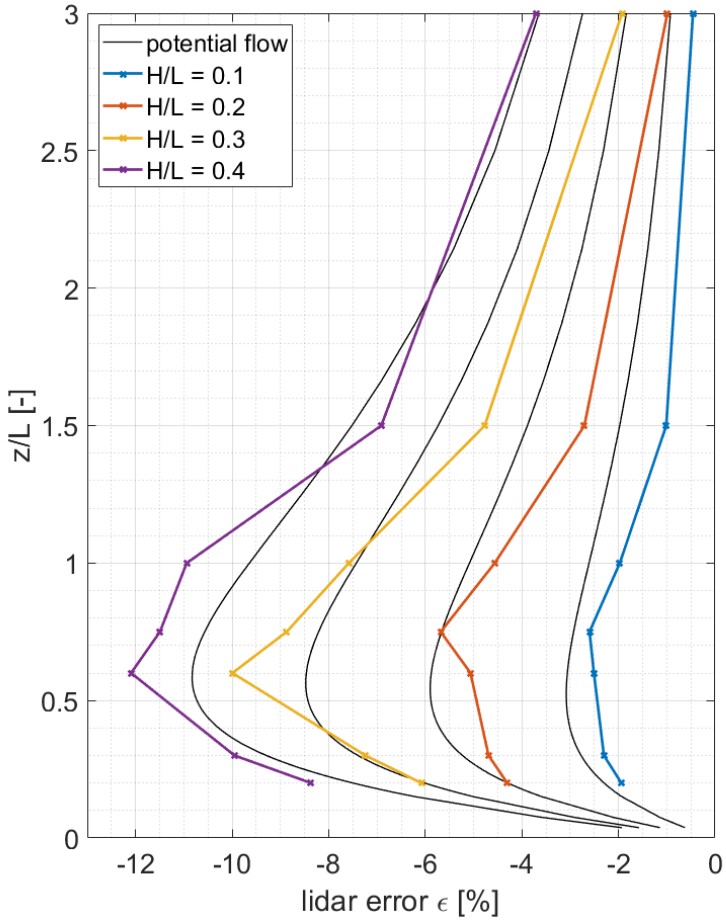

Figure 5.28: Lidar error $\boldsymbol{\varepsilon}$ in dependence of the ratio $\boldsymbol{H/L}$ between $\boldsymbol{z/L}$ ratios from 0 to 3. Results are based on WEng (colored) and the potential flow model (black). The roughness length $\boldsymbol{z_0}$ is set to 0.005 m. From right to left, the black lines refer to the increasing $\boldsymbol{H/L}$ ratios.

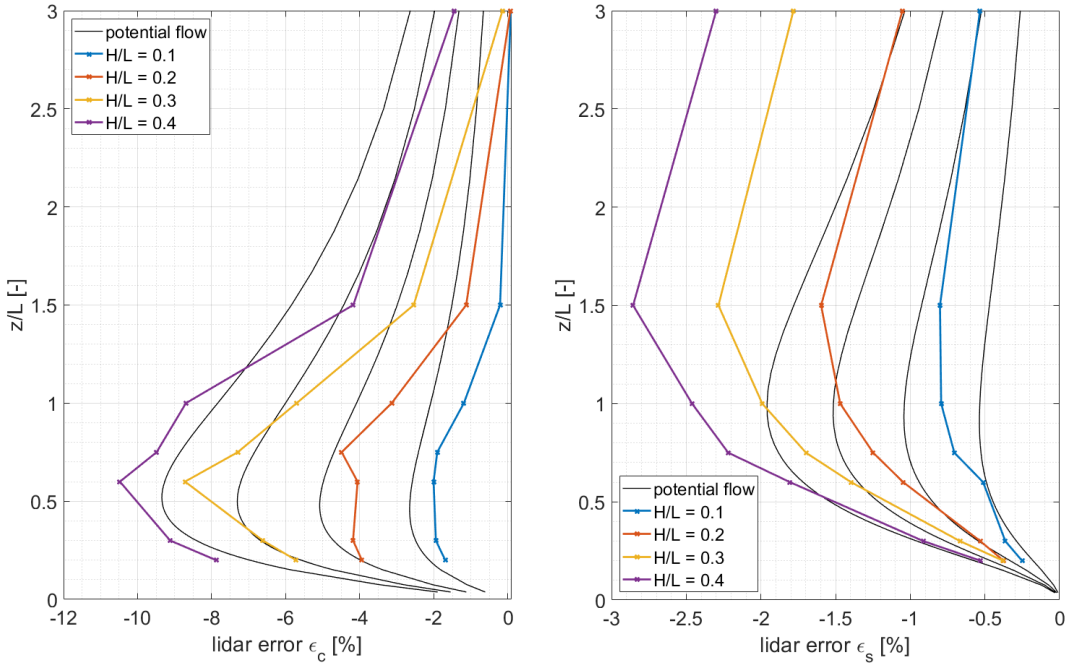

Figure 5.29: Lidar error $\boldsymbol{\varepsilon_c}$ (left) and $\boldsymbol{\varepsilon_s}$ (right) in dependence of the ratio $\boldsymbol{H/L}$ between $\boldsymbol{z/L}$ ratios from 0 to 3. Results are based on WEng (colored) and the potential flow model (black). The roughness length $\boldsymbol{z_0}$ is set to 0.005 m. From right to left, the black lines refer to the increasing $\boldsymbol{H/L}$ ratios.

Following the same approach as in the previous chapter, the lidar error can be split up into the parts ε_c and ε_s, giving the error part resulting from flow curvature and the part resulting from speed-up effects (Figure 5.29).

In this case, the shape of both curves differs clearly from the potential flow model results. For z/L of 1.5 to 3 the estimated lidar error ε_c decreases much faster than in the reference. The resulting lidar errors are, therefore, significantly smaller than those estimated by the potential flow model. For smaller z/L the shape of the curves for ε_c is comparable to that for the total error ε.

The estimated lidar error ε_s that is caused by speed-up effects, on the other hand, strongly exceeds that from the reference for all z/L from 0.6. The maximum values of ε_s are found at a z/L 1.5, which is significantly larger than in the potential flow model.

The combination of the two error sources brings the total estimated lidar error from WEng close to that from the reference, although there are considerable deviations in the two error parts. However, also in WEng ε_s is generally much smaller than ε_c.

In a second step, the surface roughness length has been modified in WEng, setting values of 0.005 m, 0.1 m and 0.5 m. The results for ε, ε_c and ε_s are shown in Figure 5.30 and Figure 5.31 for an H/L ratio of 0.3.

The maximum lidar error from WEng is found for z/L of 0.6 for all roughness lengths and exceeds the maximum from the reference by about 2 % for a z_0 of 0.005 m. Larger roughness lengths decrease the lidar errors significantly. This dependence on roughness length becomes most obvious for increasing z/L values. While the lidar error is about 5 % for z/L of 1.5 and a very low roughness length, it decreases to about 2 % for high roughness. For small z/L of 0.2 and 0.3, the results for the three different roughness lengths are comparable and all very close to the reference.

Splitting up the lidar error into the flow curvature part ε_c and the speed-up part ε_s again, reveals that the general shape of the error curve is dominated by ε_c. It reaches up to 7.5 to 8.5 % in the maximum and then significantly decreases for larger and smaller hills. It is interesting to note that the decrease for small hills above z/L = 1 is much faster than in the potential flow model. Additionally, the lidar error ε_c becomes 0 % for the lowest roughness at about z/L = 3 and even reaches positive values for larger roughness reaching up to +1.5 %

The speed-up induced error ε_s gives a much smaller part of the total lidar error. It increases up to z/L of 1.5 and then slightly decreases again. The maximum value is about 2.25 % for low roughness and about 3 % for the highest roughness. Here, an increased roughness length results in larger lidar errors. A systematic increase in ε_s is found for all simulations. Again, the results for small roughness and relative large hills are very close to those from the potential flow model.

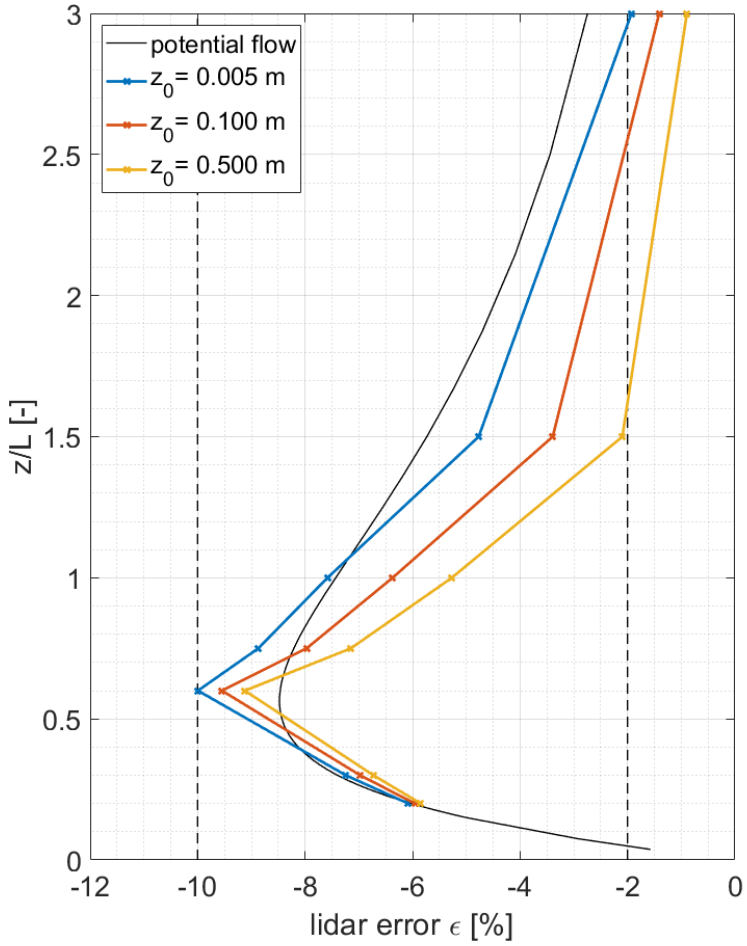

Figure 5.30: Lidar error $\boldsymbol{\varepsilon}$ in dependence of the roughness length $\boldsymbol{z_0}$ between $\boldsymbol{z/L}$ ratios from 0 to 3. Results are based on WEng (colored) and the potential flow model (black) for an $\boldsymbol{H/L}$ ratio of 0.3.

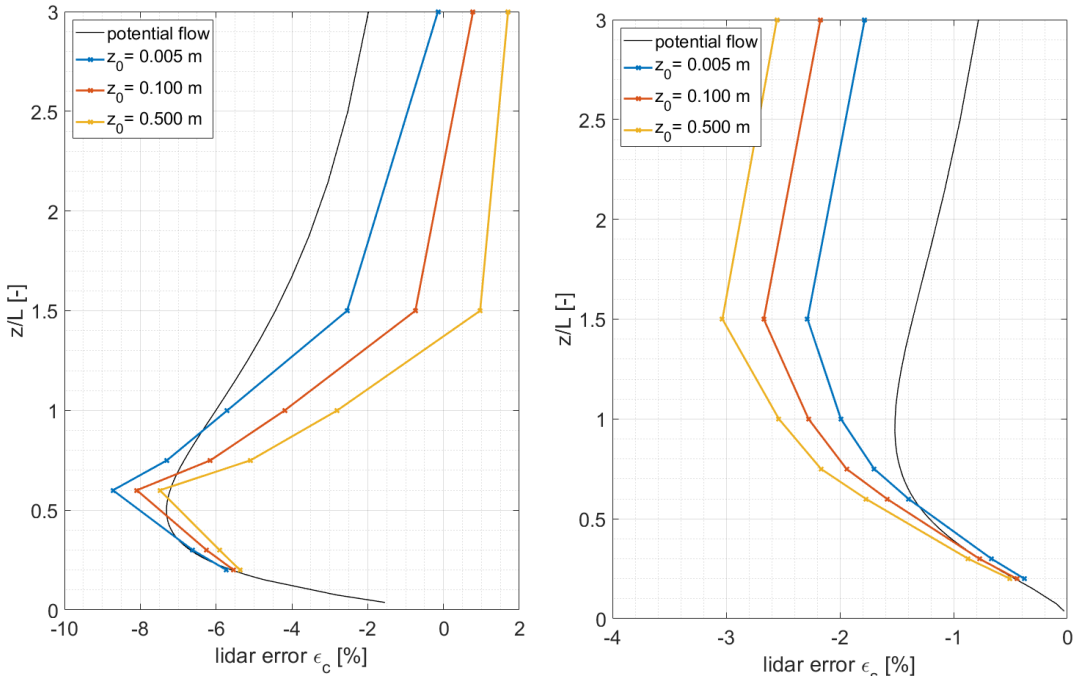

Figure 5.31: Lidar error $\boldsymbol{\varepsilon_c}$ (left) and $\boldsymbol{\varepsilon_s}$ (right) in dependence of the roughness length $\boldsymbol{z_0}$ between $\boldsymbol{z/L}$ ratios from 0 to 3. Results are based on WEng (colored) and the potential flow model (black) for an $\boldsymbol{H/L}$ ratio of 0.3.

5.2.2.2 Meteodyn WT

Figure 5.32 to Figure 5.35 sum up the results from Meteodyn WT simulations with the three different roughness values z_0 of 0.005 m, 0.1 m and 0.5 m for the whole set of terrain cases.

First the total lidar error ε and its parts ε_c and ε_s are shown for the lowest roughness length z_0 of 0.005 m. Each of the four different H/L sets is compared to the results from the potential flow model. This allows for a general comparison of the results from the RANS CFD model for only slightly asymmetric flow fields to the fully symmetric results from the inviscid model.

The shape of the curves for the total lidar error ε for the lowest roughness length shown in Figure 5.28 is comparable to those from the potential flow model. However, for all four H/L ratios, the lidar error from Meteodyn WT is smaller when compared to the reference. The difference between the reference and Meteodyn WT increases for increasing H/L ratios. The maximum values for ε can be found at roughly the same z/L ratios as in the reference: For H/L ratios of 0.1, 0.2 and 0.3 the maximum is less pronounced and located at a z/L of 0.6 to 0.75, which is a slight shift to larger z/L than in the reference. For a H/L ratio of 0.4, the maximum can clearly be seen at a z/L of 0.6. At these points, the total lidar error ε is -2.5 %, -5.0 %, -7.2 % and -9.6 %.

For z/L ratios below the maximum point, there is a strong decrease of ε for H/L values of 0.2, 0.3 and 0.4. For the least inclined hill shape with a H/L ratio of 0.1, only a small decrease of the total lidar error for small z/L is found. For z/L ratios larger than 0.75, ε is continuously decreasing. For all H/L ratios, the results from Meteodyn WT get closer to the reference for smaller and larger z/L ratios than at the maximum point.

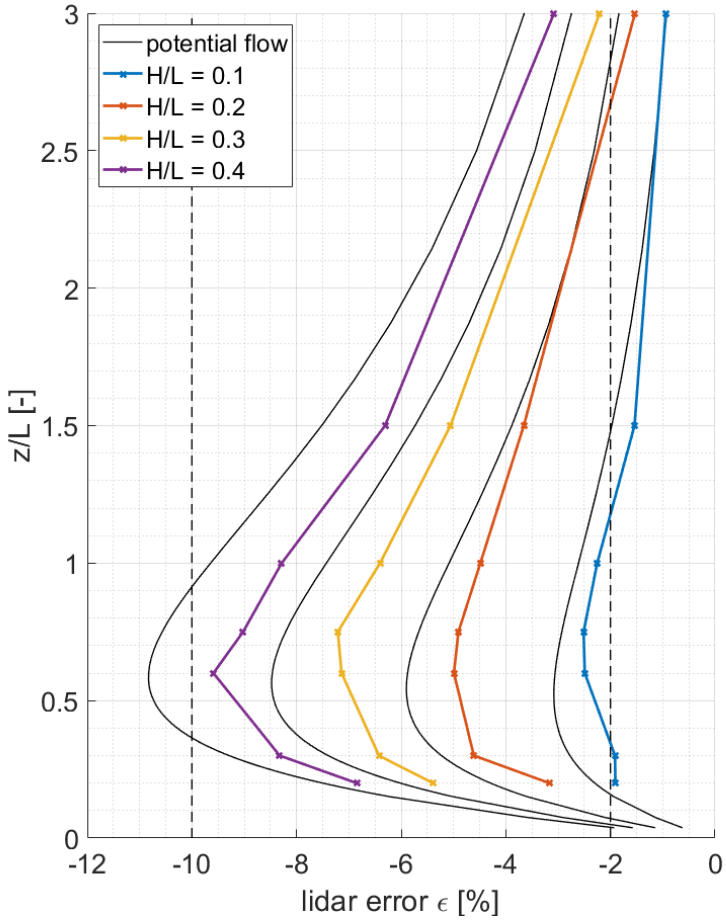

Figure 5.32: Lidar error $\boldsymbol{\varepsilon}$ in dependence of the ratio $\boldsymbol{H/L}$ between $\boldsymbol{z/L}$ ratios from 0 to 3. Results are based on Meteodyn WT (colored) and the potential flow model (black). The roughness length $\boldsymbol{z_0}$ is set to 0.005 m. From right to left, the black lines refer to the increasing $\boldsymbol{H/L}$ ratios.

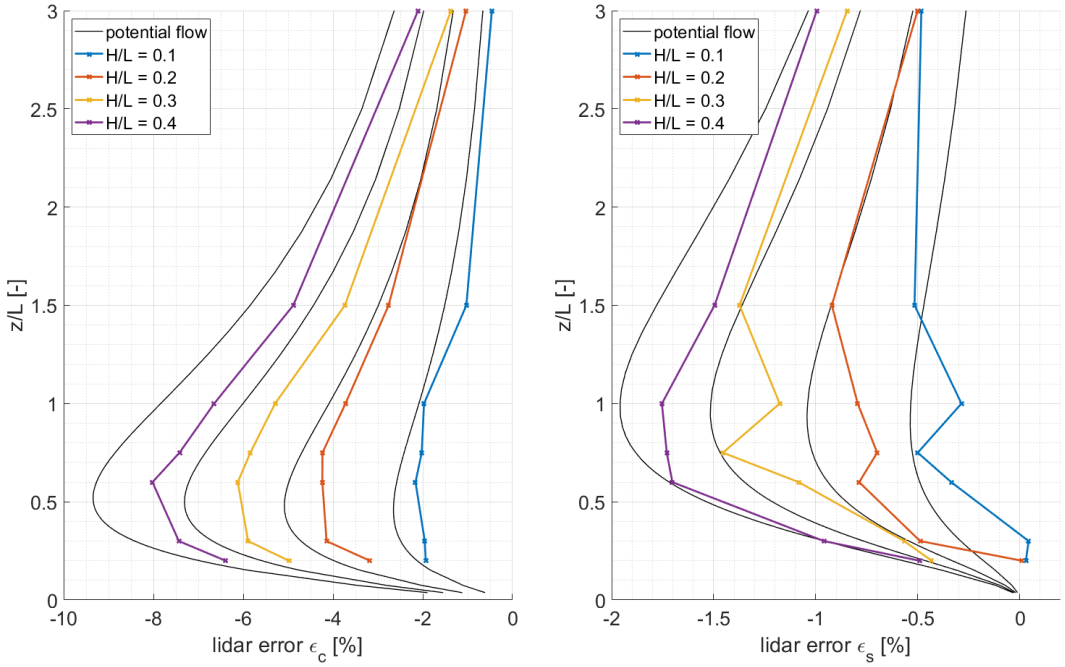

Figure 5.33: Lidar error $\boldsymbol{\varepsilon_c}$ (left) and $\boldsymbol{\varepsilon_s}$ (right) in dependence of the $\boldsymbol{H/L}$ ratio between $\boldsymbol{z/L}$ ratios from 0 to 3. Results are based on Meteodyn WT (colored) and the potential flow model (black). From right to left, the black lines refer to the increasing $\boldsymbol{H/L}$ ratios.

The results for the total lidar error ε from Meteodyn WT can also be split up into the error parts ε_c and ε_s (Figure 5.33 left and right). From this, the individual part of these two can be illustrated.

The lidar error due to flow curvature, ε_c, as can be seen in the left part of Figure 5.33, dominates the general shape of the error curves. Its maximum point is slightly below that of the total lidar error at a z/L of about 0.6. Maximum errors ε_c reach from -2.16 %for an H/L ratio of 0.1 up to 8.0 % for the highest ratio of 0.4. As for the total lidar error, there are differences between the potential flow model and the results from Meteodyn WT, which are highest around the maximum points and then decrease for larger and smaller z/L ratios. The results for ε_c are relatively close to the reference for H/L ratios of 0.1 and 0.2 for the whole z/L interval.

Looking at the speed-up induced error part, ε_s, it can be seen that the shape of the curves is comparable to that from the potential flow model. However, except for the highest H/L ratio of 0.4, there are fluctuations in the model results, which seem random. Having investigated the model data in detail, the reason for this could be identified: Due to limited precision of the exported data from the model software (one position after the decimal point), the calculation results are fluctuating for cases with minimal differences between the wind speeds at the measurement points. This is especially true for the low absolute values of the speed-ups between the lidar measurement points and for small H/L ratios where the influence of the hill geometry on the flow is relatively small. These fluctuations are not present in the potential flow model and WEng, as they both use high precision floating point numbers during the calculation. For Meteodyn WT, the model results had to be exported from the software in a proprietary data format for further analysis in Matlab. During the course of the doctoral thesis, it was not possible to persuade the developer of the software to implement an enhanced version of the export function. The fluctuations for the estimation of small lidar errors based on Meteodyn WT must, therefore, be treated as an individual source for model uncertainty.

The absolute values of the lidar error due to speed-up effects that can be seen in Figure 5.33 (right) are comparable to those from the potential flow model. For z/L ratios around 1.0, there are differences to the reference towards smaller lidar errors. The maximum lidar errors ε_s range from 0.5 % for small H/L ratios to about 1.75 % for the highest H/L ratios.

Analogous to the previous chapter, the influence of the roughness length z_0 is presented for the three different used values of 0.005 m, 0.1 m and 0.5 m for an H/L ratio of 0.3. Detailed results for other H/L ratios can be found in the appendix.

Figure 5.34 shows the total lidar error ε for the different roughness length. While the curve for the lowest roughness length has a pronounced maximum value and the shape of the curve is comparable to that from the potential flow, this is no longer the case for higher roughness length. For a z_0 of 0.1 m ,the lidar errors are generally smaller for all z/L ratios, except the lowest two 0.2 and 0.3. For these, the model results are very close to each other. At the maximum point, the lidar error is decreased by about 1 % for the medium roughness length. The decrease of ε is even stronger for a roughness length of 0.5 m. Here, ε is decreased by another 1 % for all z/L ratios. However, the general shape of the error curve stays similar. For the highest roughness length, the lidar error decreased below 2 % for a z/L of 2.5.

Figure 5.35 splits up the total lidar error ε into its parts ε_c and ε_s. Depending on roughness length, the speed-up induced part of the lidar error, ε_s reaches up to 1.25 % to 1.5 %. Again, significant fluctuations can be found in the results, which make it difficult to assess the actual shape of the error curve.

As the lidar error ε_c, that is caused by flow curvature, is about four times larger than ε_s, the shape of the error curve is dominated by this part. ε_c reaches maximum values of 5.8 % for large roughness lengths and 7.2 % for small roughness length. For z/L ratios from 1.5 to 3.0 and below 0.3, there is only a small difference between the low and the medium roughness length. For the part around the maximum value, these two curves differ by up to 0.5 %. The lidar errors for the highest roughness lengths are again systematically smaller for all z/l ratios.

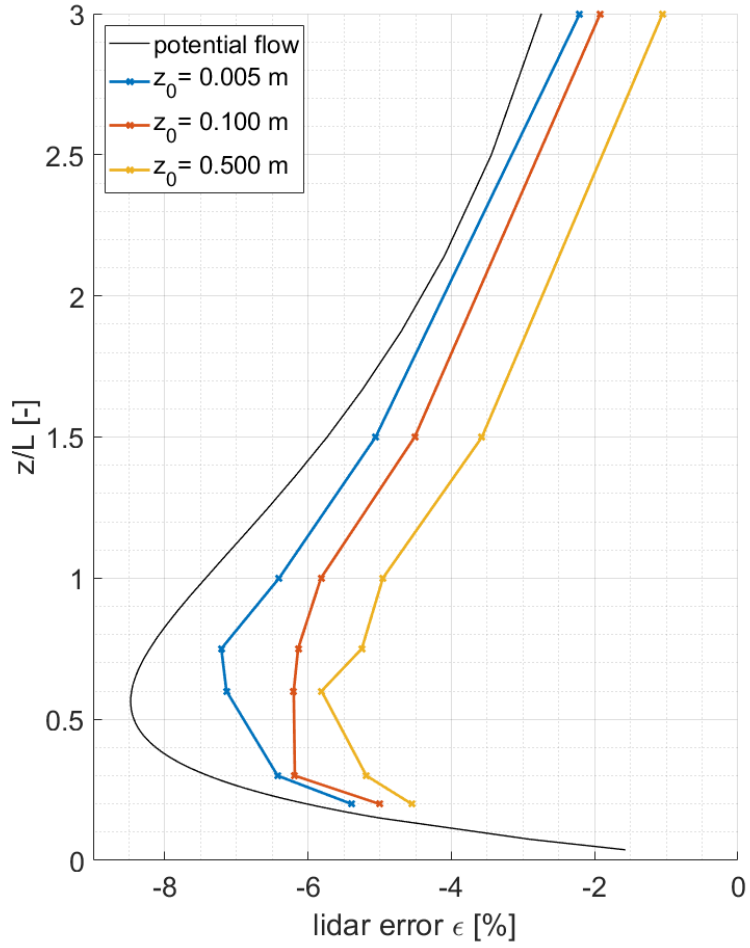

Figure 5.34: Lidar error $\boldsymbol{\varepsilon}$ in dependence of the roughness length $\boldsymbol{z_0}$ between $\boldsymbol{z/L}$ ratios from 0 to 3. Results are based on Meteodyn WT (colored) and the potential flow model (black) for an $\boldsymbol{H/L}$ ratio of 0.3.

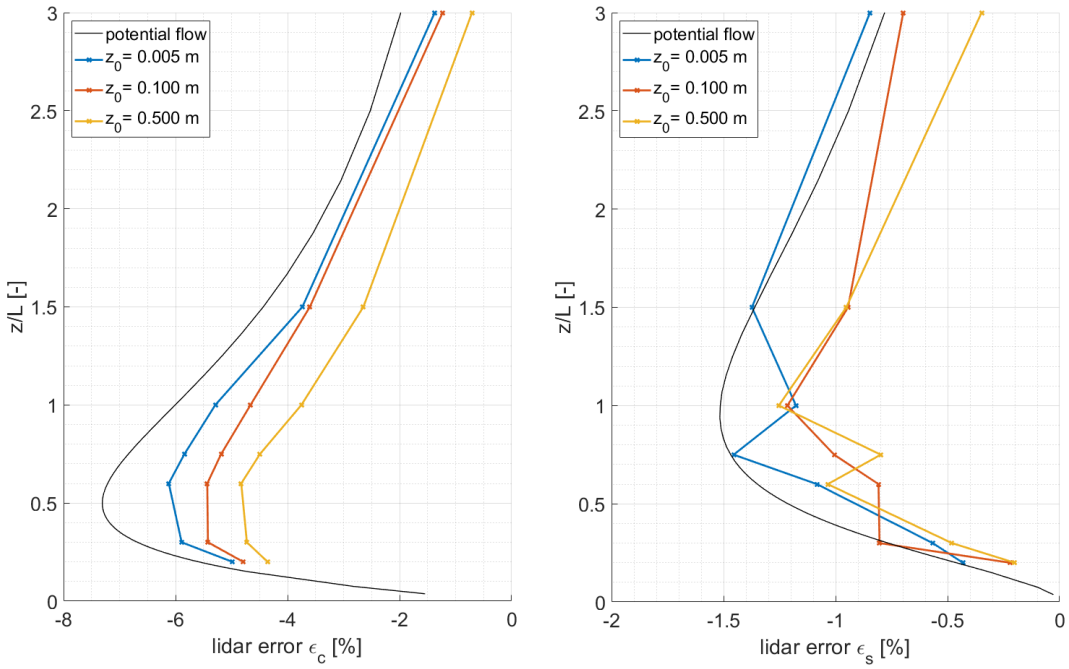

Figure 5.35: Lidar error $\boldsymbol{\varepsilon_c}$ (left) and $\boldsymbol{\varepsilon_s}$ (right) in dependence of the roughness length $\boldsymbol{z_0}$ between $\boldsymbol{z/L}$ ratios from 0 to 3. Results are based on Meteodyn WT (colored) and the potential flow model (black) for an $\boldsymbol{H/L}$ ratio of 0.3.

5.2.3 Forest height and density

The following sup-chapter shows the lidar error results from Meteodyn WT for forested cases. First, a case with small tree heights of 10 m and low forest densities is shown. This case is used as a consistency analysis for the transition between the high roughness case without forest and a case with minimal influence from the forest model.

Afterward, results for ε, ε_c and ε_s are presented for different tree heights and different forest densities at a H/L ratio of 0.3. More results for other H/L ratios can be found in the appendix.

Figure 5.36 shows the results of the comparison between the high roughness ($z_0 = 0{,}5m$) cases without forest model and the low and sparse forest cases ($h_t = 10m$, low forest density) for the four different H/L ratios. It can be seen that the lidar error ε is comparable for the two settings for nearly all cases, although there are some minor deviations between the two.

Figure 5.37 splits up the lidar error into its parts ε_c (left) and ε_s (right). Also here – except some results – the absolute values of ε_c are comparable between the two cases. For the speed-up induced error, there is much fluctuation in the results (see explanation above). However, it can be noted that the speed-up errors are in the same order for both cases and that they are systematically increasing for larger H/L ratios.

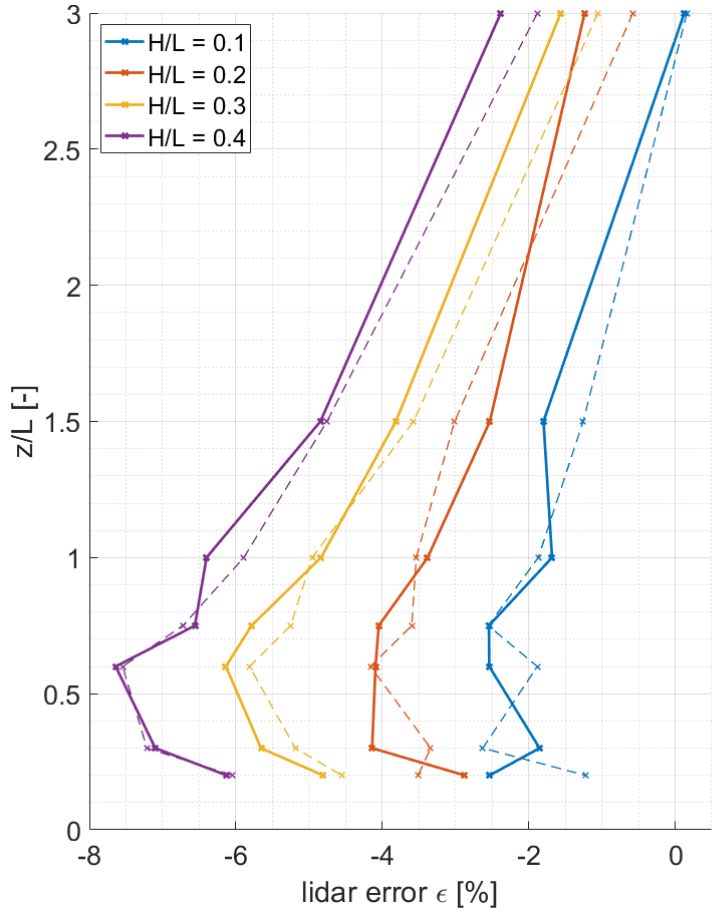

Figure 5.36: Lidar error $\boldsymbol{\varepsilon}$ in dependence of the ratio $\boldsymbol{H/L}$ between $\boldsymbol{z/L}$ ratios from 0 to 3 for a high roughness length $\boldsymbol{z_0 = 0,5m}$ (dashed lines) and a forest ($\boldsymbol{h_t = 10m}$, low forest density), i.e., a very sparse forest (solid lines). Results are based on Meteodyn WT.

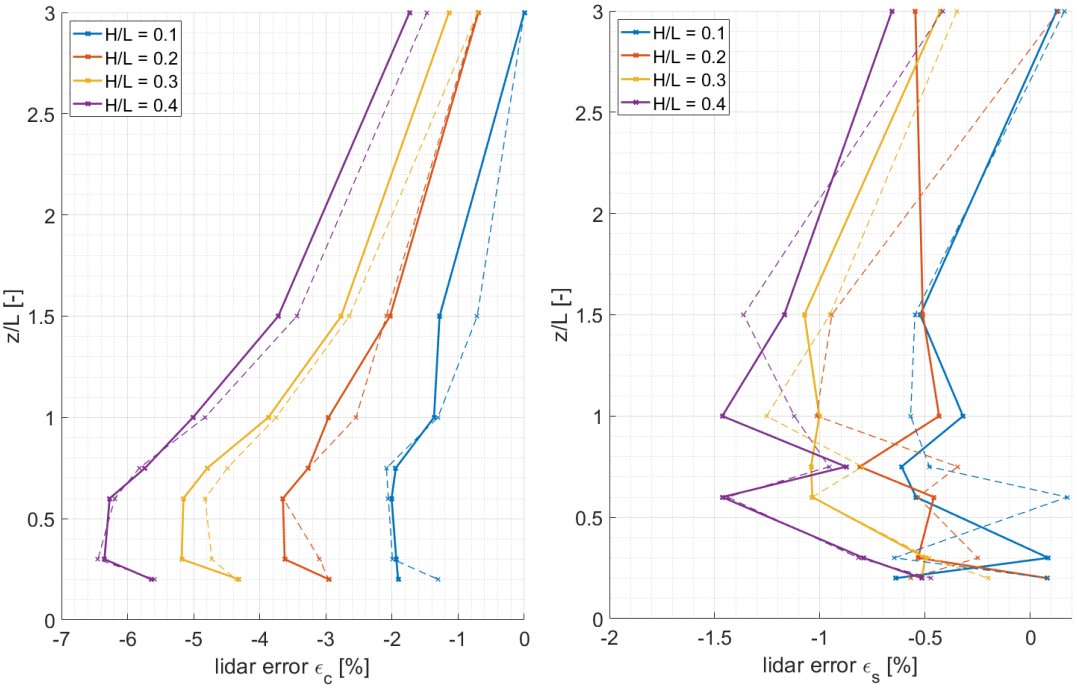

Figure 5.37: Lidar error $\boldsymbol{\varepsilon_c}$ (left) and $\boldsymbol{\varepsilon_s}$ (right) in dependence of the ratio $\boldsymbol{H/L}$ between $\boldsymbol{z/L}$ ratios from 0 to 3 for a high roughness length $\boldsymbol{z_0 = 0,5m}$ (dashed lines) and a forest ($\boldsymbol{h_t = 10m}$, low forest density), i.e., a very sparse forest (solid lines). Results are based on Meteodyn WT.

5.2.3.1 Forest height

Figure 10.11, Figure 10.12, Figure 5.38 and Figure 5.39 show the impact of different tree heights on the total lidar error and the two distinct parts. The results are shown for an H/L ratio of 0.2 and 0.3, to illustrate that the influence of the forest on the lidar error is different, depending on terrain inclination.

The total lidar error ε for a H/L ratio of 0.2 shows a significant dependence on tree height (Figure 10.11). Highest lidar errors are found for small tree heights of 10 m and. When increasing the tree height to 20 m and 30 m, ε decreases for all z/L ratios but the largest. Although maximum values for the lidar error can still be seen around z/L ratios of 0.6, the shape of the curves is not entirely comparable with that from the potential flow model as a reference.

Figure 10.12 shows the lidar error parts ε_c and ε_s for the same H/L ratio. The speed-up induced part of the error (right-hand side of the plot) is small in this case and does not exceed -0.8 %. However, it is interesting to note that ε_s reaches a minimum around 0 % for tree heights of 20 m and 30 m for a z/L ratio of 1.5, while it stays at -0.4 % for the smallest trees of 10 m. Maximum ε_s occur aroung z/L ratios of 0.6.

When looking at the flow curvature part of the lidar error (left-hand side of the plot), a clear dependence on tree height is found. Increasing the tree height results in decreased ε_c, which is particularly true for z/L ratios between 0.3 and 1.0. There is almost no influence of the tree height for z/L ratios of 0.2 and 3.0. The shape of the error curve is comparable to that from the reference for a tree height of 10 m, showing a clear maximum at z/L ratio of 0.6. For larger tree height, the shape of the curve changes.

For the larger H/L ratio of 0.3, the total lidar error ε, as shown in Figure 5.38, is also dependent on tree height. However, when comparing it to the results in Figure 10.11 for a lower H/L ratio of 0.2, it can be seen that the shape of the curves is different. There is still a general tendency towards smaller lidar errors for increasing tree heights, especially when increasing it from 10 m to 20 m or 30 m. The results for 20 m and 30 m are very similar for z/L ratios of 0.3 to 1.0. A significant difference for these tree heights can only be seen at a z/L ratio of 1.5.

Regarding the flow curvature induced part of the error ε_c for the H/L ratio of 0.3, which is shown in Figure 5.38 (left), also a clear dependence on tree height can be seen for all z/L ratios but 3.0. The largest errors can be found for a tree height of 10 m, reaching up to a maximum value of -5.2 % at a z/L of 0.3. The maximum error is decreased to -3.8 % for a tree height of 30 m. However, the difference in ε_c between the results for 20 and 30 m, high trees is smaller than for the H/L of 0.2 cases.

The influence of tree height on speed-up induced lidar errors ε_s is also different from the H/L of 0.2 cases. The results in Figure 5.38 (right) show that the strongest speed-ups occur for small tree heights for z/L ratios 1.0 and 1.5. For z/L ratios of 0.3, 0.6 and 0.75, this behavior is reversed and strongest speed-ups are observed for tree heights of 30 m.

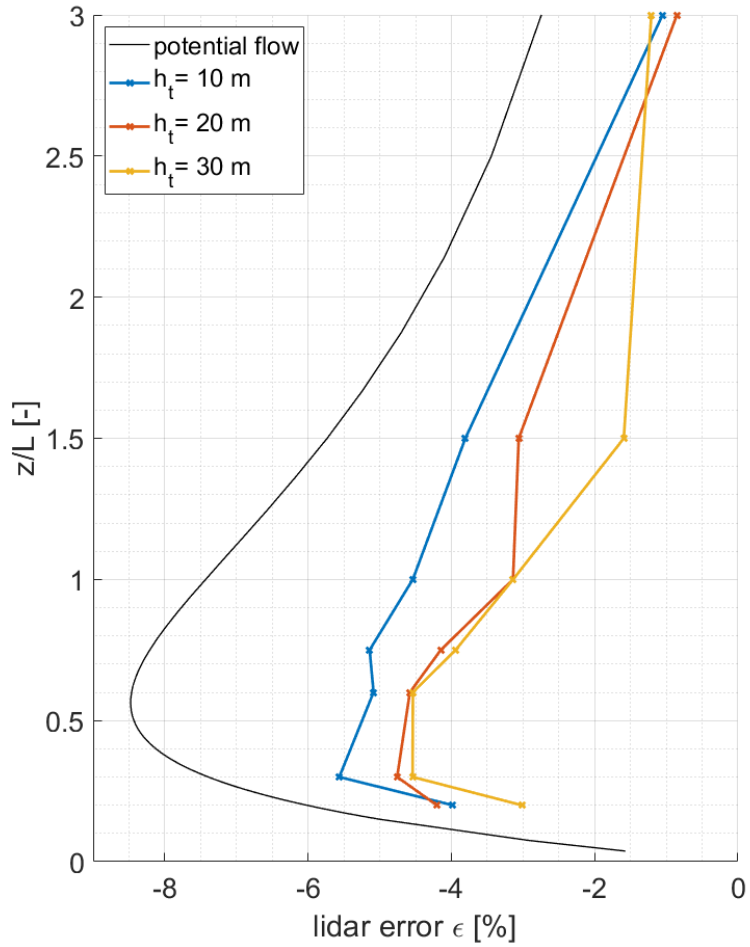

Figure 5.38: Lidar error $\boldsymbol{\varepsilon}$ in dependence of tree heights $\boldsymbol{h_t}$ between $\boldsymbol{z/L}$ ratios from 0 to 3. Results are based on Meteodyn WT (colored) and the potential flow model (black) for an $\boldsymbol{H/L}$ ratio of 0.3.

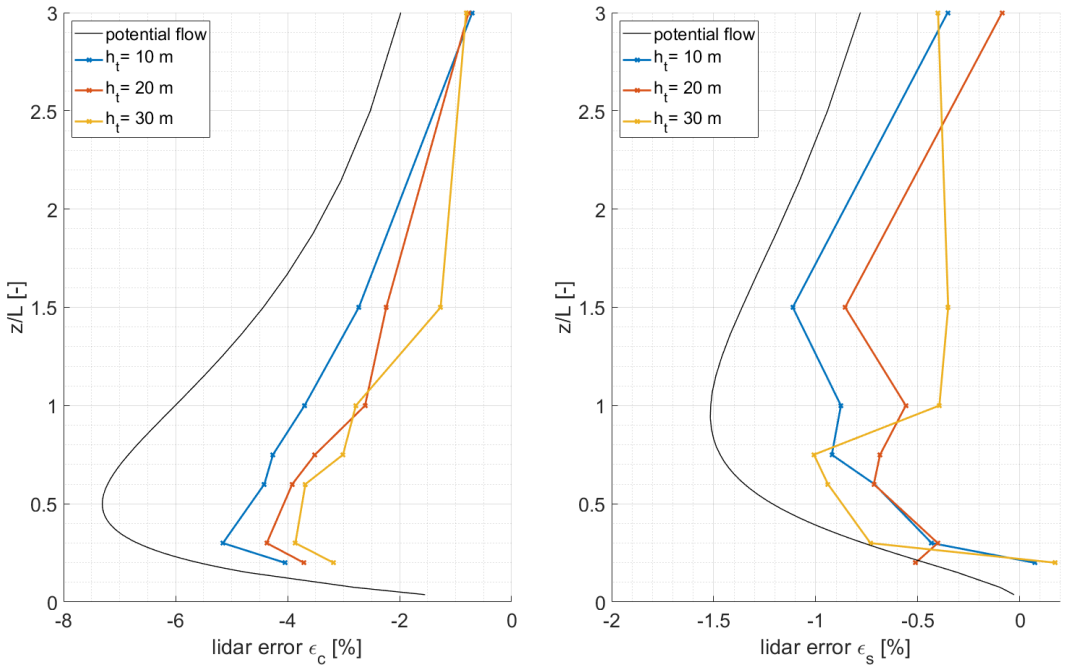

Figure 5.39: Lidar error $\boldsymbol{\varepsilon_c}$ (left) and $\boldsymbol{\varepsilon_s}$ (right) in dependence of tree heights $\boldsymbol{h_t}$ between $\boldsymbol{z/L}$ ratios from 0 to 3. Results are based on Meteodyn WT (colored) and the potential flow model (black) for an $\boldsymbol{H/L}$ ratio of 0.3.

5.2.3.2 Forest density

To analyze the influence of forest density on the lidar error results from Meteodyn WT for an H/L ratio of 0.3 are exemplarily shown in Figure 5.40 and Figure 5.41. The results cover the three possible parameter variations “low,” “medium” and “high” forest density for a forest with 30 m tree height. A significant tree height has been chosen in order to increase the influence of forest density on the results.

However, for many z/L ratios, there is only a small dependence on forest density. Particularly a change from medium to high forest density has not much impact on the results for the lidar error ε. The largest differences between the results for the three different forest densities can be observed at a z/L ratio of 1.0. Here the maximum lidar error of about -4 % occurs for low forest density and the minimum of -2.2 % for high forest density.

Splitting up the lidar error into ε_c and ε_s in Figure 5.41 shows that the differences in ε_c are small and the shape of the error curve is similar for all three forest densities. Differences in the shape of the curve for the total lidar error ε are mainly caused by the influence of ε_s. As illustrated in Figure 5.41 (right), the shape of the error curves differs for the different forest densities, although the absolute values of ε_s are small. However, the observed effects are strong enough to impact the total lidar error, as the differences in ε_c are relatively small.

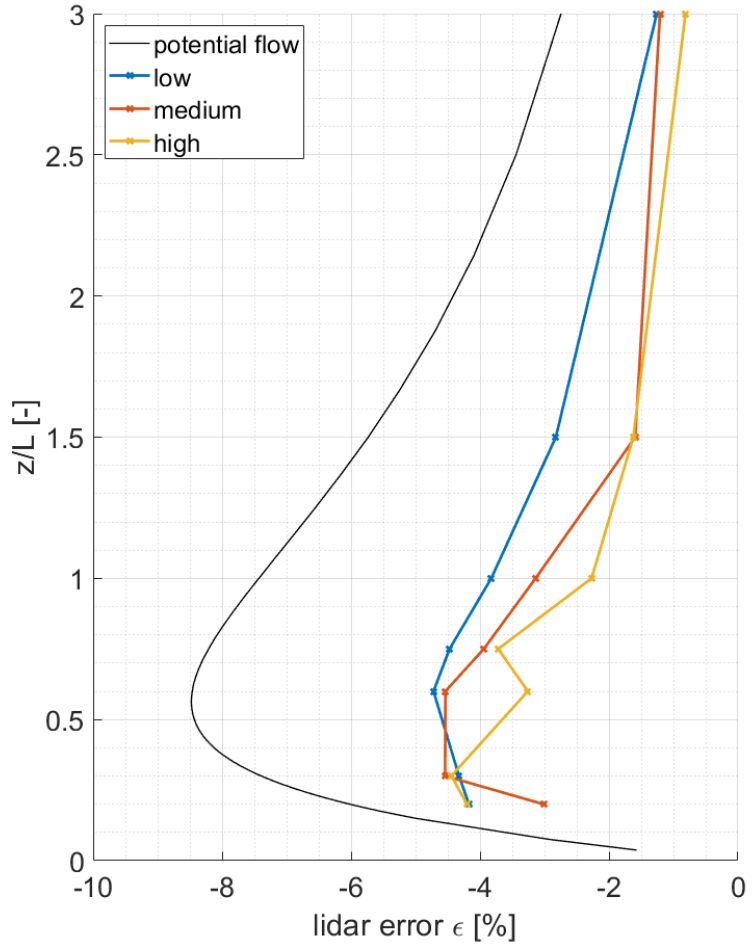

Figure 5.40: Lidar error $\boldsymbol{\varepsilon}$ in dependence of forest density between $\boldsymbol{z/L}$ ratios from 0 to 3. Results are based on Meteodyn WT (colored) and the potential flow model (black) for an $\boldsymbol{H/L}$ ratio of 0.3.

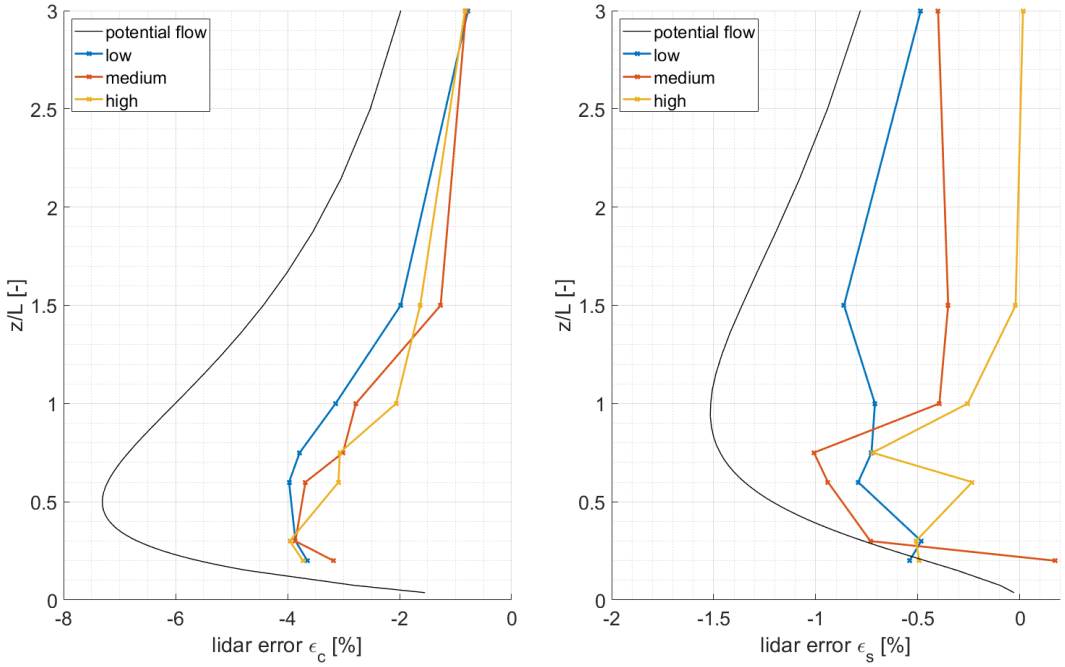

Figure 5.41: Lidar error $\boldsymbol{\varepsilon_c}$ (left) and $\boldsymbol{\varepsilon_s}$ (right) in dependence of forest density between $\boldsymbol{z/L}$ ratios from 0 to 3. Results are based on Meteodyn WT (colored) and the potential flow model (black) for an $\boldsymbol{H/L}$ ratio of 0.3.

5.2.4 Atmospheric stability

In order to analyze the influence of different atmospheric stability conditions, the stability class in Meteodyn WT has been modified for a part of the simulation cases. The influence of the stability parameter is most severe for medium to large H/L ratios. Additionally, the computational effort to create results for a wide range of stability cases for individual hill geometries and parameter settings is large. Therefore, this part of the study has been limited to an H/L ratio of 0.3 and to the cases of low roughness, high roughness and medium dense forest with a tree height of 20 m.

The results presented in Figure 5.42 to Figure 5.47 sum-up these results for the four chosen stability classes very unstable, neutral, stable and strongly stable. These four out of ten possible stability classes in Meteodyn WT cover the whole possible range. Calculations have been carried out for all stability classes in-between those four, but the effects found are systematic and it is, therefore, sufficient to show only this excerpt.

Starting with the low roughness case of $z_0 = 0{,}005m$, Figure 5.42 shows the results for the total lidar error ε for an H/L ratio of 0.3 and the four different stability classes. First, it can be seen that ε decreases from hthe ighest values for very unstable cases to lower values for strongly stable cases. This influence differs for different z/L ratios. There is only a small dependence of the lidar error for z/L ratios of 0.2 and 0.3, as well as 3.0. The difference between the results increases for medium z/L ratios between 0.6 and 1.0. In addition, the location of the maximum lidar error is dependent on atmospheric stability. While for unstable cases, the maximum ε is found at a z/L ratio of 0.75, the value decreases 0.3 for strongly stable cases. The most considerable difference between the results can be found at the maximum point for very unstable cases with a ε of about 8 % compared to only 5.25 % for strongly stable cases. It is also interesting to note that the maximum point for unstable cases is very close to the reference line from the potential flow model.

Looking at the individual contribution of ε_c and ε_s to the total lidar error for different atmospheric stabilities (Figure 5.43) shows that, for the low roughness case, the flow curvature induced effects dominate. There is a systematic decrease in lidar error ε_c when coming from very unstable cases to neutral, stable and strongly stable cases for almost all z/L ratios. The differences are largest between z/L ratios of 0.6 to 1.5. The location of maximum error changes with atmospheric stability. While for unstable cases a clear maximum of ε_c of -6.6 % can be found at a z/L of 0.75, the maximum for strongly stable cases is -5 % at a z/L of 0.3. For very low z/L of 0.2 and the highest value of 3.0, the dependence of ε_c on atmospheric stability is relatively small.

When looking at the speed-up induced part of the lidar error ε_s in Figure 5.43 (right), it can be noted that the largest speed-ups can be found for very unstable and neutral cases. The lidar error ε_s then significantly decreases for stable and strongly stable cases, which is particularly true for z/L ratios between 0.6 and 1.5.

Looking at the high roughness cases with a z_0 of 0.5 m (Figure 5.44), the tendency of the influence of atmospheric stability is consistent with what has already been described for the low roughness length. Largest lidar errors ε can be found for very unstable cases. Then, the lidar error is systematically reduced for neutral, stable and strongly stable cases. This effect is significant for z/L ratios between 0.6 and 1.5. However, there is an exception for unstable cases with z/L ratios below 0.6. Here the shape of the error curve is different and significantly lower lidar errors are found, which are even smaller than for the stable cases at these z/L ratios.

For the high roughness cases, the maximum lidar error can be found at a z/L ratio of 0.6 for very unstable cases and at 0.3 for strongly stable cases. The maximum lidar error reaches up to -6.25 % for very unstable and about -2.5 % for strongly stable atmospheric conditions.

The speed-up induced part of the lidar error ε_s for the high roughness case is also sensitive to atmospheric stability. In Figure 5.45 (right), it can be seen that especially for z/L ratios between 1.0 and 3.0, the errors significantly decrease with increased atmospheric stability. While ε_s is close to zero for strongly stable cases, it reaches up to -1.3 % for very unstable cases.

The atmospheric stability has also been varied for a forested case with 30 m tree height and medium forest density. The results for the total lidar error are shown in Figure 5.46. Again, a clear tendency of reduced lidar errors for increasing atmospheric stability can be seen. Largest lidar errors occur for very unstable stability conditions, with a clear maximum at a z/L ratio of 0.6 and a lidar error ε of about -6 %. Coming to neutral, stable and strongly stable cases, the maximum is again shifted towards lower z/L ratios. The maximum error for strongly stable cases is -2.3 % and can be found at a z/L ratio of 0.3. The shape of all error curves is different from that for low and high roughness cases. Below and above the maximum, there is a relatively sharp decrease in lidar errors, which pronounces the maximum points. For the largest z/L ratio of 3.0, the influence of atmospheric stability is relatively small.

Figure 5.47 shown the lidar error split up into its parts ε_c and ε_s for the forested case. The shape and tendency for ε_c to that for the total error, although maximum errors can be found around a z/L ratio of 0.3 for all stability classes.

For ε_s, also a clear tendency of reduced errors for increased atmospheric stability can be seen in Figure 5.47 (right). Most substantial speed-up induced lidar errors can be found for unstable cases at z/L ratios of 0.6 and 0.75.

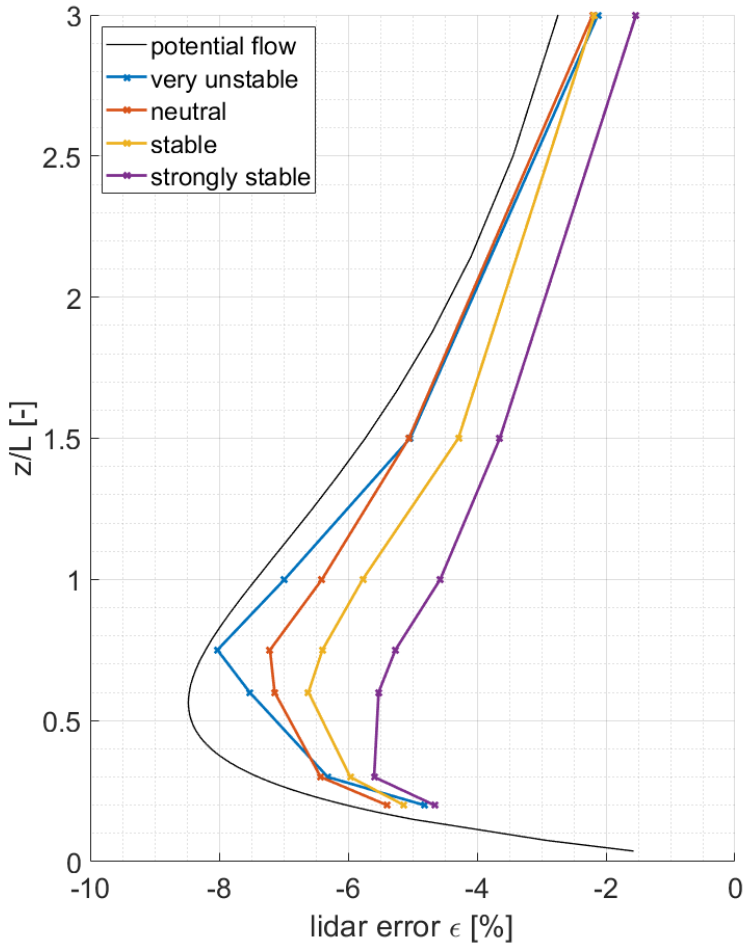

Figure 5.42: Lidar error $\boldsymbol{\varepsilon}$ in dependence of atmospheric stability between $\boldsymbol{z/L}$ ratios from 0 to 3. Results are based on Meteodyn WT (colored) and the potential flow model (black) for an $\boldsymbol{H/L}$ ratio of 0.3 for a low roughness length $\boldsymbol{z_0}$ of 0.005m.

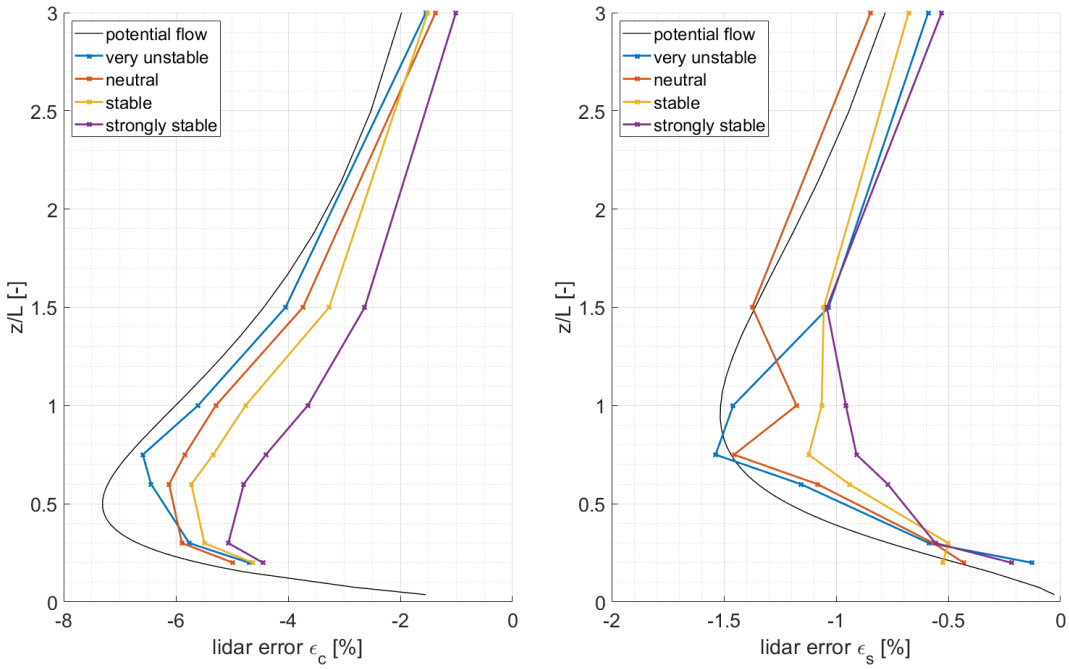

Figure 5.43: Lidar error $\boldsymbol{\varepsilon_c}$ (left) and $\boldsymbol{\varepsilon_s}$ (right) in dependence of atmospheric stability between $\boldsymbol{z/L}$ ratios from 0 to 3. Results are based on Meteodyn WT (colored) and the potential flow model (black) for an $\boldsymbol{H/L}$ ratio of 0.3 for a low roughness length $\boldsymbol{z_0}$ of 0.005m.

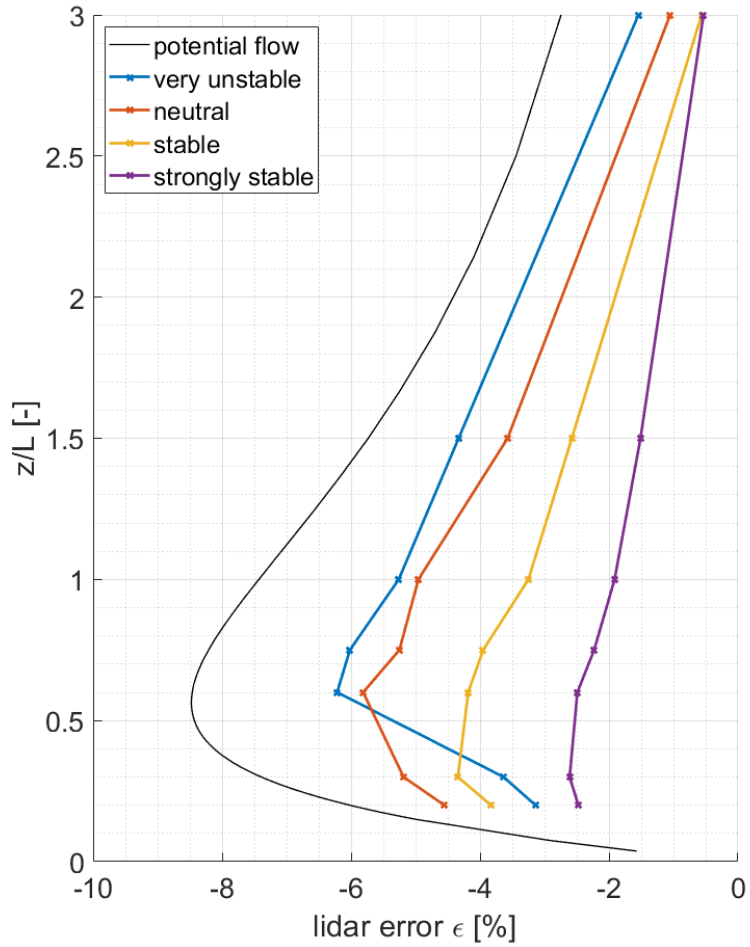

Figure 5.44: Lidar error $\boldsymbol{\epsilon}$ in dependence of atmospheric stability between $\boldsymbol{z/L}$ ratios from 0 to 3. Results are based on Meteodyn WT (colored) and the potential flow model (black) for an $\boldsymbol{H/L}$ ratio of 0.3 for a high roughness length $\boldsymbol{z_0}$ of 0.5m.

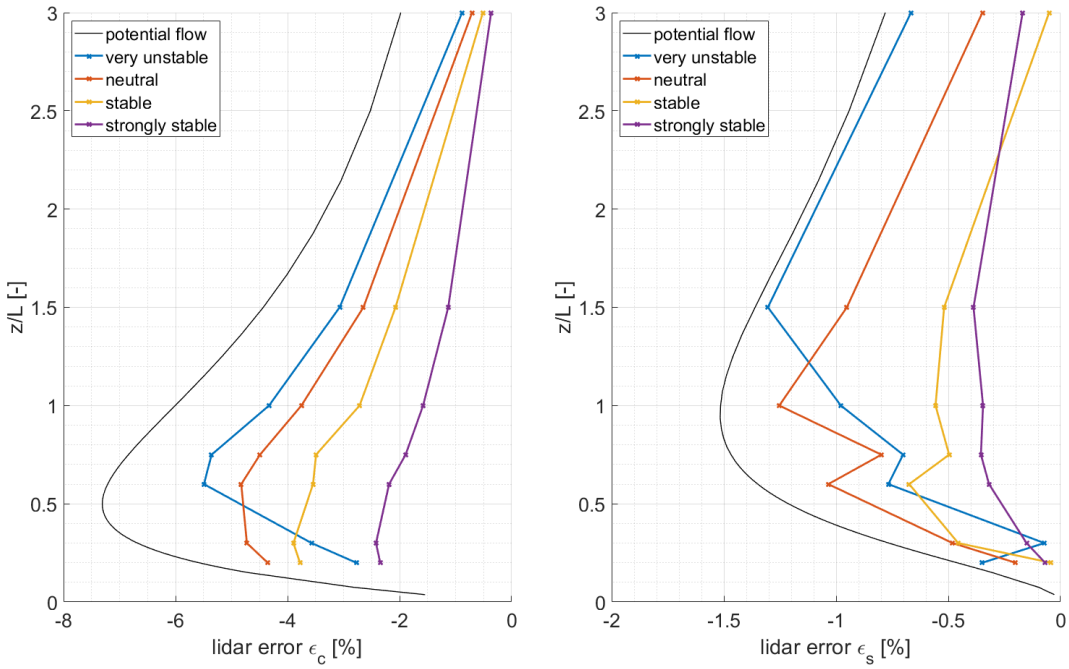

Figure 5.45: Lidar error $\boldsymbol{\epsilon_c}$ (left) and $\boldsymbol{\epsilon_s}$ (right) in dependence of atmospheric stability between $\boldsymbol{z/L}$ ratios from 0 to 3. Results are based on Meteodyn WT (colored) and the potential flow model (black) for an $\boldsymbol{H/L}$ ratio of 0.3 for a high roughness length $\boldsymbol{z_0}$ of 0.5m.

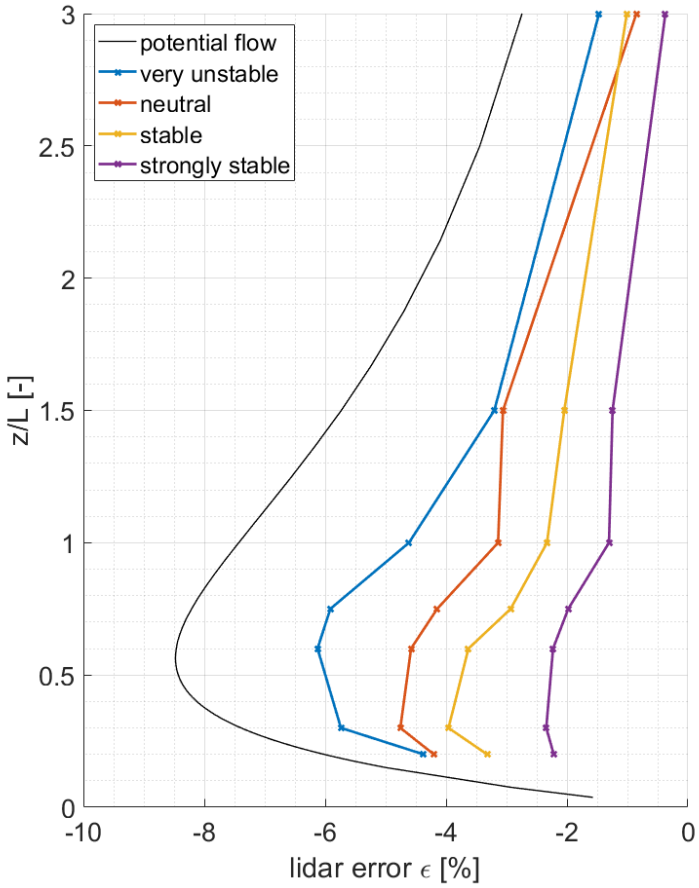

Figure 5.46: Lidar error $\boldsymbol{\varepsilon}$ in dependence of atmospheric stability between $\boldsymbol{z/L}$ ratios from 0 to 3. Results are based on Meteodyn WT (colored) and the potential flow model (black) for an $\boldsymbol{H/L}$ ratio of 0.3 for the forested case with a tree height $\boldsymbol{h_t = 20m}$ and a medium forest density.

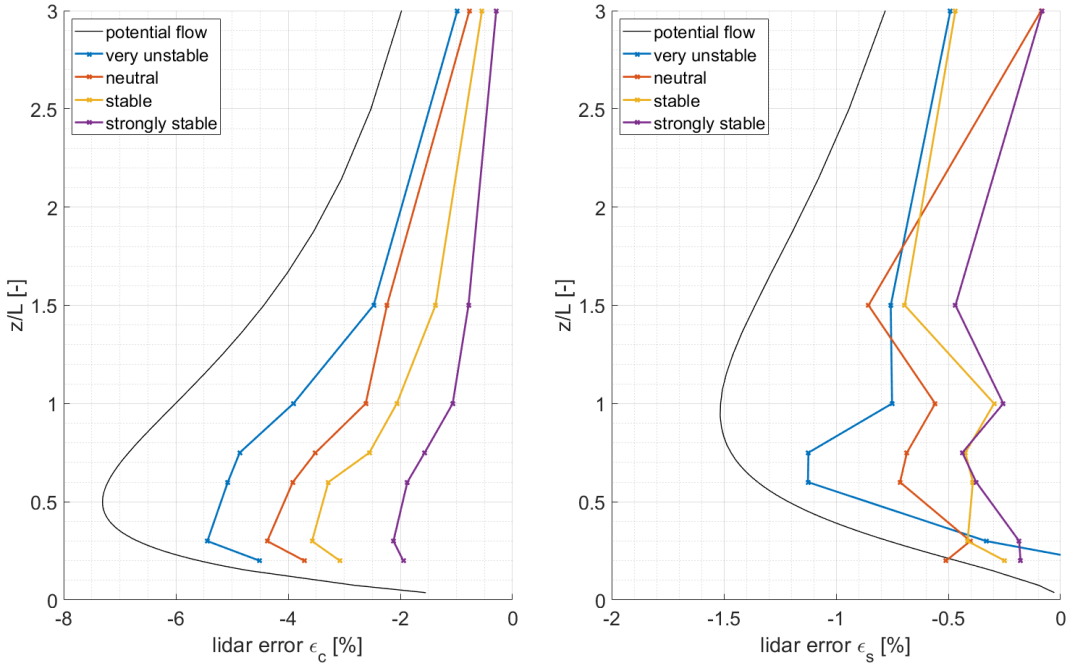

Figure 5.47: Lidar error $\boldsymbol{\varepsilon_c}$ (left) and $\boldsymbol{\varepsilon_s}$ (right) in dependence of atmospheric stability between $\boldsymbol{z/L}$ ratios from 0 to 3. Results are based on Meteodyn WT (colored) and the potential flow model (black) for an $\boldsymbol{H/L}$ ratio of 0.3 for the forested case with a tree height $\boldsymbol{h_t = 20m}$ and a medium forest density.

5.2.5 Measurement height

The influence of measurement height, respectively, the height above ground z at the location of the measurement device, is already part of all previously presented figures in chapter 0. For a constant L, the dimensionless measure z/L on the y-axis illustrates the influence of increasing the measurement height on the lidar error. For example, for a hill half-width L of 250 m, the range of z/L from 0.2 to 3.0 covers measurement heights from 50 m to 750 m. The influence of measurement height on the lidar error for a particular hill geometry can, therefore, be analyzed for each model and shown parameterization in this chapter.

However, due to limitations in setting up the model domain, it was not possible to follow this approach of a fixed L and increasing z values for the required parameter space (compare chapter 4.5) in practice. Thus, the value of L was changed for the different H/L ratios in order to cover z/L values from 0.2 to 3.0 for WEng and Meteodyn WT. This, however, assumes the validity of creating the dimensionless measure z/L and use it for both, the influence of diverse L values of different hill geometries and the influence of increasing z on the lidar error.

All results presented so far have been generated for a fixed z of 150 m as this is a typical measurement height in wind energy applications and was appropriate to be used in all model setups. The purpose of the following chapter is to validate the above-explained assumption about the applicability of z/L for the potential flow model as a reference and different parameterizations of the flow model Meteodyn WT. For this, results for ε, ε_c and ε_s have been calculated for four different measurement heights (50, 100, 150 and 200 m). As the same model data has been used for this, the z/L range is shifted, but still covers the most relevant ranges (compare Table 5). The range of the y-axis has been increased to 4.0 in order to cover all results for a measurement height of 200 m.

Table 5: Range of z/L ratios for different values of z.

Measurement height	Minimum z/L	Maximum z/L
50	0.067	1.0
100	0.133	2.0
150	0.200	3.0
200	0.267	4.0

Because the potential flow model is inviscid and, therefore, fully symmetric, the results for different z are equivalent. In the following figures, a single line is, therefore sufficient to represent the reference model.

In Meteodyn WT, friction due to roughness, forest and turbulence results in asymmetric flow fields that cause differences between the four analyzed z values. The following figures show how far the non-dimensional display of the results can be kept up in this case.

Starting with the low roughness case ($z_0 = 0{,}005m$), Figure 5.48 shows the results for the total lidar error ε for the four different measurement heights z. In this case ,the results for all four are very close together, only showing minor deviations around z/L of 0.4 to 0.8.

When separating the two effects of flow curvature and speed-up into ε_c and ε_s (Figure 5.49, left and right plot), there is still a lot of consistency in the non-dimensional plots for different measurement heights. This is in particular true for ε_c, while the small values of ε_s show a bit of sensitivity to the measurement height. However, as these values are very small in magnitude, this sensitivity cannot be seen as significant.

For the high roughness cases with a z_0 of 0.5 m show that the shape and magnitude of the lidar errors is mostly independent of the measurement height z that is used for calculation. There are only small and unsystematic differences between the four chosen measurement heights. When separating the total lidar errors into its parts ε_c and ε_s, most results are also very close together. In particular, for the flow curvature induced part of the error ε_c the shape of the curves is nearly identical. The results are given in Figure 10.7 and Figure 10.8 in Appendix 10.3.

Also, for the forested case, deviations are relatively small for the total lidar error ε. However, for the flow curvature induced part of the error, the shape and magnitude of the results for the lowest measurement height of 50 m is significantly different from the other results. A reason for this might be that a measurement height of 50 m is already very close to the forest height of 20 m, which has a considerable impact on the flow field close to the ground (Figure 10.9 and Figure 10.10 in Appendix 10.3.).

Summing up these results, it can be concluded that in most cases, the non-dimensional approach is applicable and results from a fixed z can be transferred to other values as well.

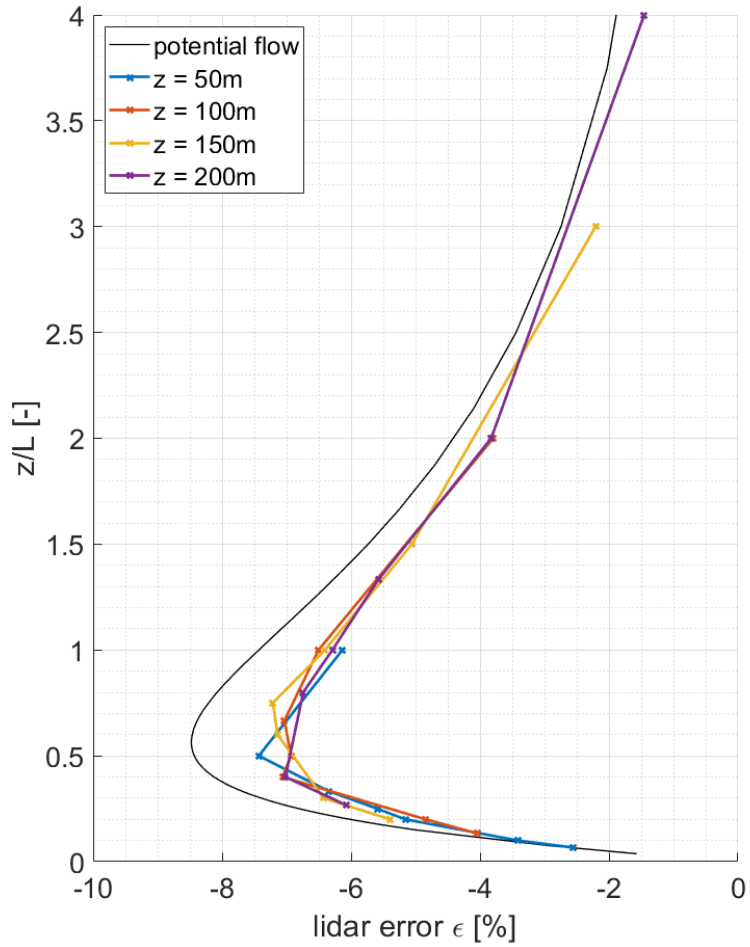

Figure 5.48: Lidar error $\boldsymbol{\varepsilon}$ in dependence of the measurement height z that is used to calculate the $\boldsymbol{z/L}$ ratio. Results are based on Meteodyn WT (colored) and the potential flow model (black) for an $\boldsymbol{H/L}$ ratio of 0.3 for a low roughness length $\boldsymbol{z_0}$ of 0.005m.

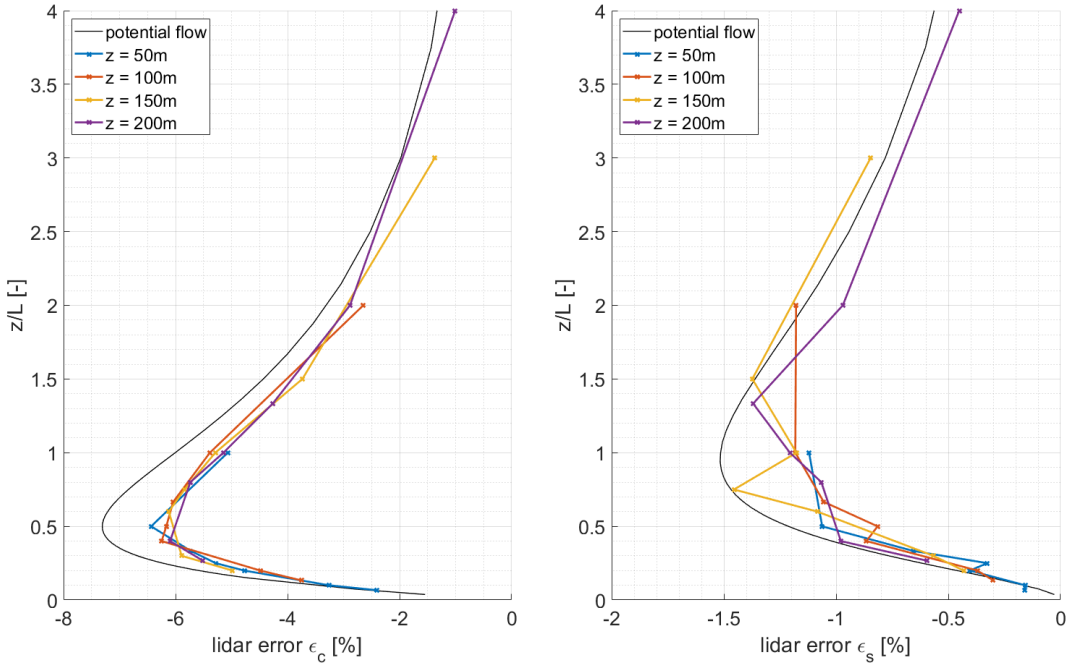

Figure 5.49: Lidar error $\boldsymbol{\varepsilon_c}$ (left) and $\boldsymbol{\varepsilon_s}$ (right) in dependence of the measurement height z that is used to calculate the $\boldsymbol{z/L}$ ratio. Results are based on Meteodyn WT (colored) and the potential flow model (black) for an $\boldsymbol{H/L}$ ratio of 0.3 for a low roughness length $\boldsymbol{z_0}$ of 0.005m.

5.2.6 Half-cone opening angle

The following chapter is illustrating the influence of changing the half-cone opening angle φ of the lidar measurement geometry on ε. Again, to separate and analyze the individual contribution of φ, the lidar error is separated into ε_c and ε_s. Results are first presented for the potential flow model as a reference. Then, exemplary results based on Meteodyn WT are shown, which allow for a determination of the influence of φ in the presence of roughness and forest in neutral atmospheric conditions. The half-cone angle has been changed from 30° to 20° and 10°.

Figure 5.50 shows the lidar error ε for the four H/L ratios and the three different half-cone opening angles φ. When decreasing the half-cone angle, there is also a slight decrease in the lidar error. This is particularly true for z/L ratios between 0.3 and 1.0, which is in the range of the maximum lidar error. For larger z/L ratios, the influence of φ on the lidar error decreases. For small z/L, the influence is also only marginal.

Figure 5.51, which shows the lidar error split up into ε_c and ε_s, enables to retrace of the individual contribution of flow curvature and speed-up effects on the total lidar error ε. It becomes obvious that decreasing the half-cone opening angle significantly decreases ε_s (right plot). While ε_s reaches up to -2 % for an H/L ratio of 0.4 for a φ of 30°, it falls below -0.25 % for all H/L ratios for an angle of 10°.

Decreasing φ has a contrary influence on ε_c, which is shown in Figure 5.51, left plot. While there is almost no influence for the lowest two z/L ratios, there is an increase of ε_c for half-cone angles of 20° and 10° when compared to the original 30°. This difference is largest for z/L above 0.5 and persists up to z/L of 3.

The superposition of the two opposing effects results in the total effect on ε as it is shown in Figure 5.50.

When looking at the influence of the half-cone opening angle on the results based on flow simulations with Meteodyn WT in Figure 10.13, Figure 5.52 and Figure 10.14, it becomes obvious that the interdependency with the model parameterization is complex.

For the low roughness case and a H/L ratio of 0.3, it can be seen that the lidar error ε can be reduced for all z/L ratios when the half-cone opening angle is decreased to 10°. The decrease is largest for a z/L ratio of 1.0, where the difference is about 1 %. There are only small differences between a φ of 30° and one of 20°. Significant differences only occur for a z/L of 0.6.

However, when looking at the results for a high roughness length in Figure 5.52, the impact of a smaller half-cone opening angle is different. There is only marginal influence between z/L ratios of 0.6 and 1.5 and for the largest ratio, ε is increasing in comparison to 20 and 30° angles. For the lowest ratios of 0.2, 0.3 on the other hand, there is a significant decrease for a small φ.

Changing the half-cone opening angle in the forest case with medium dense forest and a tree height of 20 m (Figure 10.14), the difference between the three lines is very small and there is no systematic influence. Only for the largest z/L ratio of 3.0, the lidar error is decreased by more than 1 %.

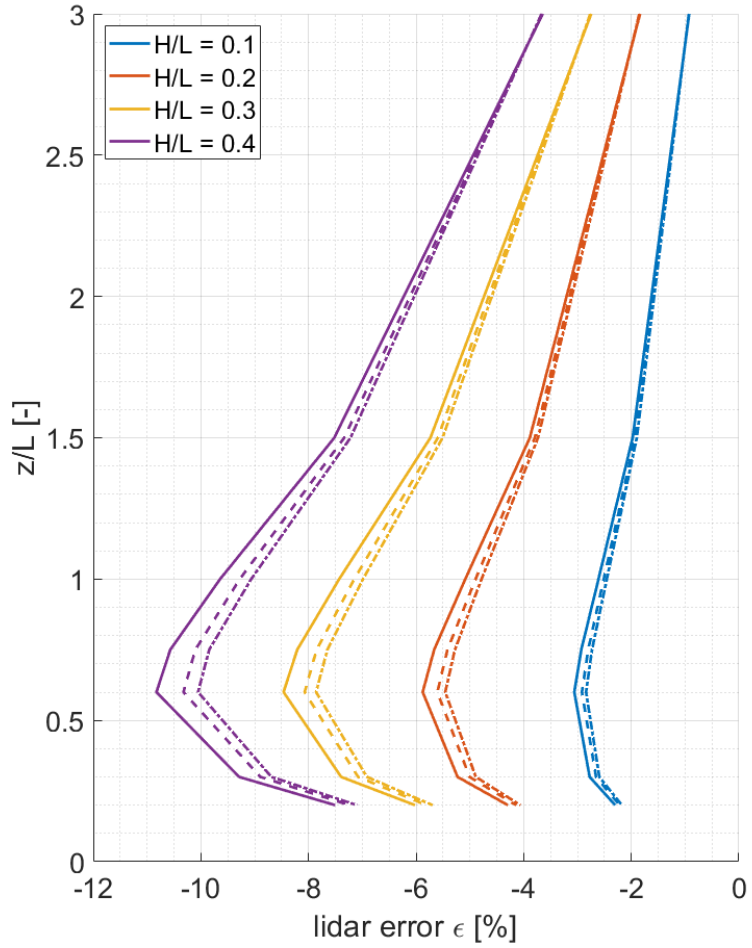

Figure 5.50: Lidar error $\boldsymbol{\varepsilon}$ in dependence of the $\boldsymbol{H/L}$ ratio for the half-cone opening angles $\boldsymbol{\varphi}$ of 30° (solid lines), 20° (dashed lines) and 10° (dot-dashed lines) between $\boldsymbol{z/L}$ ratios from 0 to 3. Results are based on the potential flow model.

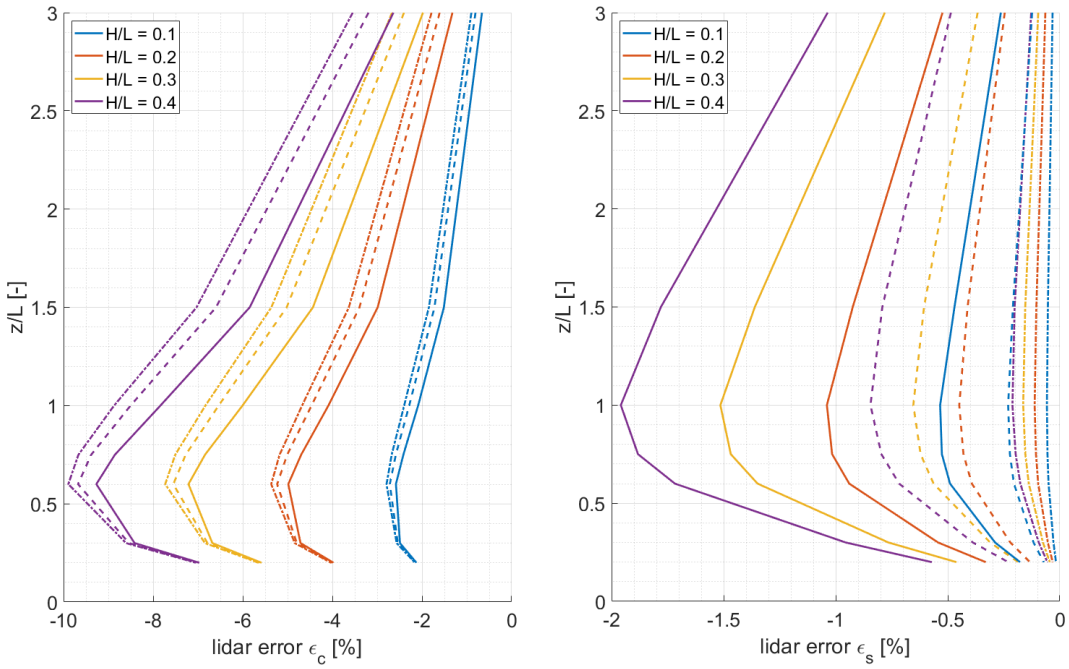

Figure 5.51: Lidar error $\boldsymbol{\varepsilon_c}$ (left) and $\boldsymbol{\varepsilon_s}$ (right) in dependence of the $\boldsymbol{H/L}$ ratio for the half-cone opening angles $\boldsymbol{\varphi}$ of 30° (solid lines), 20° (dashed lines) and 10° (dot-dashed lines) between $\boldsymbol{z/L}$ ratios from 0 to 3. Results are based on the potential flow model.

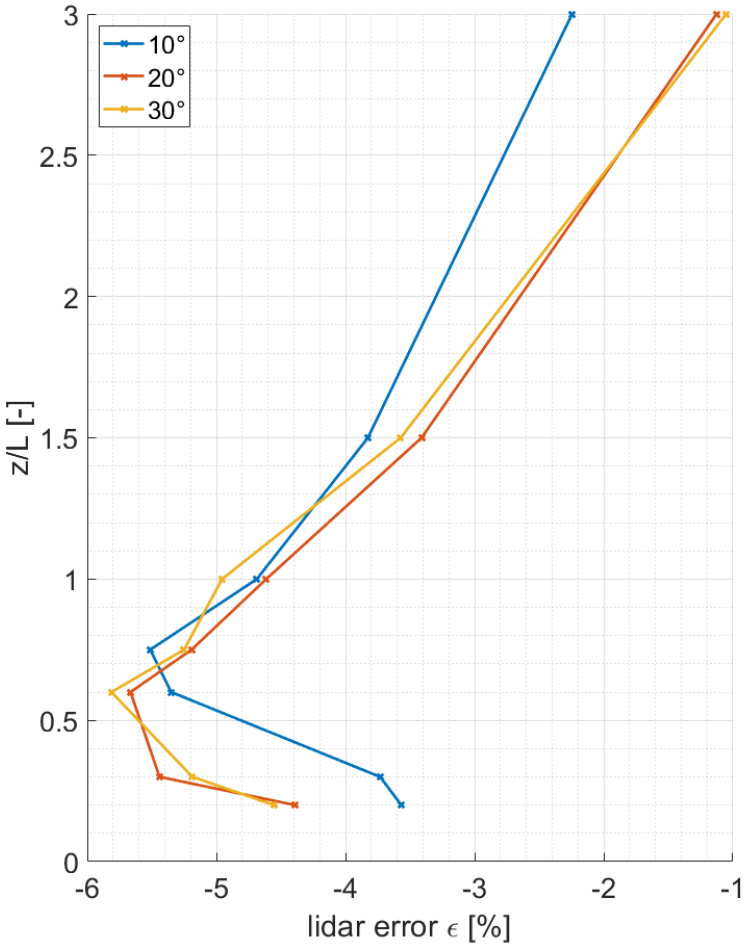

Figure 5.52: Lidar error $\boldsymbol{\varepsilon}$ in dependence of the half-cone opening angles between $\boldsymbol{z/L}$ ratios from 0 to 3. Results are based on Meteodyn WT for a high roughness length $\boldsymbol{z_0}$ of 0.5 m and a $\boldsymbol{H/L}$ ratio of 0.3.

6 Evaluation with real-world data

The focus of the present thesis is the model-based parameter study that is presented in chapter 5. However, in order to connect the findings to real-world experiments, the following chapter presents results from a measurement campaign that compares lidar data to data from mast-based cup anemometry.

The presented measurement site is equipped with a 200 m high wind measurement mast. Several months of lidar wind measurements have been carried out at that site, in order to create a dataset that enables a comparison of both methods. Details about the measurement site and the used measuring devices are presented in chapter 6.1. That subchapter also provides a basic overview of the available measurement data and its quality check. Basic statistics are given in this chapter in order to validate the usability of the data set.

Due to the context of this thesis, an alternative evaluation approach has been used that aims at integrating the evaluation results into the non-dimensional presentation of the findings of the parameter study. For this, the actual terrain of the measurement site is fitted to Gaussian hill shapes for several wind directions. This approach is described in chapter 6.2.

The results of the evaluation, i.e., the comparison of real-world measurement data to the findings from the model-based parameter study is given in chapter 6.3. The aim of this subchapter is to evaluate the applicability of the generic findings of this thesis to real-world sites. Results of a comparison of mast and lidar data have been analyzed in Klaas et al. (2015). The individual contributions of the authors to that paper are given in Appendix 10.4, mainly focusing on the contributions of the author of this thesis. However, in this thesis, the presentation of the results is extended. Additionally, a different approach is chosen, which includes them to the overall structure of this thesis.

The evaluation chapter concludes with a presentation of a model-based lidar error estimation with the CFD RANS model Meteodyn WT, which uses the full terrain data of the measurement site. A parameter-variation is presented, to underline the importance of using an appropriate model parameterization to accurately estimate the lidar error.

6.1 Measurement campaign

The following sub-chapter provides details of the measurement campaign that has been carried out at Fraunhofer IEE's complex terrain test site at Rödeser Berg in central Germany (6.1.1). The data that has been collected during this measurement campaign is briefly described in chapter 6.1.2.

6.1.1 Measurement site and equipment

Within the project "Utilization of Inland Wind Power," funded by the BMWi, the Fraunhofer IEE erected a 200 m high wind measurement mast. As the primary purpose of the project was the investigation of wind characteristics at complex and forest sites, the mast was placed at the "Rödeser Berg," which is a hill in Northern Hesse, close to the city of Kassel.

The measurement site is described, e.g., in Klaas et al. (2015), from which most of the following information are taken. The geo-coordinates of the measurement mast are

51° 21’ 46’’ N 9° 11’ 43’’ E. The lidar was located in direct proximity of the mast (about 4 m of distance to the mast structure). While the majority of the hill is forested, a small clearing was chosen for the measurement site. With regards to the expected main wind direction (south-south-west), the measurement site is located at the top of the hill. Perpendicular to this direction there are several more crests, some of which surmounting the measurement site.

A map of the orography is given in Figure 6.2, representing the altitudes in an area of approximately 6 by 6 km² around the measurement site. The measurement mast is located at an altitude of 390 m. In the southwestern direction, the terrain falls off to about 230 m to a small creek before a plain at 270 to 290 m is reached. Also, in the northeastern direction, the terrain declines to about 270 m in altitude. Hill slopes close to the mast are reaching up to 10-15°, particularly for the 210-270° direction sectors (west to south-south-west) and the 60-90° sectors (north-east to east). The ridge of the Rödeser Berg extends perpendicular to these directions. In its wider surroundings, the orography is characterized by diverse hills of comparable heights.

The satellite image shown in Figure 6.3 illustrates the patchiness of the terrain. While the hills are mostly covered with forest, the valleys are dominated by agricultural use as well as villages and small cities. When looking at the closer surroundings of the measurement site, the clearing in which the mast is located can be recognized. Additionally, there are several more clearings in the forest that can be seen in the image. There is forest for about 2 km when coming from the main wind direction towards the measurement site. In the opposite direction, the forest already ends at about 600 m behind the mast.

Figure 6.1: 200 m wind measurement mast at the complex terrain test site “Rödeser Berg” of Fraunhofer IEE.

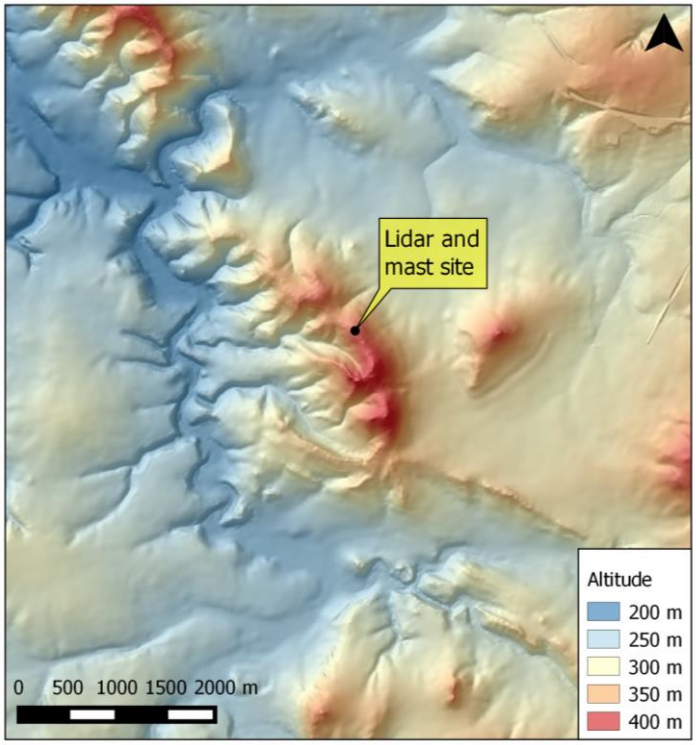

Figure 6.2: Orography of the measurement location (black dot, geographical data from HVBG (2010), modified by T. Klaas). LiDAR and mast measurements are located on top of a ridge that is oriented from north-west to south-east. Most significant inclinations are to the west and south-west (10-15°) (approx. main wind direction) and the north-east (10°). The illustration is a reprint from Klaas et al. (2015).

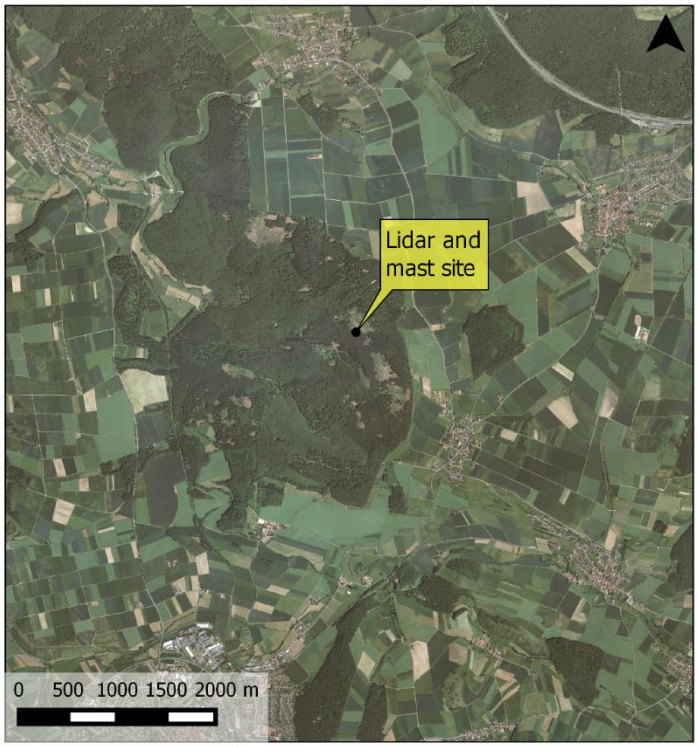

Figure 6.3: Satellite image of the location of the mast-LiDAR inter-comparison (black dot, geographical data from HVBG (2010), modified by T. Klaas). The measurements are located within a small clearing surrounded by forest. To the west and south-west, the ground is covered with mixed forest up to approx. 2 km distance. The image is a reprint from Klaas et al. (2015).

As can be seen in the photo in Figure 6.1, the measurement mast is constructed as a rectangular lattice tower. Due to its small side length of 1.05 m, it is supported by guy-wiring every 20 m. In accordance with IEC 61400-12-1 (International Standard IEC 61400-12-1:2017), the effects due to flow distortion at the sensors are kept at 0.5 %. This is achieved by a low solidity of 0.220 (below 100 m) and 0.204 (above 100 m) and boom lengths of 5.40 m. The cup anemometers are mounted at 1 m high pole above the boom ends. There are mostly two opposed booms at each measurement height, which are mounted around 140° and 320°perpendicular to the assumed main wind direction. The exact values of the booms are slightly deviating (compare Table 1 in Klaas et al. (2015)).

There are numerous wind and meteorological sensors mounted on the mast. Only a part of these is used for the lidar mast inter-comparison. At the chosen measurement heights of 80, 120, 160 and 200 m, there are mostly Thies Clima "first-class" advanced cup anemometers mounted, with the exception of a Thies Clima Ultrasonic Anemometer 3D, which is located at the 320° boom at 80 m height. All sensors but the top anemometer at 200 m height are mounted pairwise at opposed booms as described above. A detailed description of the sensors is given in Klaas et al. (2015). Wind directions were measured by the lidar and wind vanes mounted on the mast. Wind vanes at 132 m and 187 m height were used, chosen according to the minimum vertical distance to the actual wind speed sensor.

The Doppler lidar that is used for the data comparison is a Leosphere Wincube v1. The measurement geometry is given in Figure 3.2 and the basic equations for wind vector reconstruction are explained in chapter 3.1. The measurement device has a half-cone opening angle of about 28°, which is very close to 30° and, therefore, comparable to the values used in the parameter study. The lidar has been configured to measure at the same heights as the measurement mast. The direction offset of the first laser beam from the north was 10°.

6.1.2 Data basis

The measurement campaign took place from January 21st to June 30^{th,} 2012. Within this period, 10-minute mean values of wind speed and wind direction were acquired. The total number of possible data points for this period is 22,752. This number is reduced due to technical failures, data quality checks and data filters to assure that only high-quality data is used for the comparison.

The exact number of valid data points is given in Table 2 of Klaas et al. (2015). It varies with height and lies between about 7,000 and 10,000 10-minute mean values per height. Wind speeds below 4 m/s were rejected and periods of icing were filtered out. Additionally, the lidar data was filtered for a 10-minute data availability of 80 %, which means that in each time interval of 10 minutes, the share of available high-resolution measurements from the lidar must be at least 80 %. An algorithm was used to choose data from the one or the other sensor on each height, depending on wind direction. This allows the exclusion of mast shadowing effects on the wind sensors.

For the comparison of mast and lidar data for specific wind direction sectors, it is of utter importance that enough data pairs are available for the individual sector. The number of data points per sector is shown in Figure 6.4. For most sectors, there are then 50 data points available, which allows for the calculation of reasonable statistics.

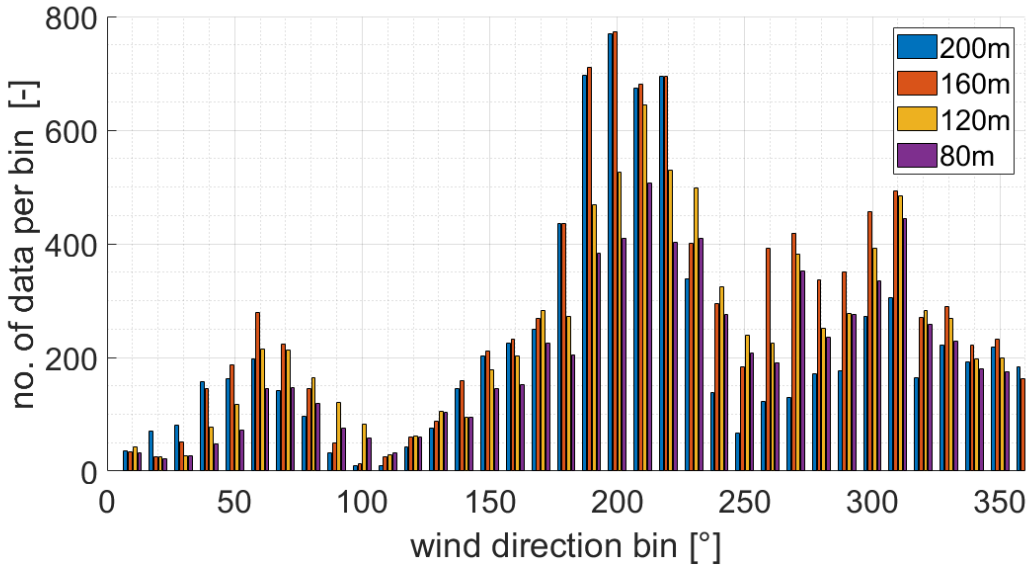

Figure 6.4: Number of data points per wind direction bin for different heights. The values indicate the number of 10 min periods for which both LiDAR and mast data were available after the filter criteria described in the text were applied. The figure is a modified reprint from Klaas et al. (2015).

6.2 Evaluation approach

The model-based parameter study presented in chapter 5 is limited to two-dimensional Gaussian hills. In order to enable a comparison to real-world cases, a relation between the Gaussian hills and the actual terrain must be found.

The approach chosen for the evaluation in this thesis is to approximate the terrain slices for chosen wind directions by Gaussian hill shapes. To find a reasonable approximation, the hill height H and the hill half-width L is found on the basis of a least-squares algorithm. However, the results for H and L are sensitive to the lengths of the terrain slice taken into account for the approximation. Under consideration of the distance of the lidar measurement points and the dimensions of the Gaussian hills that have been analyzed in this thesis, a reasonable terrain interval is in the order of +-500 m upwind and downwind of the lidar location. By this, it can also be assured that significant local terrain variations are approximated with sufficient quality.

Having attributed the different wind directions to distinct Gaussian hill shapes then allows calculating z/L ratios for the measurement heights from the measurement campaign. The associated measured lidar errors can then be compared to the results from the parameter study for different H/L ratios and the correspondent roughness or forest parameterizations.

Due to the complex terrain shape of the Rödeser Berg, not all wind direction sectors can be approximated by Gaussian hills. In order to ensure a reasonable evaluation, several sectors have been selected. Possible wind directions for the approximation are the intervals from 50 to 120 ° and the opposed sectors from 230 to 300°. However, the best approximation is possible for the sectors 70, 80, 110, 250, 260 and 290°. Exemplarily the fits for four wind direction sectors are shown in Figure 6.5.

The H, L, H/L and z/L values for the chosen wind direction sectors are given in Table 6.

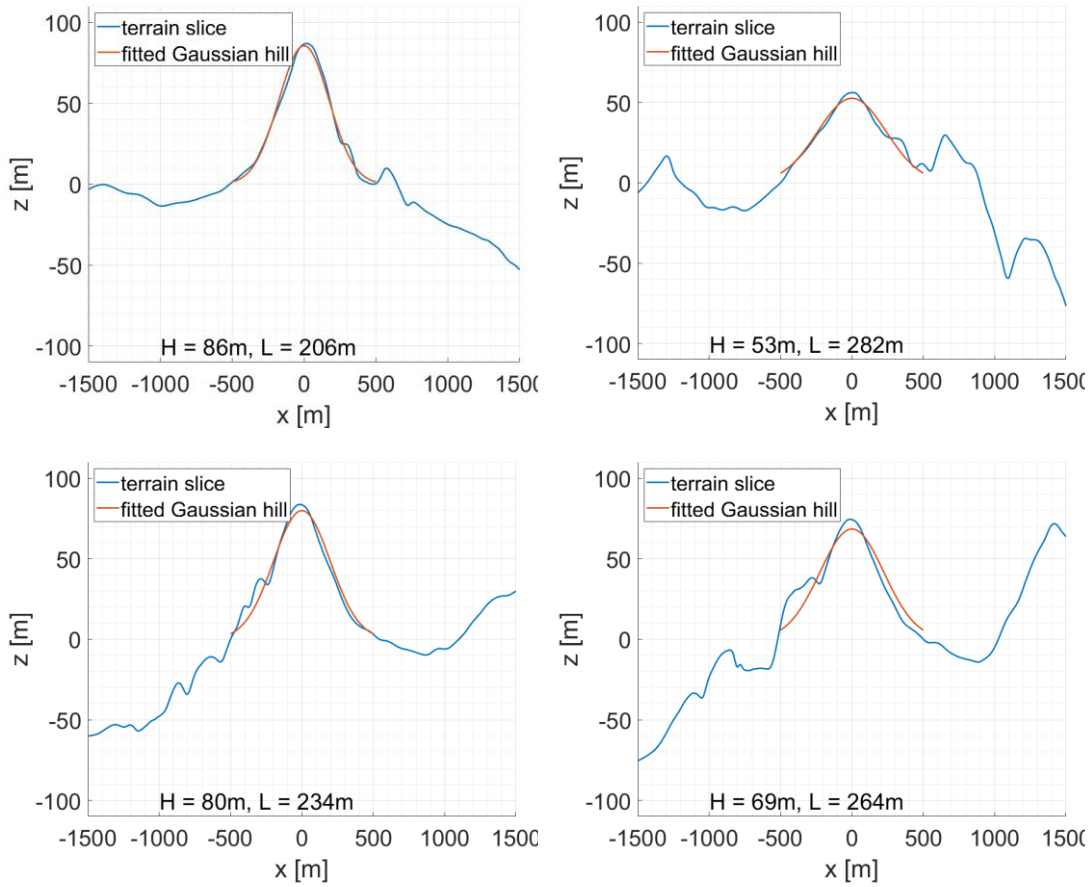

Figure 6.5: Four examples of Gaussian hill fits to terrain slices at the evaluation site Rödeser Berg. The sectors are 70° (upper left), 110° (upper right), 260° (lower left), 270° (lower right). The ***H*** and ***L*** values are given in the figure.

Table 6: Results of Gaussian hill fits for chosen wind direction sectors. ***L***, ***H*** and ***H/L*** are given for each wind direction sector. The results are symmetric for opposed direction sectors. The ***z/L*** ratios are given for the four chosen measurement heights 80, 120, 160 and 200 m.

sector [°]			**50**	**60**	**70**	**80**	**90**	**100**	**110**	**120**
			230	**240**	**250**	**260**	**270**	**280**	**290**	**300**
L [m]			251	208	206	234	264	304	282	315
H [m]			84	86	86	80	69	69	53	38
H/L			0,33	0,41	0,42	0,34	0,26	0,23	0,19	0,12
z [m]	80	**z/L**	0,32	0,38	0,39	0,34	0,30	0,26	0,28	0,25
	120		0,48	0,58	0,58	0,51	0,45	0,39	0,42	0,38
	160		0,64	0,77	0,78	0,68	0,61	0,53	0,57	0,51
	200		0,80	0,96	0,97	0,85	0,76	0,66	0,71	0,64

6.3 Evaluation results

The following sub-chapters are presenting the results of the evaluation. First, results are summarized, e.g., by comparing wind profiles of the mean wind speed measured by the lidar and the cup-anemometers (chapter 6.3.1). Additionally, results of linear regression for several heights and the direction-dependent deviation between mast and lidar are shown for the chosen heights.

The second sub-chapter than gives the results from the non-dimensional evaluation described in chapter 6.2. Non-dimensional plots of z/L versus epsilon are shown for the different chosen wind directions. The applicability of the method is validated and possible drawbacks and advantages are discussed.

6.3.1 Lidar-mast deviations

When comparing the mean wind speeds for the whole measurement period, as illustrated in the wind profile in Figure 6.6, it can be noted that the overall deviations are relatively small. With 0.67 m/s, the largest deviations are found for the lowest measurement height of 40 m. This could be explained by the small vertical distance to the forest canopy at about 30 m above ground. Only a slight increase of the absolute deviations with increasing measurement height is found when comparing results from 60 m to 200 m measurement height. However, these deviations are significantly smaller than those at 40 m (0.11 m/s for 60 m and 0.18 m/s for 200 m).

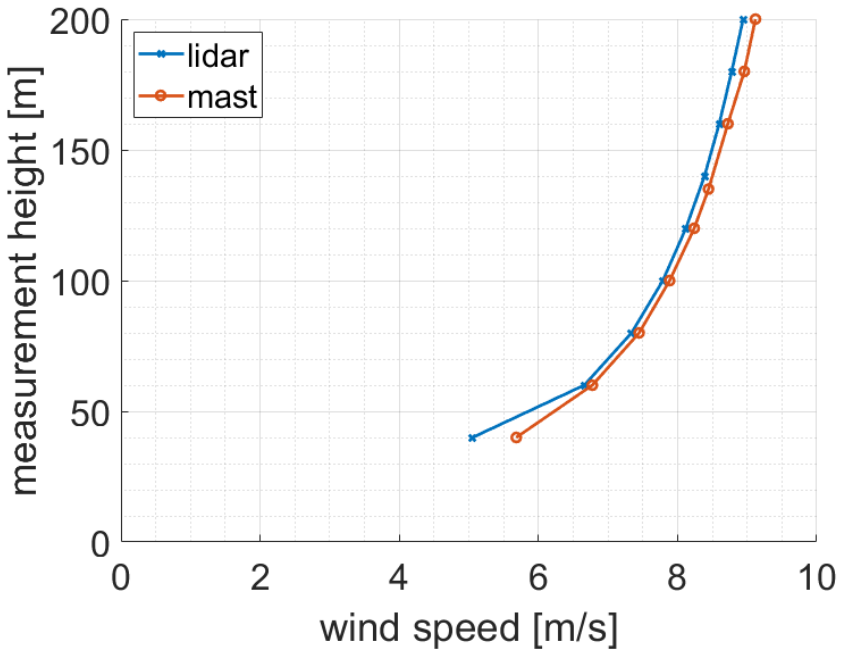

Figure 6.6: Comparison of the mean wind profile measured with the lidar (blue) and the cup and sonic anemometers at the wind measurement mast (red). In this case, all available sensors have been used and a quality check was carried out as described for the other sensors in chapter 6.1.2). Measurement data is available between 40 m and 200 m. Only time stamps where data is available for all measurement heights simultaneously are used in order to ensure comparability.

Looking at the scatter plots and linear regression for the four chosen heights 80 m, 120 m, 160 m and 200 m, which are all well above the forest, it can be seen that the results are very similar (Figure 6.7). There is a high correlation with an R^2 of 0.99 for all measurement heights. The slope is closest to one for 160 m measurement height, giving a deviation of about 2 % between mast and lidar. The offset value is in the order of 0.1 m/s for all measurement heights, which is very close to zero.

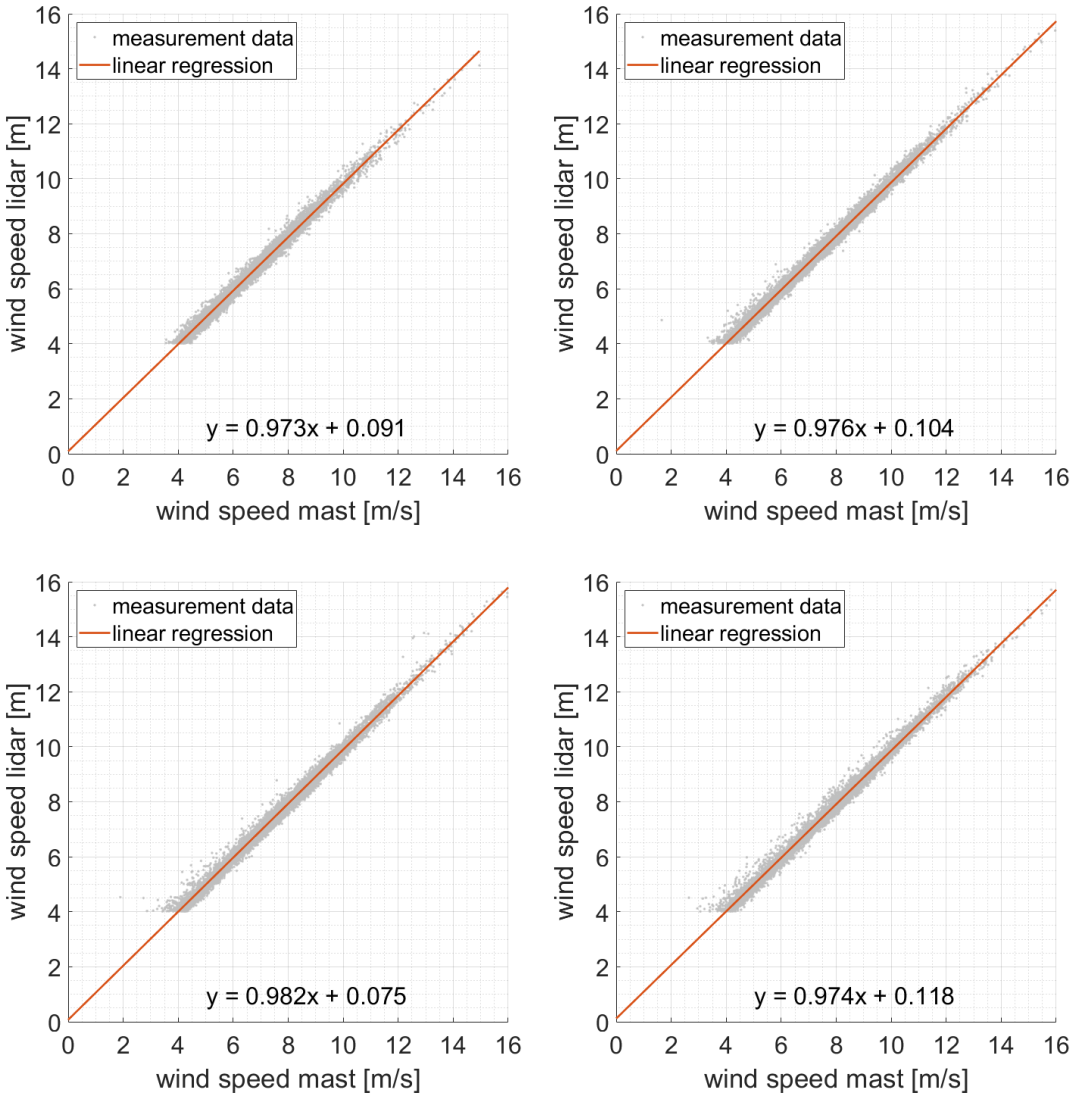

Figure 6.7: Scatter plots and linear regressions of the lidar-mast inter-comparison for the four chosen heights 80 m (upper left), 120 m (upper right), 160 m (lower left) and 200 m (lower right). Wind speeds of the lidar are shown on the y-axis, wind speeds of the mast are shown on the x-axis. The coefficients of the linear regression are given in the plots. The R-squared value is 0.99 for all measurement heights. Results from 80 m and 200 m are reprints from Klaas et al. (2015).

The influence of terrain complexity becomes most severe when looking at the relative deviations lidar and mast measurements (lidar error ε) versus wind direction for the four mentioned measurement heights (Figure 6.9 to Figure 6.12). For all heights are clear dependence of the lidar error on wind direction is found. Largest lidar errors are found for 240° to 260° with about -5 % at 80 m and about 3 % at 160 m measurement height. Opposed wind direction sectors are showing the second-highest lidar errors, which are only slightly smaller. There is a clear transition to positive deviations

between mast and lidar measurements at perpendicular wind direction sectors. This behavior can be explained by the fact that for these wind directions, the measurement site is located in between two other peaks at the ridge of Rödeser Berg, resulting in a valley-like wind flow (compare Klaas et al. (2015).

For all results, it can be noted that there is a significant scatter of the lidar error around the mean value. The standard deviation of the lidar error is in the order of 2 %, although there are many outliers beyond this value for all measurement heights. Possible explanations for the scattering could be diurnal variations in atmospheric stability (and turbulence) as well as changes in wind direction within the 10-minute averaging interval that result in changes of flow curvature and speed-up.

The lidar errors for the four different heights are compared with each other in Figure 6.8 (compare also Figure 5 in Klaas et al. (2015)). Here it becomes evident that, except from the 80 m measurement height, all results are relatively similar. Slightly larger lidar errors can be found for many wind direction sectors for the 200 m measurement height. The most significant deviations are found 240° to 280° wind direction sectors at 80 m measurement height. Here the lidar errors exceed those found at the other measurement heights by up to 3 % (at the 270° sector). Also, in the north-eastern sectors, there are significant deviations from the other measurement heights.

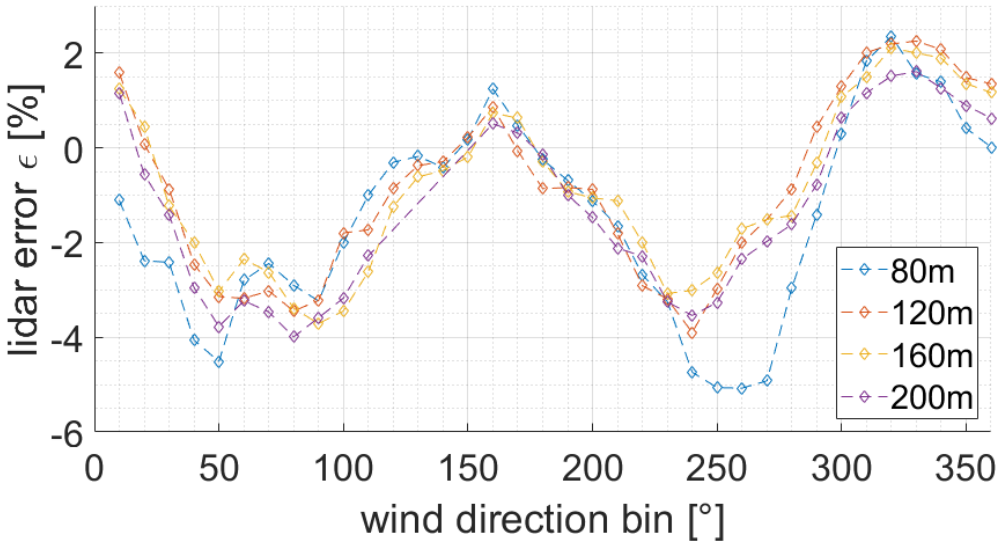

Figure 6.8: Lidar error $\boldsymbol{\varepsilon}$ derived from measurement data versus wind direction at the four chosen heights given in the legend. The lidar error is calculated based on an average for a bin size of +/-5° for each 10° bin from 0 to 360° wind direction. Only wind speeds higher than 4m/s were used. Due to a lightning protection pole next to the top-anemometer, the data between 110° and 160° is excluded for this height. The figure is a modified reprint from Klaas et al. (2015).

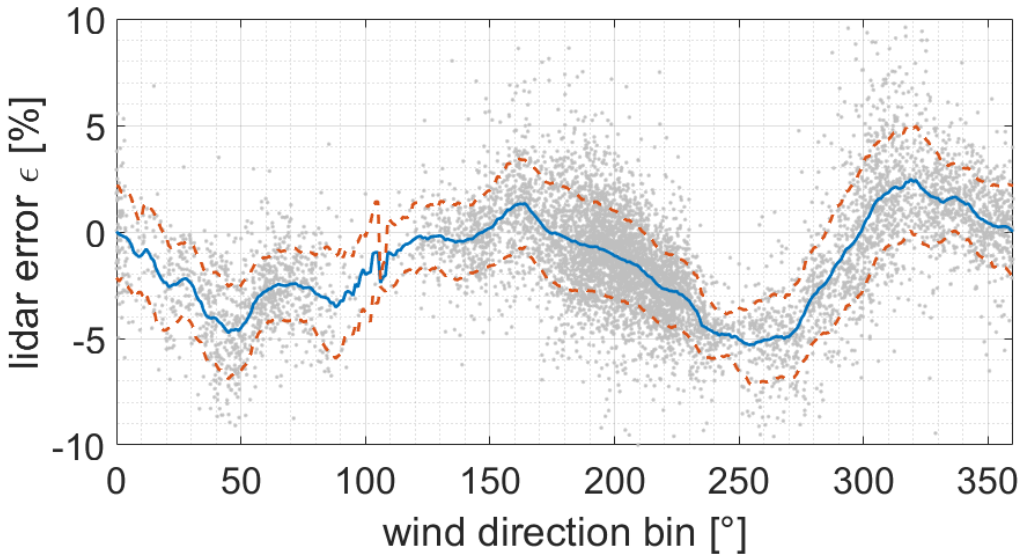

Figure 6.9: Lidar error $\boldsymbol{\varepsilon}$ derived from measurement data versus wind direction at 80 m height. The lidar error is calculated based on a moving average for a bin size of +/-5° for each degree from 0 to 360° wind direction (blue line). The positive and negative standard deviation for each calculation is added to the mean value and shown in dashed red lines. Only wind speeds higher than 4 m/s were used.

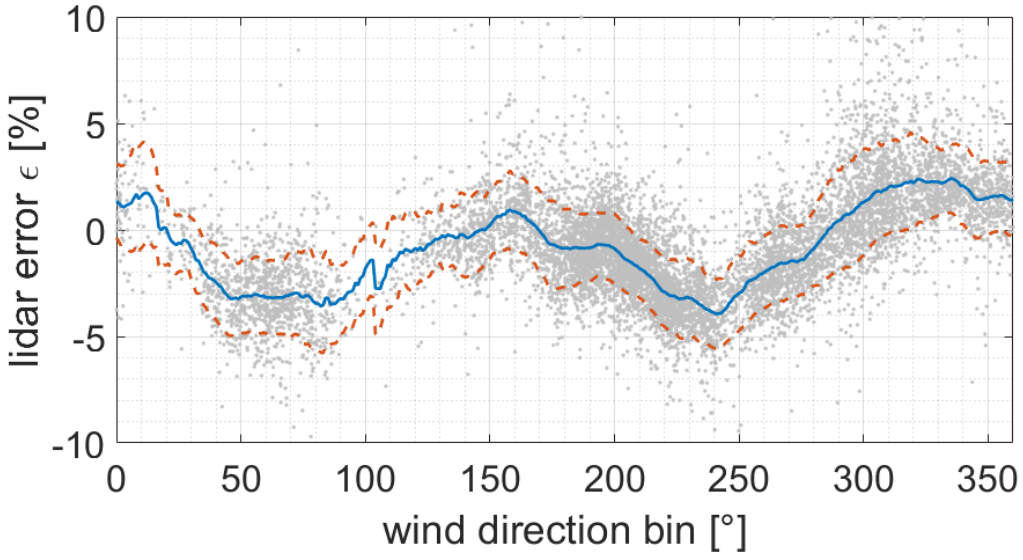

Figure 6.10: Lidar error $\boldsymbol{\varepsilon}$ derived from measurement data versus wind direction at 120 m height. The lidar error is calculated based on a moving average for a bin size of +/-5° for each degree from 0 to 360° wind direction (blue line). The positive and negative standard deviation for each calculation is added to the mean value and shown in dashed red lines. Only wind speeds higher than 4 m/s were used.

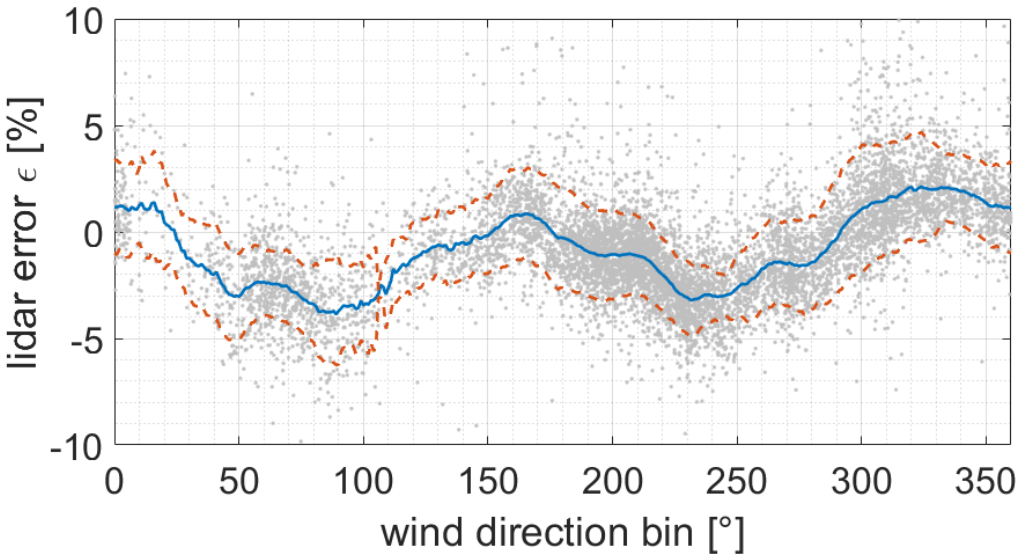

Figure 6.11: Lidar error $\boldsymbol{\varepsilon}$ derived from measurement data versus wind direction at 160 m height. The lidar error is calculated based on a moving average for a bin size of +/-5° for each degree from 0 to 360° wind direction (blue line). The positive and negative standard deviation for each calculation is added to the mean value and shown in dashed red lines. Only wind speeds higher than 4 m/s were used.

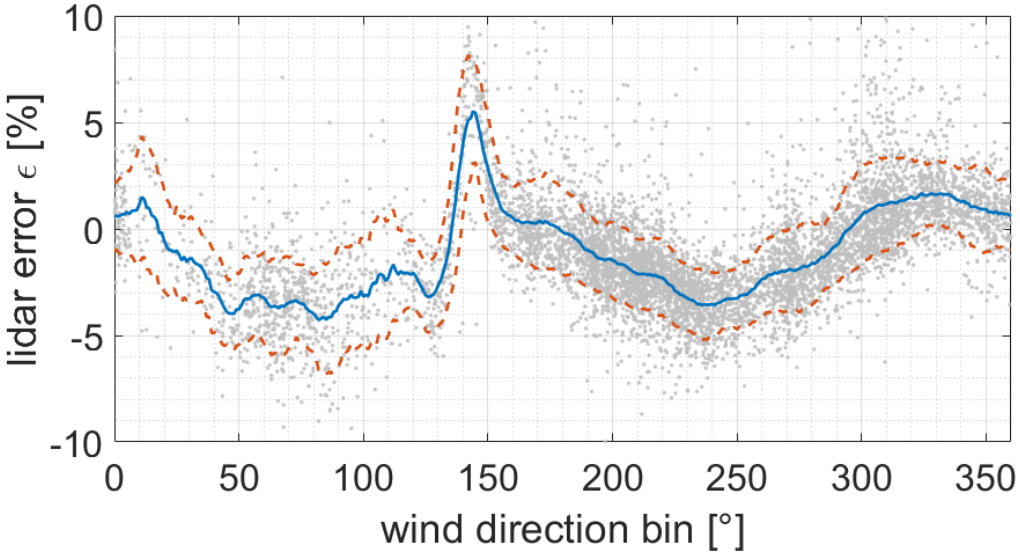

Figure 6.12: Lidar error $\boldsymbol{\varepsilon}$ derived from measurement data versus wind direction at 200 m height. The lidar error is calculated based on a moving average for a bin size of +/-5° for each degree from 0 to 360° wind direction (blue line). The positive and negative standard deviation for each calculation is added to the mean value and shown in dashed red lines. Only wind speeds higher than 4 m/s were used. A lightning protection pole next to the top-anemometer causes the spike around 145° wind direction.

6.3.2 Non-dimensional representation

Figure 6.13 to Figure 6.16 show the results of the non-dimensional evaluation for the four different H/L ratios 0.1, 0.2, 0.3 and 0.4. The Gaussian hill fits given in Table 6 are assigned to the four H/L ratios and compared to the results from the parameter study based on Meteodyn WT for a tree height of 30 m and medium forest density.

The measured lidar errors are grouped into those for northwestern sectors (filled markers) and those for southwestern sectors (unfilled markers). Following from the symmetry between these two groups, the evaluation data points always occur pairwise. Also, the four measurement heights 80 m, 120 m, 160 m and 200 m are represented by different markers in the figures.

By this, it is possible to analyses the influence of measurement height on the results as well as the influence of the different upwind and downwind characteristics of the terrain for the two opposed wind direction sector groups.

Figure 6.13 shows the results for a H/L ratio of 0.1. For northeastern sectors the measured lidar errors are of the same magnitude than those from the simulations. Also, the tendency of increasing lidar errors with increasing measurement height becomes obvious in this representation.

When looking at the southwestern sectors, the evaluation results are different. For most of the sectors, the measured lidar errors are positive, which is contrary to the expected negative errors attributed to the Gaussian hills. The reason for this might be the fact that the terrain shape upwind to the actual measurement site has a significant influence on the actual flow curvature and speed-up effects at the measurement site. However, there are some sectors with negative errors also in the southwestern group that are close to the simulation results as well.

The largest group of evaluation data points is assigned to the H/L ratio of 0.2, and the results are illustrated in Figure 6.14. Again, it can be noted that there is a difference between the southwestern and the northwestern group. While there is a tendency towards larger lidar errors for the northwestern sectors, all results for southwestern sectors – except for two data pairs – show smaller lidar errors. All results are generally in the same magnitude as the simulation results, although there is much scattering. For the northwestern sectors, there is a tendency of increasing lidar errors with increasing measurement height and most of the data points are close to the simulation results. There is one exception for a data point at 80 m measurement height, which shows significantly larger lidar errors than all other northwestern sectors. Most of the southwestern data points are shifted towards lower lidar errors when compared to the opposed northeastern sectors. However, there are no positive measured lidar errors, but the smallest lidar error is around -0.8 % for one data point at 120 m measurement height. There is one data point at 80 m measurement height that shows significant deviation and the overall highest lidar error of about -5 %, which significantly exceeds the simulation results.

The results for a H/L ratio of 0.3 are shown in Figure 6.15. It first can be noted that all but two data points are showing lidar errors below those from the simulation. For the northwestern sectors, most of the measured lidar errors are close to the simulation results. While there are some cases where the lidar errors for the southwestern sectors are smaller, there are also cases where the measured errors for southwestern sectors

are significantly increased when compared to the opposite directions. Largest lidar errors can be found for two data points at 80 m measurement height.

For the largest H/L ratio of 0.4, the measured lidar errors are compared to the simulation results in Figure 6.16. As there are only two opposed wind direction sectors that fall into this category, this is the smallest evaluation group. Except for one data point for a southwestern sector at 80 m measurement height, all measured results are significantly smaller than those given by the simulation. Again there is a tendency of increasing lidar errors for increasing measurement height.

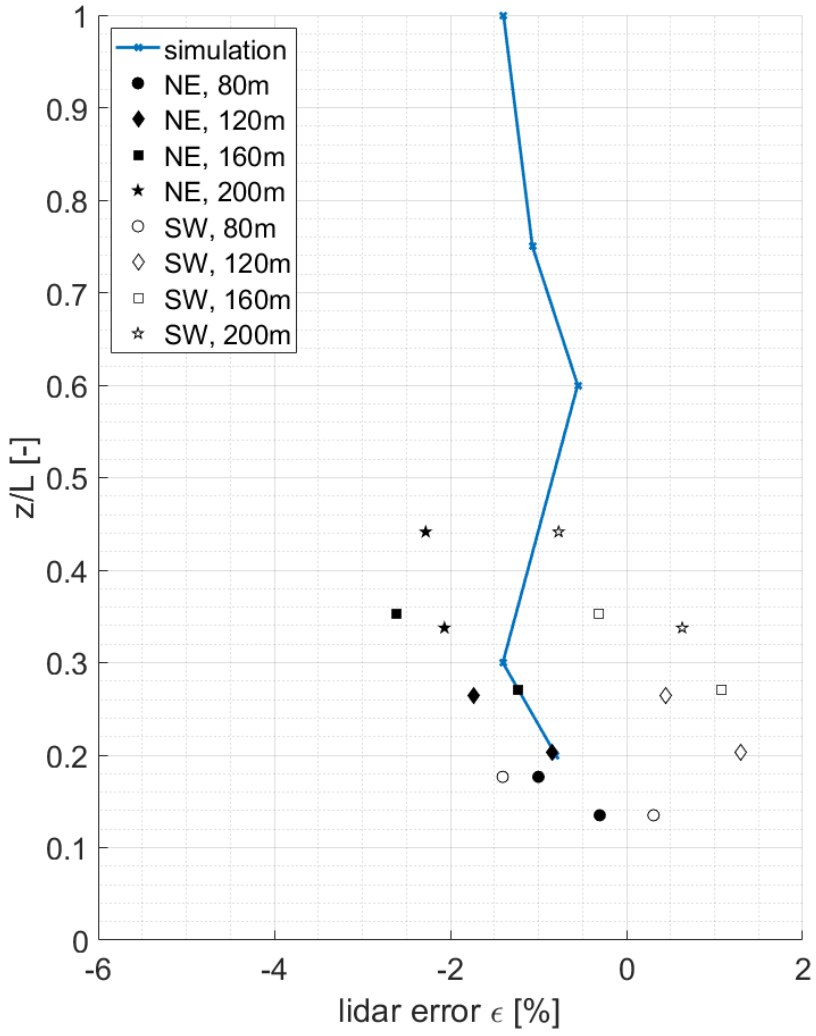

Figure 6.13: Non-dimensional ratio $\boldsymbol{z/L}$ versus the lidar error $\boldsymbol{\epsilon}$ for an $\boldsymbol{H/L}$ ratio of 0.1. The markers represent the measured lidar errors for the chosen wind direction sectors according to Table 6 for the four different measurement heights 80 m, 120 m, 160 m and 200 m. The filled markers represent the measurements for north-western wind directions, the unfilled markers for south-western directions.

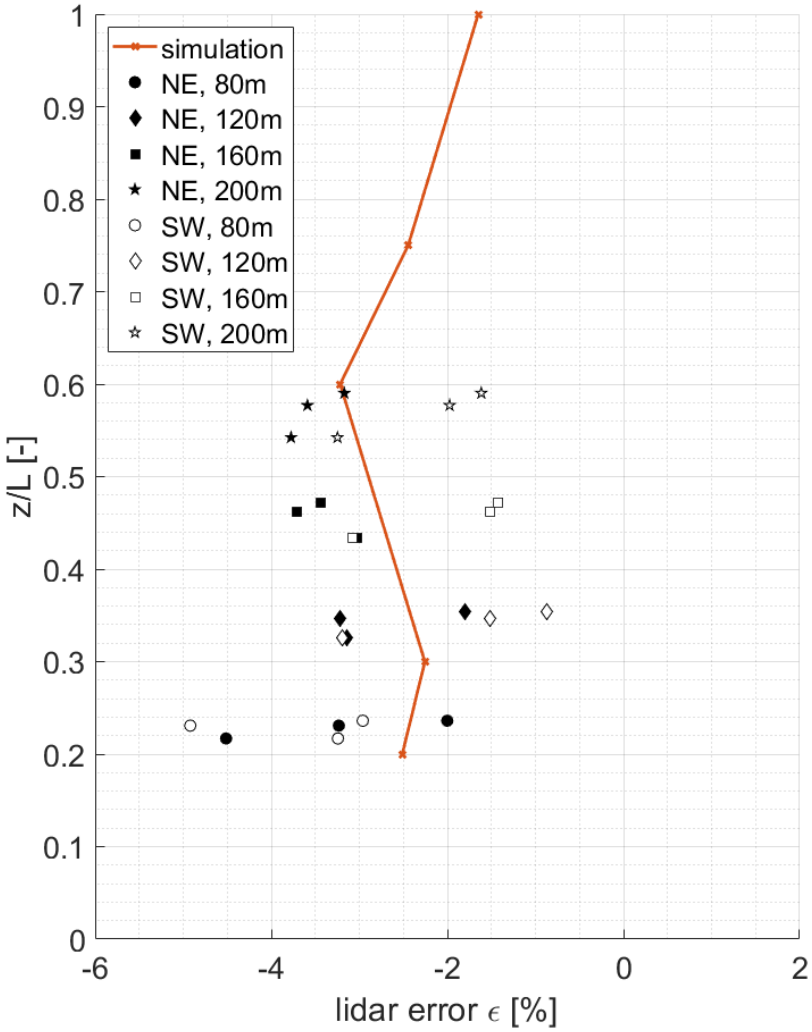

Figure 6.14: Non-dimensional ratio $\boldsymbol{z/L}$ versus the lidar error $\boldsymbol{\varepsilon}$ for an $\boldsymbol{H/L}$ ratio of 0.2. The markers represent the measured lidar errors for the chosen wind direction sectors according to Table 6 for the four different measurement heights 80 m, 120 m, 160 m and 200 m. The filled markers represent the measurements for north-western wind directions, the unfilled markers for south-western directions.

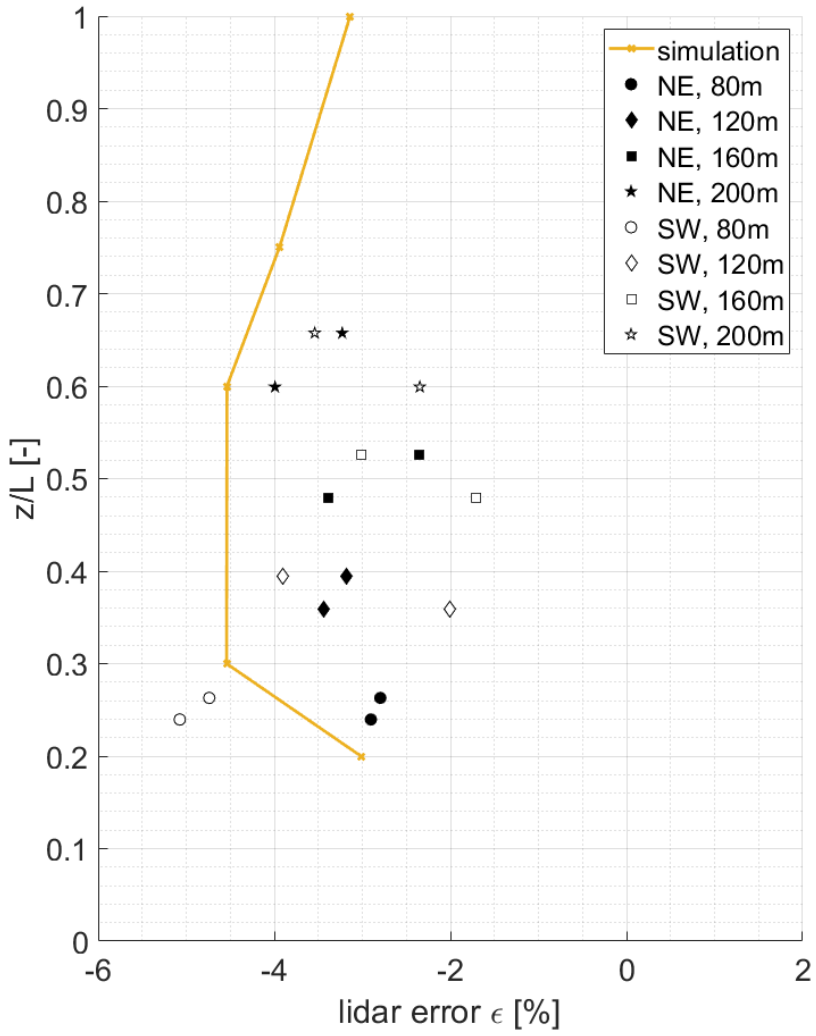

Figure 6.15: Non-dimensional ratio $\boldsymbol{z/L}$ versus the lidar error $\boldsymbol{\epsilon}$ for an $\boldsymbol{H/L}$ ratio of 0.3. The markers represent the measured lidar errors for the chosen wind direction sectors according to Table 6 for the four different measurement heights 80 m, 120 m, 160 m and 200 m. The filled markers represent the measurements for north-western wind directions, the unfilled markers for south-western directions.

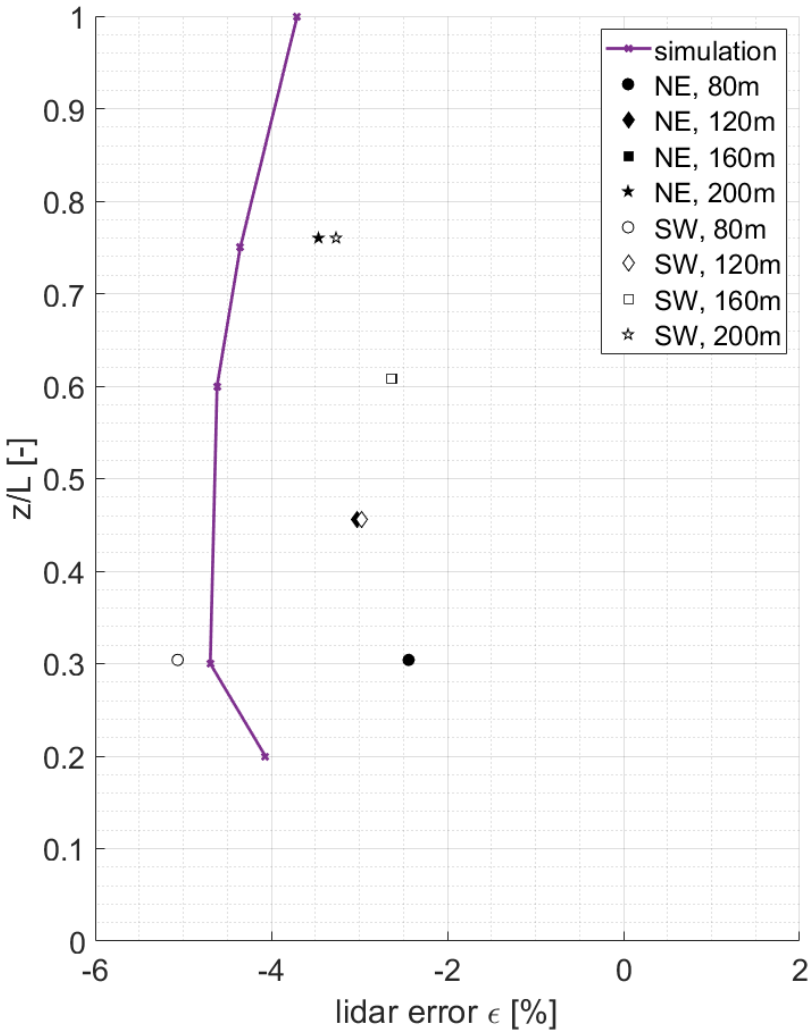

Figure 6.16: Non-dimensional ratio $\boldsymbol{z/L}$ versus the lidar error $\boldsymbol{\varepsilon}$ for an $\boldsymbol{H/L}$ ratio of 0.1. The markers represent the measured lidar errors for the chosen wind direction sectors according to Table 6 for the four different measurement heights 80 m, 120 m, 160 m and 200 m. The filled markers represent the measurements for north-western wind directions, the unfilled markers for south-western directions.

6.4 Lidar error estimation with flow models

The lidar error can be estimated under consideration of the full three-dimensional terrain model of the area around Rödeser Berg, including information about land-use and forest (compare Figure 6.2and Figure 6.3). This has been done in Klaas et al. (2015) with three different flow models. One of the models was Meteodyn WT, which has also been used to analyze most of the parameter variations within chapter 5.

The extension of the model domain was 20 by 20 km² and 36 wind direction sectors (10° bins) were modeled. Measured lidar errors were accordingly binned to 10° sectors for the comparison. To illustrate the influence of roughness and forest parameterization, which has also been found within chapters 5.2.2.2 and 5.2.3 of this thesis, results with and without forest are compared to the actual measurement results in Figure 6.17. The forest was parameterized with a height of 30 m and high forest density. The no. of cells in Meteodyn WT was 766,640, ensuring a high vertical and horizontal resolution in the proximity of the lidar site (compare table 4 in Klaas et al. (2015)).

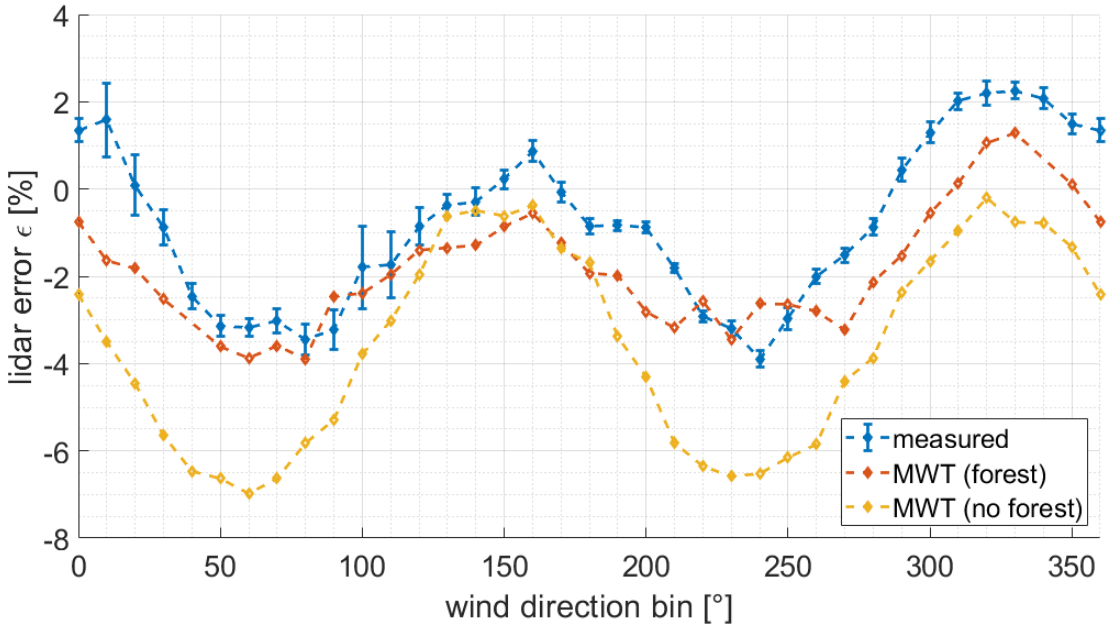

Figure 6.17: Comparison of lidar error estimations with Meteodyn WT for two different parameterizations to the measured lidar error at 120 m height versus wind direction bins. The error bars on the measured data indicate the confidence intervals. The red line shows the best result achieved with Meteodyn WT using a forest parameterization with 30 m tree height and high forest density. The yellow line is showing results without forest modeling but with high surface roughness. The figure is a modified reprint from Klaas et al. (2015).

Within this sub-chapter, the model results are exemplarily shown for a measurement height of 120 m. However, results for the measured lidar error in Figure 6.8 emphasize that the differences between the upper heights (120 to 200 m) are relatively small for all wind direction sectors.

In compliance with the results of the parameter-study that is presented in chapter 0, the estimated lidar errors without consideration of forest are significantly higher than those with forest modeling. Since the surroundings of the actual measurement site are

forested, the deviation between measured and estimated lidar errors are largest when not using forest modeling at all (Figure 6.17).

The model results under consideration of forest in Figure 6.17 represent the best results that could be achieved with the model by adapting the parametrization of the forest. While the shape of the measured error curve is captured by both model parameterizations, the magnitude of the estimated lidar error only fits the measurement results for the forested case. However, for many wind direction sectors, the estimated lidar errors still deviate from the measurements. This is particularly true for those wind direction sectors where positive deviations between measurement mast and lidar measurements occur (10°, 20°, 160° and 290° to 360°).

However, also for many sectors with negative lidar errors (underestimation), the modeled errors are up to 1 % larger than those found in the measurements (compare Klaas et al. (2015), chapter 4.2). Linking these findings to the non-dimensional evaluation presented in the previous chapter 6.3.2, the deviations between estimated and measured lidar errors are systematic. The reason for these deviations remains unclear. A detailed classification, as well as a verification before and after a measurement campaign, might provide helpful information on systematic deviations between cup anemometers and a distinct lidar device (Gottschall et al. 2011). Unfortunately, there is no verification available of the lidar used in the measurement campaign that is evaluated in this dissertation.

7 Conclusions

The overall research question of this dissertation is: “How well do lidars measure at complex terrain sites and which factors are influencing the magnitude of the lidar error?“ Following this question, five hypotheses are developed in chapter 2, each dealing with one of the five major influencing factors on the lidar error in complex terrain. Furthermore, a novel approach is introduced, that separates the individual influence of flow curvature (ε_c) and speed-up effects (ε_s) on the total lidar error ε.

The concluding chapter provides links to these hypotheses, sums up the results and evaluates them concerning the initial assumptions (chapter 7.1). Finally, it provides concluding remarks on the key findings and outlines the implications of the findings for real-world applications (chapter 7.2).

7.1 Evaluation of hypotheses

Evaluation of hypothesis A) *“The lidar error is dependent on orographic complexity. It increases with increasing terrain curvature that causes the wind flow to bend and accelerate.”*

Starting with the orographic complexity of the measurement site (chapter 5.2.1), it is found, that the non-dimensional parameter H/L (i.e. the ratio of hill height over hill half-width) has by far the most important influence on the magnitude of the lidar error ε. Based on the potential flow model results, the maximum ε found for a H/L ratio of 0.1 is about -3 %. It increases significantly up to -11 % for a H/L ratio of 0.4. Maximum errors found for the linearized model WEng (-2.5 % to -12 %) and the RANS CFD model Meteodyn WT (-2 % to -9.5%) differ from the potential flow model but are of comparable magnitude. However, WEng provides significantly larger lidar errors than the potential flow model at the maximum point for H/L ratios of 0.3 and 0.4.

Following from this, hypothesis A) can generally be confirmed. Increasing terrain complexity is found to increase the lidar error significantly. However, taking into account the interdependency between measurement height and hill dimensions, solely considering the H/L ratio as a measure of terrain complexity is not sufficient to evaluate the effects on the lidar error.

Evaluation of hypothesis B) *“The lidar error is dependent on measurement height. It decreases with increasing height, while terrain effects on the wind flow diminish.”*

The non-dimensional approach followed within this dissertation allows for an analysis of the influence of orographic complexity with regards to measurement height above ground z and hill half-width L, represented as the non-dimensional parameter z/L (compare, e.g. Figure 5.25). Based on a constant half-cone opening angle φ of 30°, the results from all three used models show a well-defined dependence of the lidar error ε on z/L for each of the four H/L ratios that were analyzed (0.1, 0.2, 0.3 and 0.4). Starting from negligible errors at the lowest z/L, a steep increase is found when increasing z/L. Here the lidar error reaches a maximum at z/L between 0.5 to 0.6 for H/L ratios between 0.1 and 0.4. Afterward, it decreases for increasing z/L. Depending on the H/L ratio, the errors fall below -2 % for z/L between 1.5 for the least inclined and 5.0 for the steepest hills.

There are two ways to interpret this dependency: First, z/L increases when increasing the measurement height z for a fixed L. For small measurement heights, the measurement points of the lidar are close together. Resulting from that, the difference in horizontal wind speed between the two opposed measurement points and the reconstruction point directly above the lidar is small or negligible (compare e.g. Figure 5.21). Additionally, for symmetric hill-flow, the curvature of the streamline directly above the hilltop is zero (compare e.g. Figure 5.1). It then steadily increases upwind and downwind along the flanks of the hill up to the inflection points. At a low measurement height, the measurement points are close to the zero-curvature point. As a result, the lidar error due to flow curvature is small. With increasing measurement height, both effects significantly increase as well, causing the lidar error to increase. Then, with a further increase of measurement height, the measurement points are leaving the flanks of the hill and the area of strongest flow curvature and highest speed-up effects. After the maximum point, this contrary effect causes the lidar error to decrease for large measurement heights.

Second, an increasing z/L is also found for a fixed measurement height and a decreasing hill half-width L. Based on this, small z/L can be interpreted as large or wide hills that are significantly larger than the dimensions of the lidar measurement geometry (compare e.g. Figure 5.3). Large z/L on the other hand, are representing small or narrow hills that are significantly smaller than the dimensions of the lidar measurement geometry (compare e.g. Figure 5.2). For large hills, the flow curvature and speed-up effects at the two opposed measurement points are then small, because the points are close to the hilltop. For small hills, the two effects are also small, because the measurement points are far upwind and downwind from the measurement location. Between these extreme cases, there is a ratio between the hill size and the size of the measurement geometry that causes maximum lidar errors, i.e., at z/L between 0.5 and 0.6, as described above.

Concerning the lidar error parts ε_c (caused by flow curvature) and ε_s (caused by speed-up effects) it is found, that ε_c is responsible for about more than 90 % of the total lidar error for small z/L, for about 85 % at the maximum point and about 70-75 % for larger z/L. Additionally, the maximum ε_s is found at an z/L of about 1.0, whereas the maximum ε_c is found at about 0.5. The overlay of the two effects shifts the maximum of ε towards a z/L of 0.6.

The results show that hypothesis B) can be confirmed, regarding the assumption that, for increasing measurement height, the influence of complex terrain on the wind flow becomes negligible. However, there is no linear decrease of lidar error with increasing measurement height, but a complex dependency between z/L, H/L and the lidar error ε. In particular, maximum lidar errors are found between z/L of 0.5 to 0.6, representing the worst measurement configuration.

Evaluation of hypothesis C) *"The lidar error in complex terrain is dependent on terrain roughness. It is, in particular, sensitive to the presence or absence of forest. Roughness and forest increase shear and turbulence and facilitate flow separation effects. All these effects influence the flow curvature and speed-up."*

The effects of terrain roughness on the lidar error are analyzed for the two models WEng and Meteodyn WT in chapter 5.2.2. First, it can be noted that for low roughness length z_0 of 0.005 m, the results of both models are closest to those from the inviscid potential flow model. However, increasing the roughness length has a significant effect on the resulting lidar errors. Lidar errors are decreasing with increasing roughness

length and smallest errors are found for the roughness length z_0 of 0.5 m. The result is consistent for all four H/L that were considered in this study. However, because lidar errors are small for an H/L ratio of 0.1, also the effect of increasing the roughness length is small here. For the highest H/L ratio of 0.4, increasing the roughness lengths significantly reduces the maximum lidar error from in Meteodyn WT from -9.5 % to -7.5 %.

Adding forest to the terrain model in Meteodyn WT has a significant influence on the lidar error as well (chapter 5.2.3). Results for a very sparse forest with low tree heights are comparable to those from the high roughness case. However, increasing the three height in medium and high forest density cases results in an overall decrease of the lidar error. Again, this result is found for all four H/L ratios. For an H/L ratio of 0.4 the lidar error at the maximum point is reduced from -6.5 % for a tree height of 10 m to -4.5 % for a tree height of 30 m. The model-based findings are validated by measurement data from the forested site Rödeser Berg (chapter 6), which underlines the necessity to consider forest.

In WEng, increasing the roughness length decreases the lidar error as well. However, at the maximum point around z/L between 0.5 and 0.6, the estimated lidar errors still exceed those from the potential flow model. As there is no forest model in WEng, the significant effects from the forest are not representable.

Although surface roughness has a small influence on ε_s in Meteodyn WT, it is found that mainly flow curvature and therefore ε_c is impacted by surface roughness. This is also true for forested cases, although the impacts of ε_c and ε_s are more complicated, because of strong asymmetries in the flow field. However, there is a substantial discrepancy between ε_c and ε_s from Meteodyn WT and WEng. For z/L exceeding 1.0, WEng shows a significant underestimation of the flow curvature effects and, at the same time, a significant overestimation of the speed-up effects at the flanks of the hill. Following findings from the literature, this is typical behavior of linearized flow models (e.g., Bowen and Mortensen (1996)).

From this, it can be concluded that the rougher the terrain, the smaller the resulting lidar errors, which confirms hypothesis C). Additionally, the presence of forest significantly decreases the estimated lidar errors. Both effects can be explained by the increasing asymmetry of the hill flow, in particular at the lee-side (Belcher et al. 2012; Ross and Vosper 2005). In particular, the critical slope for flow separation is reduced by the influence of the forest (Ross and Vosper 2005).

Evaluation of hypothesis D) *"The lidar error in complex terrain is dependent on atmospheric stratification. It decreases for stable cases, which is because, in this case, the wind flow is less bent when passing a hill."*

Diverse atmospheric stability conditions are evaluated in chapter 5.2.4 based on the stability model implemented in Meteodyn WT (chapter 4.3.3). It is found that in the three analyzed situations (low surface roughness, high surface roughness and medium dense forest at a H/L ratio of 0.3) atmospheric stability has a significant influence on the resulting lidar error.

In most simulations, the lidar error increases for unstable and very unstable stratification, when compared to the neutral cases. This increase is relatively small for the low roughness case and is below a difference of 1 %. For the forested case, the lidar error at between a z/L of 0.3 and 1.0 is about 1-1.5 percentage points larger than in the neutral case.

For stable and strongly stable cases, on the other hand, the lidar error is decreased for most simulations in comparison to neutral stratification. This effect is strongest for the highest stability class "strongly stable" with an L^* of 60 m. Here, the lidar error is decreasing from -7.5 % to -5.5 % at the maximum point in the low roughness case, from -5.75 % to -2.5 % in the high roughness case and from -4.5 % to -2.25 % in the forested case.

From these findings, it can be concluded that hypothesis D) can be confirmed. Atmospheric stability has a considerable impact on the flow over a hill. Flow curvature and speed-up are modified in a way that influences the magnitude of the lidar error. In particular, the strong decrease of flow curvature under stable stratification significantly reduces the estimated lidar error.

Evaluation of hypothesis E) *"The lidar error is dependent on the half-cone opening angle of the lidar measurement geometry. It decreases when the angle is decreased because the measurement points are closer together and the wind vectors are more similar."*

Based on the novel approach of splitting up the lidar error ε into its parts ε_c and ε_s, it is possible to systematically analyze the influence of reduced half-cone opening angles φ on the lidar error in complex terrain (chapter 5.2.6).

Only a small dependency of ε on φ is found in the results from the potential flow model. At the maximum point of a z/L of 0.6 and for the maximum H/L ratio of 0.4 the difference in ε between a φ of 10° and 30° is less than 1 %. For all other z/L and H/L ratios, the influence is smaller than that.

However, splitting up the lidar error ε into its two parts provides a detailed insight into the individual influence of flow curvature and speed-up effects on the total lidar error for the different magnitude of φ. First, it can be concluded that ε_s is significantly reduced for smaller φ. While it reaches up to -2 % for a H/L ratio of 0.4 at the maximum point for the standard value of 30°, it is well below -0.5 % for a φ of 10°. Contrary to that, the error part ε_c increases for most z/L with decreasing φ. The difference in the results is largest for a z/L of 1.5, where ε_c increases from -6 % to -7 % for an H/L ratio of 0.4. For all other z/L and H/L, the influence is smaller but consistently present. The superposition of these two opposite effects leads to an overall small decrease of the lidar error ε. However, compared to the other influencing factors, it is marginal considering the results from the potential flow model.

Despite these findings, when looking at rough and forested cases from Meteodyn WT, it is found that the dependence of ε on the half-cone opening angle is complex. Strongest effects are found for the forested and, therefore, most asymmetric case. Decreasing φ to 10° leads to a significant decrease in ε by up to 20 % for small z/L below 0.6. For large z/L, on the other hand, ε increases by about 1 % for φ decreased to 10°. These findings show the complex interrelation between the position of the measurement points, the actual structure of the flow field and the resulting lidar error. Contrary to the findings from the literature study (Bingöl et al. 2009; Foussekis 2009), the half-cone opening angle can significantly influence the resulting lidar error, in particular in complex flow situations, e.g., at forested hills where the flow is asymmetric.

Summing up these findings, it can be noted that hypothesis E) can be confirmed. However, the relationship between lidar error ε and half-cone opening angle φ is more

complex than thought, particularly when looking at the lidar error parts ε_c and ε_s. An individual adaption of the half-cone angle in dependence of the flow field at the actual measurement site can be reasonable.

7.2 Concluding remarks

The concept of separating the lidar error ε into its parts ε_c and ε_s has proven to be a capable tool to analyze and identify the impact of the different influencing factors on the lidar error. Although flow curvature is responsible for the major part of the lidar error, speed-up effects are not negligible. It is shown that depending on the z/L ratio, 10-30 % of the total lidar error can be attributed to speed-up. Lidar error estimation methods should, therefore, take into account both effects. Simplified approaches, solely based on flow inclination angles at the measurement points, are not recommended for complex terrain sites.

The influence of measurement height is found to be complicated. It is, for most cases, characterized by a steep increase of the lidar error with increasing measurement height, followed by a maximum point at a measurement height equal to roughly 60 % of the hill half-width L. The lidar error decreases again and becomes negligible at a z equal to about 1.5 to 5 times the hill half-width. A lidar error estimation previous to the measurement campaign under consideration of planned the measurement heights is therefore mandatory.

For the first time, the influence of decreasing the half-cone opening angle φ could be analyzed in detail and for both symmetric and asymmetric flow fields. Based on the potential flow model and for low roughness cases in the RANS CFD model, opposed effects of reduced half-cone opening angles are found on ε_c and ε_s. This explains the small differences in the total lidar error for symmetric flows. Contrary to the findings in the literature (Bingöl et al. 2009; Foussekis 2009; Bradley 2012) it turned out that in case of complex, asymmetric flow above rough or forested terrain, φ can significantly influence the lidar error. An adaption of φ to the flow conditions at the actual measurement site and height could significantly reduce the lidar error in certain cases.

When comparing the results of the potential flow and the linearized model to the RANS model for large H/L ratios and, in particular, high roughness lengths and forested cases, the limitations of the simple models become apparent. It can be concluded that potential flow and linearized models should not be applied at forested and rough sites with significant terrain inclination. These models will generally overestimate the lidar error because they are not capable of modeling non-linear or detached flow effects in the lee of the hill, which occur due to increased surface roughness or the presence of forest. The evaluation campaign confirms these findings. Neglecting the influence of the forest on the flow results in huge overestimations of the lidar error in comparison to the measurements. Best results of lidar error estimation are achieved when adding the forest to the model. It can be concluded that – despite the generally more complex flow characteristics at forested sites – lidar errors are reduced due to the presence of forest or high surface roughness.

The influence of atmospheric stability in the lidar error estimations from Meteodyn WT was significant, particularly for stable stratification. At sites were significant changes in atmospheric stability occur, the lidar error could potentially be overestimated by modeling solely neutral stratification. However, the work presented

in this thesis was a first attempt in considering different atmospheric stability classes for lidar error estimation. A detailed evaluation is needed to validate the results.

Because many different model parameterizations are considered within this dissertation, it is difficult to carry out a full evaluation of the findings. An evaluation approach was developed that sorts measurement results of lidar errors at real-world sites into the structure of the non-dimensional parameter study (chapter 6.2). The approach was successfully tested at the forested complex terrain test site "Rödeser Berg", where measurement data from a 200 m measurement mast is compared to data from a Doppler wind lidar (chapter 6.1). The evaluation provides reasonable results for wind directions with H/L ratios in the order of 0.1 and 0.2 (compare e.g. Figure 6.14). However, for orographically more complex wind directions that are comparable to H/L ratios of 0.3 and 0.4, the measured lidar errors are mostly smaller than the estimations from the flow model (compare e.g. Figure 6.15). An overestimation of the lidar errors for these wind direction sectors is also found when a three-dimensional terrain model is taken into account (Figure 6.17). It is therefore questionable if either the model or the measurements comprehend a systematic error at the analyzed site. Multiple sites with high measurement masts and diverse orographic complexity and surface roughness characteristics are needed to enhance the data basis for a profound non-dimensional evaluation (compare chapter 8). Additionally, the influence of the direction offset of the laser beams from the north at the lidar error could be taken into account.

As an overall summary, it can be concluded, that the findings of this dissertation clearly show that orographic complexity, roughness and forest characteristics, as well as atmospheric stability, have a significant influence on lidar error estimation. The dissertation provides helpful guidance on the choice and parameterization of flow models as well as on the design of methods for lidar error estimation. The results emphasize that the use of a RANS CFD model in conjunction with an appropriate forest model is crucial to achieving reasonable lidar error estimations in complex terrain. If atmospheric stability variation at a measurement site plays a key role, the influence on the flow characteristics will also significantly affect the lidar error at those sites and should be considered in the modeling. Under certain flow conditions, particularly in complex and forested terrain, the half-cone opening angle can additionally affect the magnitude of the lidar error. The exact configuration of the used lidar device must, therefore, be known to estimate the lidar error. In the context of a wind resource assessment, an accurate estimation of the prospective lidar errors should be carried out before the measurement campaign. By taking into account the additional uncertainty of the lidar error correction, it is then possible to make an early decision on whether a lidar measurement is feasible at the given site (compare chapter 3.3).

8 Outlook

The results of the dissertation show that RANS CFD models should be preferred for lidar error estimations in complex terrain, in particular at sites with high roughness length or in the presence of forest. However, recent standards and guidelines such as the IEC standard 61400-12-1 (International Standard IEC 61400-12-1:2017) or the German technical guideline of wind resource assessments TR6 (FGW e.V. 2017) either recommend to use simple models (e.g., linearized models) to estimate the lidar error or provide inexplicit guidance. Based on the findings of this dissertation, it should be achieved that state-of-the-art RANS CFD models that are capable of modeling the wind flow above forested terrain replace the current recommendations in future revisions.

In order to accomplish this and for a better validation of the findings of this thesis, a broader basis of measurement data would be beneficial. Ideally, a measurement campaign with the specific purpose to validate the key findings of this dissertation could be designed at and around a forested hill. The measurement site should be carefully chosen under consideration of the dimensions H and L of the hill parallel to the prevailing wind directions. Furthermore, the possible z/L ratios should be examined, so that the dependence of the lidar error on height can be validated. The measurement site should at least be equipped with a high measurement mast and a Doppler lidar.

In particular, with regards to atmospheric stability, three-dimensional terrain could enable an investigation of more complex flow patterns in different stability situations. Especially for stable stratification, where the flow could tend to stream around the hill, rather than over it, the results might be different for three-dimensional terrain (Leo et al. 2016). For this, probably a more advanced atmospheric stability model will be needed, which includes the temperature equation (Meteodyn 2014). So far, there is no evaluation of the influence of atmospheric stability on the lidar error based on measurement data available in the literature.

As described in chapter 6.3.1, the lidar error derived from measurement data shows much scattering around the mean value. An analysis of this behavior is difficult without detailed data of the flow conditions at the measurement points of the lidar. In a future research campaign, a measurement setup could be designed that allows measuring the three-dimensional wind vector close to the measurement points of a Doppler lidar. In conjunction with advanced remote sensing technology, such as scanning lidars, a complete picture of the flow along and around a three-dimensional hill could be created. By this, also the effects of forest and atmospheric stability on speed-up, flow inclination and flow separation in the lee of the hill could be analyzed in more detail. A profound model validation could be based on this detailed data basis, leading to more accurate lidar error estimations in the future.

Beyond the pathway of using conventional Doppler lidar profilers in complex terrain and correct their error by flow modeling, also the application of novel technologies is possible. In chapter 1.3.6, different current research projects are described that develop lidars with alternative measurement principles. However, these lidar devices are not yet available. Upcoming research projects must first evaluate their applicability for wind energy applications in complex terrain.

Scanning Doppler lidars in so-called “multi-lidar” setups, where two to three lidars are measuring with intersecting probe volumes, can significantly reduce the lidar error in

complex terrain (compare e.g. Pauscher et al. (2016)). On the other hand, these devices are expensive when compared to lidar profilers and it is labor-intensive to operate them over a more extended period. Depending on future developments, they could become a valuable tool for many wind energy applications, providing more insight into the actual flow characteristics at complex terrain sites (Mann et al. 2017). The model-study in this dissertation shows, that the half-cone opening angle of a lidar can have a significant influence on the resulting lidar error. Scanning lidars offer the possibility to evaluate this finding by adapting the elevation angle of the laser beam to evaluate the model results. An optimization routine could be developed that aims at lower lidar errors by adjusting the half-cone opening angle to the site-specific flow characteristics. Evaluation against a measurement mast and a standard Doppler lidar with a constant half-cone opening angle would be needed, to validate this concept.

Additional and more complex flow features such as flow separation, which might occur in very complex terrain situations, have not been treated within the context of this thesis. For this, a non-stationary flow model could be used to analyze the influence of periodic recirculation phenomena behind escarpments. Such a model, together with more advanced turbulence modeling, could also help to explain the scatter that occurs in ten-minute values of lidar measurement errors in real-world applications.

9 Publication bibliography

Albers, Axel (2006): Evaluation of ZephIR. Edited by Deutsche WindGuard Consulting GmbH. Varel. Available online at https://windguard.de/veroeffentlichungen.html?file=files/cto_layout/img/unternehmen/veroeffentlichungen/2006/Evaluation%20of%20Zephir.pdf, checked on 4/25/2019.

Albers, Axel; Janssen, Ailt-Wiard (2008): Evaluation of Windcube. Internal Project. Deutsche WindGuard Consulting GmbH. Varel.

Antoniou, I.; Courtney, Michael S.; Jørgensen, Hans E.; Mikkelsen, T.; Hunerbein, S. Von; Bradley, Stuart et al. (2007): Remote sensing the wind using Lidars and Sodars.

Antoniou, I.; Ejsing Jørgensen, Hans; Mikkelsen, T.; Friis Pedersen, Troels; Warmbier, G.; Smith, D. (2004): Comparison of wind speed and power curve measurements using a cup anemometer, a LIDAR and a SODAR. In European Wind Energy Association (EWEA) (Ed.): Scientific proceedings. London, pp. 47–51.

Ayotte, Keith W. (2008): Computational modeling for wind energy assessment. In *Journal of Wind Engineering and Industrial Aerodynamics* 96 (10-11), pp. 1571–1590. DOI: 10.1016/j.jweia.2008.02.002.

Basse, Alexander; Callies, Doron; Hahn, Berthold (2017): Windmessungen und Windgutachten für die Standortbewertung von Windenergieanlagen an Land: Methoden und Analyse. With assistance of Daniela Niethammer. Edited by Deutsch-französisches Büro für die Energiewende (DFBEW). Fraunhofer IWES. Kassel. Available online at https://energie-fr-de.eu/de/windenergie/nachrichten/leser/hintergrundpapier-zu-windmessungen-und-windgutachten-fuer-die-standortbewertung-von-wea.html.

Bechmann, A.; Sørensen, N. N.; Berg, J.; Mann, J.; Réthoré, P.-E. (2011): The Bolund Experiment, Part II: Blind Comparison of Microscale Flow Models. In *Boundary-Layer Meteorol* 141 (2), pp. 245–271. DOI: 10.1007/s10546-011-9637-x.

Behrens, Paul; O'Sullivan, J.; Archer, R.; Bradley, Stuart (2012): Underestimation of Monostatic Sodar Measurements in Complex Terrain. In *Boundary-Layer Meteorol* 143 (1), pp. 97–106. DOI: 10.1007/s10546-011-9665-6.

Belcher, S. E.; Finnigan, J. J.; Harman, Ian N. (2008): Flow through forest canopies in complex terrain. In *Ecological Applications* (18), pp. 1436–1453.

Belcher, S. E.; Harman, Ian N.; Finnigan, J. J. (2012): The Wind in the Willows: Flow in Forest Canopies in Complex Terrain. In *Annual Review of Fluid Mechanics* (44), pp. 479–504.

Bezault, Céline; Sanquer, Stéphane; Nadah, Mohamed (2012): Correction tool for Lidar in complex terrain based on CFD outputs. In EWEA (Ed.): EWEA 2012 Proceedings. Brussels. Available online at http://proceedings.ewea.org/annual2012/allfiles2/1258_EWEA2012presentation.pdf, checked on 8/4/2015.

Bingöl, F. (2009): Complex terrain and wind lidars. Dissertation. Technical University of Denmark, Roskilde. Risoe National Laboratory for Sustainable Energy.

Bingöl, Ferhat; Mann, Jakob; Foussekis, Dimitri (2009): Conically scanning lidar error in complex terrain. In *Meteorologische Zeitschrift* 18 (2), pp. 189–195.

BMWI (2014): Bekanntmachung. Forschungsförderung im 6. Energieforschungsprogramm "Forschung für eine umweltschonende, zuverlässige und bezahlbare Energieversorgung". Edited by Bundesministerium der Justiz und für Verbraucherschutz. Berlin.

BMWI (2018a): Innovationen für die Energiewende. 7. Energieforschungsprogramm der Bundesregierung. Edited by Bundesministerium für Wirtschaft und Energie (BMWi). Berlin.

BMWI (2018b): Sechster Monitoring-Bericht zur Energiewende - Energie der Zukunft. Berichtsjahr 2016 - Kurzfassung. Edited by Bundesministerium für Wirtschaft und Energie (BMWi).

Boquet, M.; Parmentier, R.; Sauvage, L.; Cariou, Jean-Pierre; Albergel, A. (2010): Theoretical, CFD Analysis and Correction Methodology of Lidar Wind Profile Measurement in Complex Terrain. In EWEA (Ed.): EWEC 2010 Proceedings. Brussels.

Bowen, A. J.; Mortensen, N. G. (1996): Exploring the limits of WAsP the wind atlas analysis and application program. In A. Zervos, H. Ehmann, P. Helm (Eds.): 1996 European Union wind energy conference. Proceedings: H.S. Stephens and Associates, pp. 584–587.

Bradley, Stuart (2008): Wind speed errors for LIDARs and SODARs in complex terrain. In *IOP Conf. Ser.: Earth Environ. Sci.* 1, p. 12061. DOI: 10.1088/1755-1315/1/1/012061.

Bradley, Stuart (2012): A Simple Model for Correcting Sodar and Lidar Errors in Complex Terrain. In *J. Atmos. Oceanic Technol.* 29 (12), pp. 1717–1722. DOI: 10.1175/JTECH-D-12-00106.1.

Bradley, Stuart; Strehz, Alexander; Emeis, Stefan (2015): Remote sensing winds in complex terrain - a review. In *Meteorologische Zeitschrift* PrePub. Available online at https://www.schweizerbart.de/papers/metz/detail/prepub/84734/Remote_sensing_winds_in_complex_terrain_a_review.

Buck, Matthias; Graf, Andreas; Graichen, Patrick (2019): European Energy Transition 2030: The Big Picture. Ten Priorities for the next European Commission to meet the EU's 2030 targets and accelerate towards 2050. Edited by Agora Energiewende. Berlin.

Bundesregierung (2010): Energiekonzept für eine umweltschonende, zuverlässige und bezahlbare Energieversorgung.

Callies, Doron (2014): Analyse des Potenzials der Onshore-Windenergie in Deutschland unter Berücksichtigung von technischen und planerischen Randbedingungen. Dissertation. Universtität Kassel, Kassel.

Cariou, Jean-Pierre (2007): An innovative and autonomous 1.5µm coherent lidar for PBL wind monitoring. 14th Coherent Laser Radar Conference 2007 (CLRC XIV). Snowmass, 2007.

Clifton, Andrew (2015): Remote Sensing of Complex Flows by Doppler Wind Lidar. Issues and Preliminary Recommendations. Edited by National Renewable Energy Laboratory (NREL). Boulder, Colorado.

Clifton, Andrew; Clive, Peter; Gottschall, Julia; Schlipf, David; Simley, Eric; Simmons, Luke et al. (2018): IEA Wind Task 32: Wind Lidar Identifying and Mitigating Barriers to the Adoption of Wind Lidar. In *Remote Sensing* 10 (3), p. 406. DOI: 10.3390/rs10030406.

Clive, Peter J. M. (2008): Compensation of bias in Lidar wind resource assessment. In *Wind Engineering* 32 (5), pp. 415–432.

Courtney, Michael S.; Wagner, Rozenn; Lindelöw, Petter (2008): Testing and comparison of lidars for profile and turbulence measurements in wind energy. In *IOP Conf. Ser.: Earth Environ. Sci.* 1 (1).

Dellwik, E.; Jensen, Niels Otto; Landberg, Lars (2004): Winds and forests. General recommendations for using WAsP. Workshop on Trees. Scotland, 2004.

Dellwik, Ebba; Landberg, Lars; Jensen, Niels Otto (2006): WAsP in the Forest. In *Wind Energy* 9 (3), pp. 211–218.

EEA (2009): Europe's onshore and offshore wind energy potential. An assessment of environmental and economic constraints. Luxembourg: Publications Office (Technical report (European Environment Agency. Online), 6/2009).

EEA (Ed.) (2018): Renewable energy in Europe — 2018. Recent growth and knock-on effects. Copenhagen (EEA Report, 20/2018).

Eggert, M.; Gutsmuths, C.; Müller, H.; Többen, H. (2015): A New Bistatic Wind Lidar for Highly Resolved Wind Vector Measurements. In DEWEK (Ed.): DEWEK 2015 Proceedings.

Emeis, Stefan (2011): Surface-Based Remote Sensing of the Atmospheric Boundary Layer. Dordrecht: Springer Netherlands (Atmospheric and Oceanographic Sciences Library, 40).

Emeis, Stefan (2014): Current issues in wind energy meteorology. In *Met. Apps* 21 (4), pp. 803–819. DOI: 10.1002/met.1472.

Emeis, Stefan (2018): Wind energy meteorology. Atmospheric physics for wind power generation. 2nd ed. Berlin, New York: Springer (Green energy and technology).

Emeis, Stefan; Harris, Michael; Banta, Robert M. (2007): Boundary-layer anemometry by optical remote sensing for wind energy applications. In *Meteorologische Zeitschrift* 16 (4), pp. 337–347.

ETIP Wind (2016): Strategic research and innovation agenda 2016. Edited by European Technology & Innovation Platform on Wind Energy (ETIP Wind). Brussels.

ETIP Wind (2018): Strategic Research and Innovation Agenda 2018. Edited by European Technology & Innovation Platform on Wind Energy (ETIP Wind). Brussels.

European Commission (2018): Communication from the Commission to the European Parliament, the European Council, the Council, the European Economic and Social Committee, the Committee of the Regions and the European Investment Bank. A Clean Planet for all A European strategic long-term vision for a prosperous, modern, competitive and climate neutral economy. Brussels.

European Commission (2019): Report from the Commission of the European Parliament, the Council, the European Economic and Social Committee and the

Committee of the Regions. Renewable Energy Progress Report. Edited by European Commission. Brussels.

FGW e.V. (2017): Technische Richtlinien für Windenergieanlagen Teil 6 (TR6). Bestimmung von Windpotenzial und Energieerträgen. Revision 10. Edited by FGW e.V. Berlin.

Fiedler, Stephan; Krebs, Henning; Müller, Stefan; Theunert, Sabine (2015): Ringvergleich Windgutachten des BWEWindgutachterbeirats. Ablauf und Ergebnisse. Edited by Bundesverband Windenergie (BWE). Available online at https://www.wind-energie.de/fileadmin/redaktion/dokumente/publikationen-oeffentlich/beiraete/windgutachterbeirat/20160208-ergebnisbericht-ringvergleich-windgutachten.pdf, checked on 12/10/2019.

Finnigan, J. J.; Belcher, S. E. (2004): Flow over a hill covered with plant canopy. In *Q.J Royal Met. Soc.* 130 (596), pp. 1–29.

Foken, Thomas (2016): Angewandte Meteorologie. Berlin, Heidelberg: Springer Berlin Heidelberg.

Foussekis, Dimitri (2009): Investigating Wind Flow properties in Complex Terrain using 3 Lidars and a Meteorological Mast. In EWEA (Ed.): EWEC 2009 Proceedings. Brussels.

Foussekis, Dimitri (2011): Operation of the Windcube V2 lidar at CRES Test Station. With assistance of N. Stefanatos, F. Mouzakis. Edited by Center for Renewable Energy Sources and Saving (CRES). Pikermi, Greece.

Fujii, Takashi; Fukuchi, Tetsuo (Eds.) (2005): Laser remote sensing. Boca Raton: Taylor & Francis (Optical engineering, 97).

Garratt, John Roy (1994): The atmospheric boundary layer. 1. paperback ed. (with corr.). Cambridge u.a: Univ. Press (Cambridge atmospheric and space science series).

Gottschall, J.; Courtney, M. (2010): Verification test for three WindCube"T"M WLS7 LiDARs at the Høvsøre test site (RISØ-R--1732(EN)).

Gottschall, Julia; Courtney, Michael S.; Wagner, Rozenn; Jørgensen, Hans E.; Antoniou, I. (2011): Lidar profilers in the context of wind energy - a verification procedure for tracable measurements. In *Wind Energy* 15 (1), pp. 147–159.

Gottschall, Julia; Lindelöw-Mardsen, Petter; Courtney, Michael S. (2009): Verification of the SgurrEnergy Galion lidar using mast-mounted instruments. Risoe National Laboratory.

HALO Photonics (2019): HALO Photonics Website. Galion. HALO Photonics. Available online at http://halo-photonics.com/Galion_LiDAR_system.htm, checked on 11/29/2019.

Harris, Michael; Locker, I.; Douglas, N.; Girault, Romain; Abiven, C.; Brady, O. (2010): Validated adjustment of remote sensing bias in complex terrain using CFD. In EWEA (Ed.): EWEC 2010 Proceedings. Brussels.

Howard, Allen Q.; Naini, Thomas (2012): Four Methods for LIDAR Retrieval of Microscale Wind Fields. In *Remote Sensing* 4 (8), pp. 2329–2355. DOI: 10.3390/rs4082329.

Hurley, Peter J. (1997): AN EVALUATION OF SEVERAL TURBULENCE SCHEMES FOR THE PREDICTION OF MEAN AND TURBULENT FIELDS IN COMPLEX TERRAIN. In *Boundary-Layer Meteorol* 83 (1), pp. 43–73. DOI: 10.1023/A:1000217722421.

HVBG (2010): Digitales Landschaftsmodell / Digitales Geländemodell. Wiesbaden: Hessische Verwaltung für Bodenmanagement und Geoinformationen.

IPCC (Ed.) (2015): Climate change 2014. Synthesis report. With assistance of R. K. Pachauri, Leo Meyer. Geneva, Switzerland: Intergovernmental Panel on Climate Change.

IPCC (2018): Global warming of 1.5°C. IPPC Special Report - Summary for Policymakeres. Edited by IPCC. Geneva, Switzerland.

Jackson, P. S.; Hunt, J. C. R. (1975): Turbulent wind flow over a low hill. In *Q.J Royal Met. Soc.* 101 (430), pp. 929–955. DOI: 10.1002/qj.49710143015.

Jiang, Zixiao; Blondel, P.; Xie, Xin; Delauney, Didier: Atmospheric stability characterization for CFD computations. Edited by Meteodyn. Nantes, France.

Jokela, T.; Antikainen, P.; Vignaroli, A.; Öhrvall, F.; Mannelqvist, T.; Eriksson, D. (2013): Windcube Validation Measurements in Northern Sweden. In EWEA (Ed.): EWEA 2013 Proceedings. Brussels.

Khadiri-Yazami, Zouhair; Callies, Doron; Bosewitz, M.; Vöcking, P.; Baulig, C.; Klaas, B., Predehl, K. (2019): A novel multi-LiDAR system for accurate wind and turbulence measurements in complex terrain – State of the project. In Wind Europe (Ed.): Wind Europe Technology Workshop. 5th Edition. Resource Assessment 2019. Brussels, 27.-28.06.2019. Brussels.

Kim, Hyun-Goo; Meissner, Catherine (2017): Correction of LiDAR measurement error in complex terrain by CFD: Case study of the Yangyang pumped storage plant. In *Wind Engineering* 41 (4), pp. 226–234. DOI: 10.1177/0309524X17709725.

Kindler, Detlef; Oldroyd, Andrew; MacAskill, Allan; Finch, Danny (2007): An eight month test campaign of the Qinetiq ZephIR system. Preliminary results. In *Meteorologische Zeitschrift* 16 (5), pp. 479–489.

Klaas, Tobias; Pauscher, Lukas; Callies, Doron (2015): LiDAR-mast deviations in complex terrain and their simulation using CFD. In *metz*. DOI: 10.1127/metz/2015/0637.

Krishnamurthy, R.; Boquet, M. (2014): Case studies of WINDCUBE measurement uncertainty for complex terrrain unsing Flow Complexity Recognition. In EWEA (Ed.): EWEA 2014 Proceedings. Brussels.

Lackner, Matthew; Rogers, Anthony; Manwell, James (2007): Uncertainty Analysis in Wind Resource Assessment and Wind Energy Production Estimation. In : 45th AIAA Aerospace Sciences Meeting and Exhibit. 45th AIAA Aerospace Sciences Meeting and Exhibit. Reno, Nevada. [Reston, VA]: [American Institute of Aeronautics and Astronautics], p. 257.

Leo, Laura S.; Thompson, Michael Y.; Di Sabatino, Silvana; Fernando, Harinda J.S. (2016): Stratefied flow past a hill: Dividing streanline concept revisited. In *Boundary Layer Meteorology* (159), pp. 611–634.

Leosphere (2017): Windcube FCR measurements. Principles, performance and recommendations for use of the Flow Complexity Recognition (FCR) algorithm for the Windcube ground-based Lidar. Paris.

Lindelöw, Petter (2007): Fiber based coherent lidars for remote wind sensing. PhD.

Lütkehaus, Insa; Salecker, Hanno; Adlunger, Kirsten (2013): Potenzial der Windenergie an Land. Studie zur Ermittlung des bundesweiten Flächen- und Leistungspotenzials der Windenergienutzung an Land. Edited by Umweltbundesamt. Dessau-Roßlau.

Mann, J.; Angelou, N.; Arnqvist, J.; Callies, D.; Cantero, E.; Arroyo, R. Chávez et al. (2017): Complex terrain experiments in the New European Wind Atlas. In *Philosophical transactions. Series A, Mathematical, physical, and engineering sciences* 375 (2091). DOI: 10.1098/rsta.2016.0101.

Mann, Jakob; Ott, Soeren; Joergensen, Bo Hoffmann; Frank, Helmuth P. (2002): WAsP Engineering 2000. Edited by Risoe National Laboratory. Roskilde, Denmark.

Masurowski, Frank (2016): Eine deutschlandweite Potenzialanalyse für die Onshore-Windenergie mittels GIS einschließlich der Bewertung von Siedlungsdistanzenänderungen. Dissertation. Universität Osnabrück, Osnabrück.

Measnet (2016): MEASNET Prrocedure: Evaluation of Site-Specific Wind Conditions. Version 2. Measnet.

Mehnert, Sebastian (2017): Modellierung des Einflusses der Gesamtunsicherheit von Windgutachten auf die langjährige Windpark-Projektfinanzierung. Bachelorarbeit. Universität Kassel, Kassel. Fachgebiet Integrierte Energiesysteme.

Meissner, Catherine; Boquet, M. (2011): Correction of lidar remote sensing measurements by CFD simulations. In EWEA (Ed.): EWEA 2011. Brussels. European Wind Energy Association (EWEA).

Meteodyn (2014): Software documentation. Edited by Meteodyn. Nantes, France.

Meteodyn (2017): Meteodyn WT 5.3. Webinar. Edited by Meteodyn. Nantes, France.

Mikkelsen, T. (2014): Lidar-based Research and Innovation at DTU Wind Energy – a Review. In *J. Phys.: Conf. Ser.* 524, p. 12007. DOI: 10.1088/1742-6596/524/1/012007.

NRG Systems (2018): NRG Systems Purchases Direct Detect Lidar Technology Developed by Pentalum, Pairs Industry Leading Service with Market Leading Remote Sensing Value. Press Release. Hinesburg, VT, USA. Available online at https://www.nrgsystems.com/news-media/nrg-systems-purchases-direct-detect-lidar-technology-developed-by-pentalum-pairs-industry-leading-service-with-market-leading-remote-sensing-value/, checked on 11/29/2019.

Oertel, Stefan; Eggert, Michael; Gutsmuths, Christian; Wilhelm, Paul; Müller, Harald; Többen, Helmut (2019): Validation of three-component wind lidar sensor for traceable highly resolved wind vector measurements. In *J. Sens. Sens. Syst.* 8 (1), pp. 9–17. DOI: 10.5194/jsss-8-9-2019.

Palma, J.M.L.M.; Castro, F. A.; Ribeiro, L. F.; Rodrigues, A. H.; Pinto, A. P. (2008): Linear and nonlinear models in wind resource assessment and wind turbine micro-

siting in complex terrain. In *Journal of Wind Engineering and Industrial Aerodynamics* 96 (12), pp. 2308–2326. DOI: 10.1016/j.jweia.2008.03.012.

Pauliac, Romain (2009): WINDCUBE User's Manual. Edited by Leosphere SAS. Orsay, France.

Pauscher, Lukas; Callies, Doron; Klaas, Tobias; Foken, Thomas (2018): Wind observations from a forested hill: Relating turbulence statistics to surface characteristics in hilly and patchy terrain. In *Meteorol. Z.* 27 (1), pp. 43–57. DOI: 10.1127/metz/2017/0863.

Pauscher, Lukas; Vasiljevic, Nikola; Callies, Doron; Lea, Guillaume; Mann, Jakob; Klaas, Tobias et al. (2016): An Inter-Comparison Study of Multi- and DBS Lidar Measurements in Complex Terrain. In *Remote Sensing* 8 (9), p. 782. DOI: 10.3390/rs8090782.

Rathmann, O.; Mortensen, N. G.; Landberg, L.; Bowen, A. (1996): Assessing the accuracy of WAsP in non-simple terrain. In M. Anderson (Ed.): Wind energy conversion 1996. Proceedings: Mechanical Engineering Publications Limited, pp. 413–418.

Rohrig, Kurt (2018): Windenergie Report Deutschland 2017. With assistance of Michael Durstewitz, Guillaume Behem, Volker Berkhout. Edited by Kurt Rohrig. Fraunhofer-Institut für Energiewirtschaft und Energiesystemtechnik IEE. Kassel.

Ross, A. N.; Arnold, S.; Vosper, S. B.; Mobbs, S. D.; Dixon, N.; Robins, A. G. (2004): A comparison of wind-tunnel experiments and numerical simulations of neutral and stratified flow over a hill. In *Boundary-Layer Meteorol* 113 (3), pp. 427–459. DOI: 10.1007/s10546-004-0490-z.

Ross, A. N.; Vosper, S. B. (2005): Neutral turbulent flow over forested hills. In *Q.J Royal Met. Soc.* 131 (609), pp. 1841–1862.

Schorer, Till; Neddermann, Bernd; Molly, Jens Peter (2015): Kurzstudie zum 1-stufigen EEG Vergütungsmodell im Rahmen der Ausschreibung für Windenergieprojekte. UL International GmbH - DEWI im Auftrrag von Landesverband Erneuerbare Energien NRW e.V. Wilhelmshaven. Available online at www.lee-nrw.de/wp-content/uploads/2015/11/DEWI_RS15_04608_final.pdf, checked on 12/11/2019.

Shannak, B.; Träumner, K.; Wieser, A.; Corsmeier, U.; Kottmeier, Ch (2012): Flow characteristics above a forest using light detection and ranging measurement data. In *Proceedings of the Institution of Mechanical Engineers, Part C: Journal of Mechanical Engineering Science* 226 (4), pp. 921–939. DOI: 10.1177/0954406211417944.

Smith, David A.; Harris, Michael; Coffey, Adrian S. (2006): Wind Lidar Evaluation at the Danish Wind Test Site in Hoevsoere. In *Wind Energy* 9, pp. 87–93.

Stein, Detlef (2014): Spidar Performance Verification at DNV GL Test Site in Janneby, Germany. With assistance of Andreas Beeken, Peter Frohböse. Edited by GL Garrad Hassan Deutschland GmbH.

Stull, Roland B. (1988): An Introduction to Boundary Layer Meteorology. Dordrecht: Springer Netherlands.

The European Parliament and the Council of the European Union (2009): Directive 2009/28/EC of the European Parliament and of the Council of 23 April 2009 on the promotion of the use of energy from renewable sources and amending and subsequently repealing Directives 2001/77/EC and 2003/30/EC. 2009/28/EC. In *Official Journal of the European Union*.

The European Parliament and the Council of the European Union (2018): Directive (EU) 2018/ 2001 of the European Parliament and of the Council of the of 11 December 2018 - on the promotion of the use of energy from renewable sources. 2018/2001. In *Official Journal of the European Union*.

TPWind (2014): Strategic Research Agenda / Market Deployment Strategy. Edited by European Wind Energy Technology Platform. Brussels.

Troen, Ib (1989): European wind atlas. Roskilde: Risø National Laboratory.

Troen, Ib; Baas, A. de (1990): A spectral diagnositic model for wind flow simulations in complex terrain. In American Meteorological Society (Ed.): 9. Symposium on turbulence and diffusion, vol. 9. With assistance of N.O. Jensen, L. Kristensen, S.E. Larsen. Boston, MA, pp. 243–249.

UNFCCC (2016): Decision 1/CP.21. Adoption of the paris agreement. Paris.

UNFCCC (2019): Paris Agreement. Status of Ratification. Available online at https://unfccc.int/process/the-paris-agreement/status-of-ratification, checked on 4/17/2019.

Vasiljevic, Nikola (2014): A time-space synchronization of coherent Doppler scanning lidars for 3D measurements of wind fields. Dissertation. Technical University of Denmark, Roskilde. DTU Wind Energy.

Wagner, Johannes; Gerz, Thomas; Wildmann, Norman; Gramitzky, Kira (2019): Long-term simulation of the boundary layer flow over the double-ridge site during the Perdigão 2017 field campaign. In *Atmos. Chem. Phys.* 19 (2), pp. 1129–1146. DOI: 10.5194/acp-19-1129-2019.

Wagner, Rozenn; Bejdic, Jasmin (2014): Windcube + FCR test in Hrgud, Bosnia & Herzegovina Final Report. DTU Wind Energy.

Wandinger, Ulla (2005): Introduction to Lidar. In Claus Weitkamp (Ed.): Lidar. Range-Resolved Optical Remote Sensing of the Atmosphere. New York, NY: Springer Science+Business Media Inc (Springer Series in Optical Sciences, 102).

Weitkamp, Claus (Ed.) (2005): Lidar. Range-Resolved Optical Remote Sensing of the Atmosphere. New York, NY: Springer Science+Business Media Inc (Springer Series in Optical Sciences, 102). Available online at http://site.ebrary.com/lib/alltitles/docDetail.action?docID=10134024.

Werner, Christian (2005): Doppler Wind Lidar. In Claus Weitkamp (Ed.): Lidar. Range-Resolved Optical Remote Sensing of the Atmosphere. New York, NY: Springer Science+Business Media Inc (Springer Series in Optical Sciences, 102).

Wilson, J. D.; Finnigan, J. J.; Raupach, M. R. (1998): A first-order closure for distrurbed plant-canopy flows, and its application to winds in a canopy on a ridge. In *Q.J Royal Met. Soc.* 124, pp. 705–732.

International Standard IEC 61400-12-1:2017, 3/3/2017: Wind energy generation systems - Part 12-1: Power performance measurements of electricity producing wind turbines.

IEC 61400-12-1, 2013: Wind turbines - Part 12-1: Power performance measurements of electricity producing wind turbines (2nd Committee Draft)).

10 Appendix

10.1 Model equations for Meteodyn WT

All of the following equations are taken from the software documentation of Meteodyn WT (Meteodyn 2014). They are based on the assumption of steady-state, incompressible and isotherm flow and the RANS equations.

Mass conservation equation:

$$\frac{\partial \rho \bar{u}_i}{\partial x_i} = 0$$

Momentum conservation equation:

$$-\frac{\partial\left(\rho \bar{u}_j \bar{u}_i\right)}{\partial x_j} - \frac{\partial \bar{p}}{\partial x_i} + \frac{\partial}{\partial x_j}\left[\mu\left(\frac{\partial \bar{u}_i}{\partial x_j} + \frac{\partial \bar{u}_j}{\partial x_i}\right) - \rho\overline{u'_i u'_j}\right] + F_i = 0$$

Reynolds stress tensor:

$$-\rho\overline{u'_i u'_j} = \nu_t\left(\frac{\partial \bar{u}_i}{\partial x_j} + \frac{\partial \bar{u}_j}{\partial x_i}\right)$$

Turbulent viscosity:

$$\nu_t = k^{1/2} L_T$$

Turbulent kinetic energy:

$$k = \frac{1}{2} u'_i u'_i$$

Turbulent kinetic energy transport equation:

$$U_j \frac{\partial k}{\partial x_j} = p_k - \varepsilon + \frac{\partial}{\partial x_j}\left[\left(\frac{\nu_t}{\sigma_k}\right)\frac{\partial k}{\partial x_j}\right], with \begin{cases} \varepsilon = C_\mu \dfrac{\nu_t}{L_T} k \\ p_k = \nu_t\left(\dfrac{\partial \bar{u}_i}{\partial x_j} + \dfrac{\partial \bar{u}_j}{\partial x_i}\right)\dfrac{\partial \bar{u}_j}{\partial x_j} \end{cases}$$

Turbulent length scale:

$$L_T = \sqrt{2}{S_m}^{3/2} l \begin{cases} \frac{1}{l} = \left(\frac{1}{l_0} + \frac{1}{\kappa z}\right), where\ z = height \\ C_\mu = \frac{4S_m}{B_1} \\ S_m = \begin{cases} 1{,}96\frac{(0.1912 - R_{if})(0.2341 - R_{if})}{(1 - R_{if})(0.2231 - R_{if})}, if\ R_{if} < 0.16 \\ 0.085, if\ R_{if} \geq 0.16 \end{cases} \\ B_1 = 16.6 \\ l_0 = 100m \\ \kappa = 0{,}41 \end{cases}$$

Through the flux Richardson number R_{if} the turbulence model takes into account atmospheric stability. The flux Richardson number is calculated based on the Monin-Obukhov length.

10.2 Stability model equations for Meteodyn WT

The equations for the stability models (and the boundary conditions) of Meteodyn WT are given in the following sub-chapters. The following equations are an excerpt from Meteodyn (2014) and not all details are given.

Generally computations are based on the geostrophic wind u_g:

$$\left(\frac{u_g}{u_*}\right)^2 = \left(\ln\left(\frac{z_h}{z_0}\right) - A_2\right)^2 + {B_2}^2$$

Where A_2 and B_2 are empirical constants taken from (Garratt 1994).

10.2.1 Two layer model for classes 0 to 6

Wind speed profiles in the two-layer model:

$$z < z_s: \quad \bar{u} = \frac{u_*}{\kappa}\left[\ln\left(\frac{z}{z_0}\right) - \Psi\left(\frac{z}{L^*}\right)\right]$$

$$z_s < z < z_h: \quad \bar{u} = u_g - \left(u_g - u_{zs}\right)\frac{\ln\left(\frac{z_h}{z}\right)}{\ln\left(\frac{z_h}{z_s}\right)}$$

$$z > z_h: \quad \bar{u} = u_g$$

The function $\Psi\left(\frac{z}{L^*}\right)$ corrects the logarithmic wind profiles for atmospheric stability in dependence of the Monin-Obukhov-Length (Meteodyn 2014).

10.2.2 Three layer model for classes 7 to 9

Wind speed profiles in the three-layer model:

$$z \le z_s: \qquad \bar{u} = u_* \left[\ln\left(\frac{z}{z_0}\right) + 5\frac{z}{L^*} \right]$$

$$z_s < z < z_h: \qquad \bar{u} = u_* \left[\ln\left(\frac{z}{z_0}\right) + 5\frac{z_s}{L^*} + 5\frac{z - z_s}{L_{trans}} \right]$$

$$z_h < z \le 3z_h: \qquad \bar{u} = u_* \left[\ln\left(\frac{z}{z_0}\right) + 5\frac{z_s}{L^*} + 5\frac{z_h - z_s}{L_{trans}} + 5\frac{z - z_h}{L_{out}} \right]$$

$$3z_h < z: \qquad \bar{u} = u_* \left[\ln\left(\frac{z}{z_0}\right) + 5\frac{z_s}{L^*} + 5\frac{z_h - z_s}{L_{trans}} + 5\frac{2z_h}{L_{out}} \right]$$

The factors L_{trans} and L_{out} are the so-called slope coefficients in the transitional layer and the outer layer (compare Figure 4.2) (Meteodyn 2014).

10.3 Additional result plots

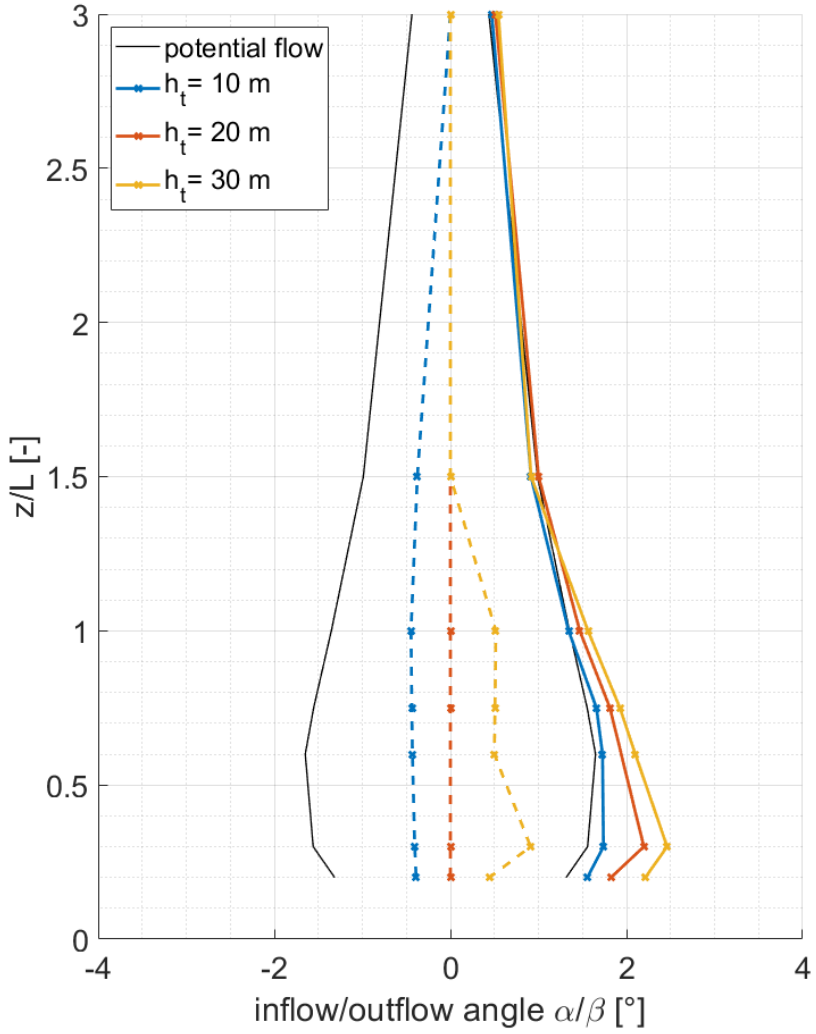

Figure 10.1: Inflow angle α (dashed) and outflow angle β (solid) in dependence of tree height $\boldsymbol{h_t}$. Results from Meteodyn WT (colored) and from the potential flow model (black) at 150 m measurement height and for a $\boldsymbol{\varphi}$ of 30° for an H/L ratio of 0.2. The forest density is medium.

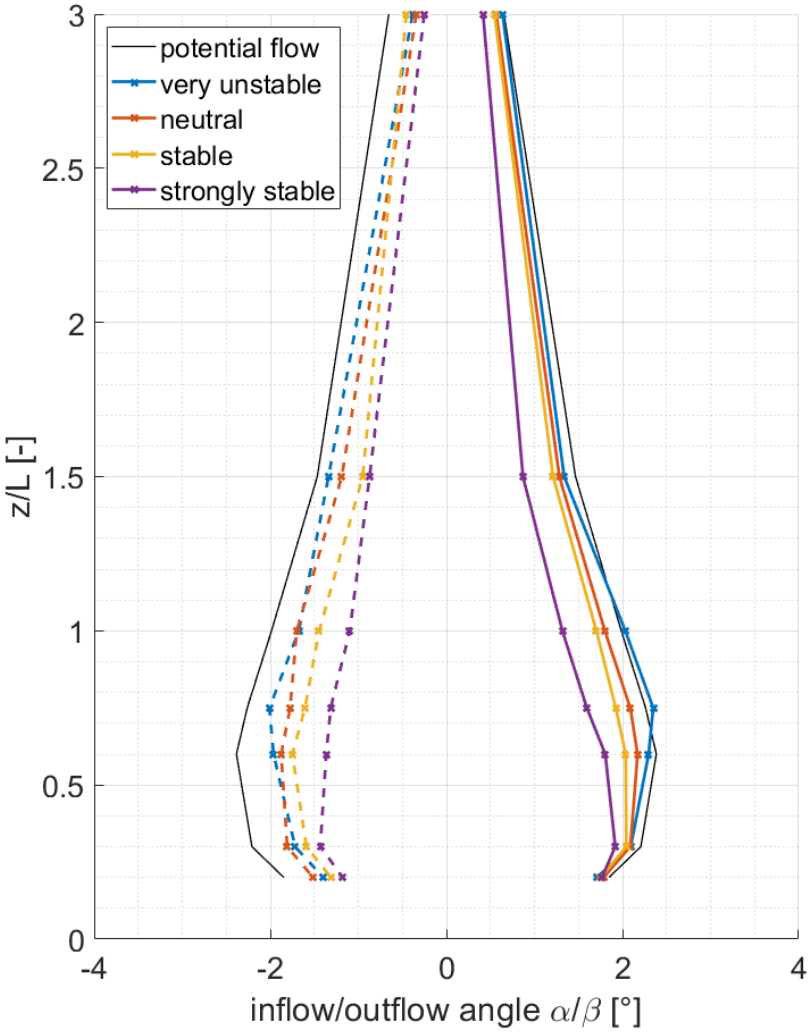

Figure 10.2: Inflow angle α (dashed) and outflow angle β (solid) in dependence of atmospheric stability**.** Results from Meteodyn WT (colored) and from the potential flow model (black) at 150 m measurement height and for a $\boldsymbol{\varphi}$ of 30° for an H/L ratio of 0.3. Meteodyn WT results for a low roughness length $\boldsymbol{z_0}$ of 0.005 m.

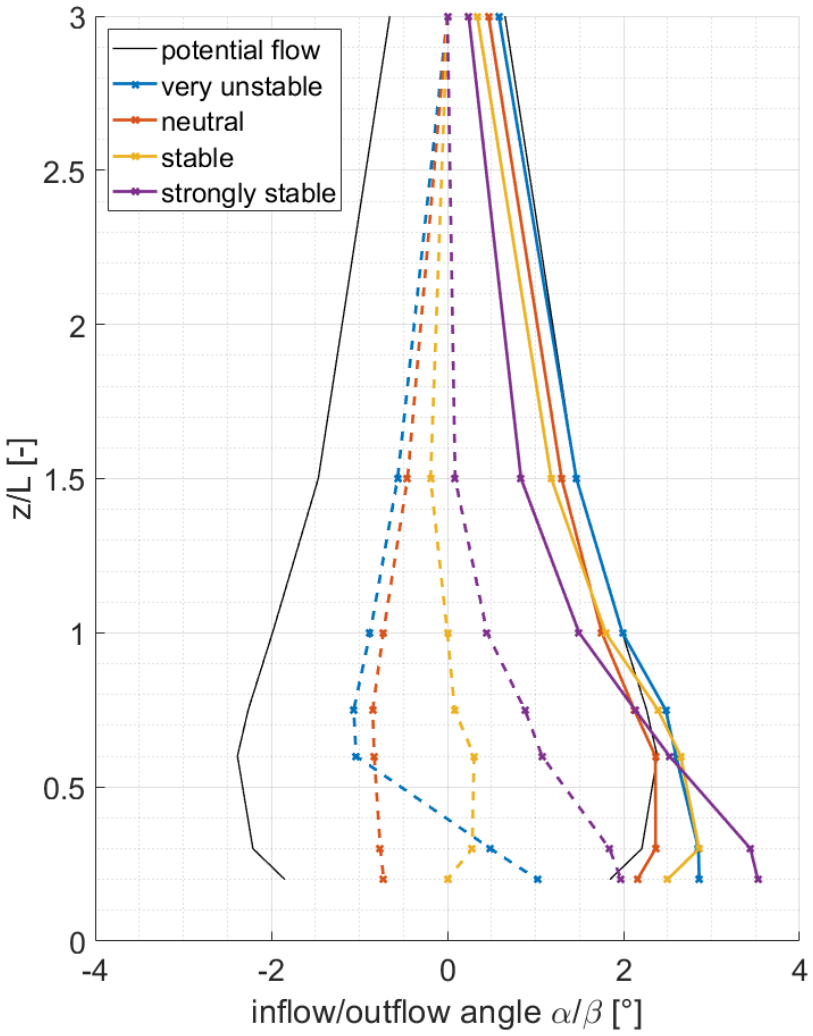

Figure 10.3: Inflow angle α (dashed) and outflow angle β (solid) in dependence of atmospheric stability**.** Results from Meteodyn WT (colored) and from the potential flow model (black) at 150 m measurement height and for a $\boldsymbol{\varphi}$ of 30° for an H/L ratio of 0.3. Meteodyn WT results for a high roughness length $\boldsymbol{z_0}$ of 0.5 m.

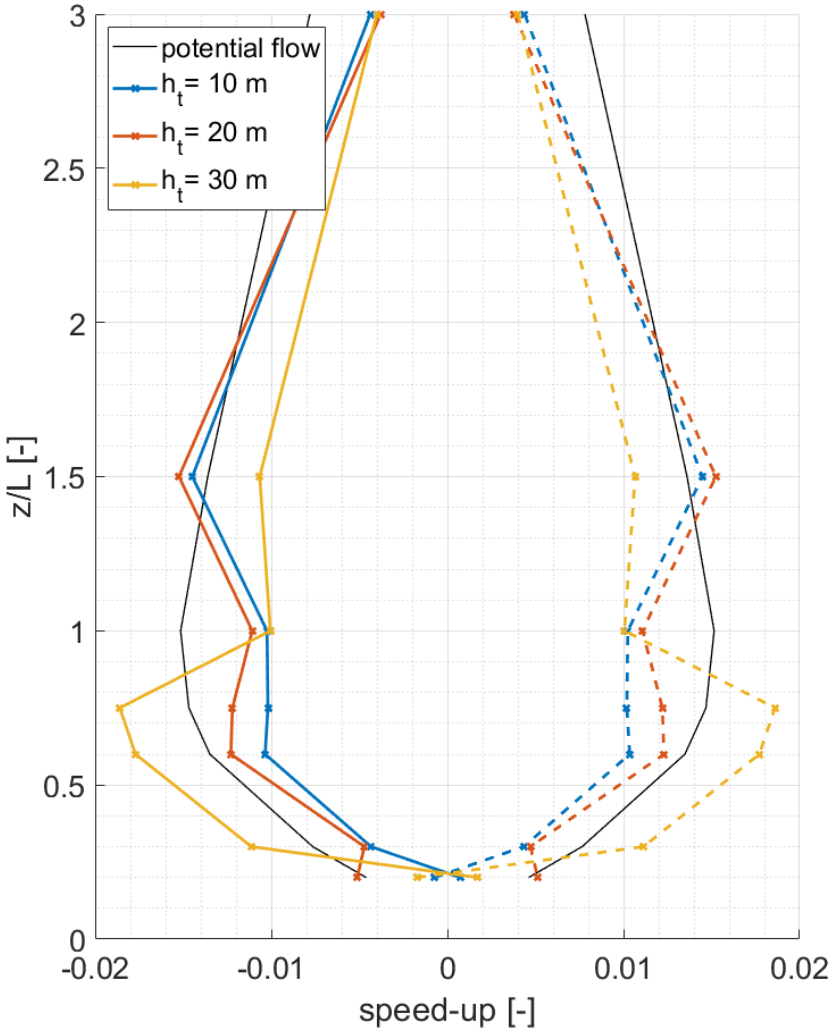

Figure 10.4: Speed-ups at inflow (dashed) and outflow (solid) in dependence of tree height $\boldsymbol{h_t}$. Results from Meteodyn WT (colored) and from the potential flow model (black) at 150 m measurement height and for a $\boldsymbol{\varphi}$ of 30° for an H/L ratio of 0.2. The forest density is medium.

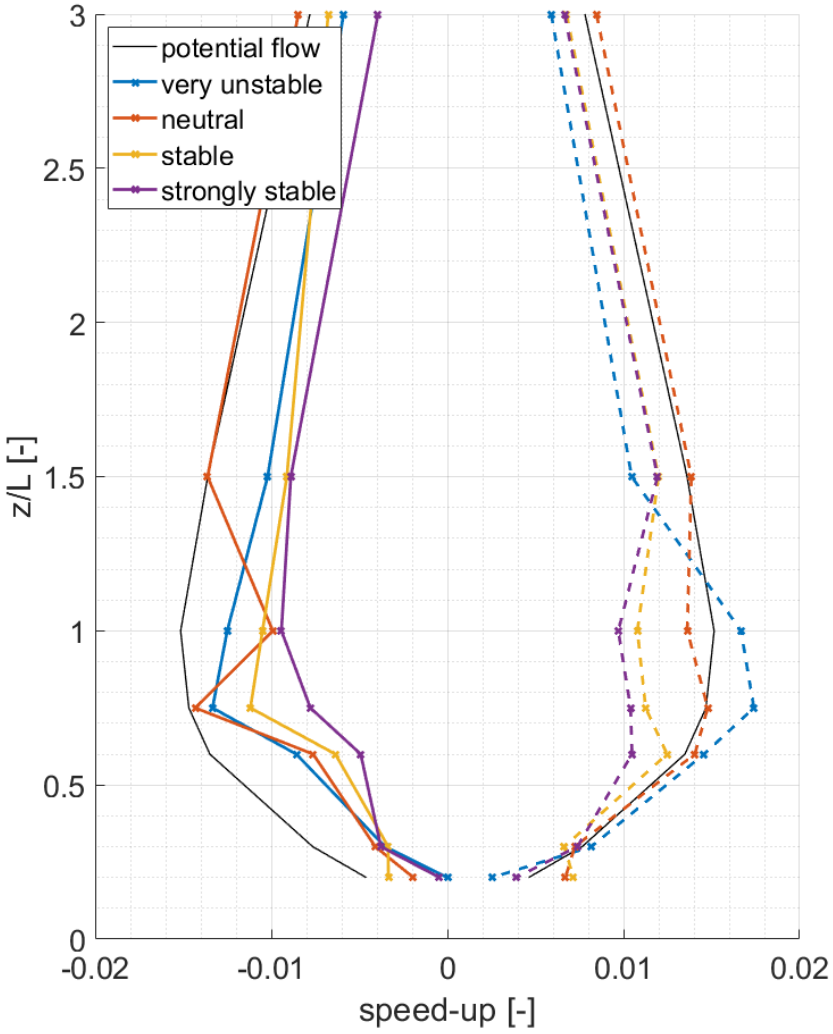

Figure 10.5: Speed-ups at inflow (dashed) and outflow (solid) in dependence of tree height $\boldsymbol{h_t}$. Results from Meteodyn WT (colored) and from the potential flow model (black) at 150 m measurement height and for a $\boldsymbol{\varphi}$ of 30° for an H/L ratio of 0.2. The forest density is medium.

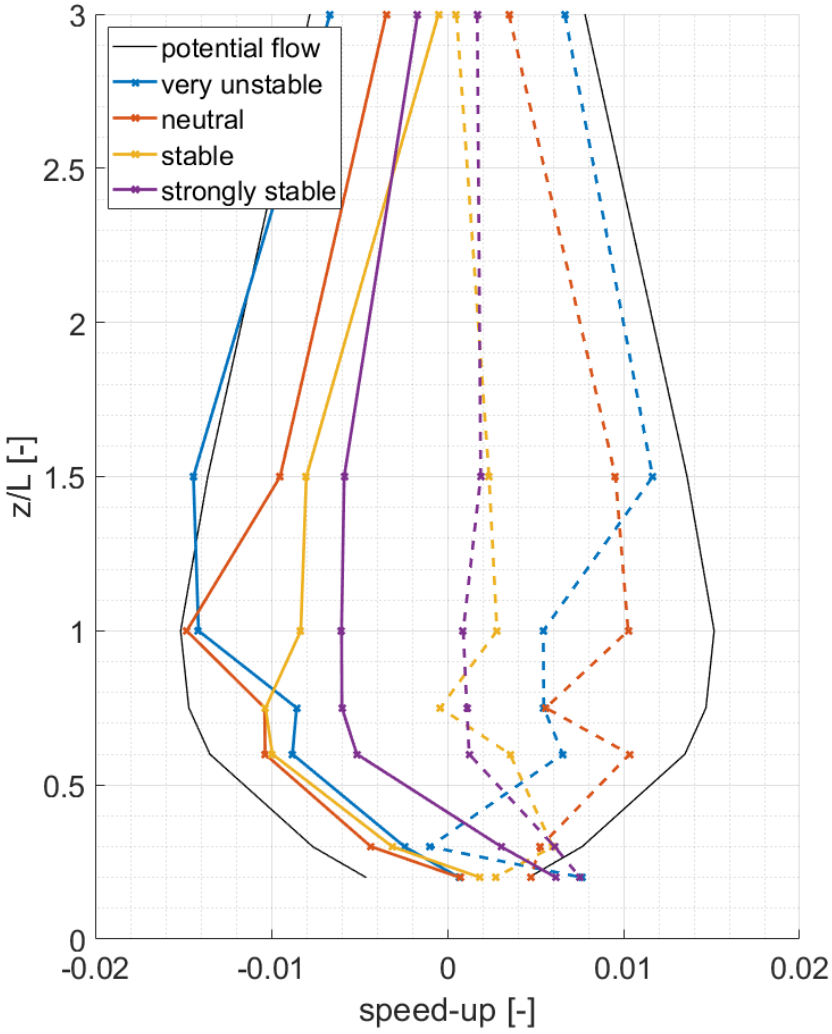

Figure 10.6: Speed-ups at inflow (dashed) and outflow (solid) in dependence of atmospheric stability**.** Results from Meteodyn WT (colored) and from the potential flow model (black) at 150 m measurement height and for a $\boldsymbol{\varphi}$ of 30° for an H/L ratio of 0.3. Meteodyn WT results for a high roughness length $\boldsymbol{z_0}$ of 0.5 m.

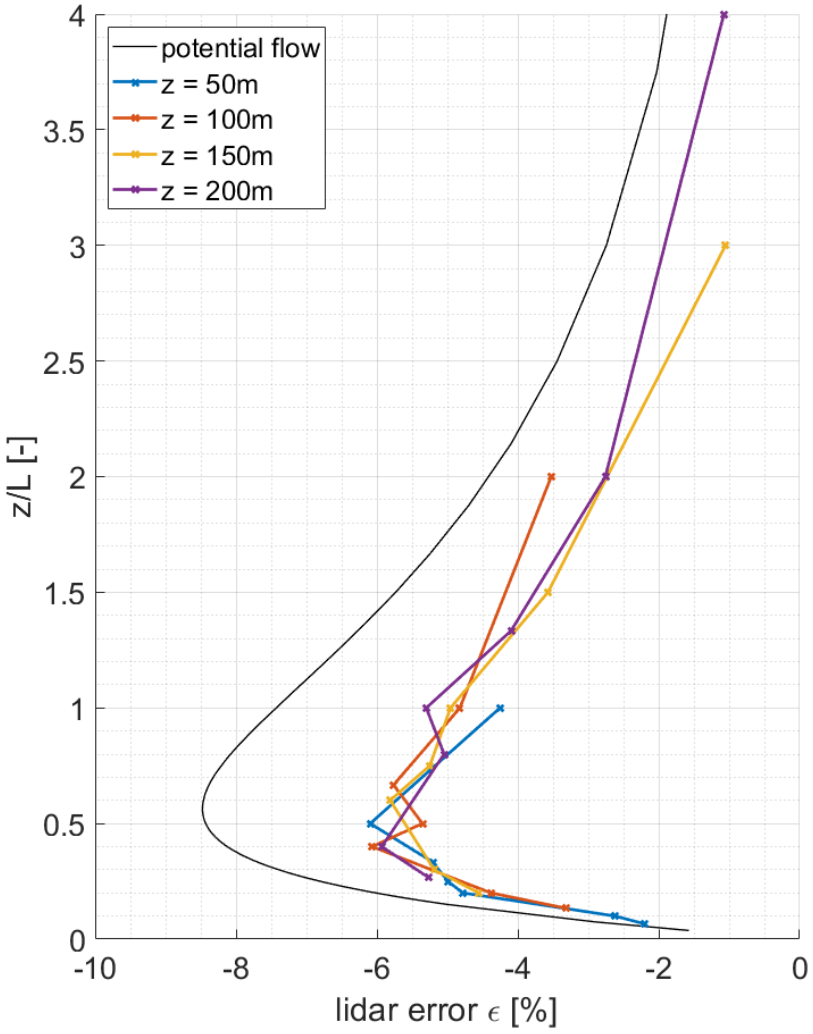

Figure 10.7: Lidar error $\boldsymbol{\varepsilon}$ in dependence of the measurement height z that is used to calculate the z/L ratio. Results are based on Meteodyn WT (colored) and the potential flow model (black) for an H/L ratio of 0.3 for a low roughness length $\boldsymbol{z_0}$ of 0.5m.

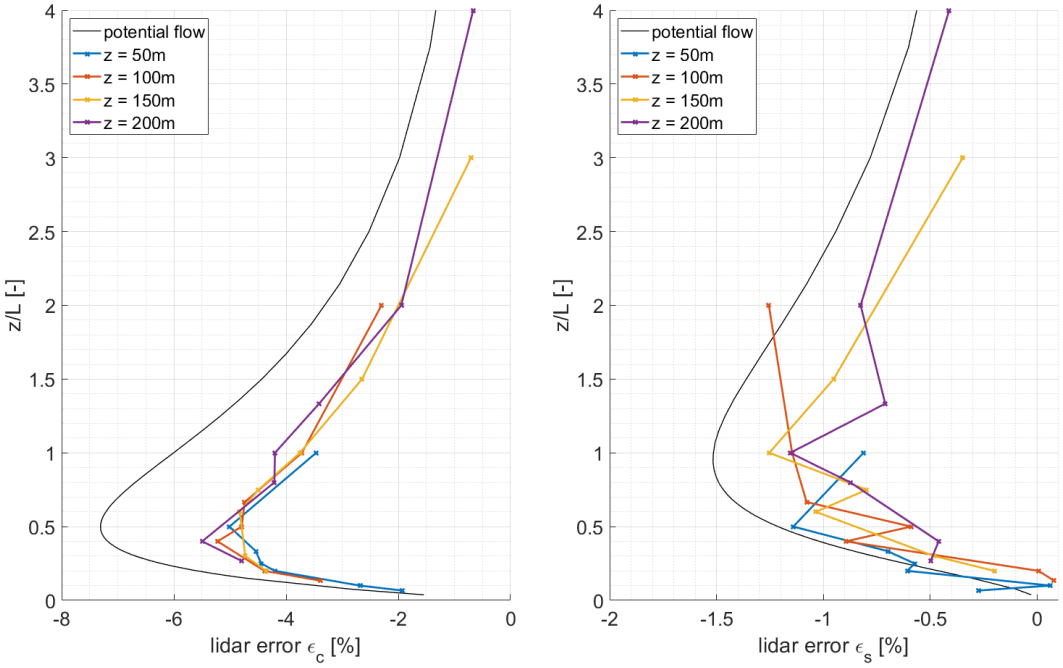

Figure 10.8: Lidar error $\boldsymbol{\varepsilon_c}$ (left) and $\boldsymbol{\varepsilon_s}$ (right) in dependence of the measurement height z that is used to calculate the z/L ratio. Results are based on Meteodyn WT (colored) and the potential flow model (black) for an H/L ratio of 0.3 for a low roughness length $\boldsymbol{z_0}$ of 0.5m.

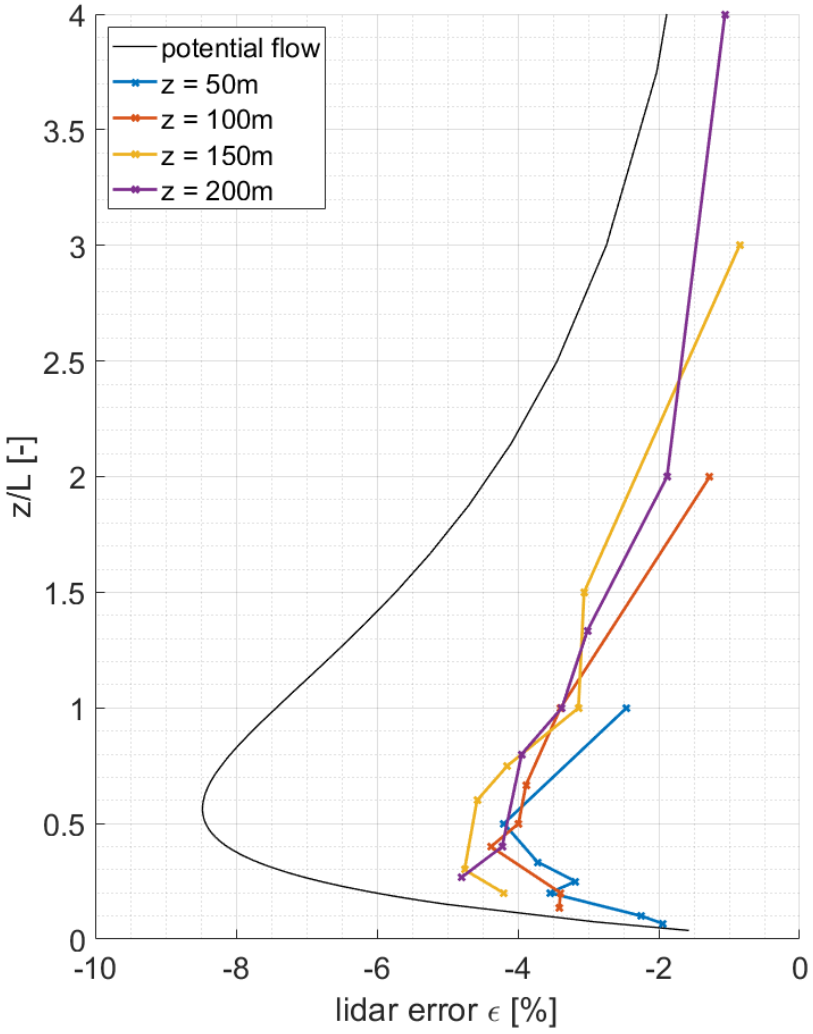

Figure 10.9: Lidar error $\boldsymbol{\varepsilon}$ in dependence of the measurement height z that is used to calculate the z/L ratio. Results are based on Meteodyn WT (colored) and the potential flow model (black) for an H/L ratio of 0.3 for the medium forest case with $\boldsymbol{h_t = 20m}$ and medium forest density.

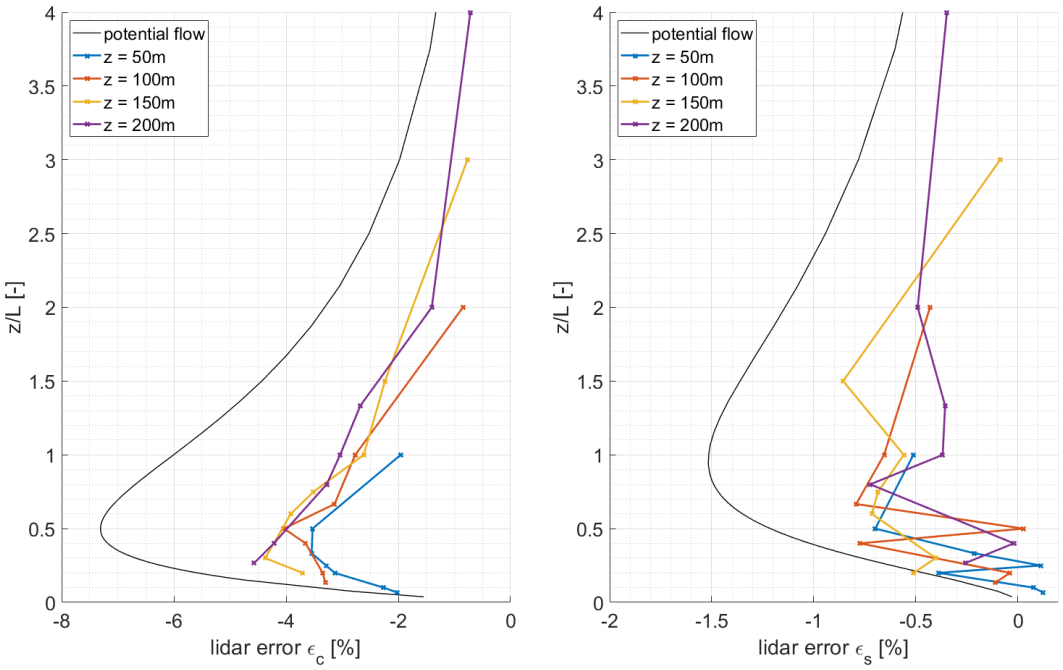

Figure 10.10: Lidar error $\boldsymbol{\varepsilon_c}$ (left) and $\boldsymbol{\varepsilon_s}$ (right) in dependence of the measurement height z that is used to calculate the z/L ratio. Results are based on Meteodyn WT (colored) and the potential flow model (black) for an H/L ratio of 0.3 for the medium forest case with $\boldsymbol{h_t = 20m}$ and medium forest density.

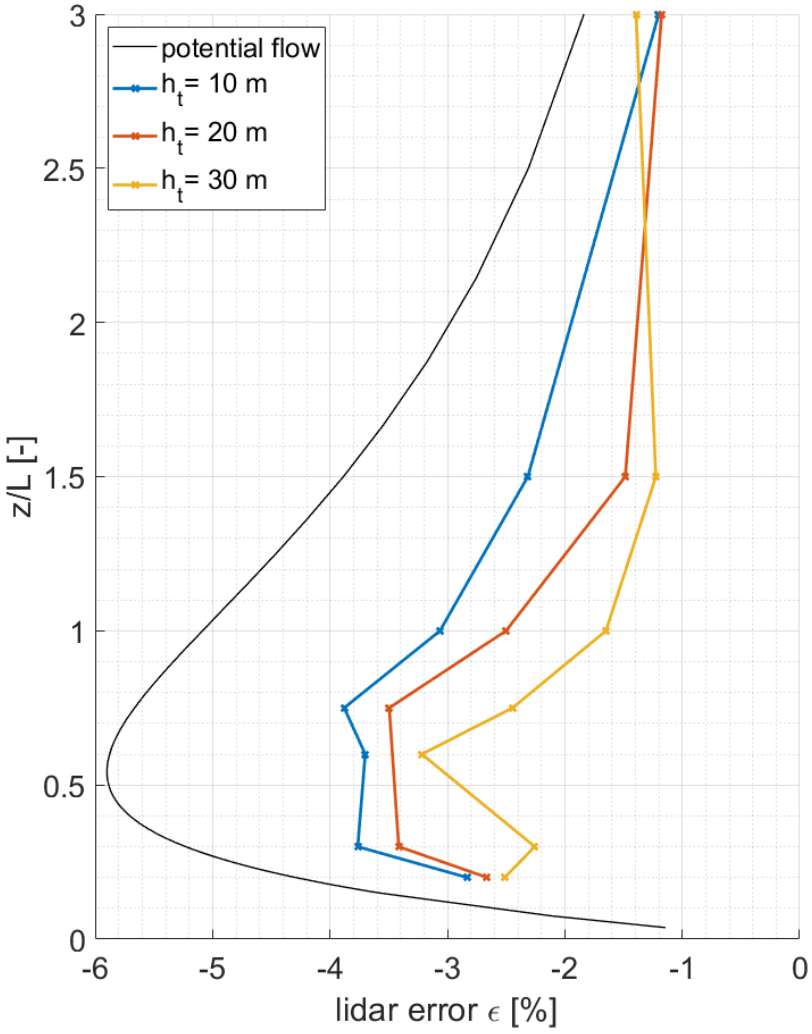

Figure 10.11: Lidar error $\boldsymbol{\varepsilon}$ in dependence of tree heights $\boldsymbol{h_t}$ between z/L ratios from 0 to 3. Results are based on Meteodyn WT (colored) and the potential flow model (black) for an H/L ratio of 0.2.

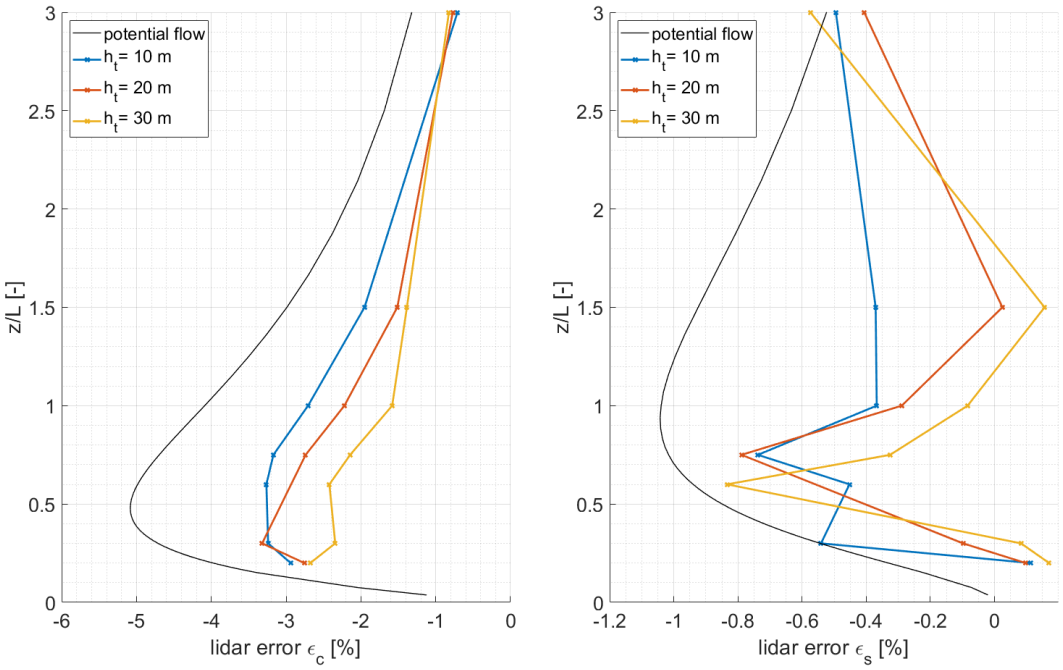

Figure 10.12: Lidar error $\boldsymbol{\varepsilon_c}$ (left) and $\boldsymbol{\varepsilon_s}$ (right) in dependence of tree heights $\boldsymbol{h_t}$ between z/L ratios from 0 to 3. Results are based on Meteodyn WT (colored) and the potential flow model (black) for an H/L ratio of 0.2.

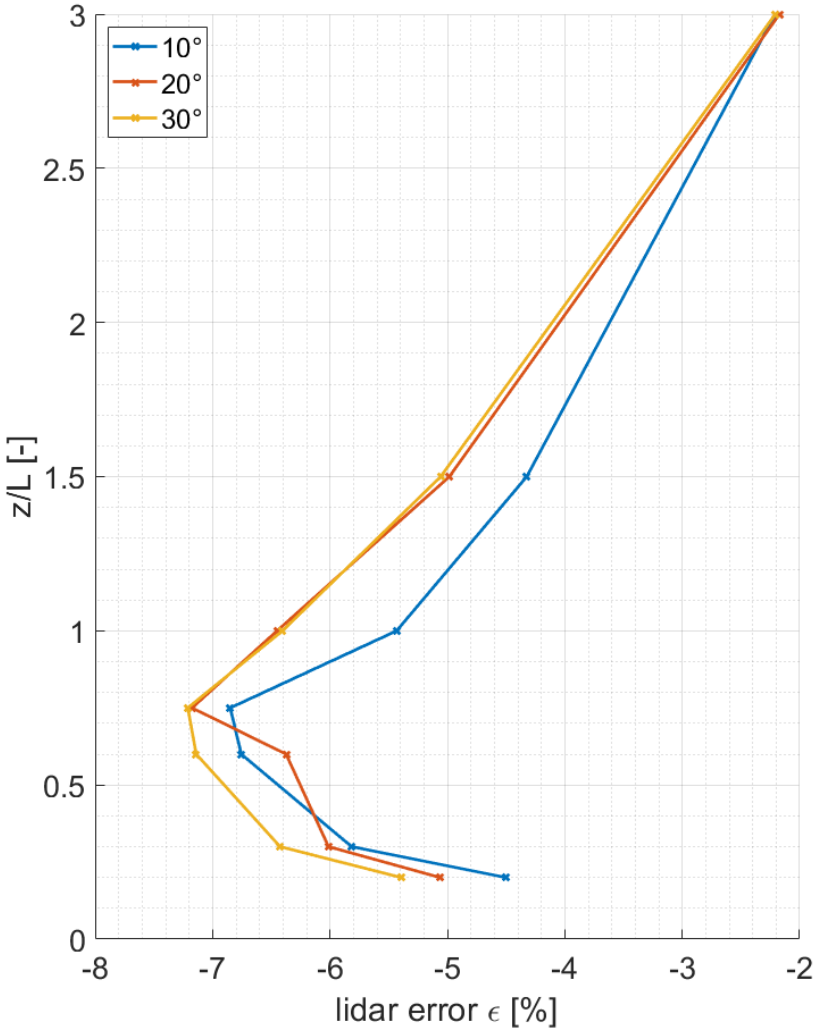

Figure 10.13: Lidar error $\boldsymbol{\varepsilon}$ in dependence of the half-cone opening angles between z/L ratios from 0 to 3. Results are based on Meteodyn WT for a high roughness length $\boldsymbol{z_0}$ of 0.005 m.

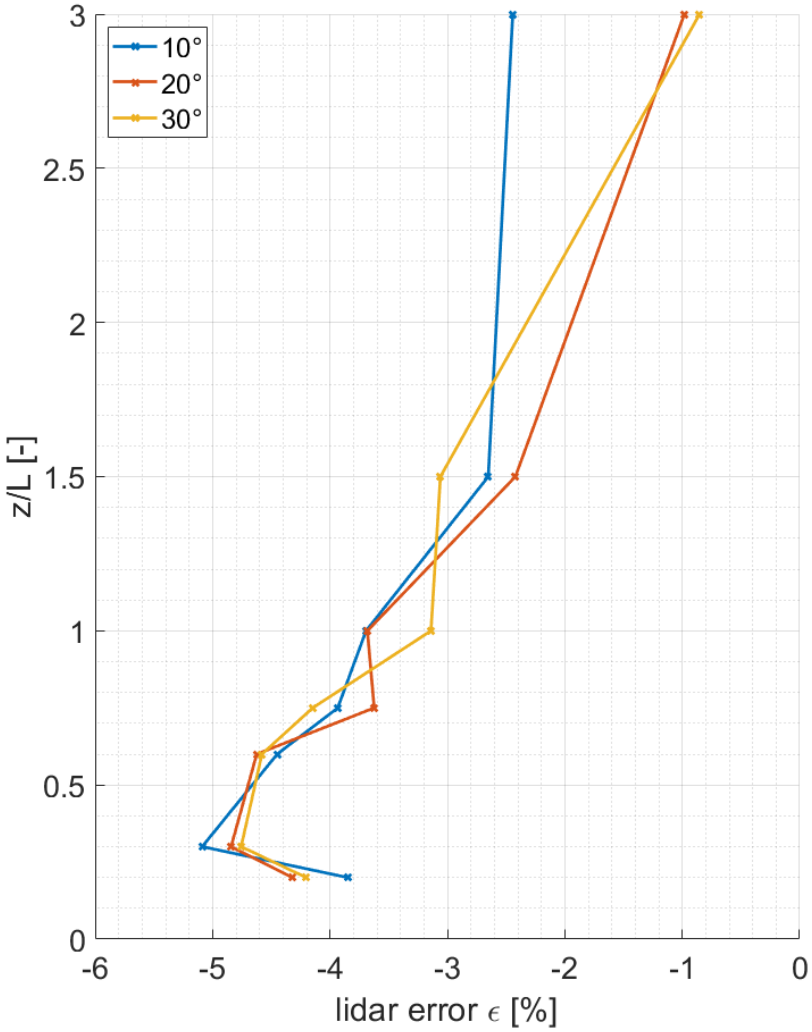

Figure 10.14: Lidar error $\boldsymbol{\varepsilon}$ in dependence of the half-cone opening angles between z/L ratios from 0 to 3. Results are based on Meteodyn WT for a medium dense forested case with a tree height of 20 m.

10.4 Author contributions to Klaas et al. 2015

Klaas, Tobias; Pauscher, Lukas; Callies, Doron (2015): LiDAR-mast deviations in complex terrain and their simulation using CFD. In *metz*. DOI: 10.1127/metz/2015/0637.

I managed the research project “Utilization of Inland Wind Power”, funded by the German Federal Ministry for Economic Affairs and Energy (BMWi), in which the measurement campaign took place. The project was originally initiated and planned by Doron Callies. Together with the technical staff of Fraunhofer IEE and Doron Callies, I planned and supervised the measurement campaign with a Leosphere Windcube v1 lidar next to the 200 m measurement mast at Rödeser Berg.

Furthermore, my role was the quality control and analysis of the lidar and mast data. Together with Lukas Pauscher, who had a supervisory role in this, I set up the methods and aims for the statistical data analysis and comparison of the lidar and mast data. I developed the program code in MATLAB that was used for data analysis.

I carried out the flow simulations with the tools WAsP Engineering 2.0, WindSim and Meteodyn WT that are presented in the study. I developed the program code in MATLAB for comparing the simulation results and the measured data. I adapted the available WAsP Engineering scripts to fit the lidar error estimation method given in the paper and developed the program code for lidar error estimation based on the WindSim and Meteodyn WT data in MATLAB. Based on the idea of Lukas Pauscher, I carried out and analyzed the simulations with different forest parameterizations.

I had the lead in writing the manuscript and finalizing the manuscript. Lukas Pauscher had a supervisory role in this and also contributed text to sections 1, 2, 3.1, 4.1, 4.2 and 5. Apart from that, Lukas Pauscher provided many valuable suggestions and discussion during the writing of the manuscript. Doron Callies participated in the writing process, also, with valuable suggestions, discussions and proofreading.

List of symbols

f_0	Frequency of the emitted laser light at the lidar
Δf	Frequency shift due to Doppler shift
f	Resulting frequency after Doppler shift
c	Speed of light
v_r	Radial wind speed
φ	Half-cone opening angle of the lidar measurement geometry
θ	Azimuth angle of the lidar measurement geometry
u	x-component of the wind speed vector
v	y-component of the wind speed vector
w	z-component of the wind speed vector
x	x-coordinate positive from west to east
y	y-coordinate positive from south to north
z	z-coordinate positive upwards or height above ground
N	North
E	East
S	South
W	West
v_{r1}	Radial wind speed at measurement point 1 (North)
v_{r2}	Radial wind speed at measurement point 2 (East)
v_{r3}	Radial wind speed at measurement point 3 (South)
v_{r4}	Radial wind speed at measurement point 4 (West)
v_{r5}	Radial wind speed at measurement point 5 (Center)
i	Index of the i-th measurement location or wind speed component at the i-th measurement location
$\boldsymbol{V}$	Wind speed vector
$\boldsymbol{V_L}$	Wind speed vector at the lidar location at measurement height
$\boldsymbol{V_4}$	Wind speed vector at the western measurement point
$\boldsymbol{V_2}$	Wind speed vector at the eastern measurement point
α	Inflow inclination angle
β	Outflow inclination angle
ε	Lidar error
ε_c	Lidar error due to flow curvature
ε_s	Lidar error due to speed-up effects
$\hat{u}$	x-component of the wind speed estimated by the lidar

$v_{r,in}$	Radial wind speed at the inflow measurement point
$v_{r,out}$	Radial wind speed at the outflow measurement point
V_{in}	Magnitude of the wind speed vector at the inflow
V_{out}	Magnitude of the wind speed vector at the outflow
u_{in}	x-component of the wind speed at the inflow
u_{out}	x-component of the wind speed at the outflow
k	Ratio of magnitude of the wind speed vector at the inflow over magnitude of the wind speed vector at the outflow
Δu	Speed-up between measurement point and x-component of the wind speed at the measurement location above the lidar
d	Displacement height
z_0	Roughness length
κ	Van-Karman constant
u_*	Friction velocity
ψ	Stream function in the potential flow model
η	z-coordinate-axis in the potential flow model (cylinder centered)
ζ	x-coordinate-axis in the potential flow model (cylinder centered)
η_0	Streamline in the potential flow model
H	Hill height
L	Hill half-width
R	Cylinder radius in the potential flow model
ζ_L	x-location of the lidar in the potential flow model
η_L	y-location of the lidar in the potential flow model
A	Ratio of tree height to roughness in Meteodyn WT
h_t	Tree height
F_V	Volume force due to forest modeling in Meteodyn WT
C_d	Drag force coefficient for forest density in Meteodyn WT
$\boldsymbol{U}$	Wind vector in Meteodyn WT
ρ	Air density
ε	Dissipation term in Meteodyn WT (only used in chapter 4.3.3 with this meaning, otherwise it is the lidar error)
ε_{cc}	Viscous dissipation in Meteodyn WT
ε_{fd}	Form drag dissipation in Meteodyn WT
C_μ	Term in turbulence model of Meteodyn WT
L_T	Turbulent length scale in Meteodyn WT
ν_T	Turbulent viscosity in Meteodyn WT
k	Turbulent kinetic energy in Meteodyn WT

l	Mixing length in Meteodyn WT
a	Parameter in the forest model of Meteodyn WT
l_0	Initial mixing length in Meteodyn WT
L^*	Monin-Obukhov length
Q_H	Kinematic heat flux
g	Gravitational constant
T	Air temperature
c_p	Specific heat
$\overline{w'T'}$	Heat flux
z_s	Height of surface layer in Meteodyn WT
z_h	Height of Transitional layer in Meteodyn WT

List of abbreviations

ABL	Atmospheric Boundary Layer
AEP	Annual energy production
BMWi	German Federal Ministry for Economic Affairs and Energy
CFD	Computational fluid dynamics
CW	Continuous wave
DBS	Doppler Beam Swinging
EU	European Union
FCR	Flow complexity recognition
Fraunhofer IEE	Fraunhofer Institute for Energy Economics and Energy System Technology
IEC	International Electrotechnical Commission
IPCC	Intergovernmental Panel on Climate Change
lidar	Light detection and ranging
MOST	Monin-Obukhov similarity theory
MWT	Meteodyn WT
NEWA	New European Wind Atlas
RANS	Reynolds-averaged Navier-Stokes
RSS	Root-sum-square technique
sodar	Sound detection and ranging
SRTM	Shuttle Radar Topography Mission
VAD	Velocity Azimuth Display
WEng	WAsP Engineering
WRA	Wind resource assessment

Erklärung nach §4, Abs. 9 der Promotionsordnung

Ich versichere, dass ich die von mir vorgelegte Dissertation selbständig angefertigt, die benutzten Quellen und Hilfsmittel vollständig angegeben und die Stellen der Arbeit − einschließlich Tabellen, Karten und Abbildungen −, die anderen Werken im Wortlaut oder dem Sinn nach entnommen sind, in jedem Einzelfall als Entlehnung kenntlich gemacht habe; dass diese Dissertation noch keiner anderen Fakultät oder Universität zur Prüfung vorgelegen hat; dass sie − abgesehen von unten angegebenen Teilpublikationen − noch nicht veröffentlicht worden ist, sowie, dass ich eine solche Veröffentlichung vor Abschluss des Promotionsverfahrens nicht vornehmen werde. Die Bestimmungen der Promotionsordnung sind mir bekannt. Die von mir vorgelegte Dissertation ist von Prof. Dr. Stefan Emeis betreut worden.

Tobias Klaas, 10.01.2020